This work introduces forward-dynamics simulations of a musculoskeletal system, in which all components are represented as volumetric objects. Furthermore, the mechanical behaviour of the muscle-tendon complexes are modelled using the theory of finite elasticity.
To demonstrate the feasibility of the framework the Upper Limb Model is introduced. It consists of three bones (humerus, ulna and radius), a one-degree-of-freedom elbow joint, and an antagonistic muscle pair (biceps and triceps brachii), and takes into consideration the contact between the muscles and the humerus.
Numerical studies have shown that the proposed Upper Limb Model is capable of predicting realistic arm moments and muscle forces for the entire range of muscle activation and arm motion. Additionally, first realistic insights in muscle-bone contact forces and fibre stretch distributions are possible.

Michael Sprenger

ISBN 978-3-946412-01-4

M. Sprenger

Modelling the Musculoskeletal System

CBM-02 (2015)

A 3D Continuum-Mechanical Model for Forward-Dynamics Simulations of the Upper Limb

Michael Sprenger

Universität Stuttgart

A 3D Continuum-Mechanical Model for Forward-Dynamics Simulations of the Upper Limb

Von der Fakultät Bau- und Umweltingenieurwissenschaften und
dem Stuttgart Research Centre for Simulation Technology
der Universität Stuttgart zur Erlangung der Würde
eines Doktor-Ingenieurs (Dr.-Ing.)
genehmigte Abhandlung

von

Dipl.-Ing. Michael Sprenger

aus

Aalen

Hauptberichter:	Prof. Oliver Röhrle, PhD
1. Mitberichter:	Prof. Dr.-Ing. Stefan Diebels
2. Mitberichter:	Jun.-Prof. Dr. Syn Schmitt

Tag der mündlichen Prüfung: 9. Oktober 2015

Institut für Mechanik (Bauwesen) der Universität Stuttgart
Research Group on Continuum Biomechanics and Mechanobiology
Prof. Oliver Röhrle, Ph. D.
2015

Report No.: CBM-02
Institut für Mechanik
Lehrstuhl für Kontinuumsmechanik
Research Group on Continuum Biomechanics and Mechanobiology
Universität Stuttgart, Germany, 2015

Editor:
Prof. O. Röhrle, Ph. D.

Institut für Mechanik
Lehrstuhl für Kontinuumsmechanik
Research Group on Continuum Biomechanics and Mechanobiology
Universität Stuttgart
Pfaffenwaldring 7
70569 Stuttgart, Germany

ISBN 978–3–946412–01–4
(D93 – Dissertation, Universität Stuttgart)

Acknowledgements

Diese Arbeit ist im Rahmen meiner Tätigkeit als wissenschaftlicher Mitarbeiter bei der SimTech Research Group für Continuum Biomechanics and Mechanobiology am Institut für Mechanik (Bauwesen), Lehrstuhl II der Universität Stuttgart entstanden. Während dieser Zeit haben viele Menschen inner- aber auch außerhalb der Uni zur Realisierung dieser Arbeit beigetragen und dafür möchte ich allen danken. Obwohl hier nicht Alle persönlich angesprochen werden können, geziehmt es sich doch, auf die ein oder andere Person einzugehen.

Zu aller erst möchte ich natürlich meinem Chef und Doktorvater Oliver Röhrle danken, der die Ehre hatte meinen Kollegen Thomas Heidlauf und mich als seine ersten Doktoranden betreuen zu dürfen. Über die vielen Jahre hatte er nicht nur immer ein offenes Ohr für fachliche Belange, sondern auch für alle Anderen. Niemand wird gerne ständig verbessert oder angewiesen etwas anders zu machen. Aber mit etwas Abstand kann ich sagen, dass ich immer von seinem Rat profitiert habe.

Zum Glück hat sich der kollegiale Austausch am Institut nicht immer nur auf das Fachlichliche beschränkt, sondern hat sich bei vielen sich bietenden Gelegenheiten sehr viel bunter gestaltet. Von allen Kollegen habe ich wohl am meisten Zeit mit meinen langjährigen Bürokollegen, Thomas Heidlauf und Sergio Morales Ortuño, verbracht. Obwohl die Büros im Laufe der Zeit immer kleiner zu werden schienen, war die Atmosphäre immer produktiv und entspannt. Später sogar musikalisch. Eigentlich müsste man den Kreis der Kollegen sogar noch erweitern. Denn zu Beginn meiner Promotion gab es eine enge Zusammenarbeit mit der Abteilung für Modellierung und Simulation im Sport des Instituts für Sport- und Bewegungswissenschaften und Nils Karajan. Ich glaube, alle haben von der Weltsicht der jeweils anderen profitiert. Aus dieser produktiven Gemeinschaft ist z.B. der Workshop für junge Nachwuchswissenschaftler in der Mechanik mit dem Schwerpunkt Biomechanik entstanden, der zufällig immer in der nähe eines Skigebietes stattfand.

Danken muss ich natürlich auch unseren Computeradministratoren insbesondere David Koch, Maik Schenke, Patrick Schröder und Reiner Dietz. Wie wichtig sie sind, merkt man immer erst, wenn etwas nicht mehr geht.

Speziellen Dank gilt auch jenen, die versucht haben meine Dissertation sprachlich adequat anzupassen. Namentlich waren dies Sook-Yee Chong, Daniel Wirtz, Mylena Mordhorst, Kai Häberle, Michelle Zasada, Ellankavi Ramasamy und natürlich Cécile Lascaux.

Further, I would like to thank the guys from the Gold Coast Campus at the Griffith University in Australia where I stayed for three beautiful months. First, Prof. David Lloyd for providing the opportunity to stay at his institute and Meg for helping me with organisational details. David Saxby, Hoa and Gramsy always had a helping hand, especially when I needed help conducting my experiments. Pauline and Massimo helped me to process and analyse my data by providing the forward-inverse model adapted to my needs. Wenx made my stay a real pleasure by offering me a room in her beach house.

Und natürlich möchte ich auch meiner Familie danken, die es mir in den letzten Jahren

zwar nicht immer leicht gemacht hat, aber mir trotzdem immer einen Rückhalt bot und mir alles gegeben hat, was sie konnte. Ganz zu schweigen von einer unbekümmerten Kindheit und Jugend.

Zuletzt möchte ich der Deutschen Forschungsgemeinschaft (DFG) danken, die den ersten Teil meiner Arbeit im Rahmen des Exzellenzclusters Simulation Technology (EXC 310/1-2) an der Universität Stuttgart finanziert hat. Später wechselte die Finanzierung und deshalb möchte ich mich auch dem European Research Council under the European Union's Seventh Framework Programme (FP7/2007-2013), ERC Starting Grant LEAD under grant agreement n° 306757 danken.

Contents

Deutsche Zusammenfassung

Jeder Mensch braucht seinen Bewegungsapparat – zu fast allen Aktivitäten. Solange er reibungslos funktioniert, macht man sich darüber kaum Gedanken. Sobald sich das aber ändern sollte und man nach den Ursachen sucht, merkt man schnell wie komplex der ganze Bewegungsapparat ist.

Untersuchungen am Lebewesen sind immer heikel, insbesondere am Lebenden. Zusätzlich zu dem schon komplexen Normalzustand, wie auch immer dieser zu definieren ist, gibt es noch eine fast unendliche Vielfalt an Abnormalitäten. Will man die Kinetik von Bewegungsapparaten, also die Bewegung von unter Einwirkung von Kräften beschleunigten Körpern, untersuchen, kann man ohne in den Körper hinein zu schauen nur äußere Kräfte messen. Ist man aber z.B. daran interessiert wie groß die Kräfte sind, die auf einen Prothesenstumpf, auf eine Bandscheibe oder auf eine Hüftgelenkspfanne wirken, ist man immer mit dem Problem konfrontiert, dass man den Bewegungsapparat nicht einfach messen oder in ihn hineinschauen kann. Also was tun?

Der erste Schritt den Bewegungsapparat zu untersuchen waren, in vitro Experimente; also Untersuchungen am Objekt, das sich nicht in seiner natürlichen Umgebung befindet. Da diese nur sehr eingeschränkt über die wirklich vorherrschenden Zustände Einsicht geben können, bemüht man sich schon seit vielen Jahrzehnten um mathematische Modelle von Bewegungsapparaten. Da diese Modelle schnell Gleichungssysteme hervorbringen, die nicht mehr analytisch zu lösen sind, kann der Computer behilflich sein, diese Systeme numerisch zu lösen.

Der Stand der Technik von Computermodellen, die den menschlichen Bewegungsapparat abbilden, basieren fast ausschließlich auf Mehrkörpersimulationen. Dabei werden die starren Körper zu Massenpunkten mit dazugehörigem Flächenträgheitstensor reduziert. Die Bewegungen der einzelnen Körper erfüllen die *Newton-Euler* Gleichungen. Die Modelle für die berücksichtigten Muskeln basieren weitestgehend auf der Idee von Hill (1938) und werden durch ein mechanisches Ersatzsystem beschrieben. Diese Muskelmodelle können mittels gewöhnlichen Differentialgleichungen formuliert werden (Hardt, 1978; Patriarco et al., 1981; Zajac, 1989; Günther et al., 2007). Geometrisch wird deren Wirkungslinie durch einen Ansatz- und einen Endpunkt definiert. Neuere Modelle beinhalten via-Punkte und Umlenkflächen an denen die Richtung des Muskels angepasst werden kann (Garner and Pandy, 2000). Trotzdem oder gerade wegen ihrer Einfachheit sind diese Modelle im Stande mehrere zig Muskeln zu berücksichtigen und damit den menschlichen Bewegungsapparat so realitätsnah abzubilden, dass ganze Bewegungsmuster untersucht werden können (Pandy et al., 1990; Günther and Ruder, 2003). Aufgrund ihrer geometrischen Reduktion sind Mehrkörpersimulationen jedoch nur sehr eingeschränkt in der Lage Fragestellungen, wie z.B. die Kontaktkräfte zwischen verschiedenen Objekten, die Druckverteilung in einem Prothesenstumpf oder die Druckverteilung in einem Hüftgelenk, zu erörtern.

Kontinuumsmechanische Ansätze sind dazu generell besser in der Lage, da sie struk-

turelle und lokale Effekte sowie verschiedene Eigenschaften, wie z.B. komplexe Muskelgeometrien, Faserverläufe, Muskelaktivierungsprinzipien, Mikrostrukturen und Muskelknochenkontakt, berücksichtigen können. Aufgrund des erheblich höheren Rechenaufwandes ist der kontinuumsmechanische Ansatz jedoch nur sehr eingeschränkt einsetzbar. Deshalb ist es wichtig, geeignete Lösungsstrategien zu entwickeln, um das Potential dieses Ansatzes besser ausschöpfen zu können.

Der aktuelle Stand der Technik von kontinuumsmechanischen Modellen bemüht sich noch fast ausschließlich mit der Untersuchung einzelner Muskeln. Die bekannten Muskelmodelle unterscheiden sich methodologisch in unterschiedlichen Bereichen in ihrer Komplexität, da ein gesamtheitliches Modell noch zu vielschichtig wäre. Die wichtigsten Arbeiten berücksichtigen den elektrochemischen Zellzustand und koppeln ihn zur Mechanik (Heidlauf and Röhrle, 2014; Röhrle et al., 2008), zusätzlich zum reinen Muskelgewebe auch die Sehne (Lemos et al., 2005), komplexe Muskelgeometrien (Böl et al., 2011), komplexe Faserverteilungen (Blemker and Delp, 2005; Fernandez et al., 2012), Mikrostrukturen (Sharafi and Blemker, 2010; Sharafi et al., 2011) oder Kontakt (Fernandez and Hunter, 2005). Aufgrund der Vor- aber auch der Nachteile der, wie bereits zuvor motiviert, verschiedenen Ansätze gilt es sich neuartige Lösungsstrategien auszudenken, die es ermöglichen offene Fragestellungen zu erörtern und zu beantworten.

Es is ein intrinsisches Problem des Bewegungsapparates, dass jedes Gelenk im Körper weniger Freiheitsgrade besitzt als Muskeln an ihm agieren. Deshalb stellt sich immer das mathematisch nicht eindeutig zu lösende Problem, wie die jeweiligen Gelenkmomente auf die agierenden Muskeln verteilt werden müssen. Das daraus entstehende sogenannte Muskelredundanzproblem lässt sich mit zwei Ansätzen beschreiben: vorwärts- oder invers-dynamisch. Die Ansätze unterscheiden sich darin, dass beim vorwärts-dynamischen Ansatz die Muskelaktivität bekannt ist oder für eine Bewegung mit vorgegebenen Start- und Zielpunkt bestimmt werden müssen. Die daraus resultierenden Muskelkräfte ergeben eine Bewegung. Beim inversen Ansatz wird die Bewegung vorgegeben und es müssen die Muskelkräfte oder -momente bestimmt werden, um die die vorgegebene Bewegung zu ermöglichen. Beide Ansätze haben ihre Vor- und Nachteile (Erdemir et al., 2007; Otten, 2003).

Das Ziel dieser Dissertation ist es, einen ersten Ansatz zu entwickeln, der es ermöglicht, kontinuumsmechanische Muskelmodelle zu verwenden, um deren Vorteile bei der Untersuchung (von Teilen) des Bewegungsapparates zu nutzen. Da kontinuumsmechanische Modelle auch in naher Zukunft noch zu rechenintesiv sein werden, um das Muskelredundanzproblem zu lösen, müssen neue Methoden entwickelt werden. So kann das Modell durch geschickte Modellannahmen soweit vereinfacht werden, bis es lösbar wird und dennoch die Realität ausreichend abbilden kann. Als Alternative könnte eine Kopplung zu anderen Methoden geschaffen werden.

Um ein Modell mit kontinuumsmechanischen Muskeln zu entwickeln, das sowohl als eigenständiges Modell verwendet werden kann als auch zu anderen Modellansätzen gekoppelt werden kann, wird ein möglichst einfacher Teil des Bewegungsapparates gewählt. Für diese Arbeit wird der rechte Arm, bestehend aus Humerus, Radius und Ulna gewählt. Dabei bilden die drei Knochen im Ellbogen ein einfaches eindimensionales Scharniergelenk. Da ein Scharniergelenk nur einen Rotationsfreiheitsgrad besitzt, reicht ein antagonistisches Muskelpaar, um eindeutige Bewegungen zu ermöglichen. Als antagonistisches Muskelpaar werden Triceps und Biceps Brachii gewählt. Somit umgeht man auch das

Muskelredundanzproblem. Weitere Synergisten werden vernachlässigt. Mit Hilfe des gewählten mechanischen Ersatzsystems ist es nun möglich, das eingeführte Armmodell mit Berücksichtigung der Momentenbilanz des Unterarms, der sich aus Ulna und Radius bildet, bezüglich des Ellbogenrotationszentrums zu untersuchen. Da den Muskeln die Muskelaktivität vorgegeben wird und die sich einstellende Gleichgewichtsposition untersucht wird, handelt es sich bei dem hier vorgestellten Modell um einen vorwärtsdynamischen Ansatz.

Dazu wird in Kapitel 1 der aktuelle Stand der Forschung, für die Untersuchung des Bewegungsapparates im Allgemeinen und für den Arm im Speziellen, vorgestellt. Um die Komplexität des menschlichen Bewegungsapparates und deren Komponenten darzustellen, werden in Kapitel 2 die anatomischen und physiologischen Grundlagen des Bewegungsapparates vorgestellt. Da biologische Gewebe, so auch Muskeln, großen Deformationen ausgesetzt sind, wird in Kapitel 3 das kontinuumsmechanische Konzept der Finiten Elastizität eingeführt. In Kapitel 4 wird das Konstitutivmodell für den Muskel und den Muskel-Sehnen Apparat entwickelt. Das entstehende Randwertproblem lässt sich leider nur numerisch lösen. Deshalb wird in Kapitel 5 die Finite Elemente Methode eingeführt, die zur räumlichen Diskretisierung verwendet wird. Um das Potential des volumetrischen Ansatzes voll auszuschöpfen, wird zwischen den agierenden Muskeln und dem Humerus Kontakt berücksichtigt. Die kontaktmechanischen, -physikalischen bzw. die -numerischen Grundlagen werden in Kapitel 6 vorgestellt. In Kapitel 7 wird das Oberarmmodell entwickelt. Es beginnt mit der Einführung der Anatomie des Oberarms, und beinhaltet des Weiteren die Modellannahmen für die beteiligten Objekte, die angewandten Randbedingungen, die verwendeten Muskelsehnenmaterialparameter und das mechanische Ersatzsystem, um nach einem physiologischen Gleichgewicht lösen zu können. Da die Hebelarme eine wichtige Größe zur Bestimmung des Gelenkmomentes sind, werden zwei verschiedene Methoden vorgestellt. Die erste Methode, die von An et al. (1984) entwickelt wurde, wird schon viele Jahre in der Forschung verwendet und zeigte gute Resultate. Die zweite Methode wird erst durch die Verwendung eines volumetrischen Ansatzes und durch die vektorielle Beschreibung möglich. In Kapitel 8 werden drei Alternativen zur Lösung des Muskelredundanzproblem dargestellt. Dafür wird im ersten Schritt die Muskelaktivität vorgegeben und untersucht, ob das Armmodell einen Gleichgewichtszustand finden kann. Im zweiten Schritt wird ein vorwärts-invers-dynamisches Modell verwendet, um realistische Muskelaktivitäten zu generieren. Dazu wurden Messungen durchgeführt, bei denen mit einem Dynamometer das Elbogenmoment und die Körperhaltung und mit EMG-Elektroden die Muskelaktivität gemessen wurde. Eine dritte Möglichkeit, die Kopplung von kontinuumsmechanischen Modellen zu Mehrkörpersimulationen, wird nur skizziert, ist aber einen vielversprechenden Ansatz für zukünftige Forschung. Kapitel 9 stellt die Ergebnisse der beiden Muskel über ihren kompletten Bewegungsraum dar. Dabei wurden Muskelkräfte, Faserstretchverteilungen und die Auswirkungen der Kraftschraube ermittelt. In Kapitel 9.2 wird gezeigt, dass das Armmodell eine Gleichgewichtslage findet. Des Weiteren wird das Konvergenzverhalten und der Einfluss der verschieden Hebelarme untersucht. In Kapitel 9.3 werden die Ergebnisse des vorwärts-invers-dynamischen Modells vorgestellt um es mit den Ergebnissen des Armmodells zu vergleichen. Kapitel 10 diskutiert die Ergebnisse und setzt sie in Relation zueinander. Kapitel 11 zieht ein Fazit und gibt Anregungen für die Fortführung dieser Arbeit.

Nomenclature

The common notation of modern tensor calculus is used in this monograph. Moreover, the particular symbols are chosen according to the established nomenclature of our institute (Ehlers, 2010).

Conventions

Index and suffix conventions

$i, j, n, \ldots$	indices (control variables) as super- or subscripts
d	dimensional index
e	element index
m	index referring to the involved muscle or external force, i.e. $m \in \{B, T, E\}$ for biceps, triceps, and external load
$\mathrm{d}(\,\cdot\,)$	differential operator
$\partial(\,\cdot\,)$	partial derivative operator
$\dot{(\,\cdot\,)} = \mathrm{d}(\,\cdot\,)/\mathrm{d}t$	total time derivatives
$\mathrm{grad}\,(\,\cdot\,)$	gradient with respect to the current configuration
$\mathrm{Grad}\,(\,\cdot\,)$	gradient with respect to the reference configuration
$\mathrm{div}\,(\,\cdot\,)$	divergence with respect to the current configuration
$\mathrm{Div}\,(\,\cdot\,)$	divergence with respect to the reference configuration
$\det(\,\cdot\,)$	determinant operator
$\mathrm{tr}\,(\,\cdot\,)$	trace operator
$\mathrm{cof}(\,\cdot\,)$	cofactor operator
$(\,\cdot\,)^T$	transverse operator
$(\,\cdot\,)^{-1}$	inverse operator
$\delta(\,\cdot\,)$	test functions of primary unknowns
$\bar{(\,\cdot\,)}$	prescribed quantities
$\tilde{(\,\cdot\,)}$	measures related to the closest point projection
$(\,\cdot\,)_0$	initial values or values in the reference configuration
$(\,\cdot\,)^h$	spatially discretised quantities within numerical investigations
$(\,\cdot\,)_n$	time discretised quantities at $t = t_n$ time within numerical investigations
$(\,\cdot\,)^C$	referring to the area where contact may occur
$(\,\cdot\,)^M$	referring to the master body

$(\cdot)^S$	referring to the slave body
$(\cdot)^\chi$	referring to the mechanical primary variable
$(\cdot)^p$	referring to the hydrostatic pressure as primary variable

Symbols

The order of the table is Greek before Latin following calligraphic letters. Small letters precede capital letters.

Symbol	Unit	Description
α	[-]	muscle activation
$\beta_1, \beta_2, \beta_3$	[-]	coefficients defining the second-order activation dynamics
γ_1, γ_2	[-]	coefficients defining the second-order activation dynamics
γ_{M}	[-]	material parameter distinguishing between muscle and tendon tissue
γ_{ST}	[-]	material parameter distinguishing between muscle-tendon or other isotropic soft tissue
ϵ_N	$[\mathrm{N/m^3}]$	contact penalty factor
ε		threshold parameter
θ	$[^\circ]$	elbow flexion angle
λ_i	[-]	eigenvalues of a tensor
λ	[-]	fibre stretch
λ_f	[-]	muscle fibre stretch
λ_f^{opt}	[-]	optimal muscle fibre stretch
μ	$[\mathrm{N/m^3}]$	shear modulus
$\nu_{\mathrm{asc/desc}}$	[-]	material parameter of Ψ_{active} that influences the steepness of the belly curve
ρ	$[\mathrm{kg/m^3}]$	material density
σ_{max}	$[\mathrm{N/m^2}]$	stress that a maximally activated muscle can produce at optimal length λ_f^{opt}
$\boldsymbol{\phi}$	[-]	vector valued global basis function for the ansatz function
$\boldsymbol{\psi}$	[-]	vector valued global basis function for the test function
$\Delta W_{\mathrm{asc/desc}}$	[-]	material parameter of Ψ_{active} that influences the width of the belly curve
Γ		spatial boundary of the aggregate body $\mathcal{B}$
Γ^C		boundary, where contact may occur
Γ^σ		boundary, where *Neumann* boundary conditions apply
Γ^u		boundary, where *Dirichlet* boundary conditions apply
Ψ	$[\mathrm{J/m^3}]$	volume specific strain energy function
Ψ_{muscle}	$[\mathrm{J/m^3}]$	volume specific strain energy function of the muscle

Ψ_{MTC}	$[\,\mathrm{J/m^3}\,]$	volume specific strain energy function of the muscle-tendon complex
Ψ_{aniso}	$[\,\mathrm{J/m^3}\,]$	anisotropic part of the volume specific solid strain energy function
Ψ_{iso}	$[\,\mathrm{J/m^3}\,]$	isotropic part of the volume specific strain energy function
Ω		spatial domain of the aggregate body $\mathcal{B}$
Ω^h		discretised domain
Ω_e^h		discretised finite element domain
$\hat{\Omega}$		reference finite element domain, described in local coordinates
ξ^d	$[\,\text{-}\,]$	contravariant, convective curvilinear coordinate line
$\boldsymbol{\xi}$	$[\,\text{-}\,]$	contravariant, convective curvilinear coordinate lines, where $\boldsymbol{\xi} = \{\xi^1, \xi^2\}$ in $\mathbb{R}^2$ and $\boldsymbol{\xi} = \{\xi^1, \xi^2, \xi^3\}$ in $\mathbb{R}^3$
$\boldsymbol{\tau}$	$[\,\mathrm{N/m^2}\,]$	*Kirchhoff* stress tensor
$\boldsymbol{\chi}$	$[\,\text{-}\,]$	placement function
$\boldsymbol{\Phi}_e$	$[\,\text{-}\,]$	isogeometric mapping operator
c_1, c_2, c_5	$[\,\mathrm{N/m^2}\,]$	material parameter of Ψ_{iso}
c_3	$[\,\mathrm{N/m^2}\,]$	material parameter of Ψ_{aniso}
c_4	$[\,\text{-}\,]$	material parameter of Ψ_{aniso}
d	$[\,\mathrm{s}\,]$	electromechanical delay
$\tilde{d}$	$[\,\mathrm{m}\,]$	shortest distance resulting from shortest distance projection
$\mathrm{d}a$	$[\,\mathrm{m^2}\,]$	actual area element
$\mathrm{d}\mathbf{a}$	$[\,\mathrm{m^2}\,]$	orientated actual area element
$\mathrm{d}A$	$[\,\mathrm{m^2}\,]$	reference area element
$\mathrm{d}v$	$[\,\mathrm{m^3}\,]$	actual volume element
$\mathrm{d}V$	$[\,\mathrm{m^3}\,]$	reference volume element
e	$[\,\mathrm{V}\,]$	filtered and rectified EMG signal
$\mathfrak{e}$	$[\,\mathrm{J/kg}\,]$	mass specific internal energy
g_N	$[\,\mathrm{m}\,]$	gap function
f_l	$[\,\text{-}\,]$	function describing the active force-length relation of a skeletal muscle
f_t	$[\,\text{-}\,]$	function describing the activation state of a skeletal muscle
f_v	$[\,\text{-}\,]$	function describing the force-velocity relation of a skeletal muscle
l	$[\,\mathrm{m}\,]$	scalar valued lever arm
p	$[\,\mathrm{N/m^2}\,]$	hydrostatic pressure
r	$[\,\mathrm{J/kg\,s}\,]$	mass-specific external heat supply

t	[s]	time
t_N	[N/m^2]	normal (frictionless) contact pressure
u	[-]	neural activation
w_k	[-]	weighting factor at *Gauss* point k
A	[-]	shape factor defining muscle activation
E	[-]	finite number of discrete, non-overlapping finite elements
E_{eff}	[-]	effective value of the *Green-Lagrange*an strain tensor
F_m	[N]	scalar valued force
F_m^0	[N]	maximum isometric muscle force
I_1, I_2, I_3, I_4	[-]	principal invariants of the deformation tensors
J	[-]	*Jacob*ian determinant
L_M	[m]	muscle length
$\dot{L}_M$	[m/s]	muscle contraction velocity
M	[Nm]	moment or torque
M_{FD}	[Nm]	moment resulting from the forward dynamics model
M_{ID}	[Nm]	moment resulting from the inverse dynamics model
N	[-]	number of DoFs
N_F	[-]	number of arbitrary forces
N_i	[-]	nodal basis function
$\mathbf{a}$		preferred fibre direction in the current configuration
$\mathbf{b}$	[kg/s^2]	mass specific body force vector
$\mathrm{d}\mathbf{f}_s$	[N]	incremental surface force
$\mathbf{e}_i$	[-]	(Cartesian) basis of orthonormal vectors
$\mathbf{l}_i$		tangent vectors of the convective surface coordinates
$\mathbf{l}_m$	[m]	lever arm vector of muscle m
$\mathbf{m}_i$	[-]	eigenvectors of $\mathbf{C}$ related to the reference configuration
$\mathbf{n}$	[-]	outward-oriented unit surface normal vector
$\mathbf{n}_i$	[-]	eigenvectors of $\mathbf{B}$ related to the actual configuration
$\mathbf{q}$	[J/m^2 s]	heat flux vector
$\mathbf{r}$	[m]	vector pointing from $\mathbf{x}_s$ to the point of action, $\mathbf{x}_m$, where the resulting moment is minimal
$\mathbf{t}$	[N]	surface traction vector
$\boldsymbol{u}, \boldsymbol{v}, \boldsymbol{w}$		solution vector of primary variables
$\mathbf{u}$	[m]	displacement vector
$\mathbf{x}(\mathbf{X}, t)$	[m]	actual position vector
$\dot{\mathbf{x}}(\mathbf{X}, t)$	[m/s]	velocity vector
$\ddot{\mathbf{x}}(\mathbf{X}, t)$	[m/s^2]	acceleration vector

$\mathbf{x}_e, \mathbf{X}_e$	[m]	nodal values of nodes belonging to an element e
$\mathbf{x}_s$	[m]	barycentre
$\mathbf{A}$	[N/m^2]	*Almansi*an strain tensor
$\mathbf{B}$	[-]	left *Cauchy-Green* deformation tensor
$\mathbf{C}$	[-]	right *Cauchy-Green* deformation tensor
$\mathbf{E}$	[-]	*Green-Lagrange*an strain tensor
$\mathbf{F}$	[-]	deformation gradient
$\mathbf{F}_m$	[N]	force vector of muscle m
$\mathbf{I}$	[-]	tensor identity
$\mathbf{J}_e$	[-]	*Jacob*ian of the isogeometric mapping
$\mathbf{K}$		generalised stiffness matrix
$\mathbf{L}$	[1/s]	spatial velocity gradient
$\mathbf{M}$	[Nm]	resulting moment vector
$\mathbf{M}_\perp$	[Nm]	the perpendicular part of the resulting moment where $\mathbf{M}_\perp \perp \mathbf{R}$
$\mathbf{M}_\parallel$	[Nm]	the parallel part of the resulting moment where $\mathbf{M}_\parallel \| \mathbf{R}$
$\mathbf{N}_e$	[-]	set of nodal basis functions N_i for the element e
$\mathbf{P}$	[N/m^2]	1$^{\text{st}}$ *Piola-Kirchhoff* stress tensor
$\mathbf{Q}$	[-]	proper orthogonal rotation tensor
$\mathbf{Q}_{\boldsymbol{\xi}}$	[-]	reflexion tensor
$\mathbf{Q}_{\boldsymbol{\xi}}^{(\phi)}$	[-]	rotation matrix inducing rotation by ϕ
$\mathbf{R}_i, \mathbf{R}$	[N]	nodal and total residual vector
$\mathbf{R}_m$	[N]	resulting muscle force
$\mathbf{S}$	[N/m^2]	2$^{\text{nd}}$ *Piola-Kirchhoff* stress tensor
$\mathbf{T}$	[N/m^2]	*Cauchy* stress tensor
$\mathbf{U}, \mathbf{V}$	[-]	right and left stretch tensors of the polar decomposition of $\mathbf{F}$
$\mathbf{X}$	[m]	reference position vector
$\mathcal{B}$		aggregate body
$\mathcal{G}$		overall variational formulation containing the weak forms
$\mathcal{G}^\chi$		variational formulation containing the weak forms of the mechanical problem
$\mathcal{G}^p$		variational formulation containing the weak forms of the incompressibility constraint
$\mathcal{G}^C$		variational formulation containing the weak forms of the contact problem
$\mathcal{H}^1$		*Sobolev* space
$\boldsymbol{\mathcal{M}}$	[-]	structural tensor

$\mathcal{O}$	fixed origin in an *Euclid*ian space
$\mathcal{O}_3$	group of all orthogonal transformations
$\mathcal{P}$	material point of aggregate $\mathcal{B}$
$\mathcal{R}$	response functions
$\mathcal{S}$	space of the ansatz or trial functions
$\mathcal{SG}_3$	symmetry groups
$\mathcal{SO}_3$	group of all proper orthogonal transformations
$\mathcal{T}$	space of the test functions
$\mathcal{V}$	process variables
$\boldsymbol{\mathcal{W}}$	force wrench
$\mathfrak{f}$	generalised right-hand side vector of the resulting global system of equation
$\mathfrak{g}$	generalised matrix resulting from the algebraic side condition
$\mathfrak{K}$	generalised stiffness matrix

Acronyms

Symbol	Description
2-d	two-dimensional
3-d	three-dimensional
DoF	degree of freedom
DoFs	degrees of freedom
ACh	chemical messenger or neurotransmitter
ACSA	anatomical cross-section area of a skeletal muscle
ADP	adenosine diphosphate
ATP	adenosine triphosphate
BC	boundary condition
BVP	boundary-value problem
Ca^{2+}	calcium ion
CE	contractile element
Cl^{-}	chloride ion

CMISS	An interactive computer program for Continuum Mechanics, Image analysis, Signal processing and System Identification
ECM	extracellular matrix
EMG	electromyography
FEM	finite element method
FIM	Forward-Inverse model
IBVP	initial-boundary-value problem
K^+	potassium ions
MBS	multi-body simulation
MVC	maximum voluntary contraction
MTC	muscle-tendon complex
Na^+	sodium ion
ODE	ordinary differential equations
PCSA	physiological cross-section area of a skeletal muscle
PDE	partial differential equations
PEE	parallel elastic element
SSE	serial elastic element
TDM	tendon displacement method
VRLA	vector-resulting lever arm
VRLA+	vector-resulting lever arm determined by including the effects of the muscle force wrench

Anatomical directional terms

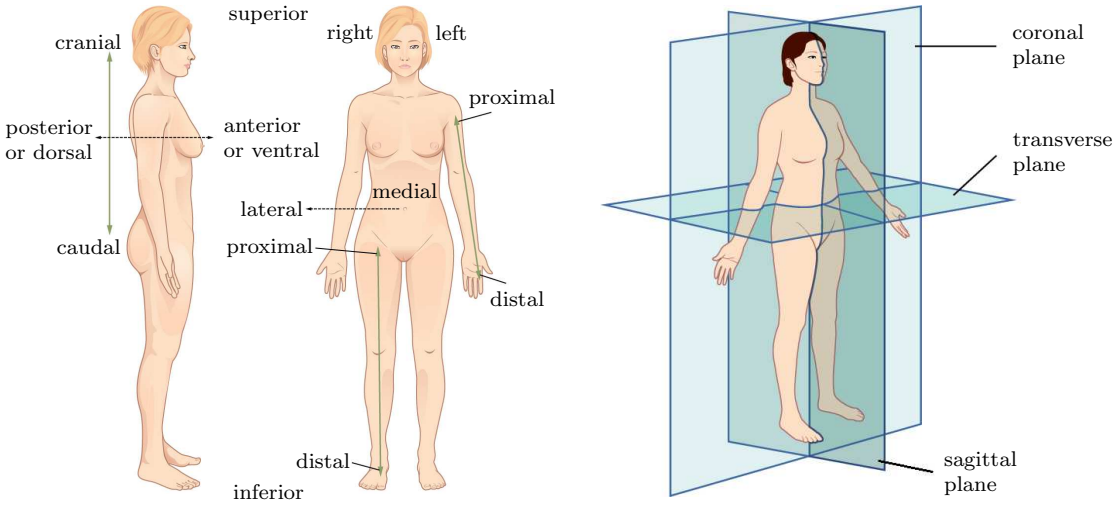

(a) *directional terms* **(b)** *human planes*

Figure 0.1: *Anatomical directional terms, adapted from OpenStax College (2013).*

1 Introduction and Overview

1.1 Motivation

For engineers, the motivation to answer unresolved questions often comes from a combination of a lack of knowledge and technology and curiosity. The process of finding a solution to this questions always goes hand in hand with developing new methods. Answering these questions regarding the anatomy and physiology of biological tissues are especially challenging. Nevertheless, this thesis tries to contribute to get a better understanding of the complexities of the musculoskeletal system.

In the past, many anatomically related questions could be answered by in-vitro experiments. Yet, physiological and functional tissues are mostly only investigated in a limited sense in abnormal conditions or outside their normal biological context. In-vivo experiments are rarely applicable for ethical reasons. For approximately the last 50 years, in-silico experiments widened the possibilities to investigate biological tissues. Computational models enable to toy with functional parameters so as to test, verify and understand natural phenomena. Obviously, investigations using computational models are only as good as their models. Here, verification and validation play a crucial role. However, the problem is conducting biological experiments on living tissues is rather difficult. Hence, only limited data for comparison is available.

This thesis focuses on the musculoskeletal apparatus. Status quo attempts to simulate (parts of) the musculoskeletal system are based on multi-body simulations. They include the use of lumped-parameter models to represent muscle-tendon complexes to investigate the kinetics of the musculoskeletal system. Multi-body models use a discrete modelling approach, in which the components of the musculoskeletal system are typically assumed to be rigid. From a mechanical point of view, they are characterised by discrete mass points and their respective moments of inertia. The *Hill*-type muscle models have gained acceptance for adequately representing the muscle-tendon complexes as a lumped-parameter modelling approach. As they have been successfully applied for many decades, they are well validated by experiments. Geometrically, they are linear objects that span from the muscles' origin to their insertion points and they lack any contour or volumetric representation. While the path of the muscle force can be enhanced by defining wrapping surfaces or via-points to improve muscle force orientation, such lumped-parameter models are not capable of representing detailed structural characteristics. Due to the relatively small number of DoFs, multi-body models are computational feasible. Hence, a large number of muscles can be utilised to investigate movements.

Yet, experimental measurements have shown that structural characteristics have a strong impact on the overall behaviour of biological soft tissues. Burkholder et al. (1994) states that the fibre length and fibre type distribution are the most functionally significant parameters in determining skeletal muscle mechanics, whereas the architectural properties of fibres are the most structurally significant parameters. Furthermore, Holzapfel

et al. (2000) concluded that the total stress within biological soft tissue is the sum of the contributions from various muscular constituents, including the ground matrix, individual fibres, and the interactions between fibres.

More recently, further insights into the musculoskeletal system are inspired by employing continuum-mechanical skeletal muscle models. Due to the different modelling approaches, structural properties and local actions can be included, while paying it with higher computational costs. The key advantage of such models is to include spatial quantities such as fibre field architectures, local activation principles, complex geometries, or contact mechanics. The drawbacks of continuum-mechanical based models are (i) the lack of a large pool of physiological validation measurements, (ii) the high computational cost, (iii) an increase in modelling complexity imposing restrictions on the usability and (iv) that state-of-the-art simulations merely focus on muscles in isolation. They only include specific aspects of skeletal muscles such as tendon tissue or complex electro-mechanical models, but not the entire muscle in its complexity.

While single muscle investigations are crucial, one only obtains a better understanding of the musculoskeletal system, if one investigates its mechanical and physiological properties.

This thesis develops a methodology appealing to continuum-mechanical muscle models in order to investigate a musculoskeletal system. As musculoskeletal systems are complex, many assumptions need to be made in order to tackle the challenging task.

1.2 State-of-the-Art Musculoskeletal System Modelling

In general, there are two different kind of model approaches: phenomenological and physiological.

The phenomenological modelling approach is – to put it in exaggerated terms – a model fit to observed or measured data. The physiological modelling approach tries to reflect natural phenomena by using a bottom to top approach. This means, small scale effects are modelled and are up-scaled to yield a macroscopic behaviour which can reproduce experimental data. The more naturally occurring phenomena are taken in consideration within a model, the closer one comes to achieving a physiologically motivated model.

1.2.1 Skeletal Muscle Modelling

One intrinsic feature of musculoskeletal systems is that they are overdetermined, i.e. there exist more muscle actuators acting on a joint than the DoF of the respective joints (Section 2.4.1). To solve this so called muscle redundancy problem, further assumptions need to be made. In general, there are two different modelling approaches to solve the dynamics of the musculoskeletal system:

Inverse dynamics: The body motion and external forces are provided by experiments. Muscle forces and joint torques reproducing the observed motion, are computed. As each time step can be solved independently from the others, this approach can be solved explicitly making it numerically efficient. A conceptional drawback of the inverse-dynamics approach is that it is not capable of addressing in a direct fashion co-contraction, as the gross moment resulting from two different muscles can result

from different situations, i.e. $\Delta M(\theta = 45°) = M_T(\alpha = 0.01) - M_B(\alpha = 0.01) = 4-3 = M_T(\alpha = 1) - M_B(\alpha = 1) = 40-39 = 1$ [Nm] and it is not possible to predict a unique movement.
Possible inverse-dynamics approaches used to solve the muscle redundancy problem are: (i) relate the muscle force to the muscle dimension, e.g. the PSCA (Alexander and Vernon, 1975), (ii) use of experimental data such as EMG to determine the muscle activation (Hof and Van Den Berg, 1977), (iii) identify muscle grouping, e.g. agonist and antagonist muscles, to reduce the number of activatable muscles (Morrison, 1970; Schipplein and Andriacchi, 1991), or (iv) choose appropriate objective functions to solve optimisation problems so as to minimise the work done (Seireg and Arvikar, 1973), the joint moment (Crowninshield and Brand, 1981), or the contact force in the joint (Seireg and Arvikar, 1975). Forster et al. (2004) presented a first approach to predict the muscle co-contraction by solving an optimisation problem.

Forward dynamics: In forward dynamics, the motion is a consequence of predicted muscle forces and joint moments, i.e. muscle forces can be considered as a model input and the resulting movements as model output. As the current state of the musculoskeletal system also depends on the previous one, the solution for each time step cannot be solved independently. The resulting movement needs to be computed implicitly. Hence, the control or optimisation process is more computational intensive than that of the inverse-dynamics approach. Naturally, the muscle forces need to be predicted by a model, as they cannot be measured experimentally.
The activation pattern to achieve a specific target is either guided by the use of: (i) control mechanisms such as trajectory control, e.g. λ-model (equilibrium point hypothesis) by Feldman (1986); Lorussi et al. (2006), (ii) experimental data, e.g. EMG data to employ activation dynamics to convert EMG-signal into muscle activation (Buchanan et al., 2004), or (iii) objective functions, where an optimisation problem is solved so as to minimise the work done, the joint moment, and joint contact forces, or to maximise jump height (Pandy et al., 1990; Anderson and Pandy, 2001; Anderson, 1999).

The objective functions for the optimisation need to be specified to obtain meaningful solutions with respect to specific goals, e.g. energy minimisation during walking or joint stability due to co-contraction. Depending on the researchers' preferences, the choice of the cost function can be quite subjective. Reviews on inverse and forward-dynamics simulations for rigid-body simulations can be found in Erdemir et al. (2007) and Otten (2003). A review on objective functions can be found in Maas (2014).

The parameters within the cost function depend on the modelling parameters of the musculoskeletal system, in particular the modelling parameters of the muscular actuators. The magnitude of the exerted muscle forces is either linearly related to the muscles' cross section (PCSA) (Barbenel, 1974) or obtained by lumped-parameter models.

Lumped-Parameter Skeletal Muscle Models

State-of-the-art mechanical skeletal muscle models reduce the anatomical and physiological complexities of the muscle to a few physiological parameters. The three-element

Hill-type models (Zajac, 1989; Anderson and Pandy, 2001) are by far the most commonly used skeletal muscle models for analysing movement.

These lumped-parameter models are simple but well established. These models have been employed in numerical simulations for several decades to investigate locomotion (of parts) of the musculoskeletal system due to their comparatively small number of DoFs.

The development of the prominent muscle models was first introduced by Hill (1938). *Hill* performed quick-release experiments on a sartorius muscle of a frog to determine the necessary parameters of Equation (1.1). In quick release experiments, fully activated muscles are pre-stretched and subjected to a constant load. While releasing the muscle, the muscle's contraction velocity and force are measured. This relation can be mathematically expressed as

$$(\dot{L}_m + b)\,(F_m + a) = b\,(F_m^0 + a)\,. \tag{1.1}$$

Herein, a and b are muscle parameters and F_m^0 is the maximal force at a current deflection length L_m. The maximal force F_m^0 depends on L_m because the number of possible attachable cross-bridges within muscle fibres strongly depends on the stretch of a muscle fibre, see Section 2.4.2 and Figure 2.10.

Equation (1.1) demonstrates a hyperbolic relation between the force, F_m, and the contraction velocity, $\dot{L}_m$: i.e. the higher the load applied to the muscle, the lower the contraction velocity, see Figure 1.1a. His model employs an equation of state, initially introduced by *van der-Waals* for real gas to describe the contraction of a fully tetanised muscle.

Hill's mathematical model, describing only fully tetanised muscles, was extended to a rheological model (lumped-parameter model) using three mechanical elements, see Figure 1.1b. The model consists of a contractile element, CE, which reflects the active contractile contribution of the muscle described in Equation (1.1), a spring in parallel, PEE, representing the intrinsic elasticity of the muscle fibre's connective tissue, while a second spring in series, SEE, describes the muscle's passive behaviour (inactivated stretching of the muscle) and the tendons. This relatively simple lumped-parameter model is also able to represent single twitches, and can be further extended by the utilisation of springs and dash-pots for more accurate representations, e.g. viscoelastic behaviour (Günther et al., 2007). With time, many suggestions have been made to improve the material description by adding springs and dampers to the system.

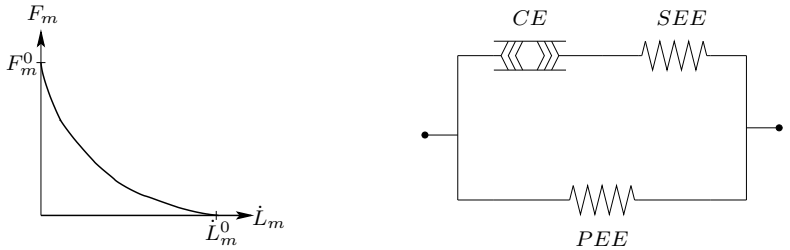

(a) *force-velocity relation described by* Equation *(1.1)*

(b) *3-element Hill-type muscle model*

Figure 1.1: *Components of the Hill-type muscle model.*

The small number of DoFs enables the study of complex movement patterns. Each muscle can be described by a set of ordinary differential equations. The input parameters

for one-dimensional *Hill*-type like skeletal muscle models are the muscle activation α, the muscle length L_m and the muscle contraction velocity $\dot{L}_m$. The output is the muscle force, F_m.

State-of-the-art investigations on the human musculoskeletal system are carried out using multi-body or rigid-body simulations. These are discrete modelling approaches, where the components of the musculoskeletal system are assumed to be rigid. They are mechanically characterised by discrete mass points and their moments of inertia. The *Newton-Euler* equations are solved to describe the combined translational and rotational dynamics of rigid bodies. By including up to several tens of *Hill*-type muscle models, the resulting multi-body models enable investigations into kinetics of musculoskeletal systems of daily movements, e.g. human walking (Hardt, 1978; Patriarco et al., 1981). These models be used in either forward or inverse-dynamics approaches (Erdemir et al., 2007).

Geometrically speaking, the *Hill*-type muscle models are linear objects that are spanned between the muscles' origin and insertion points within the rigid-body model. The point of origin, the direction of force, and the muscle insertion define the line of action of the lumped-parameter skeletal muscle models. The muscles' line of action may be redirected through via-points or wrapping surfaces (Garner and Pandy, 2000).

The most significant drawback of this approach is the large geometrical simplification like for the pennation angle of a muscle. Hereby, neither geometrical nor local effects can be considered. For pennation angles smaller than 20°, the impact is usually neglected (Schmitt, 2006). For larger angles, a constant pennation angle is considered to include the muscle fibre architecture.

The big advantage of the resulting rigid-body simulations is its computational feasibility. Due to the relatively small number of DoFs in rigid-body models, including *Hill*-type muscle models, the indeterminate system can be solved either by an inverse or a forward-dynamics optimisation approach.

Volumetric Skeletal Muscle Models

More recently, further insights into the musculoskeletal system are aspired by employing continuum-mechanical skeletal muscle models. Due to the different modelling approach, structural properties and local actions can be included, yet paying it in form of the lack of a large pool of physiological validation measurements, with high computational costs, with the increase in modelling complexities imposing restrictions to the usability, and the restriction that state-of-the-art simulations focus on muscles in isolation (Blemker et al., 2005; Böl and Reese, 2008; Oomens et al., 2003; Lemos et al., 2001; Wang et al., 2013). Only specific skeletal muscle aspects are included, e.g. tendon tissue (Lemos et al., 2005), micro-mechanical considerations (Yucesoy et al., 2002; Sharafi and Blemker, 2010; Sharafi et al., 2011), or complex electro-mechanical models (Röhrle et al., 2008; Röhrle, 2010; Heidlauf and Röhrle, 2014), complex geometries (Böl et al., 2011), or contact mechanics (Fernandez and Hunter, 2005), but not the muscle in its entire complexity.

While early muscle models were mostly lumped-parameter models, Van Leeuwen and Spoor (1992) published a study that reports a first step towards investigating skeletal muscles using a numerically stable solution scheme to predict the spatially varying hydrostatic pressure and the shape of a muscle. They pointed out, that some existing models for pennate muscles violate mechanical equilibrium, and it is not enough to define a unique

pennation angle that is valid for the whole muscle. Their approach involves a description of single fibres and its curvature, to investigate different 2-dimensional fibre architectures. Each fibre attaches to tendinous sheets while all tendinous sheets unite at the central tendon. Due to fibre contraction, the fibre bends and the interstitial fluid builds up the hydrostatic pressure.

Van Donkelaar et al. (1995) created a finite element mesh of a rat's gastrocnemius medialis muscle using medical images. The muscle includes muscle tissue, and special care was taken to mesh the tendinous tissue. Vankan et al. (1995) used the mesh to simulate blood flow through the muscle, which is considered to be a fully saturated porous medium. In this study, the muscle tissue is assumed to behave linearly elastic.

The first model using a finite element approach to investigate the mechanical behaviour of skeletal muscles was presented by Johansson et al. (2000). For the dynamic formulation, which was implemented in ANSYS and solved explicitly, a nearly isovolumetric pressure-displacement formulation was used. The main purpose of the investigation was to investigate the impact of the muscle mass on the dynamic response of the muscle. The user material for the muscle stress is additively split into an isotropic part σ_{fib}, which represents the muscle matrix, and an anisotropic part, which represents the impact of the muscle fibre. A hyperelastic *Mooney-Rivlin* material was chosen for the matrix. The fibre contribution, σ_{fib}, is introduced to

$$\sigma_{\text{fib}} = \sigma_{\max}\, f_t\, f_v(\dot{L}_m)\, f_l(L_m) + \sigma_{\text{pas}}\,. \tag{1.2}$$

The fibre term is split into two terms: one for the active and one for passive fibre contribution (σ_{pas}). The active contribution includes $\sigma_{\max}$, which is the maximum isometric stress at optimal fibre length, and three functions f_t, f_v, f_l, describing the muscle's activation state, the force-velocity relation, and the force-length relation, respectively. The state of activation is determined by a charge wave form function. The velocity-dependent function, f_v, is split into two parts: The concentric behaviour is described by the *Hill* relation (1.1), and the eccentric behaviour is determined by an adapted yield stress criteria. The passive contribution, σ_{pas}, depends on the strain components.

Yucesoy et al. (2002) introduced a two-domain approach to investigate the effects of force transmission between muscle fibres and extracellular matrix. The two domains are represented by two separate meshes that are linked elastically to account for the transsarcolemmal attachments of the muscle fibres cytoskeleton and extracellular matrix.

Oomens et al. (2003) assumed a superposition of the muscle stress by a passive stress (reflecting the collagen and intrinsic fibre stiffness) and an active stress (reflecting the contractile property of the muscle). Within the passive term, the matrix component is described using a *Neo-Hook*ean material law, while a nonlinear contribution takes care of the fibre contribution. At the cost of increased numerical expenses, they substituted the *Hill* relation by a more physiologically based force-velocity relation. They employed a *Huxley*-like model based on the sliding-filament theory, see Section 2.4.2. The *Huxley* model is a two-state model (attached or detached state) which determines the induced stress resulting from the degree of activation. The model unknowns are the binding distribution, a dimensionless attachment length, a scaled shortening velocity of a half sarcomere, an activation factor, which depends on the calcium level, and an overlap factor, which is a function of the actual length of a sarcomere to determine the potentially possible cross-bridges. The *Huxley* model is a system of ordinary differential equations, which

needs to be evaluated for every point of the 3D model. Herein, the determined active contribution of the stress will be transmitted to the mechanical equilibrium equations, which are solved by the FE model.

Lemos et al. (2005) also split the stress into a passive and an active part. The passive material behaviour is described by an isovolumetric *Mooney-Rivlin* material law. Additionally, tendinous tissue is considered in their model. The unwrinkling of fibrous tendon tissue is included by an exponential constitutive law. This work focused on modelling the force-length relation. The standard force-length relation for the active contribution is enhanced by including a concept for the residual force enhancement. If the muscle changes its length while maintaining muscle stimulation, the active stress does not behave as described in the force-length relation. Instead, the residual force enhancement causes the stress to linearly increase with the stiffness of the muscle tissue.

To conclude the isolated muscle investigations, the presented models are all based on a phenomenological approach. The muscle stress consists of two terms: an isotropic matrix term and an anisotropic fibre term. The isotropic term is described using a rubber like material. The fibre term has considerable differences. The approaches differ in using different force-length relations, different force-velocity relations and/or different activation principles.

For musculoskeletal system models appealing to continuum mechanical principles, Fernandez and Hunter (2005) solved the wrapping of leg muscles around the knee articulation including the patella and cartilage tissue with an inverse-dynamics approach. The rigid bodies are coupled through contact mechanics. In addition, Lee et al. (2009) presented a relatively simple muscle model, which employs linear mechanics, to visualise the motion of skin for animation purposes.

To the best knowledge of the author, Wu et al. (2013) were the first to describe muscle activation for visualising facial expressions. This was achieved by embedding muscle tissues via a finite-element mapping procedure. However, for musculoskeletal systems, such as the upper or lower limb, antagonistic muscle pairs are essential for movements. Unlike the facial simulations, joint moment equilibrium positions do not need to be taken into account.

The basis for musculoskeletal models appealing to continuum mechanical principles to simulate movements is rather sparse. Considering the advantages of continuum-mechanical principles, the following question arises: Is it possible to find a way to both benefit from using continuum-mechanical models while maintaining reasonable computational costs?

1.2.2 Modelling the Upper Limb

Before upper limb models were able to predict muscle forces acting in the upper limb system, first models focused on developing the kinematics of the upper limb. Therefore, geometrical relations for bones, joints, and muscle-tendon complexes were analysed and prescribed by dissecting cadavers (Messier et al., 1971; Amis et al., 1979). Later, models were developed that were capable of reproducing the musculoskeletal kinematics (Murray et al., 1995). It became apparent that joint motions, muscle paths, and lever arms are essential to predict forces acting in the musculoskeletal systems (Van der Helm et al., 1992; Maurel et al., 1996).

Amis et al. published in 1979 already a model for predicting the muscle forces and moments acting on the elbow and wrist. The model was established while developing an elbow prosthesis. In this work, the muscle paths were reconstructed by following the muscle centroid of cross-sections perpendicular to the longitudinal axis of the muscle. The method used to estimate the moment arms is a combination of centroid and straight-line paths, i.e. that a line between the barycentre of the muscle origin and the barycentre of the muscle insertion is assumed. The muscle forces are estimated by using the work of Alexander and Vernon (1975), which relates the muscle force to the muscle cross-section.

The development of physiological models predicting lever arms and muscle length continued for many years. Murray et al. (1995) presented a three-dimensional computer model to evaluate the muscle kinematics of the arm muscles as a function of elbow angle and supination/pronation. The kinematic model was extensively used in rigid-body simulation for both inverse and forward-dynamics approaches.

The first skeletal muscle forces were predicted experimentally by (Messier et al., 1971) and (Amis et al., 1979). Messier et al. (1971) investigated the relation of EMG data of biceps brachii and triceps brachii to muscle tension. Therefor, isometric tests were conducted. The resulting tensions, given as functions of applied load and elbow angle, were used to conclude that the muscle force is directly proportional to the averaged electromyogram and that the parameter describing the slope is independent of the muscle length. Yet, the muscle tension increases with increasing muscle length.

Buchanan et al. (1986) investigated the elbow torque for a two DoFs joint during isometric contractions. The levels of EMG activity were observed to increase with increasing joint torque in an approximately linear manner. In polar plots, conclusions were made about the participation of the different muscles for different arm movements. Muscle forces are not explicitly identified.

The group of van Zuylen et al. (1988) developed a musculoskeletal system for the upper limb. He included the biceps brachii, brachialis and brachioradialis to investigate their contribution to the overall elbow torque. The muscle dynamics was modelled with *Hill*-type models. He performed experiments to measure torques generated by twitches of motor units instead of tetanic generated torques of the whole muscle.

An et al. (1989) introduced an analytical model of the upper limb to determine the muscle force distribution across the elbow joint for various configurations. The introduced muscle model can incorporate muscles with different architectures. The three main flexor contributors were biceps brachii, brachialis and brachioradialis. Their length and lever arms are determined by experimental data.

Challis and Kerwin (1993) introduced an inverse-dynamics, rigid-body model of the upper limb. The acting flexor muscles are biceps brachii, brachialis, and brachioradialis. The muscle forces based on 15 different objective functions were compared to predictions estimated by a validated muscle model. As the objective functions showed poor correspondence, a less restrictive and simple objective function was introduced which yielded better correlation to the validated model. This objective function assumed fully activated muscles and a constant muscle force ratio determined by muscle force and the maximal exerted muscle force for each included muscle. The skeletal muscle model was *Hill*-type like, including force-length and force-velocity relations. The muscles were assumed to be maximally activated throughout the range of the movement. The kinematics of the system is determined analytically using the shortest distance between muscle origin and

insertion.

Manal et al. (2002) and Manal and Buchanan (2003) used an upper arm model to introduce a framework to convert EMG signals to muscle activation. With the model, skeletal muscle forces can be predicted reliably. Furthermore, their model could be trained in an offline phase to predict muscle forces quickly in an online phase. Using this approach, their model could be used to drive a virtual arm in real time (Manal et al., 2002).

Holzbaur et al. (2005) introduced a sophisticated upper limb model. The model includes 15 DoFs, representing the shoulder, elbow, forearm, wrist, thumb, and index finger, as well as 50 muscle compartments crossing these joints. For all participating muscles and rigid bodies, the model provides a full set of parameters. The kinematical model reproduces data obtained from dissections (Murray et al., 1995) including wrapping surfaces, via-points, and complex joint motions, including translation and rotation. The model can be used to determine muscle forces for different movements.

In conclusion, existing models of the upper limb are entirely based on rigid-body models including *Hill*-type like muscle models. For the upper limb, there exists no musculoskeletal system model appealing to volumetric muscle models. As mentioned in Section 1.2.1, Fernandez and Hunter (2005) presents a first modelling approach for the lower limb.

1.3 Outline of the Thesis

After the introductory part of this chapter, which includes the motivation and the state of the art, the relevant anatomical and physiological components of the musculoskeletal system are introduced in Chapter 2.

Chapter 3 introduces the continuum-mechanical fundamentals. As biological tissues have to withstand large deformations, the first part of this chapter deals with the Theory of Finite Elasticity. Herein, the necessary kinematic, strain, and stress relations are introduced. Within the second part of this chapter, the universally valid balance relations are introduced.

The objective of Chapter 4 is to provide the relation between stress and strain for the different components of the musculoskeletal-tendon complex, which is necessary, to solve the balance relation introduced in Section 3.2.

Chapter 5 introduces the Finite Element Method which is used to spatially discretise the evolving partial differential equations, as the emerging system of partial differential equations cannot be solved analytically but numerically. In the second section, the theoretical fundamentals are adapted to be employed by CMISS, the finite element software package.

In Chapter 6, the concept of contact mechanics is introduced. Within this thesis, the frictionless contact formulation is restricted between the elastic skeletal muscle and the rigid bone. In the second part, the fundamental concept is adapted to CMISS.

After the fundamentals are set in the preceding chapters, Chapter 7 introduces the Upper Limb Model used within this thesis (hence in capital letters). In the first section, the general anatomy of the musculoskeletal system is specified for the upper limb region. In the second section, the acting members of the Upper Limb Model are introduced including the antagonistic muscle pair together with the modelling assumptions. In Section 7.3, the equivalent static system is established which enables the investigation of the Upper Limb Model. The fourth section gives an analytical example to provide an estimate for

the magnitude of the muscle force and lever arms. In Section 7.5, the concept of the force wrench is used to investigate the mechanical behaviour of a skeletal muscle. The concept can further be used to determine the point of action of newly defined traction force and the muscle's line of action.

In Chapter 8, possible applications for the Upper Limb Model are introduced. Finding an equilibrium position is a very computationally expensive endeavour, as the muscle redundancy problem needs to be solved. To circumvent solving the muscle redundancy problem of the continuum-mechanical model, it is necessary to come up with new approaches. Within this thesis, three possibilities are outlined to investigate the converging behaviour of the selected musculoskeletal system towards an equilibrium position and whether the equilibrium position is physiologically reasonable. Section 8.1 assumes and prescribes muscle activations to circumvent solving an optimisation problem and to test whether the Upper Limb Model is able to find an equilibrium position. Alternatively to prescribing the muscle activation, in Section 8.2, both experimental data and a multi-body simulation are introduced to determine the muscle activation. For this purpose, the author was designing, conducting, and analysing experiments at Prof. Lloyd's Centre for Musculoskeletal Research at the Griffith University, Australia. The forward-inverse model was made available by the Musculoskeletal Research Group and used to analyse the experimental data. In the last section of this chapter, one of the most promising approaches to employ continuum-mechanical models is outlined. By coupling continuum-mechanical simulations to rigid-body simulations, benefits of both model worlds can be encompassed.

In the first section of Chapter 9, the results for both the rigid-tendon model as well as the muscle-tendon-complex model are presented. Section 9.2 presents the lever arms resulting from the tendon-displacement method and the vector-resulting lever arm method, the resulting elbow moments as well as the equilibrium positions, and the convergence behaviour of the in Section 8.1 introduced procedure. In Section 9.3, the conducted experiments are investigated using the forward-inverse model. Its results can further be utilised to compare the resulting muscle forces and moments determined by the different models, assumptions, and lever arms.

Chapter 10 discusses the assumptions this model is based on and reports on the resulting benefits and drawbacks. Furthermore, the results of Chapter 9 are discussed individually, are compared to the results of different model assumptions, and are compared to already existing results of the literature.

Chapter 11 gives a short summary and an outlook to proceed with modelling the musculoskeletal system appealing to a continuum-mechanical approach.

2 Musculoskeletal System

Form and intrinsic properties of biological tissues strongly influence the mechanical behaviour of interest. To set up a mechanical model, form (anatomy) and function (physiology) of the musculoskeletal system need to be introduced.

The human musculoskeletal system is a complex and dynamic system. Its primary functions are to provide form, support, protection, stability and movement. It is made up of bones, muscles, tendons, ligaments, joints and other soft connective tissues that support and bind tissues and organs together. The skeleton provides the structure while joints articulate individual bones and allow them to move against each other to cause movement. Yet, without the ability of skeletal muscles to voluntarily contract, the musculoskeletal system could only move passively. As this work focuses on modelling skeletal muscles, a brief overview is given on the anatomy of bones, ligaments and joints, whereas a more detailed description of the skeletal muscles' structure and function is given. More information about anatomic, biologic and functional fundamentals regarding the musculoskeletal system can be found in e.g. Fung (1981) or MacIntosh et al. (2006).

2.1 Bones

Bones have two basic structural components: the cortical (or compact) bone and the cancellous (or trabeculaer) interior bone, which is a spongy or honeycomb like structure. The cortical bone is a solid, dense material comprising the walls at the distal ends and the external surfaces. This type of bone is strong and resistant to bending. Cancellous bone is formed by thin bone structures, called trabeculae. These trabeculae have been observed to orient in the direction of the forces applied to the bone (*Wolff*'s law). The spongy-like structure fills the inner part of the bone, is light, and can withstand high loads.

Cartilage covers articular bony surfaces to reduce frictional forces, wear, and absorbs compressive shocks, see also Chapter 2.2. Cartilage is an avascular material, which appears to be glassy and smooth. Like all soft tissues, cartilage consists of a ground substance. The cells produce the extracellular matrix, which determines the mechanical properties of the connective tissue. The ground substance typically contains proteoglycans and is mostly composed of chondrocytes.

There are at least 206 bones in a typical adult with different sizes, shapes, compositions, and therefore, different mechanical properties. Five different types of bones can be classified:

Long bones are characterised by the diaphysis, or long shaft, which is much longer than the cross-section is wide, and the epiphysis, or heads at each end, see Figure 2.1. Most of the limb bones are long bones for example.

Short bones are more cube-shaped with a thin cortical bone layer surrounding a trabeculaer interior. Examples can be found in the ankle or the wrist.

Flat bones, as the name indicates, have two layers of cortical bone housing a trabeculaer inner bone. Examples are the sternum or the bones of the skull.

Sesamoid bones are embedded within tendons to increase the lever arm of the muscle-tendon complex. An example is the patella.

Irregular bones categorise the remaining complex shaped bones. Examples are the pelvis or the vertebras.

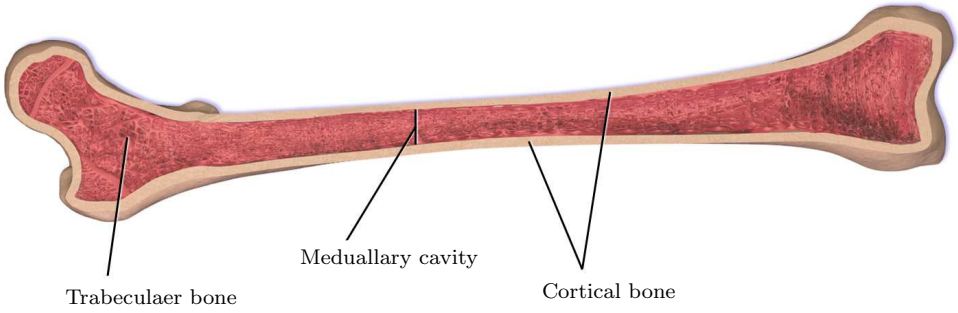

Figure 2.1: *The structure of the femur as an example of a typical long bone. Source: adapted from Blausen gallery 2014 (2014)*

Bones have a large variety of functions. The most important ones are of mechanical, synthetical and metabolic nature.
One of the key mechanical functions of bones is to build the skeleton system. It provides

- "rigid" kinematic chains by connecting bones to build joints, see Chapter 2.2,
- muscle-tendon complexes and ligaments attachment sites to transfer forces, and
- the ability to maintain an upright stance, and to protect organs.

The synthetical function of bones consists of producing blood components. Red and white blood cells are made in the bone marrow, located at the medullary cavity, within the trabeculae.
One of the most important metabolic function is to store minerals and fatty acids within the bone marrow. For example, by storing and releasing alkaline salts a pH-buffer can be provided. By adsorbing heavy metals from the blood, soft tissue can be detoxicated.

Normal human bones consist of the ground matrix, fibres and the extracellular matrix (ECM). The ground matrix is made up of minerals or inorganic substances that consist primarily of calcium and phosphate.
The ECM is also a composite material consisting of fibres and a liquid including macro molecules such as proteoglycans and polysaccharides in combination to proteins.
Minerals account for 60 to 70% of its weight, while water accounts for 5 to 8% and organic components including collagen make up the remainder of the tissue.
As mentioned above, the contents' ratio varies and bones are strongly able of adapting with environmental needs.

From a mechanical point of view, bone is a relatively hard and light composite material. In the physiological range of normal, healthy loading, the macroscopic strain-stress

relation can be considered as linear. Further, bone is a relatively brittle material with failure at strains in the range of 1–1.5%. The compressive strength is much higher than the tensile strength, which are in the range of 170 MPa and around 100 MPa, respectively. As the shear modulus is quite low ($\sim$ 50 MPa), bones can withstand high compressing forces and only small tensile and torsional forces.

2.2 Joints

The joint or articulation is defined as the location at which bones connect. The joints are constructed to allow movement and provide mechanical support. They can be classified in a structural (specifying the bone connection) or functional way (specifying the allowable degrees of freedom). Due to the numerous bone shapes, there is a large number of different joint types, where form follows function and classifications have overlaps. There are three structural types:

Fibrous joints are connected by fibrous tissues and therefore almost immovable. An example is the connection of bones in the skull.

Cartilaginous joints entirely connect bones with cartilaginous tissues. Hereby, only small movements are possible. An example of a cartilaginous joint would be the connection of the ribs at the sternum (chest).

Synovial joints, see Figure 2.2, are the most common joints and allow the largest relative motion between the bones. The difference between this joint and the first two types is that it is encapsulated by an outer membrane, which may contain ligaments, tendons, and muscles, and an inner synovial membrane, which includes the synovial fluid. The synovial fluid acts as a shock absorber, reducing the friction of the cartilage to a minimum and supplying the avascular articular capsule with nutrients by diffusion or induced convection (bone motion). Additionally, synovial joints may contain articular discs or menisci (knee), articular fat pads (knee), tendons, ligaments, and busae, which are small fluid filled capsules placed in such a way that they reduce friction and stress.

Synovial joints are the joints which one typically has in mind if one thinks of joints. From here on, this work is focused on this kind of joints.
There are six types of synovial joints. The form of the joint defines the DoFs for the bones to move with respect to each other. Less mobile joints are more stable and less frail to injuries.

Plane joints allow only in-plane gliding within the articular capsule, cf. Figure 2.3d. The opposite articular surfaces are almost flat. They are commonly small joints. This type is quite numerous and can be found for example in the hand, ankle, and vertebral processes.

Hinge joints allow a rotational motion only in one plane, cf. Figure 2.3b. The articular surfaces are strongly connected by surrounding ligaments. A good example for the hinge joint is the joint which is formed by connecting humerus and ulna. The knee joint is the largest hinge joint in the human body. Though, it allows to the one ideal hinge joint rotation additionally rotational and lateral DoFs or motions.

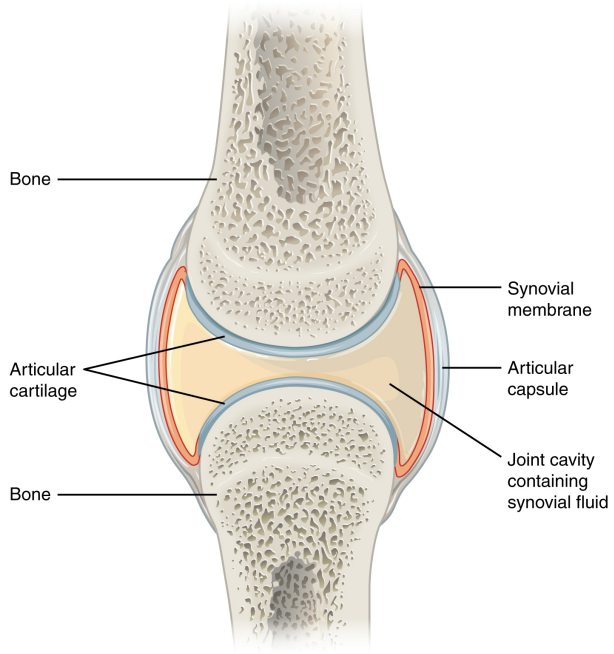

Figure 2.2: *Example of a typical synovial joint. Source: OpenStax College (2013)*

Pivot joints allow rotations of a socket around a pivot element, cf. Figure 2.3a. The main difference to the hinge joint is that the rotation in a pivot joint is only parallel to the longitudinal axis of the proximal and distal bones. Examples for such joints are the proximal and distal radioulnar joint which allow pronation and supination of the forearm.

Condyloid joints or ellipsoidal joints are joints where convex and concave bone ends allow flexion-extension and abduction-adduction movements, and a combination of both motion types, named circumduction, cf. Figure 2.3e. An example for a condyloid joint is the wrist joint. Hinge and pivot joints can both be considered as a subtype of the cylindrical joint.

In a saddle joint, the opposing surfaces are reciprocally concave-convex, cf. Figure 2.3c. It has the same DoFs as the condyloid joint. Yet, due to the open structure, it allows a wider range of motion.

Ball and socket joints, as the name already induces, consist of a ball which is placed in a socket, cf. Figure 2.3f. Hereby, all rotational DoFs are possible whereas translational movements are restricted. Examples are the shoulder and hip joints.

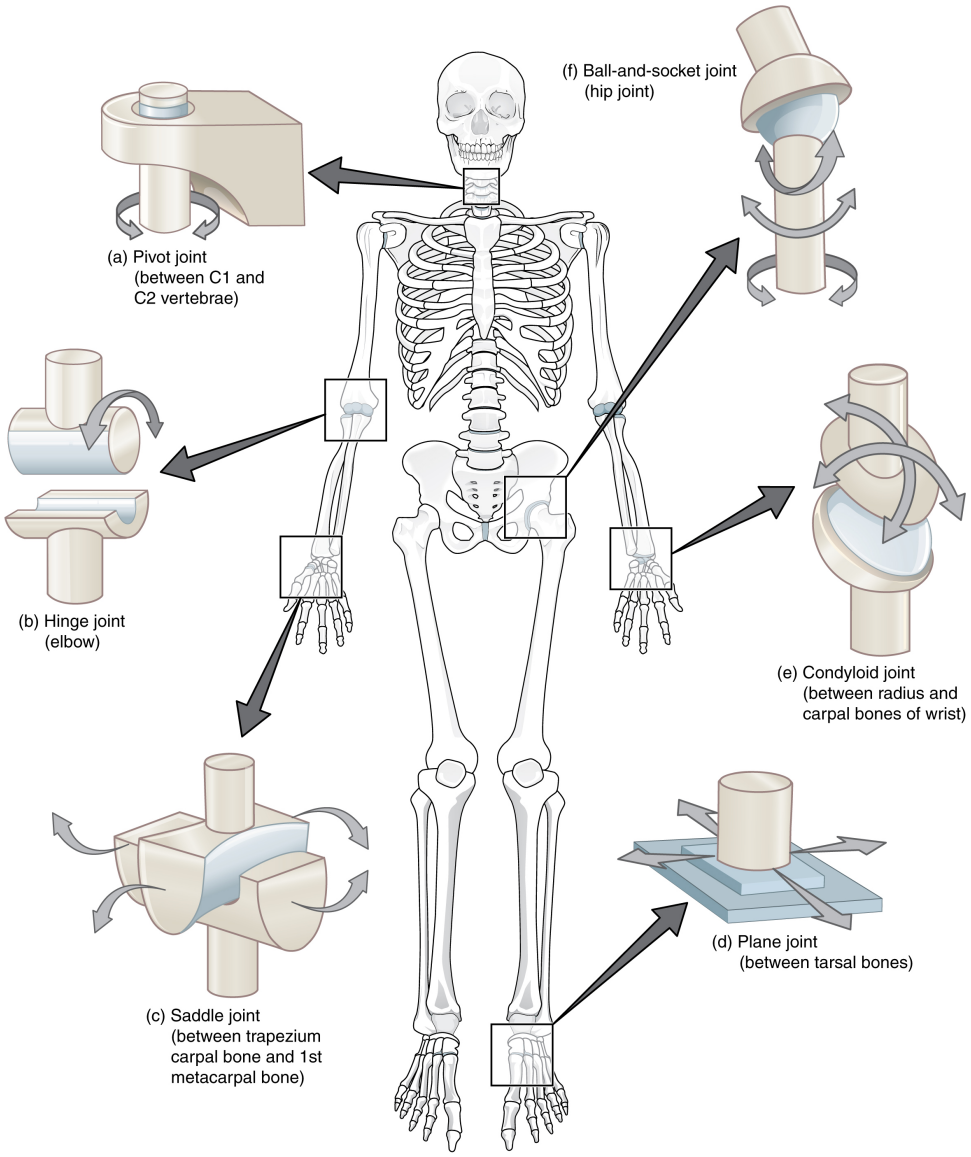

Figure 2.3: *Engineering substitutes of the physiological types of synovial joints within the body. Source: OpenStax College (2013)*

As indicated, nature is not as clearly definable as technical devices are. Hence, very often a sevenths type, the compound joint, is defined. Several types of articular joints share articular surface pairs to form a complex joint. For example, within the elbow, the humerus has two male surfaces joining the radius and the ulna, see Section 7.1.

There are various movements possible in human beings due to these different types of synovial joints. Among others, there are abduction – adduction, extension – flexion, supination – pronation and rotation, see Figure 2.4. Abduction – adduction is the movement away and towards the mid-line of the body, respectively. Extension – flexion is the movement of straightening and bending limbs at a joint, respectively. Supination – pronation refers to rotation of the forearm or foot such that in the anatomical position, the palm or sole is facing anteriorly (supination) or posteriorly (pronation). Rotation is the movement of a circular movement around a fixed point, e.g. turning the head.

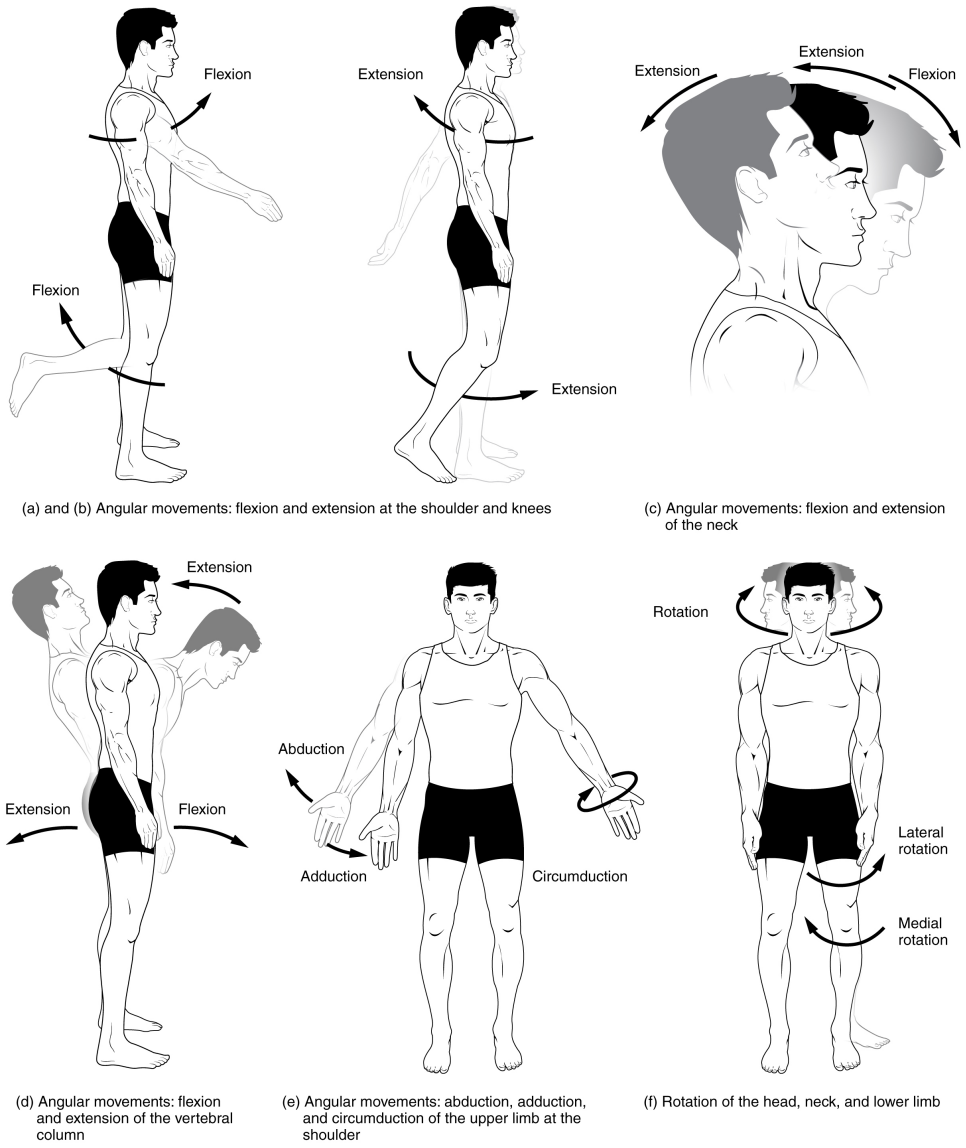

Figure 2.4: *Selection of possible joint motions. Source: OpenStax College (2013)*

2.3 Ligaments

Healthy joints allow a nearly effortless motion along preferred anatomical directions, yet abnormal motion should be prevented. As mentioned in the last section, the direction and range of motion is strongly defined by the articular surfaces. Soft tissues wrapping around the articular capsule stabilise and keep the articular surfaces together. One of the most important tissue types for this purpose are ligaments. Ligaments are arranged around the joints in such a way that they are already stretched in the neutral joint position. Further, at least one ligament band is under tension to stabilise the joint in any position of the joint. They can be subjected to extreme loads while performing their duty in restricting anatomical motions. In case of overstretching, ligaments may rupture which can lead to severe joint instabilities.

Ligaments are short bands of tough connective tissues consisting of parallel bundled

fibres embedded into the ground matrix, trapping a large amount of water. They consist of up to two-thirds of water. The dry mass consists of up to 90% collagen and some elastin. Collagen is a hierarchical structure where the fibres are mostly aligned parallel. It is the main load carrying element in soft tissues. Elastin has a non-hierarchical structure. It has a coiled organisation, is less stiff than collagen but can withstand large deformations. The fibres are embedded into the ground matrix, the extracellular matrix, which has a similar composition as in bones, including proteoglycans, glycolipids, and fibroplasts. Within the ECM, water forms a gel-like liquid.

Ligaments show a time and history dependent viscoelastic effect. Responsible for those effects is the high amount of water. Within the ligament tissue, the water's mobility is inhibited by long, charged proteoglycan molecules.

An extensive mechanically-based review can be found in Weiss and Gardiner (2001).

2.4 Skeletal Muscle-Tendon Complex

There are three different types of muscles in the human body. There are:

skeletal or striated muscles, which are attached to the bones and are responsible to make the skeleton move,

cardiac muscles, which form the heart tissue, and

smooth muscles, which can be found in internal organs and in the walls of blood vessels.

All muscles have the ability in common that they can contract. Yet, they distinguish in shape, structure, and excitation. The first group can be voluntarily controlled, whereas the latter two groups are controlled unconsciously. As this thesis deals with movements of the musculoskeletal system, the next section focuses on skeletal muscle or straited muscle.

A human being has around 650 different skeletal muscles. The overall muscles' living weight accounts for around 40-50% of our body weight. Around 50% of the energy gained by metabolic activity is spend to supply skeletal muscles. Some muscles are attached to bony processes and others to broad sheets of connective tissue, but all are directly or indirectly linked with the skeletal system. The shape or appearance of each muscle provides clues to its primary function, as form follows function. Muscles responsible for locomotion or posture are wrapped around joints. Those that support soft tissues form slings or sheets between relatively stable bony elements, e.g. the abdominal wall and the floor of the pelvic cavity consist of layers of skeletal muscles. Others guard an entrance or exit, completely encircling the opening and provide voluntary control over swallowing, defecation and urination.

As mentioned, skeletal muscles can only contract. So in order to make a joint move in different directions more muscles need to act at once. Muscles acting in opposite directions are called an antagonistic muscle pair and consist of an agonist and an antagonist. While the agonist produces a force in the primary direction of the motion, the antagonist controls the motion, slowing it down, or returning a limb to its initial position. If the motion is reversed, the muscles switch their functions. Very often, the agonist and/or the antagonist can consist of several muscles and compose a redundant system. Those groups of muscle causing a same effect are called synergists.

The muscle-tendon-complex attachment sites are defined to be the origin and the insertion of a muscle. By definition, the origin is the point where the muscle is attached to

the bone and which remains stationary, whereas the point where the muscle inserts at a bone is free to move. Very often, the origin is proximal and the insertion distal. Another criterion, which is used to define these points, is that if a muscle extends between a broad aponeurosis and a narrow tendon, the aponeurosis is the origin while the narrower tendon is the insertion.

2.4.1 Skeletal Muscle Anatomy

Skeletal muscles are an ideal sample for a hierarchically build structure, see Figure 2.5. On each scale, there are entities which are of similar composition. The largest unit is the whole muscle: It consists of many fascicles, the fascicle consists of many fibres, the fibre of many sarcomeres, and the sarcomeres of many small proteins. Each unit is surrounded by a fascia, a more or less strong connective tissue mostly made of collagen and elastin.

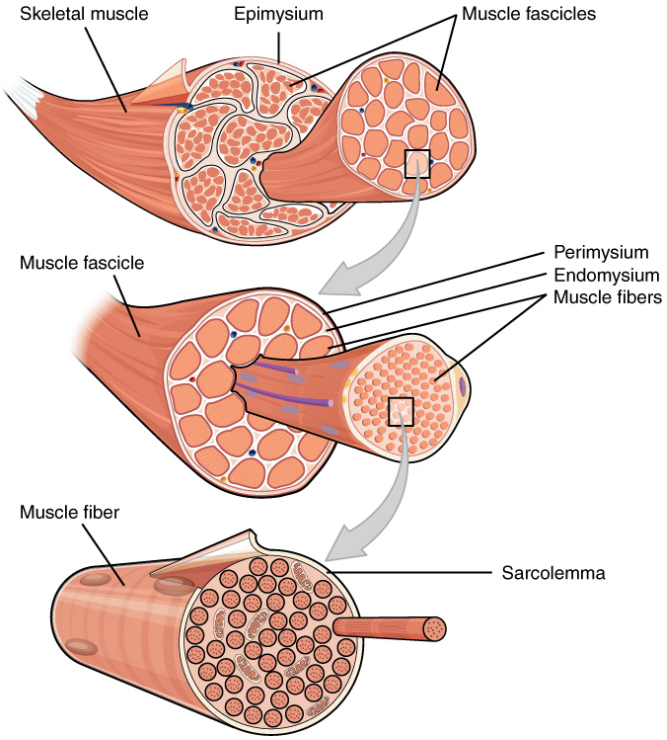

Figure 2.5: *Hierarchical structure of a skeletal muscle. Source: OpenStax College (2013)*

From an anatomical point of view, a muscle fibre can be considered as the basic anatomical unit of a skeletal muscle. The fibre is one biological cell, which can contain several hundreds of nuclei. The fibres' length can vary between a few millimeter up to 30 cm. The fibres' diameter varies between 10 to 100 μm. Each fibre is surrounded by the sarcolemna, a connective tissue which has invaginated extensions, called T-tubulus (T- as in transverse), penetrating deeply into the cell. The space between fibres is called endomysium. It is a thin layer made of lose connective tissue containing small capillaries and nerves. Many fibres (10 - 10^3) are formed in bundles, which are called fascicles. Fascicles are surrounded by a strong tissue sheath, called the perimysium. The space between fascicles

contains soft connective tissues, such as fat, nerves, arteries, and veins. The blood vessels ensure the muscles supply with oxygen and nutrients but take also care of the removal of waste products. The entire skeletal muscle consists of many fascicles, whereas all fascicles are surrounded by an even stronger sheath, the epimysium. These connective tissue coverings reinforce and support the muscle and the corresponding underlying structure. As tendon-like tissues fix the muscles to bones the amount of collagen and elastin increases gradually in the cross-section until the muscle is totally transformed into tendon tissue. The collagen and elastin fibres of the tendon tissue is then interwoven into the outer layer of bones to ensure a strong force transduction to the skeleton system. The tendon tissue can either be compact or form broad tendon-like sheets called aponeurosis, see Section 2.4.4. At the proximal end of the muscle, the junction between muscle and tendon is called myotendinous junction while the distal junction is called osteotendinous junction.

By zooming into a skeletal muscle fibre, more functional structures of skeletal muscles become apparent. A muscle fibre consists of thousands of myofibrils, which are arranged in parallel. Each myofibril is about 1 μm in diameter and is composed of an array of several thousand of myofilaments or sarcomeres, which are arranged in series. Many mitochondria, the energy producing units within a cell (see next section), are located between myofibrils. A sarcomere, along with other supporting proteins and structural components, consists of a multiple chain of connected proteins: the thick and thin filaments. The thick filament is composed of a long chain of myosin proteins. The thin filament is made of three proteins actin, tropomyosin, and troponin, where the actin makes up the bulk and provides the binding site to the myosin heads.

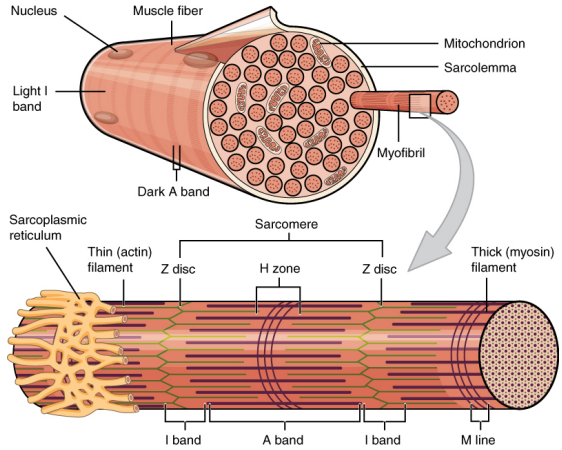

Figure 2.6: *Zooming in into a skeletal muscle fibre. Source: OpenStax College (2013)*

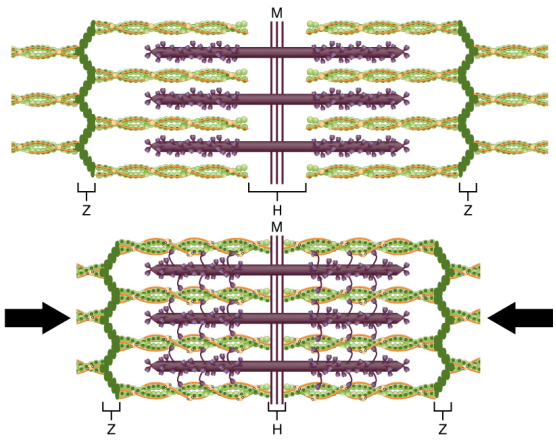

Figure 2.7: *The sliding filament model for a sarcomere contraction. Source: OpenStax College (2013)*

The two types of filaments are interlaced with various amounts of overlap, giving rise to a striated appearance and the alternative name of a striated muscle. These different bands are shown in Figure 2.6 with a gross division between A-bands (from anisotropic since it appears darker as it can polarise light) of both thick and thin filaments and I-bands (from isotropic since it appears lighter as it cannot polarise light) of just thin filaments. The thin filaments are held together by Z-discs (from the German Zwischenscheibe), which also define one repeating unit within the myofibril and the sarcomeres. Titin is a highly

elastic protein which anchors the thin filaments to the Z-discs and the myosin in the centre to the M-line. The M-line defines the centre of the H-zone (from the German helle Zone), which defines the gap between opposing thin filaments, cf. Figure 2.7. The reason why skeletal muscles are also called straighted muscles is based on the reoccurring lighter (I-band) and darker (A-band) zones within a myofibril.

The cell membrane of muscle fibres is called the sarcolemma. It is a selective permeable membrane, which under certain conditions can let pass water molecules or ions such as sodium (Na^+), potassium (K^+), calcium (Ca^{2+}) and chlorine (Cl^-) through small openings, the so-called ion channels. The sarcoplasmic reticulum, surrounding the myofibril, stores, releases, and retrieves calcium ions (Ca^{2+}).

2.4.2 Skeletal Muscle Physiology

The ingenious property of skeletal muscles is the ability to contract. Within the muscle, chemical energy provided in the form of ATP is converted to tension-producing energy. The relative motion takes place in the smallest scale within skeletal muscles, between the thick and thin filaments. As a whole skeletal muscle consists of a long series of functional units, the small contraction of a single sarcomere (approx. 10 nm) sums up, to a degree, where macroscopic changes in length lead to forces acting on bones. The bones are used as levers, the joints as fulcrum and the skeleton as a rigid system to be moved, see Section 2.4.5.

Within the next section, the underlying principles which lead to a *controlled* contraction are briefly introduced. Despite the rather complex sequences of events, an attempt is made to sketch it in a compact manner.

After deciding to contract a skeletal muscle, motor neurons fire from the brain stem and/or the spinal cord, depending on the muscle and the physiological need. The signals are travelling along axons, where a bundle axons build a nerve, arriving at the axon terminal. At the terminal, the motor neuron reaches to the fibre's neuromascular junction where the signal is fanned. Both neurons and skeletal muscle cells are electrically excitable, i.e. they are able to develop transmembrane potentials, as both are surrounded by a selective membrane enabling a potential difference between extracellular and intracellular space. An action potential is a special type of electrical signal that can travel, as a wave, along a cell membrane. This allows a signal to be transmitted quickly at long distances.

If the stimulation of the motor neuron is strong or long enough, the transmembrane potential increases sufficiently to cross the excitation threshold. After exceeding that threshold, a self-sustaining process arises during which the membrane depolarises and reverses its polarity.

Skeletal muscle fibres that are innervated by a motor neuron, coming from the same axon terminal in order to contract, are from the same motor unit. The number of muscle fibres within a motor unit is variable depending on the nature of the muscle. Commonly, it is exponentially distributed, where there are a large number of motor units including a small number of muscle fibres and a small number of motor units including a large number of muscle fibres. Smaller motor units have a lower threshold for the motor neurons to excite. Large motor units have a higher excitation threshold. So in order to produce a smooth increase of muscle force, the small motor units are recruited first, while the larger once kick in only at a high recruiting frequency and when a high force is in demand. Very

often, the small motor units include muscle fibre of type I while large motor units include type II fibres.

The action potential is transferred from the neuromuscular junction to the other side of the motor end-plate, the sarcolemna, by opening Na^+-ion channels. This process is triggered by a chemical messenger or neurotransmitter, called ACh. Once the action potential arrives at the sarcolamna, the Na^+-ion channels trigger the action potential to travel in both directions along the fibre. At each location along the fibre, the rising action potentials travel along the T-tubulus inside the cell to trigger the release of calcium ions from the sarcoplasmic reticulum. Ca^{2+}-ions bind with troponin (thin filament) to open the binding site blocked by tropomyosin. Once the binding side is free, a connection between the actin and myosin head occurs. This connection is called cross-bridge, Figure 2.8. While the myosin heads are pulling, the overlapping region, the H-band, reduces and the sarcomere shortens, cf. Figure 2.7. The reoccurring process of attaching, pulling (power stroke), and detaching between thin and thick filaments is known as a cross-bridge cycle.

ATP keeps the cross-bridge cycling running and makes the myosin pull on the actin structure. The muscle fibre will continue to shorten to an anatomical and mechanical limit, as long as the neural signaling from the motor neuron does not end and as long as ATP is available to drive the cross-bridge cycling as Ca^{2+}-ions remain in the sarcoplasm to bind to troponin and to keep the actin-binding sites open. The zone where thin and thick filaments overlap has an important impact on the muscle contraction, as it influences the amount of possible cross-bridges, cf. Figure 2.7.

For the aerobic respiration, the energy to maintain the cycling is provided by the mitochondria. Their main function is to consume oxygen and substrates to generate the vast majority of ATP while producing reactive oxygen species in the process, yet they also participate in a wide range of other cellular processes, including signal transduction, cell cycle regulation, oxidative stress, thermogenesis, and apoptosis.

In the decline phase of the action potential, Ca^{2+}-ions are adsorbed by the sarcoplasmic reticulum (reloading for the next contraction), the cross-bridge opens (the muscle relaxes), tropomyosin restores the blockage, and the contraction ends.

The muscle contraction force can be controlled by two factors: (i) the number of motor units involved in contraction and (ii) the amount of stimulus from the nervous system, see Figure 2.9. A single nerve impulse of a motor neuron will cause a motor unit to contract before relaxing. This small contraction is known as a twitch contraction. If the motor neuron provides several signals with a large enough excitation frequency, the strength and duration of the muscle contraction increases. This phenomenon is known as wave summation. If the motor neuron provides many nerve impulses with a large excitation frequency, the muscle may enter the state of tetanus, or complete and lasting contraction. A muscle will remain in tetanus until the excitation frequency reduces or the muscle becomes too fatigued to maintain the tetanic state.

As the electrical signal spreads quickly longitudinally along the fibre and the electrical conductivity is very low transversely, muscle fibre are coupled mechanically but not electro-physiologically with each other.

Due to small variations in the properties of functional units within the skeletal muscle, different fibre types can by classified by histochemical, physiological, morphological, or mechanical criteria. Most commonly, muscle fibre types are grouped histochemically – for their ATPase sensitivity – i.e. how glucose is transformed into energy. ATPase are

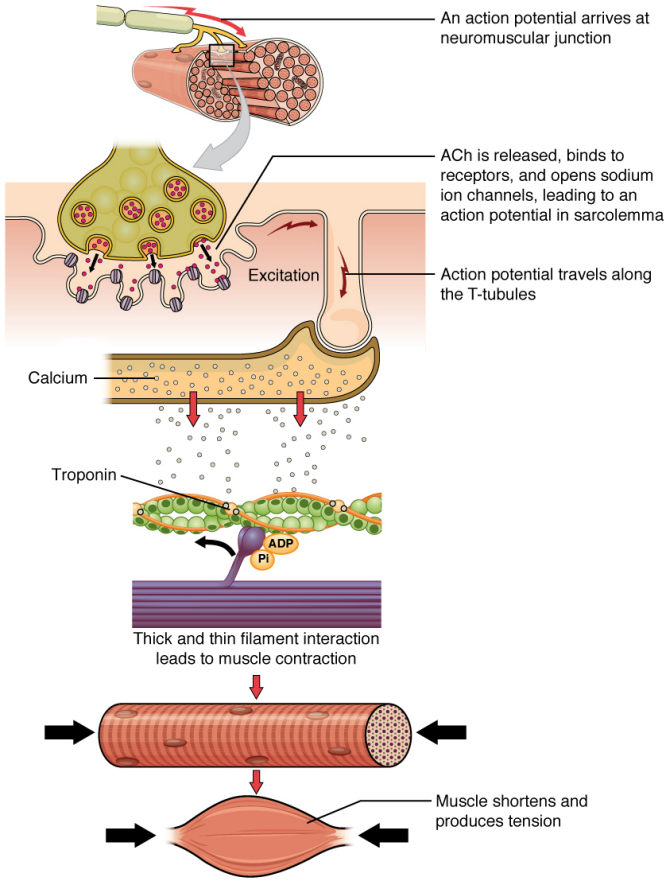

Figure 2.8: *The fundamental steps leading to a muscle contraction. Source: OpenStax College (2013)*

enzymes which make energy available by converting ATP into ADP. This can be triggered by different enzymatic processes. Oversimplified, there are three different basic skeletal muscle fibre types:

Type I fibres are small in diameter and have a histochemically high oxidative enzyme activity with a high concentration of mitochondria, using oxygen and glucose to produce ATP. This fibre type can produce a low to moderate level of force. The aerobic glycolysis is highly efficient as 36-38 ATP molecules can be produced by just one glucose molecule, and the skeletal muscle can contract continuously as long as the supply of oxygen and glucose is sufficient. Mechanically speaking, the fibre type are slow-twitch fibres, which are resistant against fatigue.

Type IIB fibres generate their energy by anaerobic glycolysis which is less efficient than aerobic respiration. Only two ATPs are produced for each molecule of glucose. Further products are lactic acids from the fermentation like process. The processes leading to the cross-bridge cycle are faster than in the slow twitch acting sarcomeres, i.e. the signal spreading and the electrochemical transmission are faster, and glucose is converted much faster into energy, hence this fibre type can contract much faster but are far less resistant to fatigue.

Type IIA fibres primarily use aerobic glycolysis. The glycolysis can switch to anaerobic,

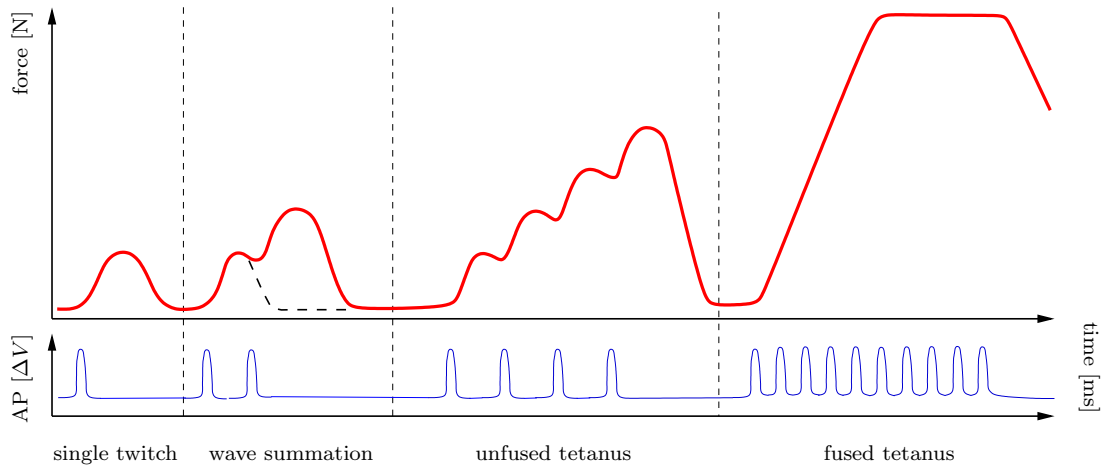

Figure 2.9: *The muscle force develops depending on the recruitment frequency: The result of a single twitch contraction can be seen in the first fraction. The force resulting from two single twitches can be seen in the second fraction. The resulting force depends both on the recruitment frequency and the duration of recruitment (number of twitches). For a recruitment frequency above 50 Hz the muscle reaches a tetanised state where the single twitch cannot be recognised anymore.*

when a high level of force is in demand, as the muscle contracts so tightly that oxygen carrying blood cannot enter the muscle. Depending on the respiration of type IIA, the characteristic of the fibre resembles more fibre type I or type IIB. Concluding, type IIA fibres are capable of being fatigue resistant while being able to twitch quickly at the same time.

Within a skeletal muscle, all muscle fibre types are present. Yet, depending on the location, functional requirements, and the development stage, a fibre type distribution can range from having a mosaic of all three types to a dominance of only one fibre type.

The number of muscle fibres is genetically defined. Therefore, the strength which a muscle can perform depends on the changing number of myofibrils and sarcomeres within a muscle fibre. An increase of muscle bulk or mass is called hypertrophy, a decrease atrophy.

The force which a sarcomere can generate depends on the overlap of thin and thick filaments or the size of the H-zone, respectively. In Figure 2.10, the sarcomere force-length relation is shown which was established in in-vitro experiments on sarcomeres.

Having the cross-bridge model in mind, the shape of the extreme points of the relation can easily be explained. A sarcomere generates the maximum force at the optimal sarcomere length. The optimal length is the length at which the number of possible cross-bridges is at a maximum. For both, compressing and stretching the sarcomere, the number of possible cross-bridges reduces, so does the generated sarcomere force, cf. Figure 2.10. The possible number of available cross-bridge connection sites at less than approximately 60% and more than 170% strain are zero.

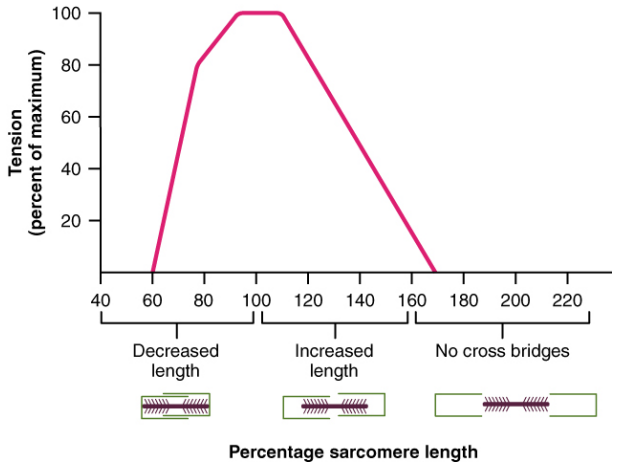

Figure 2.10: *The force-length relation for a single sarcomere. Source: OpenStax College (2013)*

2.4.3 Electromyography

Electromyography (EMG) is a technique for evaluating and recording the electrical activity produced within skeletal muscles. The electrical activity can be recorded either by surface electrodes on the skin or intramuscular using fine-wire needles. Placing surface electrodes is restricted to recording only superficial muscles. Even though, needles may be placed within living tissue, it is a non-invasive method to measure the activity of one or more underlying muscle groups. Placing needles into soft tissue can be painful, but enables the recording of deep muscles. As outlined in Section 2.4.2, muscle fibres can contract due to action potentials. EMG electrodes can measure the sum of the electrical activity of all fibres, motor unites, fascicles. The interpretation of the resulting measurements, the electromyograms, is a whole field for research itself as several problems arise while recording. Overlaying soft tissue, like skin and a varying fat layer and muscle cross-talk make it difficult to asses electrical signals to muscles.

To correlate the muscle activation to the measured EMG signals, an important parameter being used for reference purposes is the maximum voluntary contraction (MVC), see Section 8.2.2. Here, the muscle is tetanised and produces the maximum possible muscle force at a given length.

2.4.4 Tendon Tissue

The main function of tendon tissue is the force transmission between muscle and bone while they have to sustain high tensile stresses. While tendons are long cylindrical structures, aponeuroses are layers of flat, broad tendon tissue. The primary function of the aponeurosis is to join muscles fibres. The aponeurosis can either join to the main tendon or directly connect to bone. Naturally, their mechanical properties vary with shape and structural organisation and shape.

Tendons are, as well as skeletal muscles, hierarchically structured, i.e. a compound of small units build bigger compounds and each compound is surrounded by a strong tissue sheath. The tendon hierarchy is: collagen fibrils build collagen fibres, which build primary, secondary, and tertiary fibre bundles. Several tertiary bundles finally build the tendon.

Tendon tissue is similarly to ligaments and fascia connective tissue that is composed of densely packed collagen fibers. Yet, tendon tissue is, in contrast to the other two tissues, composed of a higher percentage of collagen which is additionally organised and orientated along the longitudinal axis of the main structure. Tendon tissue is composed of 60-80% water and 20-40% solids. The solid compound consists of about 90% of collagen, about 5% of proteoglycans, 2% of elastin, and inorganic components. So fare, 28 different types of collagen were found. They consist of different, differently arranged protein types. Tendon tissue consists of 95-99% of type I collagen. This collagen type is the most frequent occurring protein type in the human body. The remaining percentage varies locally and includes, among others, type II collagen within cartilaginous zones, type III collagen within vascular walls, and type X collagen in the mineralised fibrocartilage near the interface to the bone.

Tendon tissue can conserve substantial muscular energy during locomotion due to their elastic property. The viscoelastic behaviour of tendon tissue adds important damping features to the kinematic requirements of the muscle-tendon complex. Due to their slender structure, they enable the muscle belly to be at a convenient distance from the joint. Since tendon tissue is sparsely penetrated by blood vessels, they heal slowly from trauma injuries.

Tendon tissue follows a J-shaped stress-strain curve including three distinct stages. In the nonlinear toe region, the wrinkled fibres get lined and stretched. In the second, linear stage, the lined fibres get stressed. In the third stage, the tissue starts to fail. Tendons fail at strains depending on their purpose at around 6-12%. In Zajac (1989) it is mentioned that the tendon strain is 3.3% when the muscle generates its maximum isometric force. The mechanical response of tendons is dependent on the load magnitude, the load duration, and the prior loading. The tendon tissue's E-modulus can be up to 1.800 MPa (Weiss and Gardiner, 2001). Due to the large amount of containing water, the mechanical behaviour is not only elastic. Their behaviour is also affected by water in tissue movement which is trapped between charged, proteoglycan molecules. Hence, tendon shows all types of viscoelastic behaviour like creep, stress-relaxation, and hysteresis.

More information about tendons can be found in e.g. Weiss and Gardiner (2001) or Kannus (2000).

2.4.5 Macroscopic Muscle-Tendon-Complex Properties

Macroscopically, skeletal muscles can be classified from their functional properties. There are various types of classifications. In the following, those, which are important for the thesis, are introduced.

Muscles responsible for locomotion and crossing at most one joint are called monoarticular muscles. Muscles crossing two or more joints are called biarticular or multiarticular muscles, respectively. Their action on the musculoskeletal system can be quite complex and often depends on both their anatomy and the activity of other muscles at the joints in question. The brachialis, for example, is a monoarticular muscle, while the biceps brachii is a biarticular muscle.

Further muscles can be classified into being spurt or shunt. Spurt muscles originate far from the joint's fulcrum but have insertions close to the joint's fulcrum. Thus, they have short moment arms and can move the limb very rapidly but are relatively limited

in the magnitude of effective strength. Shunt muscles, on the other hand, originate close to the joint and have insertions far from the joint. This entails large moment arms and stabilising effects on the joint. Example for both types can be found at the upper limb; the biceps brachii is a spurt muscle and the brachioradialis is a shunt muscle.

Muscles can also be described by the direction the muscle fibres run in. While the muscle fibres within a single fascicle are parallel, the organisation of fascicles in the skeletal muscle can vary, as can the relationship between the fascicles and the associated tendon. There are four distinct patterns of fascicle organisation in the skeletal muscle. They can form parallel muscles, convergent muscles, pennate muscles and circular muscles. Each of the different muscle architectures are depicted in Figure 2.11 by means of one representative muscle.

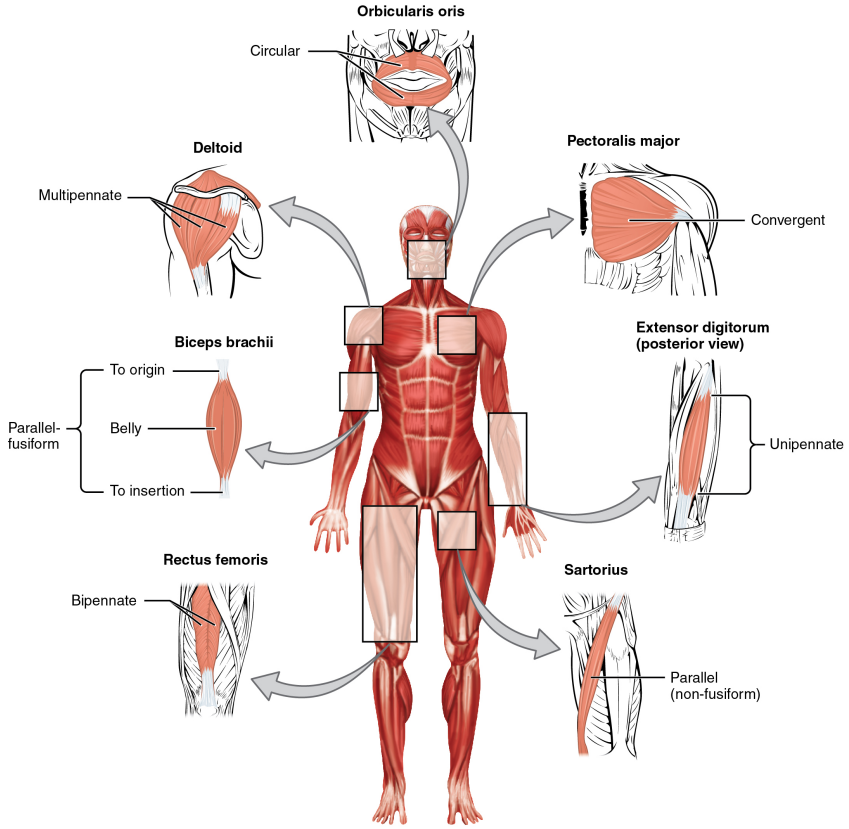

Figure 2.11: *The macroscopic arrangement of fibres is called the muscle fibre architecture. Possible architectures are shown including a specific muscle as an example. Source: OpenStax College (2013)*

Most of the skeletal muscles in the human body are parallel muscles (Martini and Nath, 2008). In a parallel muscle, the fascicles are arranged axially along the muscles belly. Some are flat bands with broad attachments at each end. Others are plump and cylindrical with tendons at one or both ends. For that case, the muscle is spindle-shaped and is called fusiform, cf. Figure 2.11 on the middle-left or in Figure 2.12a, with a central body, also known as the belly or gaster. As the fibres are parallel to the muscles belly, a contracting muscle roughly shortens to the same amount than fibres do (ca. 30%).

In a convergent muscle, see Figure 2.11, the muscle fibres typically spread out, like a

fan or a broad triangle. All fibres converge at a common attachment site. A convergent muscle has a larger versatility in its line of action, because the stimulation of only one compartment of the muscle can strongly change the direction of pull. However, when the entire muscle contracts, the muscle fibres do not pull as hard on the attachment site as a parallel muscle of same size, because it does not have one prominent muscle fibre direction.

In a pennate muscle, the fascicles form a common angle with the tendon, the pennation angle. If all muscle fibres are on the same side of the tendon, the pennate muscle is called unipennate, see Figure 2.11 and Figure 2.12b. As the pennate muscle fibres pull at this angle, the variation of the fibre length will be smaller than in a parallel muscle. Yet, the resulting force is larger, as the number of possible contracting fibres in the same cross-section is larger in a pennate muscle than in a parallel muscle. Bipennate muscles, see Figure 2.11 and Figure 2.12c, have fibres on both sides of the tendon. When the tendon branches within a pennate muscle, the muscle is said to be multipennate, see Figure 2.11.

Due to the anisotropic properties of skeletal muscle, the muscle cross-section can be described in two different ways. The physiological cross-sectional area (PCSA) is the area of the cross section of a muscle perpendicular to its fibres, generally at its largest point. It is typically used to describe the contraction properties of pennate muscles. The anatomical cross-sectional area (ACSA), on the other hand, is the area of the cross-section of a muscle perpendicular to its longitudinal axis. In a non-pennate muscle, in which the fibres are parallel to the longitudinal axis, the PCSA coincides with the ACSA, compare Figure 2.12.

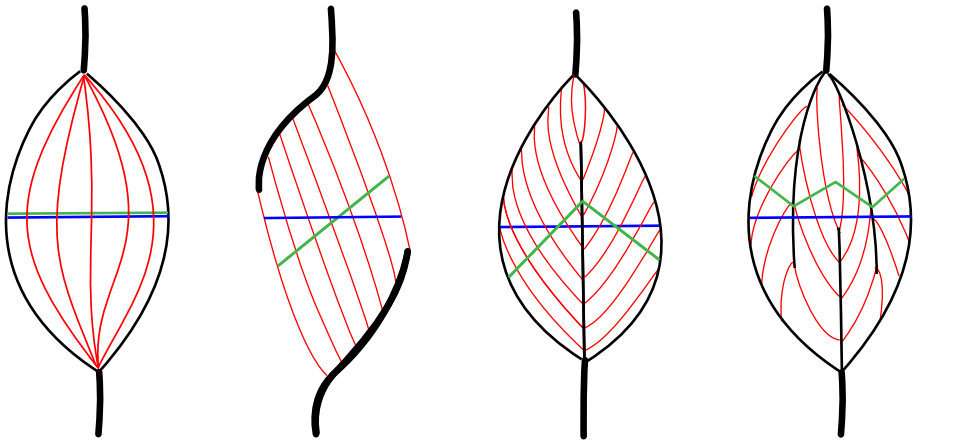

(a) *fusiform* **(b)** *unipennate* **(c)** *bipennate* **(d)** *multi-pennate*

Figure 2.12: *Different fibre architectures are indicated by the orientation of the red lines which represent the fibre running from origin to insertion. The black, bold lines indicate the tendon tissue. The difference between PCSA (green) and ACSA (blue) is defined by their different orientation with respect to the muscle longitudinal line and muscle fibre, respectively.*

When a muscle fibre is stimulated, it contracts. Yet, the macroscopic behaviour of the muscle does not have to shorten. Therefore, voluntary muscular contractions may be classified according to length changes (concentric, eccentric, and isometric), force levels (isotonic), or contraction dynamics (isokinetic): A contraction is considered

concentric, when the muscle force and the resulting motion are in the same direction,

i.e., the sarcomere and the muscle shorten.

eccentric, when the muscle force and the resulting motion are contradicting, i.e., even though the sarcomeres are pulling, the length of the muscle increases.

isometric, when the muscle force does not lead to a resulting motion, i.e., even though the sarcomeres are pulling, the length of the muscle is constant.

isotonic, when the muscle force is constant independent of the direction of motion of the muscle.

isokinetic, when the muscle changes its length with constant speed.

In a musculoskeletal system, locomotion is enabled by linking muscle-tendon tissue to bones. In conjunction with joints, these three elements build a lever system. A lever is a rigid rod or beam that is able to rotate about a fixed point called the fulcrum where both a force (or an effort) and a load (or a resistance) act. The force which moves the lever is called the effort. The force to be moved or overcome is called the resistance. The perpendicular distance between the load and effort to the fulcrum is called lever arm. Depending on the relative position to each other, three different types can be categorised leading to different specifications:

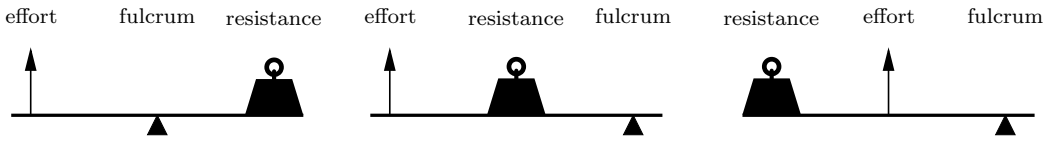

(a) *Class 1 lever* **(b)** *Class 2 lever* **(c)** *Class 3 lever*

Figure 2.13: *Depending on the set-up of effort, resistance, and fulcrum different types of levers can be defined. Each type has its advantages and disadvantages.*

Class 1: The fulcrum lies between the effort and the resistance. Depending on the length of each lever arm the effort to resistance ratio is larger or smaller than one. When the lever arm of the effort equals the one of the resistance, then the ratio is one. An example in our body is when the triceps brachii pulls on the forearm.

Class 2: The resistance lies in the middle. Hereby, the effort's lever arm is always larger than the one of the resistance. This leads to a low effort to resistance ratio and implies a slow resulting motion as the effort needs to move more than the resistance. On the other hand, high resistances can be overcome. An example can be found in our feet when we stand on our toes and lift our heels off the ground.

Class 3: The effort lies in the middle. Hereby, the resistance's lever is always longer than the one of the effort. This leads to high efforts to resistance ratios and implies a rapid resulting motion. An example is the biceps brachii pulling on the forearm.

3 Continuum-Mechanical Fundamentals

As biological tissue can undergo large deformations, the Theory of Finite Elasticity provides the mathematical framework to describe the deformed state of the system to investigate. For theoretical aspects leading beyond the presented theory, the reader is referred to standard continuum mechanics text books such as for example Holzapfel (2000) or Fung and Tong (2001).

3.1 Finite Elasticity

3.1.1 Kinematical Relations

The material body $\mathcal{B}$ is a manifold of connected material points $\mathcal{P}$. This material body is embedded in an *Euclid*ian space including a fixed origin $\mathcal{O}$. Every material point $\mathcal{P}$ in $\mathcal{B}$ has at any time t a unique position defined by its placement function $\boldsymbol{\chi}(\mathcal{P}, t) = \mathbf{x}$. For all material points in $\mathcal{B}$, this state is called the current configuration. At the initial time $t_0 = 0$, the material points $\mathcal{P}$ are said to be in their reference configuration which is defined by $\mathbf{X} = \boldsymbol{\chi}(\mathcal{P}, t_0)$.

The material points at the boundary of $\mathcal{B}$ define the surface $\Gamma_{\mathcal{B}}$. At the surface different kinds of boundary conditions can be applied. The boundary where *Dirichlet* conditions are applied is called $\Gamma^u_{\mathcal{B}}$ and the boundary where *Neumann* conditions are applied is called $\Gamma^\sigma_{\mathcal{B}}$. These boundaries are mutually exclusive and together form the entire surface, that is $\Gamma_{\mathcal{B}} = \Gamma^u_{\mathcal{B}} \cup \Gamma^\sigma_{\mathcal{B}}$ and $\Gamma^u_{\mathcal{B}} \cap \Gamma^\sigma_{\mathcal{B}} = \emptyset$.

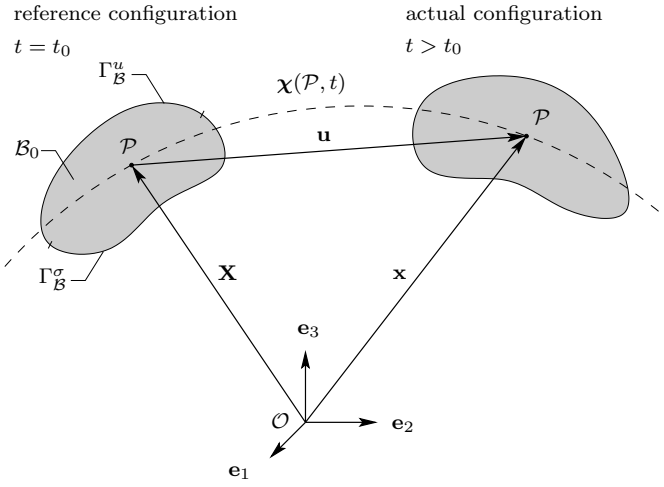

Figure 3.1: *Kinematics of a body $\mathcal{B}$.*

The motion of a material point can be described in different ways. In a material or *Lagrange*an description the behaviour refers to a material point, whereas in a spatial

or *Euler*ian description the behaviour refers to a particular spatial position. In case of solid mechanics, it is common to employ a material description and therefore express the position, motion and accelerations with respect to material coordinates $P \rightarrow \mathbf{X}$.

Using the placement function $\boldsymbol{\chi}$, the velocity and the acceleration can be obtained by

$$\dot{\mathbf{x}}(\mathbf{X}, t) = \frac{\mathrm{d}}{\mathrm{d}t}\boldsymbol{\chi}(\mathbf{X}, t)\,, \tag{3.1}$$

and

$$\ddot{\mathbf{x}}(\mathbf{X}, t) = \frac{\mathrm{d}^2}{\mathrm{d}t^2}\boldsymbol{\chi}(\mathbf{X}, t)\,, \tag{3.2}$$

respectively.

3.1.2 Deformation and Strain Measures

Due to the kinematic relationship between the reference configuration $\mathbf{X} = X_1\,\mathbf{e}_1 + X_2\,\mathbf{e}_2 + X_3\,\mathbf{e}_3$ and the actual configuration $\mathbf{x} = x_1\,\mathbf{e}_1 + x_2\,\mathbf{e}_2 + x_3\,\mathbf{e}_3$, the displacement $\mathbf{u}$ is given by

$$\mathbf{u} = \mathbf{x} - \mathbf{X}\,. \tag{3.3}$$

The displacement is a continuous, differentiable and a vector-valued function. To describe deformations and strains at a material point, the actual and the reference configuration are linked to each other by the deformation gradient $\mathbf{F}$. The latter is defined as the gradient of the motion function with respect to the reference configuration:

$$\mathbf{F} := \frac{\partial \boldsymbol{\chi}(\mathbf{x}, t)}{\partial \mathbf{X}} = \frac{\partial \mathbf{x}}{\partial \mathbf{X}}\,. \tag{3.4}$$

The determinant of $\mathbf{F}$ denoted by J,

$$J = \det \mathbf{F}\,, \tag{3.5}$$

is called the *Jacobi*an and is a measure for the volumetric change of the described deformation with respect to the reference configuration.

For the reference configuration, J is one and greater than zero all the time. Note, if the determinant of $\mathbf{F}$ equals zero, the body would collapse to a plain, line, or point which is physically not possible. If $J > 1$, the volume of $\mathcal{B}$ increases, while for $J < 1$, it reduces. A negative determinant would be non-physical.

As $\mathbf{F}$ is a two-field tensor, $\mathbf{F}$ and $\mathbf{F}^{-1}$ and their transposed are used to push forward and pull back quantities from reference to current configuration and vice versa. The left basis of $\mathbf{F}$ is in the actual configuration and the right basis in the reference configuration. Hence, the transport of a line element from the reference configuration, i.e. $\mathrm{d}\mathbf{X}$, into the current configuration is given by:

$$\mathrm{d}\mathbf{x} = \mathbf{F}\ \mathrm{d}\mathbf{X}\,. \tag{3.6}$$

Similar, the transport of an area or a volume element are obtained by:

$$\mathrm{d}\mathbf{a} = (\det \mathbf{F})\ \mathbf{F}^{T-1}\ \mathrm{d}\mathbf{A}\,, \qquad \mathrm{d}v = (\det \mathbf{F})\ \mathrm{d}V\,. \tag{3.7}$$

With the definition of the deformation gradient and the transport equations of the current line element, the *Cauchy-Green* deformation tensors can be introduced. Considering the squared lengths of a line element in the current and reference configuration,

$$\begin{aligned} \|\,\mathrm{d}\mathbf{x}\,\|^2 &= \mathrm{d}\mathbf{x}\cdot\ \mathrm{d}\mathbf{x} = (\mathbf{F}\ \mathrm{d}\mathbf{X})\cdot(\mathbf{F}\ \mathrm{d}\mathbf{X}) = \ \mathrm{d}\mathbf{X}\cdot(\mathbf{F}^T\mathbf{F})\ \ \mathrm{d}\mathbf{X} \\ &= \mathrm{d}\mathbf{X}\cdot\mathbf{C}\ \ \mathrm{d}\mathbf{X}\,, \qquad (3.8) \\ \|\,\mathrm{d}\mathbf{X}\,\|^2 &= \mathrm{d}\mathbf{X}\cdot\ \mathrm{d}\mathbf{X} = (\mathbf{F}^{-1}\ \mathrm{d}\mathbf{x})\cdot(\mathbf{F}^{-1}\ \mathrm{d}\mathbf{x}) \\ &= \mathrm{d}\mathbf{x}\cdot(\mathbf{F}^{T-1}\mathbf{F}^{-1})\ \ \mathrm{d}\mathbf{x} \\ &= \mathrm{d}\mathbf{x}\cdot\mathbf{B}^{-1}\ \ \mathrm{d}\mathbf{x}\,, \qquad (3.9) \end{aligned}$$

the right *Cauchy-Green* deformation tensor, $\mathbf{C}$, in reference configuration, and the left *Cauchy-Green* deformation tensor, $\mathbf{B}$, in the current configuration are defined.

By replacing the right and left *Cauchy-Green* deformation tensor by the product of $\mathbf{F}$ and conducting the polar decomposition on $\mathbf{F}$, the right and left *Cauchy-Green* deformation tensor can be transformed to:

$$\mathbf{C} = \mathbf{F}^T\mathbf{F} = (\mathbf{Q}\mathbf{U})^T\mathbf{Q}\mathbf{U} = \mathbf{U}^T(\mathbf{Q}^T\mathbf{Q})\mathbf{U} = \mathbf{U}\mathbf{U}\,, \qquad (3.10)$$

$$\mathbf{B} = \mathbf{F}\mathbf{F}^T = \mathbf{V}\mathbf{Q}(\mathbf{V}\mathbf{Q})^T = \mathbf{V}(\mathbf{Q}\mathbf{Q}^T)\mathbf{V}^T = \mathbf{V}\mathbf{V}\,, \qquad (3.11)$$

where $\mathbf{Q} \in SO_3$ is a proper orthogonal rotation tensor with the properties $\det\mathbf{Q} = 1$ and $\mathbf{Q}^T = \mathbf{Q}^{-1}$, while $\mathbf{U}$ and $\mathbf{V}$ are the symmetric positive definite right (material) and left (spatial) stretch tensors, respectively. One can see that the *Cauchy-Green* deformation tensors only depend on the stretch tensors and not on the rigid-body rotations. This property will be used later on for the material objectivity in Section 4.2.

While the deformation tensors describe the state of deformation itself, a strain measure relates the length in the current configuration to the length in the reference configuration. Therefore, by relating the length of infinitesimal small line elements, i.e.,

$$\begin{aligned} \|\ \mathrm{d}\mathbf{x}\|^2 - \|\ \mathrm{d}\mathbf{X}\|^2 &= \ \mathrm{d}\mathbf{X}\cdot\mathbf{C}\ \ \mathrm{d}\mathbf{X} - \ \mathrm{d}\mathbf{X}\cdot\ \mathrm{d}\mathbf{X} = \ \mathrm{d}\mathbf{X}\cdot(\mathbf{C}-\mathbf{I})\ \ \mathrm{d}\mathbf{X}\,, \\ &= \ \mathrm{d}\mathbf{x}\cdot\ \mathrm{d}\mathbf{x} - \ \mathrm{d}\mathbf{x}\cdot\mathbf{B}^{-1}\,\mathrm{d}\mathbf{x}\ = \ \mathrm{d}\mathbf{x}\cdot(\mathbf{I}-\mathbf{B}^{-1})\ \ \mathrm{d}\mathbf{x}\,. \end{aligned} \qquad (3.12)$$

the *Green-Lagrange*an strain tensor $\mathbf{E}$ and the *Almansi*an strain tensor $\mathbf{A}$ can be defined by:

$$\mathbf{E} := \tfrac{1}{2}(\mathbf{C}-\mathbf{I}) \qquad \text{and} \qquad \mathbf{A} := \tfrac{1}{2}(\mathbf{I}-\mathbf{B}^{-1})\,. \qquad (3.13)$$

The factor one half is historically motivated and results from the fact, that the linearisation of $\mathbf{E}$ and $\mathbf{A}$ around the natural state (zero deformation) should result in the engineering strain tensor $\boldsymbol{\varepsilon}$.

Spectral Representation of the Deformation Tensors

It is often convenient to employ the spectral representation of the deformation tensors to describe constitutive laws for the material behaviour. This is particularly the case for hyperelastic material laws.

As introduced in Equation (3.10) and (3.11), $\mathbf{C}$ and $\mathbf{B}$ are both products of $\mathbf{F}$, and vary only by a proper orthogonal rotation, i.e. by $\mathbf{Q}$ and $\mathbf{Q}^T$. Therefore, it can be shown that

$\mathbf{C}$ and $\mathbf{B}$ have the same eigenvalues λ_i, which are the squares of the principle stretches. Furthermore, due to the relation of $\mathbf{U}$ to $\mathbf{C}$ and $\mathbf{V}$ to $\mathbf{B}$, they all have the same mutually orthogonal eigenvectors $\mathbf{m}_i$ and $\mathbf{n}_i$, i.e.

$$\begin{aligned} (\mathbf{C} - \lambda_i \mathbf{I})\, \mathbf{m}_i &= \mathbf{0}\,, \\ (\mathbf{B} - \lambda_i \mathbf{I})\, \mathbf{n}_i &= \mathbf{0}\,. \end{aligned} \tag{3.14}$$

Applying the *Caley-Hamilton* theorem to

$$\det(\mathbf{C} - \lambda_i \mathbf{I}) = \det(\mathbf{B} - \lambda_i \mathbf{I}) = \lambda_i^3 - I_1\, \lambda_i^2 + I_2\, \lambda_i - I_3 = 0\,, \tag{3.15}$$

one obtains

$$\begin{aligned} I_1 &= \mathrm{tr}\ \mathbf{C} && = \mathrm{tr}\ \mathbf{B} && = \mathbf{F} \cdot \mathbf{F}\,, \\ I_2 &= \mathrm{tr}\ (\mathrm{cof}\, \mathbf{C}) && = \mathrm{tr}\ (\mathrm{cof}\, \mathbf{B}) && = \mathrm{cof}\, \mathbf{F} \cdot \mathrm{cof}\, \mathbf{F}\,, \\ I_3 &= \det \mathbf{C} && = \det \mathbf{B} && = (\det \mathbf{F}\,)^2\,, \end{aligned} \tag{3.16}$$

where $\mathrm{cof}(\cdot)$ is the cofactor of a tensor.

Three real-valued eigenvalues λ_i with $i = 1, 2, 3$ are obtained from the symmetric deformation tensors. The invariants can be related to the eigenvalues by

$$\begin{aligned} I_1 &= \lambda_1 + \lambda_2 + \lambda_3\,, \\ I_2 &= \lambda_1\, \lambda_2 + \lambda_2\, \lambda_3 + \lambda_1\, \lambda_3\,, \\ I_3 &= \lambda_1\, \lambda_2\, \lambda_3\,. \end{aligned} \tag{3.17}$$

3.1.3 Stress Measures

While a material body is deformed, stress is the quantity expressing the internal, mechanical state of each material point $\mathcal{P}$ to its neighbours within the body $\mathcal{B}$. The unit of stress is force per area. As forces can be related to areas in the reference or actual configuration, different stress tensors can be introduced.

Cauchy's fundamental lemma states that a tension vector $\mathbf{t}$ can be found at any cut free surface of a body, that depends in time, space and orientation on the surface normal vector $\mathbf{n}$, i.e.

$$\mathbf{t}(\mathbf{x}, \mathbf{n}, t) = -\mathbf{t}(\mathbf{x}, -\mathbf{n}, t)\,. \tag{3.18}$$

The traction vector $\mathbf{t}$ describes the impact of the force acting on the surface $\Gamma_{\mathcal{B}}$ of the body $\mathcal{B}$. If one observes the static equilibrium at an infinitesimal tetrahedron, one obtains the *Cauchy* theorem. It reformulates the surface traction vector $\mathbf{t}(\mathbf{x}, \mathbf{n}, t)$ in a more convenient quantity, the stress tensor $\mathbf{T}(\mathbf{x}, t)$. The traction vector $\mathbf{t}$ is the projection of $\mathbf{T}$ on the outward unit surface vector $\mathbf{n}$ in the current configuration. The stress tensor $\mathbf{T}$ is called *Cauchy* or true stress tensor. *Cauchy*'s theorem states:

$$\mathbf{t}(\mathbf{x}, \mathbf{n}, t) = \mathbf{T}(\mathbf{x}, t)\, \mathbf{n}\,. \tag{3.19}$$

The incremental surface force, $\mathrm{d}\mathbf{f}_s$, is given by

$$\mathrm{d}\mathbf{f}_s = \mathbf{t}\ \mathrm{d}a = (\mathbf{T}\, \mathbf{n})\ \mathrm{d}a = \mathbf{T}\ \mathrm{d}\mathbf{a}. \tag{3.20}$$

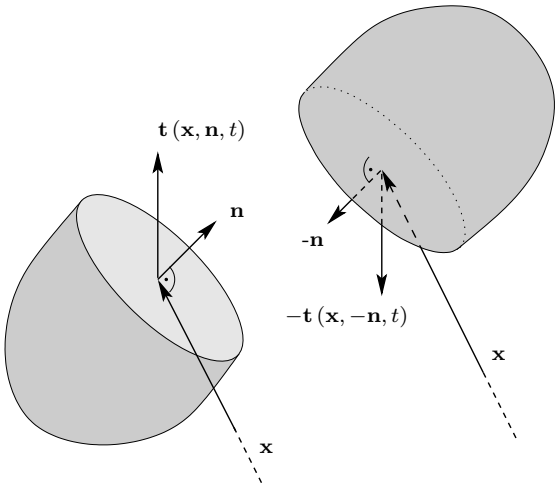

Figure 3.2: *Cauchy's Fundamental Lemma: Cut off surface of a body.*

Introducing a weighted area $\mathrm{d}\tilde{\mathbf{a}} = \dfrac{\mathrm{d}V}{\mathrm{d}v}\,\mathrm{d}\mathbf{a} = (\det \mathbf{F})^{-1}\,\mathrm{d}\mathbf{a}$, one obtains the weighted or *Kirchhoff* stress $\boldsymbol{\tau}$,

$$\mathrm{d}\mathbf{f}_s = \mathbf{T}\,(\det \mathbf{F})\,\mathrm{d}\tilde{\mathbf{a}} = \boldsymbol{\tau}\,\mathrm{d}\tilde{\mathbf{a}}. \tag{3.21}$$

Pulling the second basis of the *Kirchhoff* stress back by a co-variant transport, one gets the nominal or 1st *Piola-Kirchhoff* stress $\mathbf{P}$. This tensor is a two-field tensor with one basis in each configuration and therefore not symmetric. Yet, for experimental purposes, it is very often convenient, as it relates the measured force to the area in reference configuration.
Further, pulling back the first basis of the 1st *Piola-Kirchhoff* stress, one obtains the 2nd *Piola-Kirchhoff* stress. As both basis of this stress tensor are in the reference configuration, the stress tensor is symmetric:

$$\mathbf{P} = \boldsymbol{\tau}\,\mathbf{F}^{T-1} = (\det \mathbf{F})\,\mathbf{T}\,\mathbf{F}^{T-1}\,, \tag{3.22}$$

and

$$\mathbf{S} = \mathbf{F}^{-1}\,\mathbf{P} = (\det \mathbf{F})\,\mathbf{F}^{-1}\,\mathbf{T}\,\mathbf{F}^{T-1}\,. \tag{3.23}$$

3.2 Balance Relations

Conservation equations are based on the fact that conserved quantities cannot be produced nor lost in a closed system. If additional external influences, as fluxes and production terms, on the system are taken into account, one speaks of *balance equations*, i.e. the balance of mass, momentum, moment of momentum, and energy. Each balance law can be stated in a global or local form.

3.2.1 Mass Balance

For this work, the mass balance is not employed explicitly. The mass balance in its global and conserved form for the body $\mathcal{B}$ is axiomatically introduced by

$$\frac{\mathrm{d}}{\mathrm{d}t}\int\limits_{\Omega_\mathcal{B}} \rho \;\mathrm{d}v = 0\,. \tag{3.24}$$

After some mathematical transformations, the local form can be stated as

$$\dot{\rho} + \rho\,\mathrm{div}\,\dot{\mathbf{x}} = 0\,, \tag{3.25}$$

where $\rho = \rho\, J^{-1}$ for solid mechanics. This equation can be interpreted as the temporal change of mass, which has to be zero for a closed system, and is equal to the sum of what flows into and leaves the system.

3.2.2 Momentum Balance

The second balance equation is the momentum balance, in which the temporal change of the momentum $\rho\,\dot{\mathbf{x}}$ is balanced with the surface and body forces acting on the body $\mathcal{B}$. In global form, the balance equation is defined by

$$\frac{\mathrm{d}}{\mathrm{d}t}\int\limits_{\Omega_\mathcal{B}} \rho\,\dot{\mathbf{x}} \;\mathrm{d}v = \int\limits_{\Gamma_\mathcal{B}} \mathbf{T}\,\mathbf{n} \;\mathrm{d}a + \int\limits_{\Omega_\mathcal{B}} \rho\,\mathbf{b} \;\mathrm{d}v\,. \tag{3.26}$$

Reformulating the momentum balance by inserting the mass balance, employing *Cauchy*'s theorem (3.18), and the divergence theorem for the flux term, Equation (3.26) yields,

$$\int\limits_{\Omega_\mathcal{B}} \rho\,\ddot{\mathbf{x}} \;\mathrm{d}v = \int\limits_{\Omega_\mathcal{B}} \mathrm{div}\,\mathbf{T} \;\mathrm{d}v + \int\limits_{\Omega_\mathcal{B}} \rho\,\mathbf{b} \;\mathrm{d}v\,. \tag{3.27}$$

This relation holds for any volume $\mathrm{d}v$. Hence, the local form reduces to:

$$\rho\,\ddot{\mathbf{x}} = \mathrm{div}\,\mathbf{T} + \rho\,\mathbf{b}\,, \tag{3.28}$$

which is valid for every point $\mathbf{x}$ within the volume $\mathrm{d}v$ at time t.

3.2.3 Moment of Momentum Balance

The moment of momentum balance or angular momentum balance accounts for the temporal change of the moment of momentum $\dot{\mathbf{x}} \times \rho\dot{\mathbf{x}}$ with the inner and outer moments acting on the body. In global form, the balance reads

$$\frac{\mathrm{d}}{\mathrm{d}t}\int\limits_{\Omega_\mathcal{B}} (\mathbf{x} \times \rho\dot{\mathbf{x}}) \;\mathrm{d}v = \int\limits_{\Gamma_\mathcal{B}} (\mathbf{x} \times \mathbf{T})\mathbf{n} \;\mathrm{d}a + \int\limits_{\Omega_\mathcal{B}} (\mathbf{x} \times \rho\,\mathbf{b}) \;\mathrm{d}v\,. \tag{3.29}$$

By transforming the global balance, using the integral theorem and the momentum balance as lower balance equation, the local form yields

$$\mathbf{0} = \mathbf{I} \times \mathbf{T} \quad \Longleftrightarrow \quad \mathbf{T} = \mathbf{T}^T\,. \tag{3.30}$$

Equation (3.30) yields that the *Cauchy* stress tensor is symmetric.

3.2.4 Energy Balance

The energy balance, also known as the first thermodynamical balance law, indicates the conservation of energy. If a non-isothermal problem is considered, energetic quantities also have to be balanced. The equation balances the temporal change of the sum of internal and kinetic energy with the power resulting from the surface and body forces as well as the heat efflux over the boundary and the heat supply in the body. The global energy balance reads

$$\frac{\mathrm{d}}{\mathrm{d}t}\int\limits_{\Omega_{\mathcal{B}}} (\mathfrak{e} + \tfrac{1}{2}\,\dot{\mathbf{x}}\cdot\dot{\mathbf{x}})\;\mathrm{d}v = \int\limits_{\Gamma_{\mathcal{B}}} [(\mathbf{T}\,\dot{\mathbf{x}} - \mathbf{q})\cdot\mathbf{n}\,]\;\;\mathrm{d}a + \int\limits_{\Omega_{\mathcal{B}}} [\rho\,(\dot{\mathbf{x}}\cdot\mathbf{b}) + r]\;\;\mathrm{d}v\,. \tag{3.31}$$

Therein, $\mathfrak{e}$ represents the mass specific internal energy, $\mathbf{q}$ is the heat efflux and r is the external heat supply from a distance. The local balance reads after using the lower balances and the integral theorem as follows:

$$\rho\,\dot{\mathfrak{e}} = \mathbf{T}\cdot\mathbf{L} - \operatorname{div}\mathbf{q} + \rho\,r\,. \tag{3.32}$$

Herein, $\mathbf{L}$ is the spatial velocity gradient, $\mathbf{T}\cdot\mathbf{L}$ is the stress power, and $\operatorname{div}\mathbf{q}$ represents the heat flux over the boundary, respectively.

Stress Power and Energetic Conjugates

The product of stress and strain rates are often called the rate of internal work or the stress power, as it was introduced in Equation (3.32).

If only mechanically-related quantities are considered in Equation (3.32), this equation can be rewritten to

$$\frac{\mathrm{d}}{\mathrm{d}t}\int\limits_{\Omega_{\mathcal{B}}} \frac{1}{2}\,\rho\,\dot{\mathbf{x}}\cdot\dot{\mathbf{x}}\,\mathrm{d}v + \int\limits_{\Omega_{\mathcal{B}}} \mathbf{T}\cdot\mathbf{L}\,\mathrm{d}v = \int\limits_{\Gamma_{\mathcal{B}}} \mathbf{t}\;\cdot\mathbf{x}\,\mathrm{d}a + \int\limits_{\Omega_{\mathcal{B}}} \rho\,\mathbf{b}\cdot\mathbf{x}\,\mathrm{d}v\,. \tag{3.33}$$

The first term defines the kinetic energy of $\mathcal{B}$, the second term the internal mechanical power, or stress power, and the right-hand side defines the external mechanical power.

Further, it can be observed that the scalar product of stress and strain in the second term and their rates within the same configuration are invariant with respect to the transport to another configuration. These pairs are called energetic conjugates if their dot product accurately reflects the stored strain energy in the system. As in a *Lagrange*an setting, the specific stress power is defined with respect to the reference configuration, the conjugate pair, defined by $\mathbf{T}\cdot\mathbf{L}$, can be pulled back to

$$P_{\mathrm{int}} = \int\limits_{\Omega_{\mathcal{B}}} \mathbf{T}\cdot\mathbf{L}\,\mathrm{d}v = \int\limits_{\Omega_{\mathcal{B}}} \mathbf{T}\cdot\mathbf{L}\,\det\mathbf{F}\,\mathrm{d}V = \int\limits_{\Omega_{\mathcal{B}}} \boldsymbol{\tau}\cdot\mathbf{L}\,\mathrm{d}V\,. \tag{3.34}$$

With some algebraic tensor transformations, conjugate pairs for $\mathbf{P}$ and $\mathbf{S}$, i.e. $\{\mathbf{P},\dot{\mathbf{F}}\}$ and $\{\mathbf{S},\dot{\mathbf{E}}\}$, can be formulated in a similar way.

For conserved systems, the same procedure can be done for the mechanical or strain energy. The resulting conjugate pairs are $\{\boldsymbol{\tau},\mathbf{A}\}$, $\{\mathbf{P},\mathbf{F}\}$, and $\{\mathbf{S},\mathbf{E}\}$.

4 Constitutive Model

In the preceding theoretical parts of this thesis, the fundamentals for the kinetics (Section 3.1.1) and balance relations (Section 3.2) are derived materially independent. By the introduced balance relations, the emerging initial-boundary-value-problem (IVBP) can only be solved if the problem is well posed. This property poses several requests on the partial differential equations, the initial, and boundary conditions. One of the more trivial requests are that the number of unknowns need to equal to the number of posed equations. In order to solve the momentum balance a relation between stress and strain needs to be provided. In the following chapter, the mechanical material behaviour of a skeletal muscle is introduced to meet this requirement.

4.1 Skeletal Muscle Constitutive Modelling Assumptions

Following the status quo of skeletal muscle modelling, the mechanical behaviour of a skeletal muscle can be deduced from the physiological character of the skeletal muscle. In general, there are two possible approaches: a phenomenological and a biophysical, see Section 1.2.1. Within this thesis, a purely phenomenological approach is chosen.

As this thesis deduces a framework for a multi-muscle musculoskeletal system employing continuum mechanical muscles, the choice of a specific skeletal muscle model is not of first priority. Hence, a rather simple skeletal muscle model is employed, in which the muscle activation dynamics and cellular effects are neglected. This shall not be a limitation to this work. All methodologies developed as part of this work also hold for more complex skeletal muscle models like the chemo-electro-mechanical skeletal muscle model proposed by Heidlauf and Röhrle (2014).

From a continuum-mechanical point of view, skeletal muscles are commonly assumed to be hyperelastic and transversely isotropic. Most of biological materials, so are skeletal muscles, are water saturated and under natural occurring loads incompressible, see Section 1.2.1.

As the muscle is assumed to be hyperelastic, all processes are assumed to be reversible and isothermal. Hence, firstly, hysteresis effects are not considered. Secondly, even though the muscle activates and contracts, no energy dissipating effect are taken into consideration. Furthermore, as the velocities and accelerations are assumed to be small ($\ddot{\mathbf{x}}, \dot{\mathbf{x}} \approx 0$), only slow motions are considered. Therefore, inertia terms and viscous effects are neglected and a quasi-static formulation is chosen. Furthermore, as the velocity is considered to be small, the muscle's behaviour is independent of the contraction velocity and the force-velocity relation does not need to be considered.

The derivation of the most important anatomical skeletal muscle specific properties, such as the fibre distribution, the fibre orientation, the prestretch, and the definition of the values for different mechanical contributions, are defined in Chapter 7.

4.2 Constitutive Model Principles

To define a thermodynamically consistent set of constitutive equations and to approximate the observed behaviour of a real material under specific conditions, some requirements need to be set. These requirements are:

Determinism: The set of undetermined response functions, which have to be uniquely defined at any time t is:

$$\mathcal{R} = \{\Psi\}\,. \tag{4.1}$$

As in this thesis only elastic effects are considered, the set of responds functions reduces to a minimum.

Equipresence: The response functions may depend on the whole set of process variables $\mathcal{V}$, which are uniquely characterising the current and history state of the overall system with respect to temperature, chemical potentials, deformation and structural composition. Considering the before mentioned assumptions, the set of process variables reduces to

$$\mathcal{V} = \{\mathbf{F}, \boldsymbol{\mathcal{M}}, \mathbf{X}, \alpha\}\,, \tag{4.2}$$

where $\boldsymbol{\mathcal{M}}$ denotes the structural tensor. This set of variables uniquely defines any state of the overall body $\mathcal{B}$. It represents the geometry in the current state (deformation), the reference state (to consider inhomogeneities as e.g. locally varying fibre types), as well as the locally varying fibre field orientation of the skeletal muscle.

Local action: An object is only influenced directly by its immediate surrounding.

Material frame indifference: This principle is also called material objectivity. It states that material properties and therefore also the constitutive equations should not depend on the position of the observer. The mathematical interpretation of such an objectivity condition states that constitutive equations have to be invariant to rigid-body rotations, for e.g. a rotation $\mathbf{Q}$ of the actual configuration.

$$\overset{\star}{\Psi}\,(\mathcal{V}) = \Psi(\overset{\star}{\mathcal{V}})\,, \tag{4.3}$$

where $\overset{\star}{(\cdot)}$ indicates that the quantity in the actual configuration is rotated by $\mathbf{Q} \in \mathcal{SO}_3$. Following this requirements, some important implications for the constitutive law can be deduced.

The position vector in actual configuration reads, $\overset{\star}{\mathbf{x}} = \mathbf{Q}\mathbf{x}$. Following this procedure, the consequences for the deformation gradient are:

$$\overset{\star}{\mathbf{F}} = \frac{\partial\,\overset{\star}{\mathbf{x}}}{\partial \mathbf{X}} = \frac{\partial\,\overset{\star}{\mathbf{x}}}{\partial \mathbf{x}}\,\frac{\partial \mathbf{x}}{\partial \mathbf{X}} = \mathbf{Q}\,\mathbf{F} \quad \text{with} \quad \mathbf{Q} = \frac{\partial\,\overset{\star}{\mathbf{x}}}{\partial \mathbf{x}} \in \mathcal{SO}_3\,. \tag{4.4}$$

By this definition, $\mathbf{F}$ is not sufficing the material objectivity restriction. Further, it can be shown, that the structural tensor $\boldsymbol{\mathcal{M}}$ and the reference position vector $\mathbf{X}$

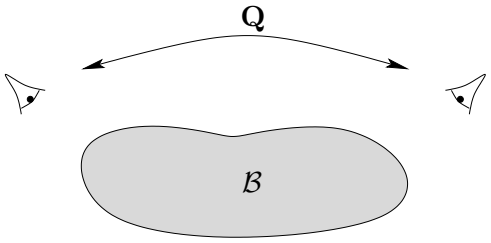

Figure 4.1: *The mechanical behaviour must be independent of the position of the observer.*

are invariant to rotations of the actual configuration, a priori. The same applies for the scalar-valued volume specific strain energy function, Ψ.

As a consequence from the mentioned facts, one can deduce that the deformation gradient is not a well suited measure for the invariance condition as

$$\Psi(\mathbf{F}, \boldsymbol{\mathcal{M}}, \mathbf{X}) \neq \Psi(\mathbf{Q}\,\mathbf{F}, \boldsymbol{\mathcal{M}}, \mathbf{X})\,. \tag{4.5}$$

By applying the right polar decomposition on the deformation gradient, $\mathbf{F}$ can be rewritten as $\mathbf{F} = \hat{\mathbf{Q}}\mathbf{U}$. Assuming that a material is objective to all orthogonal rotation tensors, it also holds for the special choice $\mathbf{Q} = \hat{\mathbf{Q}}^T$. Further, with $\hat{\mathbf{Q}}\,\hat{\mathbf{Q}}^T = \mathbf{I}$. Equation (4.5) yields,

$$\Psi(\hat{\mathbf{Q}}\,\hat{\mathbf{Q}}^T\,\mathbf{U}, \boldsymbol{\mathcal{M}}, \mathbf{X}) = \Psi(\mathbf{U}, \boldsymbol{\mathcal{M}}, \mathbf{X})\,. \tag{4.6}$$

Thus the strain energy may only depend on the referential stretching parts of the overall deformation gradient. Recalling the definitions of the deformation and strain tensors, the process variable set can be defined to:

$$\Psi(\mathbf{C}, \boldsymbol{\mathcal{M}}, \mathbf{X}) = \Psi(\mathbf{E}, \boldsymbol{\mathcal{M}}, \mathbf{X})\,, \tag{4.7}$$

and similarly to:

$$\Psi(\mathbf{B}, \boldsymbol{\mathcal{M}}, \mathbf{X}) = \Psi(\mathbf{A}, \boldsymbol{\mathcal{M}}, \mathbf{X})\,. \tag{4.8}$$

Hence, $\mathbf{C}, \mathbf{E}, \mathbf{B}$, or $\mathbf{A}$ are common measures used to formulate a constitutive relation. More information about this subject can be found in Truesdell and Noll (2004).

Universal dissipation: The process has to fulfil the entropy inequality (also called the second law of thermodynamics), which states that the entropy has to increase for dissipative processes or stay constant for reversible processes. As our constitutive model will be isothermal and hyperelastic, this restriction is fulfilled per se.

Material symmetry: All previous principles are true for all materials. Yet many materials exhibit preferred directions. Symmetry groups $\mathcal{SG}_3$ define groups of rotations for which the material orientation is invariant. The symmetry group is a subset of the orthogonal transformations, $\mathcal{SG}_3 \subset \mathcal{O}_3$.

The mechanical behaviour of isotropic materials is independent of the orientation of the specimen or the applied load. Hence, a symmetry group of $\mathcal{SG}_3 = \mathcal{O}_3$ implies

that the only possible structural tensor is $\boldsymbol{\mathcal{M}} = \mathbf{I}$, and hence refers to an isotropic material.

Materials for which the mechanical behaviour depends on the direction of either load or orientation of the specimen can be categorised into different classes in, e.g. transversely isotropy, orthotropy or prismatic isotropy.

Skeletal muscles are fibre reinforced materials with one or more preferred fibre directions, see Section 2.4.1. For this thesis, only muscles with one fibre family are considered, see Section 4.1. Materials with one fibre family are called transversely isotropic. The symmetry group for transversely isotropic materials depends on the one preferred fibre direction, $\mathbf{a}_0$. The orientation of the fibre within $\mathcal{B}$ is defined by the structural tensor, $\boldsymbol{\mathcal{M}} = \mathbf{a}_0 \otimes \mathbf{a}_0$. For the structural tensor holds

$$\boldsymbol{\mathcal{M}} = \boldsymbol{\mathcal{M}}^T\,, \quad \boldsymbol{\mathcal{M}} = \boldsymbol{\mathcal{M}}\,\boldsymbol{\mathcal{M}}\,, \quad \operatorname{tr}\boldsymbol{\mathcal{M}} = 1\,. \tag{4.9}$$

In consequence, $\mathcal{SG}_3$ for transverse isotropy is defined by

$$\mathcal{SG}_3 = \{\pm\mathbf{I}, \mathbf{Q}_{\boldsymbol{\xi}_1}, \mathbf{Q}_{\boldsymbol{\xi}_2}, \mathbf{Q}_{\boldsymbol{\xi}_3}, \mathbf{Q}_{\boldsymbol{\xi}_1}^{(\phi_1)}, \mathbf{Q}_{\boldsymbol{\xi}_2}^{(\pi)}, \mathbf{Q}_{\boldsymbol{\xi}_3}^{(\pi)}\}\,, \quad \forall\ 0 \le \phi_1 < 2\pi\,, \tag{4.10}$$

where $\mathbf{Q}_{\boldsymbol{\xi}}$ denotes the reflection tensor,

$$\mathbf{Q}_{\boldsymbol{\xi}} = \mathbf{I} - 2\,\boldsymbol{\xi} \otimes \boldsymbol{\xi} \quad \forall\ \boldsymbol{\xi} \in \{\boldsymbol{\xi}_1, \boldsymbol{\xi}_2, \boldsymbol{\xi}_3\}\,. \tag{4.11}$$

Here, $\boldsymbol{\xi}$ are mutually orthogonal unit vectors, and $\mathbf{Q}_{\boldsymbol{\xi}}^{(\phi)}$ can be determined by the *Euler-Rodrigues* formulas, i.e.

$$\mathbf{Q}_{\boldsymbol{\xi}}^{(\phi)} = \boldsymbol{\xi} \otimes \boldsymbol{\xi} + \sin\phi\,(\boldsymbol{\xi} \times \mathbf{I}) + \cos\phi(\mathbf{I} - \boldsymbol{\xi} \otimes \boldsymbol{\xi}) \quad \forall\ \boldsymbol{\xi} \in \{\boldsymbol{\xi}_1, \boldsymbol{\xi}_2, \boldsymbol{\xi}_3\}\,. \tag{4.12}$$

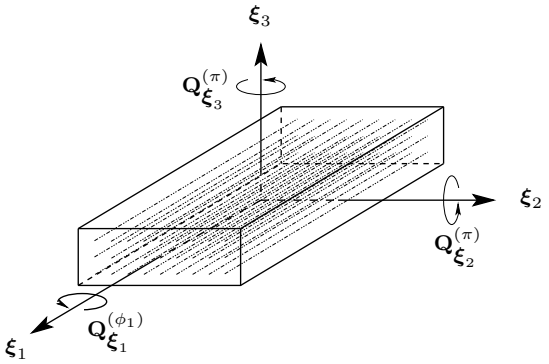

Figure 4.2: *Material symmetry for transversely isotropic materials.*

Further information can be found in Spencer (1971) and the references therein.

As a consequence from the material symmetry, further invariants, other than the three invariants defined in 3.1.2, need to be introduced. Possible invariants for describing a transversely isotropic material are

$$\begin{aligned} &\operatorname{tr}\mathbf{C},\ \operatorname{tr}\mathbf{C}^2,\ \operatorname{tr}\mathbf{C}^3,\ \operatorname{tr}\boldsymbol{\mathcal{M}}, \operatorname{tr}\boldsymbol{\mathcal{M}}^2, \operatorname{tr}\boldsymbol{\mathcal{M}}^3\,,\\ &\operatorname{tr}(\boldsymbol{\mathcal{M}}\,\mathbf{C}),\ \operatorname{tr}(\boldsymbol{\mathcal{M}}\,\mathbf{C}^2),\ \operatorname{tr}(\boldsymbol{\mathcal{M}}^2\,\mathbf{C}), \operatorname{tr}(\boldsymbol{\mathcal{M}}^2\,\mathbf{C}^2)\,. \end{aligned} \tag{4.13}$$

Remembering the properties of $\boldsymbol{\mathcal{M}}$, defined in Equation (4.9), some of the above mentioned invariants do not need to be considered. Hence, the list of integrity bases reduces to

$$\operatorname{tr}\mathbf{C},\ \operatorname{tr}\mathbf{C}^2,\ \operatorname{tr}\mathbf{C}^3\,,\operatorname{tr}(\boldsymbol{\mathcal{M}}\,\mathbf{C}),\ \operatorname{tr}(\boldsymbol{\mathcal{M}}\,\mathbf{C}^2)\,. \tag{4.14}$$

The first three invariants of (4.14) do not provide any further information if compared to the three invariance which are defined for the isotropic material in Section 3.1.2. Therefore, the following two additional invariants of (4.14)

$$I_4 = \operatorname{tr}(\boldsymbol{\mathcal{M}}\,\mathbf{C})\,, \tag{4.15}$$
$$I_5 = \operatorname{tr}(\boldsymbol{\mathcal{M}}\,\mathbf{C}^2)\,, \tag{4.16}$$

are sufficient to describe the transversely isotropic material behaviour. By reformulating (4.15), I_4 yields,

$$I_4 = \operatorname{tr}(\boldsymbol{\mathcal{M}}\,\mathbf{C}) = (\mathbf{a}_0 \otimes \mathbf{a}_0)^T \cdot \mathbf{C} = \mathbf{a}_0 \cdot \mathbf{C}\,\mathbf{a}_0 = \mathbf{F}\,\mathbf{a}_0 \cdot \mathbf{F}\,\mathbf{a}_0 = \mathbf{a}\cdot\mathbf{a}\,. \tag{4.17}$$

Herein, I_4 is the squared of the fibre stretch, where the stretch describes the actual length of the fibre. Hence, the fibre stretch, λ, can be determined by $\lambda = \sqrt{I_4}$. The remaining invariant I_5 has no physical meaning and will be omitted within this thesis.

4.3 Skeletal Muscle Model

As stated in Section 4.1, skeletal muscles are considered to behave hyperelastic. Hyperelasticity implies, that the material behaves elastic (reversible) and that the current deformation state only depends on the current state and not on any history dependent variables, i.e., a certain deformation state is not path dependent and reversible. This further implies, that the entropy η stays constant and that a potential energy exists. This potential is a measure for the elastic energy stored in the material. For an isothermal and isentropic[1] system it can be shown, that the volume-specific strain energy function, Ψ, is a potential representing the mechanical energy. Therefore, by deriving the potential energy with respect to $\mathbf{C}$, the 2$^{\text{nd}}$ *Piola-Kirchhoff* stress tensor deduces from the energetic conjugates by,

$$\mathbf{S} = \frac{\partial\Psi(\mathbf{E})}{\partial\mathbf{E}} = \frac{\partial\Psi(\mathbf{C})}{\partial\mathbf{C}}\,\frac{\partial\mathbf{C}}{\partial\mathbf{E}} = 2\,\frac{\partial\Psi(\mathbf{C})}{\partial\mathbf{C}}\,. \tag{4.18}$$

For incompressible materials, Ψ can be decomposed into an isochoric and an deviatoric part, i.e.

$$\begin{aligned}\mathbf{S} &= 2\,\frac{\partial\Psi(I_1,I_2,I_4)}{\partial\mathbf{C}} - \frac{\partial\left[p\,(I_3-1)\right]}{\partial\mathbf{C}}\\ &= 2\,\frac{\partial\Psi(I_1,I_2,I_4)}{\partial\mathbf{C}} - p\,\mathbf{C}^{-1}\,,\end{aligned} \tag{4.19}$$

[1] Characterises the constant amount of entropy of a system within a process.

where the hydrostatic pressure p, is included as a Lagrangian multiplier to enable the incompressible condition $\det \mathbf{F} - 1 = 0$, see, for example, Holzapfel (2000). This incompressibility condition is subjected to the material as an internal constraint. This algebraic constraint,

$$(\sqrt{I_3} - 1) = 0\,, \tag{4.20}$$

is employed by introducing the hydrostatic pressure, p, as an additional independent variable. It can only be determined uniquely from the equilibrium equations and the boundary conditions.

Commonly, the overall strain energy for skeletal muscles is additively split into an isotropic matrix and an anisotropic term representing the mechanical behaviour in the direction of the fibres, see Section 1.2.1 or Blemker et al. (2005); Oomens et al. (2003); Lemos et al. (2005); Röhrle et al. (2008):

$$\Psi_{\text{muscle}}(I_1, I_2, I_4) = \Psi_{\text{iso}}(I_1, I_2) + \Psi_{\text{aniso}}(I_4)\,. \tag{4.21}$$

For the isotropic contribution an incompressible *Mooney-Rivlin* (Rivlin, 1948; Mooney, 1940) material formulation is chosen such that

$$\Psi_{\text{iso}}(I_1, I_2) = c_1\,(I_1 - 3) + c_2\,(I_2 - 3)\,. \tag{4.22}$$

Herein, c_1 and c_2 are material parameters that are related to each other by the shear modulus, $\mu = 2\,(c_1 + c_2)$. The *Mooney-Rivlin* material description only fulfils the entropy inequality for c_1 and c_2 greater than zero. For more information about material laws using invariants, see Spencer (1971) or Holzapfel (2000).

The anisotropic term can be split into a passive and an active contribution, where the active part is multiplied by the homogenised muscle activation parameter $\alpha = [0, 1]$. For $\alpha = 0$ the muscle is passive or inactivated while for $\alpha = 1$, the muscle is considered to be fully activated or tetanised. For values $0 < \alpha < 1$, the activate contribution is linearly interpolated. The prescription of the muscle's activation state is rather simple. Yet, including a more complex activation dynamics would further increase the numerical costs without a methodological effect on the multi-muscle musculoskeletal system as proposed within this thesis. In summary, the anisotropic part of the strain energy function is defined by

$$\Psi_{\text{aniso}}(I_4) = \Psi_{\text{passive}}(I_4) + \alpha\ \Psi_{\text{active}}(I_4)\,. \tag{4.23}$$

The strain energy function defining the passive force-length relation, Ψ_{passive}, follows a J-shaped material behaviour. It is approximated by a polynomial energy function introduced by Markert et al. (2005). The energy function meets the requirements of polyconvexity (i.e. to guarantee the existence of a minimum), coercivity (i.e. the strain energy is consistent with the growth conditions; $\Psi \to \infty$ for $I_4 \to 0$ or $I_4 \to \infty$), and a stress-free reference state and is given by

$$\Psi_{\text{passive}} = \begin{cases} \dfrac{c_3}{c_4}(\lambda_f^{c_4} - 1) - c_3 \ln \lambda_f & \text{if } \lambda_f \geq 1 \\ 0 & \text{else}\,, \end{cases} \tag{4.24}$$

where λ_f is the muscle fibre stretch, i.e. $\lambda_f = \sqrt{I_4}$, and c_3 and c_4 are material parameters.

The strain energy defining the force-length relation for the activated muscle, Ψ_{active}, is defined as a dimensionless force-length relation following the idea of Hatze (1978):

$$\Psi_{\text{active}} = -\frac{\sigma_{\max}}{\nu_i}(\lambda_f^{\text{opt}}\,\Delta W_i)^{-\frac{1}{\nu_i}} \int_{\frac{1}{\lambda_f^{\text{opt}}\,\Delta W_i}\,\lambda_f^{\nu_i}}^{\infty} \lambda_f^{\frac{1}{\nu_i}-1} e^{-\lambda_f}\,\mathrm{d}\lambda_f\,, \tag{4.25}$$

where $\sigma_{\max}$ is the stress which a maximally activated muscle can produce at optimal length λ_f^{opt}, ν_i is the exponent and influences the steepness of the belly curve, and ΔW_i influences the width of the belly curve. Both ν_i and ΔW_i do have an index i which represents the data set for the ascending and descending part of the belly curve, respectively. The exponential-like approach of Equation (4.25) replaces the more commonly used parabolic characteristic.

Taking the derivative of the strain energy functions with respect to the right *Cauchy-Green* tensor, cf. Equation (4.19), the separate terms of the 2nd *Piola-Kirchhoff* of the isotropic part is given by

$$\mathbf{S}_{\text{iso}} = 2\,(c_1 + I_1\,c_2)\,\mathbf{I} - 2\,c_2\,\mathbf{C}\,. \tag{4.26}$$

To obtain the stress distribution of the anisotropic part, one needs to employ the chain rule as Ψ_{aniso} depends on λ_f. Hence,

$$\mathbf{S}_{\text{aniso}}(\lambda_f) = 2\,\frac{\partial \Psi_{\text{aniso}}}{\partial \mathbf{C}} = 2\,\frac{\partial \Psi_{\text{aniso}}}{\partial \lambda_f}\,\frac{\partial \lambda_f}{\partial I_4}\,\frac{\partial I_4}{\partial \mathbf{C}} = \frac{1}{\lambda_f}\frac{\partial \Psi_{\text{aniso}}}{\partial \lambda_f}\,\boldsymbol{\mathcal{M}} = \frac{1}{\lambda_f} P_{\text{aniso}}\,\boldsymbol{\mathcal{M}}\,. \tag{4.27}$$

In general, the nominal stress, $\mathbf{P}$, is defined with respect to the principal directions, $d = 1, 2, 3$ by $P_d = \frac{\partial \Psi(\lambda_d)}{\partial \lambda_d}$. As in this special case, the strain energy functions are scalar-valued functions acting only along the fibre direction, the nominal stress, $\mathbf{P}$, reduces to the scalar-valued function, P_{aniso}, multiplied by the structural tensor $\boldsymbol{\mathcal{M}}$ to take into account local heterogeneities in the fibre distribution.
Replacing $\mathbf{P}$ by the *Cauchy* stress, $\boldsymbol{\sigma}$, Equation (4.27) results to

$$\mathbf{S}_{\text{aniso}}(\lambda_f) = \frac{1}{\lambda_f^2}\,\sigma_{\text{aniso}}\,\boldsymbol{\mathcal{M}}\,. \tag{4.28}$$

Inserting Equation (4.24) into Equation (4.27), the passive contribution of $\mathbf{S}$ is:

$$\mathbf{S}_{\text{passive}} = \begin{cases} \dfrac{1}{\lambda_f^2} c_3\left(\lambda_f^{c_4} - 1\right)\boldsymbol{\mathcal{M}} & \text{if } \lambda_f \geq 1 \\ 0 & \text{else}\,. \end{cases} \tag{4.29}$$

The same applies for the active contribution of $\mathbf{S}$, which is given by the following:

$$\mathbf{S}_{\text{active}} = \begin{cases} \dfrac{\sigma_{\max}}{\lambda_f^2}\exp\left(-\left|\dfrac{\frac{\lambda_f}{\lambda_f^{\text{opt}}} - 1}{\Delta W_{\text{asc}}}\right|^{\nu_{\text{asc}}}\right)\boldsymbol{\mathcal{M}} & \text{if } \lambda_f \leq \lambda_f^{\text{opt}} \\ \dfrac{\sigma_{\max}}{\lambda_f^2}\exp\left(-\left|\dfrac{\frac{\lambda_f}{\lambda_f^{\text{opt}}} - 1}{\Delta W_{\text{desc}}}\right|^{\nu_{\text{desc}}}\right)\boldsymbol{\mathcal{M}} & \text{if } \lambda_f > \lambda_f^{\text{opt}}\,. \end{cases} \tag{4.30}$$

The advantage of choosing this formulation over the other ones is the fact that one obtains for the single component a $\mathcal{C}^1$-continuous function. The qualitative stress contributions are depicted for uniaxial constraints in Figure 4.3.

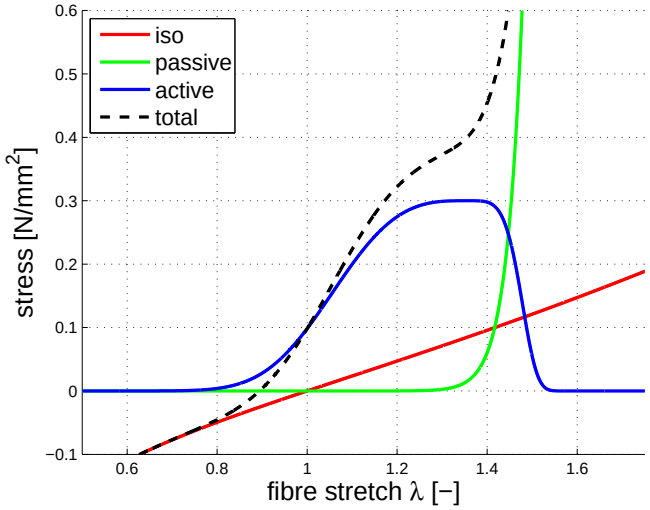

Figure 4.3: *A qualitative representation of the Cauchy stress contributions for the uniaxial case.*

If a stress free initial configuration is assumed, the initial pressure can be determined by

$$\begin{aligned}\mathbf{S}_{\text{muscle}}(\boldsymbol{\chi}, t=0) &= 2\,\frac{\partial \Psi_{\text{muscle}}(I_1, I_2, I_4)}{\partial \mathbf{C}} - p\,\mathbf{C}^{-1} = \mathbf{0} \\ &= 2\,(c_1 + I_1\,c_2)\,\mathbf{I} - 2\,c_2\,\mathbf{I} + \mathbf{0} - p\,\mathbf{I}\,.\end{aligned} \tag{4.31}$$

Using $I_1(t=0) = 3$, (4.31) reduces to the initial, scalar-valued pressure

$$p(\boldsymbol{\chi}, t=0) = 2\,c_1 + 4\,c_2\,. \tag{4.32}$$

4.4 Muscle-Tendon Complex Model

In the following, a resourceful manner of defining a material constitutive equation for a muscle-tendon complex is introduced. This is achieved by introducing only two more parameters to the skeletal muscle tissue constitutive equations introduced in Section 4.3. The first material parameter, called γ_{M}, distinguishes whether the tissue is muscle ($\gamma_{\text{M}} = 1$) or tendon ($\gamma_{\text{M}} = 0$) and the second parameter, called γ_{ST}, determines if the tissue is muscle-tendon tissue ($\gamma_{\text{ST}} = 0$) or some other soft tissue ($\gamma_{\text{ST}} = 1$), like, for example, fat. Hence, the strain energy for tissue consisting of muscle, tendon and other soft tissue is is given by

$$\Psi_{\text{MTC}} = \Psi_{\text{iso}} + (\Psi_{\text{passive}} + \alpha\,\gamma_{\text{M}}\,\Psi_{\text{active}})\,(1 - \gamma_{\text{ST}})\,. \tag{4.33}$$

The different contributions of Ψ_{MTC} are exactly the same as defined in Section 4.3. Applying Equation (4.19), the 2$^{\text{nd}}$ *Piola-Kirchhoff* of the muscle-tendon complex is,

$$\mathbf{S}_{\text{MTC}} = \mathbf{S}_{\text{iso}} + (\mathbf{S}_{\text{passive}} + \alpha\,\gamma_{\text{M}}\,\mathbf{S}_{\text{active}})\,(1 - \gamma_{\text{ST}})\,. \tag{4.34}$$

For $\gamma_{\mathrm{ST}} = 1$, the anisotropic part of the material behaviour vanishes. The soft tissue is assumed to behave as the isotropic part of the muscle tissue. Hereby, a relatively soft material is defined, where compressive forces will dominate due to the incompressibility behaviour of the tissue. For $0 < \gamma_{\mathrm{ST}} < 1$, the material exhibits anisotropic behaviour. For $\gamma_{\mathrm{ST}} = 0$ and $\gamma_{\mathrm{M}} = 1$, the material behaves to 100% like skeletal muscle tissue and coincides with the material behaviour introduced in Section 4.3. For $\gamma_{\mathrm{ST}} = 0$ and $\gamma_{\mathrm{M}} = 0$, the material reduces to tendon tissue. For any other values between zero and one, a homogenised material behaviour of the mixture is obtained by linear interpolation. Further, the different tissue material parameters are enforced by a linear interpolation:

$$\begin{aligned} c_1 &= \gamma_{\mathrm{M}}\, c_{1M} + (1-\gamma_{\mathrm{M}})\, c_{1T}\,, \\ c_2 &= \gamma_{\mathrm{M}}\, c_{2M} + (1-\gamma_{\mathrm{M}})\, c_{2T}\,, \\ c_3 &= \gamma_{\mathrm{M}}\, c_{3M} + (1-\gamma_{\mathrm{M}})\, c_{3T}\,, \\ c_4 &= \gamma_{\mathrm{M}}\, c_{4M} + (1-\gamma_{\mathrm{M}})\, c_{4T}\,. \end{aligned} \tag{4.35}$$

Herein, c_{iM} and c_{iT} are the material parameters defined in Section 4.3 for the skeletal muscle tissue and tendon tissue, respectively.

5 Finite Element Method in Space

Chapter 3 and 4 provide the fundamentals for the initial boundary value problem. It consists of the

- kinematic relations, providing the suitable strain measures (Section 3.1),
- definitions of stress (Section 3.1.3),
- local balance relations (Section 3.2), and
- constitutive equations for the skeletal muscle tissue (Chapter 4).

As quasi-static conditions are assumed, time contributions can be neglected. However, it is common to successively change the boundary conditions. Hereby, successively new BVP are declared to pretend a pseudo time-transient problem. Hence, all derivations within this chapter are carried out for one instant in time and the variable t indicating the current deformation is omitted. While body forces are assumed to be small in comparison to the internal forces, the strong formulation of the governing system reduces to:

$$\operatorname{div} \mathbf{T} = \mathbf{0}\,. \tag{5.1}$$

As it will be convenient for the contact formulation later on, Equation (5.1) is pulled back to the reference configuration, see Holzapfel et al. (2005). For the pull-back operation, (5.1) is reformulated to its global form and the area and volume elements are pulled back using Equation (3.7). As the obtained formulation is independent of the choice of the volume element, the moment balance reads:

$$\operatorname{Div} \mathbf{P}(\mathbf{X}) = \mathbf{0}\,, \quad \text{where} \quad \operatorname{Div}(\cdot) := \frac{\partial(\cdot)}{\partial \mathbf{X}} \cdot \mathbf{I}\,. \tag{5.2}$$

By including the constitutive behaviour and a complex geometry, the resulting system leads to a second-order partial differential equation for the current position, $\mathbf{x} = \boldsymbol{\chi}(\mathbf{X})$. As this system cannot be analytically solved for most BVPs, an adequate numerical framework needs to be introduced. Here, the finite element method is used to discretise the governing equations and the geometry. More information can be found in standard text books of, for example, Bonet (1997) or Zhu et al. (2005).

5.1 Fundamentals

When the finite element method is applied to a boundary value problem, the procedure can be classified into several distinct steps. Each of them will be briefly outlined. The numerical treatment is realised within CMISS and outlined in Section 5.2.

(i) Form the weak formulation based on the governing equations, here given in Equation (5.2),

(ii) chose a suitable finite element ansatz (basis functions, *Galerkin* weights),
(iii) evaluate element integrals (calculate the element stiffness matrices and right-hand side vectors),
(vi) assemble the global matrix,
(v) apply boundary conditions, and
(vi) solve the global system.

The first step is to formulate the weak formulation of the current problem. This step is important, as it is often impossible to find the correct solution of the strong formulation for the primary variables of the PDE using efficient and suitable discretisation schemes. The primary variables are the unknowns, i.e. in our case the current position, $\mathbf{x} = \boldsymbol{\chi}(\mathbf{X})$ and the hydrostatic pressure, p, arising from the incompressibility condition of Equation (4.20). The generalised assembled strong or local form of the PDEs can be represented by:

$$\begin{aligned} \operatorname{Div} \mathbf{P}(\mathbf{X}) &= \mathbf{0}\,, \\ \sqrt{I_3(\mathbf{X})} - 1 &= 0\,. \end{aligned} \tag{5.3}$$

To derive the weak formulation, the PDEs are multiplied by test functions $\delta\boldsymbol{\chi}$ and δp and integrated over the domain Ω_0 resulting in the following equivalent global system,

$$\begin{aligned} \mathcal{G}^{\chi} &= \int_{\Omega_0} \operatorname{Div} \mathbf{P}(\mathbf{X}) \cdot \delta\boldsymbol{\chi} \, \mathrm{d}V = 0\,, \\ \mathcal{G}^{p} &= \int_{\Omega_0} (J(\mathbf{X}) - 1)\, \delta p \, \mathrm{d}V = 0\,. \end{aligned} \tag{5.4}$$

Since Equation (5.3) has to be true, Equation (5.4) is true for any choice of $\delta\boldsymbol{\chi}$ and δp. By integrating Equation $(5.4)_1$ by parts, the order of the operator of the primary variable is lowered by one and the order of the operator of the test function is increased by one:

$$\begin{aligned} \mathcal{G}^{\chi} &= \int_{\Omega_0} \operatorname{Div} \mathbf{P}(\mathbf{X}) \cdot \delta\boldsymbol{\chi} \, \mathrm{d}V \\ &= \int_{\Omega_0} \mathbf{P}(\mathbf{X}) \cdot \operatorname{Grad} \delta\boldsymbol{\chi} \, \mathrm{d}V - \int_{\Gamma_0} \mathbf{t}_0 \cdot \delta\boldsymbol{\chi} \, \mathrm{d}A = 0\,. \end{aligned} \tag{5.5}$$

As a result of the integration by parts, $\mathcal{G}^{\chi}$ now contains a volumetric part and a part associated with the boundary, at which the initial traction vector $\mathbf{t}_0$ is applied as *Neumann* boundary condition. Equation $(5.4)_2$ of $\mathcal{G}^{p}$ is left untouched.

As the following procedure is in principle the same for both equations in Equation (5.4), the following procedure will be exemplarily explained using Equation $(5.4)_1$.

In order to obtain bounded results for the variational formulation, the first derivatives of the trial functions, $\mathcal{S}_{\chi}$ and test functions $\mathcal{S}_{p}$ need to be square-integrable on the domain Ω_0. This requirement is satisfied, if the functions are assumed to be $\mathcal{H}^1(\Omega)$.

$$\begin{aligned} \mathcal{S} &:= \{\, \boldsymbol{\chi} \in \mathcal{H}^1(\Omega)^d \,:\, \boldsymbol{\chi}(\mathbf{X}) = \bar{\boldsymbol{\chi}}(\mathbf{X}) \quad \text{on } \Gamma\}\,, \\ \mathcal{T} &:= \{\delta\boldsymbol{\chi} \in \mathcal{H}^1_0(\Omega)^d \,:\, \delta\boldsymbol{\chi}(\mathbf{X}) = \mathbf{0} \quad \text{on } \Gamma\}\,, \end{aligned} \tag{5.6}$$

Herein, $d \in \{1, 2, 3\}$ is an integer denoting the dimensions in space and $\bar{\boldsymbol{\chi}}$ denote the value of the *Dirichlet* boundary condition as the *Dirichlet* boundary conditions need to be satisfied exactly.

The defined trial spaces, $\mathcal{S}$, and test spaces, $\mathcal{T}$, have to be approximated by an N-dimensional subspace $\mathcal{S}^h$ and $\mathcal{T}^h$, respectively. The discrete trial and test function are defined by:

$$\begin{aligned} \boldsymbol{\chi}(\mathbf{X}) &\approx \boldsymbol{\chi}^h(\mathbf{X}) = \bar{\boldsymbol{\chi}}^h(\mathbf{X}) + \sum_{i=1}^{N} \boldsymbol{\phi}_i^h(\mathbf{X})\, \mathbf{C}_i \in \mathcal{S}\,, \\ \delta\boldsymbol{\chi}(\mathbf{X}) &\approx \delta\boldsymbol{\chi}^h(\mathbf{X}) = \sum_{i=1}^{N} \boldsymbol{\psi}_i^h(\mathbf{X})\, \delta\mathbf{C}_i \in \mathcal{T}\,, \end{aligned} \tag{5.7}$$

where $\bar{\boldsymbol{\chi}}^h$ denotes the *Dirichlet* boundary condition, $\boldsymbol{\phi}_i^h$ and $\boldsymbol{\psi}_i^h$ are the global basis functions of the respective ansatz and test functions for the node i, which only depend on $\mathbf{X}$, N indicates the total number of nodal points in the mesh, and $\mathbf{C}_i$ and $\delta\mathbf{C}_i$ are the vector-valued coefficients of dimension $\mathbb{R}^{N\times 1}$ of the discretised geometrical primary variables.

The basis functions are linearly independent and chosen in such a way, that the nodal value is equal to one at the node itself, while the nodal value for all surrounding nodes are equal to zero.

$$\phi_i^h(\mathbf{X}_j) = \delta_{ij} \qquad \text{with} \quad i, j = 1, \ldots, N\,. \tag{5.8}$$

With this property, the coefficients of the discretised primary variables coincide with the nodal values of the primary variables, $\boldsymbol{\chi}(\mathbf{X}_i)$ and the nodal values of the test function, $\delta\boldsymbol{\chi}_i$. Hence,

$$\mathbf{C}_i \equiv \boldsymbol{\chi}(\mathbf{X}_i)\,, \text{ and } \quad \delta\mathbf{C}_i \equiv \delta\boldsymbol{\chi}(\mathbf{X}_i)\,. \tag{5.9}$$

With this definition at hand, Equation (5.5) is discretised. As the number of unknowns equals the number of equations, the discretised PDE is, in principle, ready to be solved. Yet, the integration of Equation (5.5) still poses a problem. The finite element method provides a widely used solution to this issue. By partitioning the solution space of the problem into a sum of small problems, Equation (5.5) is formulated with respect to a subdomain Ω_e of finite size. The domain Ω_0 is approximated by a spatially discretised domain Ω^h, which consists of E discretised, non-overlapping elements of finite size, Ω_e^h,

$$\Omega_0 \approx \Omega^h = \bigcup_{e=1}^{E} \Omega_e^h\,. \tag{5.10}$$

The discretised small domains, Ω_e^h, are called finite elements. The union of Ω_e^h forms the FE mesh. The elements are spanned by the nodes N_e, belonging to the element Ω_e^h. As the choice of the basis functions to represent the different primary variables does not have to be the same, the number of nodes, N_e, where the primary variable are defined, can vary. The number of nodes for the spatial variable and for the hydrostatic pressure is N_e^χ and N_e^p, respectively.

To discretise the nodal values within an element, the isogeometric mapping is employed. The basic idea of the isogeometric mapping is to map a discretised, arbitrary element, Ω_e^h, into a reference element $\hat{\Omega}$. If the element geometry is transformed by a function of the same polynomial order as the ansatz function, the mapping describes the isoparametric concept. If the order of the geometric transformation is higher, one refers to it as super-parametric. In general, for each independent variable a different parametric transformation can be chosen. Within the scope of this work, the geometry and the current configuration use quadratic ansatz functions and an isoparametric concept is chosen for the placement function. The pressure is assumed to change linearly within an element resulting in a super-parametric concept for the pressure. The reference element is defined by

$$\mathbf{N}_e : \hat{\Omega} \to [0,1]^d \,, \tag{5.11}$$

where $\mathbf{N}_e$ is the set of nodal basis functions for an element e,

$$\mathbf{N}_e := \left[N_1(\boldsymbol{\xi}), \dots, N_{N_e^{DoF}}(\boldsymbol{\xi})\right]^T \,, \quad \in \mathbb{R}^{N_e^{DoF}\times 1} \,, \tag{5.12}$$

where $\boldsymbol{\xi}$ are the local coordinates of the reference element. Furthermore, the nodal values of the nodes belonging to an element e are defined by

$$\mathbf{X}_e := \left[\mathbf{X}_{e1}, \dots, \mathbf{X}_{eN_e^{DoF}}\right] \,, \quad \in \mathbb{R}^{3\times N_e^{DoF}} \,. \tag{5.13}$$

to utilise the isogeometric mapping,

$$\boldsymbol{\Phi}_e : \hat{\Omega} \to \Omega_e^h \,, \tag{5.14}$$

$$\boldsymbol{\xi} \mapsto \mathbf{X}_e \, \mathbf{N}_e(\boldsymbol{\xi}) \,, \qquad \text{with} \quad e = 1, \dots, E \,. \tag{5.15}$$

The mapping satisfies,

$$\Omega_e^h = \Phi_e(\hat{\Omega}) \,, \qquad \text{with} \quad e = 1, \dots, E \,. \tag{5.16}$$

and has the *Jacob*ian

$$\mathbf{J}_e = \nabla\Phi_e(\boldsymbol{\xi}) = \mathbf{X}_e \begin{bmatrix} \nabla N_1(\boldsymbol{\xi}) \\ \vdots \\ \nabla N_{N_e^{DoF}}(\boldsymbol{\xi}) \end{bmatrix} = \mathbf{X}_e \, \nabla\mathbf{N}_e \,, \quad \in \mathbb{R}^{3\times 3} \,. \tag{5.17}$$

Note, the basis functions, $\boldsymbol{\phi}_i^h$, consist of contributions from $\mathbf{N}_e$ defined on different elements.

With the definitions (5.11) to (5.15), the ansatz functions of an element Ω^h can now be specified by choosing the appropriate nodal contributions belonging to this particular element.

Separating the variational formulation into a sum over small domains, the problem is defined by

$$f : \Omega_0 \to \mathbb{R} \qquad \text{with} \quad f \text{ see } \mathcal{G}^\chi, \mathcal{G}^p \text{ from (5.4)} \,, \tag{5.18}$$

$$\int_{\Omega_0} f \, \mathrm{d}V \approx \int_{\Omega^h} f \, \mathrm{d}V \overset{(5.10)}{=} \sum_{e=1}^{E} \int_{\Omega_e^h} \mathrm{d}V_e$$

$$= \sum_{e=1}^{E} \int_{\Omega_e^h \overset{(5.16)}{=} \Phi_e(\hat{\Omega})} f \, \mathrm{d}V_e = \sum_{e=1}^{E} \int_{\hat{\Omega}} f(\Phi_e) \, |\det(\Phi_e)| \, \mathrm{d}V_e \,. \tag{5.19}$$

Herein, the first part is the exact statement and f is a placeholder for the variational formulations. With the first step, the solution is approximated by the discretised solution space. The integration of the discretised domain is split into a sum of many small domains using Equation (5.10). Each of the E elements is mapped by the element routine from Ω_e^h to the reference element $\hat{\Omega}$ by the isogeometric mapping, which is visualised in Figure 5.1.

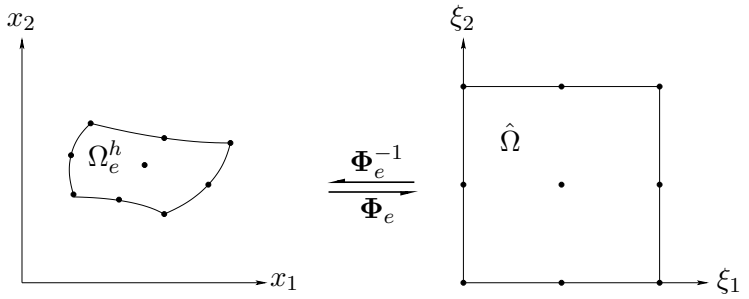

Figure 5.1: *Geometric transformation of an arbitrary rectangular 2-d element with quadratic basis functions Ω_e^h to the reference element $\hat{\Omega}$, defined in local coordinates $\boldsymbol{\xi}$.*

Within the reference element, a numerical integration scheme, such as the *Gauss*ian quadrature scheme, is employed to compute the respective integrals. The numerical integration, within one element, is carried out using K *Gauss* points. Each point k is weighted by the *Gauss*ian quadrature weights, w_k, and the sum of the weighting factors is one. The approximation of the integration for one element reads:

$$(5.19) \approx \sum_{e=1}^{E} \sum_{k=1}^{K} w_k \; f(\Phi_e) \; |\det(\Phi_e)| \tag{5.20}$$

Due to the fact that this integration is carried out on the element level with respect to the spatial reference element, the integration points and the weighting factors are always the same.

Dirichlet and *Neumann* boundary conditions are considered in the global system. For *Dirichlet* boundary conditions, the nodes are known. Hence, its contribution can be transferred to the right-hand side and the matrix can be reduced. For the *Neumann* boundary conditions, the respective force contribution is directly added to the right-hand side.

To solve the global problem, the element independent variable vectors are defined in 3 dimensions as:

$$\begin{aligned} \boldsymbol{u}_e &:= \left[\boldsymbol{\chi}^h(\mathbf{X}_1), \dots \boldsymbol{\chi}^h(\mathbf{X}_{N_e^\chi})\right]^T \in \mathbb{R}^{N_e^\chi \times 3}, \\ \boldsymbol{v}_e &:= \left[p^h(\mathbf{X}_1), \dots p^h(\mathbf{X}_{N_e^p})\right]^T \in \mathbb{R}^{N_e^p}, \\ \boldsymbol{w}_e &:= \left[\boldsymbol{u}_e^T, \boldsymbol{v}_e^T\right]^T, \end{aligned} \tag{5.21}$$

Even though the dimension of the $\boldsymbol{w}_e$ is not consistent, when a mixed-element formulation is used, the primary unknowns are stringed together to define the vectors, $\boldsymbol{w}_e$ on the

element level, and $\boldsymbol{w}$ on the global level. The global solution variable vectors are defined to:

$$\begin{aligned} \boldsymbol{u} &:= [\,\boldsymbol{u}_1, \ldots, \boldsymbol{u}_{N_e^\chi}]^T && \in \mathbb{R}^{N^\chi \times 3}\,, \\ \boldsymbol{v} &:= [\,\boldsymbol{v}_1, \ldots, \boldsymbol{v}_{N_e^p}]^T && \in \mathbb{R}^{N^p}\,, \\ \boldsymbol{w} &:= \left[\,\boldsymbol{u}_1^T, \ldots, \boldsymbol{u}_{N_e^\chi}^T,\, \boldsymbol{v}_1^T, \ldots, \boldsymbol{v}_{N_e^p}^T\right]^T . \end{aligned} \tag{5.22}$$

After the PDE is spatially discretised, the emerging system is of size $3\,N^\chi + N^p$ and the emerging global system of equations can be written as

$$\begin{aligned} \mathcal{G}_\chi &= \mathfrak{K}(\boldsymbol{u}) - \mathfrak{f} = \mathbf{0}\,, \\ \mathcal{G}_p &= \mathfrak{g}(\boldsymbol{v}) = \mathbf{0}\,, \end{aligned} \tag{5.23}$$

where $(5.23)_2$ is the algebraic side condition emerging from the incompressibility condition.

Within the framework of finite elasticity, the emerging equations are still nonlinear. Hence, linearisation is necessary. The *Newton-Raphson* method has proven to efficiently solve the nonlinear set of equations. The *Newton-Raphson* method requires the first derivative or tangent of the nonlinear functions. As the functions depend on more than just one variable, the directional derivative has to be applied, i.e. the observed function is derived with respect to each variable keeping the other variable constant at a distinct location. The tangent can be computed numerically or analytically. Within this framework, the constitutive equations are linearised numerically while the contact formulation uses an analytic tangent, cf. Section 6.1.3. As the numerical tangent is, within this framework, always determined in the reference configuration, the balance of momentum is used in the reference configuration.

5.2 Realisation within CMISS

The governing equations of finite elasticity for the FE muscle model are solved using the software package CMISS (Continuum Mechanics, Image analysis, Signal processing and System Identification), which is developed at the Auckland Bioengineering Institute, University of Auckland, New Zealand. The computational core of CMISS is called CM, which provides the necessary routines to assemble and solve the linear system. CMISS was originally designed for modelling cardiac tissue in the late 1970s and was later extended to model various biological soft tissues.

After sketching in the last section a general procedure of the finite element method, the following section provides CMISS-specific implementation details. CM solves the global-assembled system of equations using the nodal residuals.

For this work, a *Bubnov-Galerkin* method is chosen. This implies that the same type of basis functions for trial and test functions are chosen, i.e.

$$\boldsymbol{\psi}_i^h \equiv \boldsymbol{\phi}_i^h\,. \tag{5.24}$$

Assuming zero *Neumann* boundary in Equation (5.5), the nodal residual, $\mathbf{R}_i$, can be

defined to:

$$\mathbf{R}_i^{\chi} = \int_{\Omega^h} \mathbf{P}(\mathbf{X}_i)\, \frac{\partial \phi_i^{\chi,h}}{\partial \mathbf{X}}\, \mathrm{d}V\,, \qquad \in \mathbb{R}^3\,, \qquad \text{with} \quad i = 1, \ldots, N^{\chi}\,. \tag{5.25}$$

In case of a constrained node, the residuum at the constraint nodes represents the reaction force. Hence, after successfully solving the set of equations, by evaluating these equations, which have been deleted during the matrix condensation, the node reaction forces are directly evaluable. Very often, so in this case, these forces are of big interest for investigating the mechanical characteristics of the investigated system.

Following previous works using CMISS, the hydrostatic pressure is discretised linearly for optimally satisfying the *inf-sub-* or *LBB* (*Ladyschenskaja-Babuška-Brezzi*) condition (Nash and Hunter, 2000; Chung, 2008) as the spatial variables are discretised quadratically. The residual for the hydrostatic pressure is defined to:

$$R_i^{p} = \int_{\Omega^h} (J(\mathbf{X}_i) - 1)\, \phi_i^{p,h}(\mathbf{X}_i)\, \mathrm{d}V \qquad \in \mathbb{R}^1\,, \qquad \text{with} \quad i = 1, \ldots, N^{p}\,. \tag{5.26}$$

Uniting the residuals emerging from Equation $(5.4)_1$ and $(5.4)_2$ similarly to the global solution vector of Equation $(5.22)_3$, the element residual reads:

$$\mathbf{R}_e = [\mathbf{R}_{e1}^{\chi\,T}, \ldots, \mathbf{R}_{eN_e^{\chi}}^{\chi\,T}, R_{e1}^{p\,T}, \ldots, R_{eN_e^{p}}^{p\,T}]^T\,. \tag{5.27}$$

The emerging system of equations is nonlinear in the sense, that it cannot be solved in a closed-form expression. Hence, a linearisation needs to be conducted. Within CMISS, the tangent stiffness matrix, $\mathbf{K}$ is computed by directly linearising the residuum using a *Newton-Raphson* method within each element. The element stiffness matrix, $\mathbf{K}_e$ is defined by

$$\mathbf{K}_e = \frac{\partial \mathbf{R}_e}{\partial \boldsymbol{w}_e} = \begin{bmatrix} \frac{\partial \mathbf{R}_{e1}^{\chi}}{\partial \boldsymbol{\chi}^h(\mathbf{X}_1)} & \cdots & \frac{\partial \mathbf{R}_{e1}^{\chi}}{\partial \boldsymbol{\chi}^h(\mathbf{X}_{N_e^{\chi}})} & \frac{\partial \mathbf{R}_{e1}^{\chi}}{\partial p_1} & \cdots & \frac{\partial \mathbf{R}_{e1}^{\chi}}{\partial p_{N_e^p}} \\ \vdots & \ddots & \vdots & \vdots & \ddots & \ldots \\ \frac{\partial \mathbf{R}_{eN_e^{\chi}}^{\chi}}{\partial \boldsymbol{\chi}^h(\mathbf{X}_1)} & \cdots & \frac{\partial \mathbf{R}_{eN_e^{\chi}}^{\chi}}{\partial \boldsymbol{\chi}^h(\mathbf{X}_{N_e^{\chi}})} & \frac{\partial \mathbf{R}_{eN_e^{\chi}}^{\chi}}{\partial p_1} & \cdots & \frac{\partial \mathbf{R}_{eN_e^{\chi}}^{\chi}}{\partial p_{N_e^p}} \\ \frac{\partial R_{e1}^{p}}{\partial \boldsymbol{\chi}^h(\mathbf{X}_1)} & \cdots & \frac{\partial R_{e1}^{p}}{\partial \boldsymbol{\chi}^h(\mathbf{X}_{N_e^{\chi}})} & \frac{\partial R_{e1}^{p}}{\partial p_1} & \cdots & \frac{\partial R_{e1}^{p}}{\partial p_{N_e^p}} \\ \vdots & \ddots & \vdots & \vdots & \ddots & \ldots \\ \frac{\partial R_{eN_e^{p}}^{p}}{\partial \boldsymbol{\chi}^h(\mathbf{X}_1)} & \cdots & \frac{\partial R_{eN_e^{p}}^{p}}{\partial \boldsymbol{\chi}^h(\mathbf{X}_{N_e^{\chi}})} & \frac{\partial R_{eN_e^{p}}^{p}}{\partial p_1} & \cdots & \frac{\partial R_{eN_e^{p}}^{p}}{\partial p_{N_e^p}} \end{bmatrix}\,. \tag{5.28}$$

Note that the elements, $\mathbf{R}_{ei}^{\chi}$, within $\mathbf{R}_e$ are vectors in space ($\mathbf{R}_i^{\chi} \in \mathbb{R}^3$), and that the elements of the element stiffness matrix are $\dfrac{\partial \mathbf{R}_{e1}^{\chi}}{\partial \boldsymbol{\chi}^h(\mathbf{X}_2)} \in \mathbb{R}^{3\times 3}$. Exemplary, the element

residual for node number one which is derived with respect to the geometric DoF of node number two is

$$\frac{\partial \mathbf{R}^{\chi}_{e1}}{\partial \boldsymbol{\chi}^h(\mathbf{X}_2)} = \begin{bmatrix} \frac{\partial R_{1x}}{\partial x_2} & \frac{\partial R_{1x}}{\partial y_2} & \frac{\partial R_{1x}}{\partial z_2} \\ \frac{\partial R_{1y}}{\partial x_2} & \frac{\partial R_{1y}}{\partial y_2} & \frac{\partial R_{1y}}{\partial z_2} \\ \frac{\partial R_{1z}}{\partial x_2} & \frac{\partial R_{1z}}{\partial y_2} & \frac{\partial R_{1z}}{\partial z_2} \end{bmatrix} . \tag{5.29}$$

The tangent stiffness matrix can be approximated by a finite difference method

$$\begin{aligned} K^{\chi}_{eijd} &= \frac{\partial \mathbf{R}^{\chi}_{ei}}{\partial \boldsymbol{\chi}^h(\mathbf{X}_j)} \approx \frac{\mathbf{R}^{\chi}_{ei}(\boldsymbol{\chi}^h(\mathbf{X}_j)+\delta\mathbf{e}_d) - \mathbf{R}^{\chi}_{ei}(\boldsymbol{\chi}^h(\mathbf{X}_j))}{\|\delta\mathbf{e}_d\|} \\ &\text{with} \begin{cases} e & = 1, ..., E\,, \\ i, j & = 1, ..., (3\,N^{\chi}_e)\,, \\ d & = 1, 2, 3\,, \end{cases} \end{aligned} \tag{5.30}$$

where $\delta\mathbf{e}_d$ is a small perturbation in a coordinate direction. Due to the algebraic side (incompressibility) condition, the resulting tangent stiffness matrix is not positive-definite (Hughes, 2012).

The measures defined on element level are assembled to a global matrix and vectors. With these measures at hand, the global system of linearised equations is given by:

$$\mathbf{K}\,\Delta\boldsymbol{w} = -\mathbf{R} \quad \text{with} \begin{cases} \mathbf{K} \in \mathbb{R}^{(3\,N^{\chi}+N_p)\times(3\,N^{\chi}+N^{p})}\,, \\ \Delta\boldsymbol{w}, \mathbf{R} \in \mathbb{R}^{(3\,N^{\chi}+N^{p})}\,, \end{cases} \tag{5.31}$$

where $\Delta\boldsymbol{w}$ is the solution update. The initial estimate is typically set to be identical to the reference configuration, while additionally the *Dirichlet* and *Neumann* boundary conditions are applied. The initial pressure is, for a stress-free initial condition, defined by Equation (4.31).

The solution update is derived by inserting the global version of (5.28) in (5.31). When the resulting equation is solved for $\boldsymbol{w}^{\text{iter}+1}$, the solution update reads:

$$\boldsymbol{w}^{\text{iter}+1} = \boldsymbol{w}^{\text{iter}} - \left(\frac{\partial \mathbf{R}}{\partial \boldsymbol{w}}\right)^{-1} \mathbf{R} = \boldsymbol{w}^{\text{iter}} - \mathbf{K}^{-1}\,\mathbf{R}\,, \tag{5.32}$$

until $\|\mathbf{R}\| < \varepsilon$ or $\|\Delta\boldsymbol{w}\| < \varepsilon$. Within this work, the linearised system of equations is solved using a LU decomposition.

6 Contact Mechanics

In order to fully take advantage of the volumetric approach, a contact formulation is considered. The contact formulation provides a framework which enables the mechanical description of the interaction of two or more deformable bodies. Therefore, including a contact formulation into a continuum-mechanical approach opposes purely kinematic and dynamic descriptions of contact, which would occur between rigid bodies.

The contact mechanical framework can be considered as an additional module within the continuum-mechanical finite element framework. There exists already a wide range of contact mechanics formulations including friction, adhesion and/or wear within static, quasi-static, or even under dynamic conditions, see Wriggers (2002) or Laursen (2002) and the references therein. These concepts can be decomposed into phenomena acting in contact normal direction, such as, for example, gap-functions, contact pressure, adhesion, or in tangential contact surface direction, such as friction or more complex actions such as wear.

However, as the focus of this work is not on contact mechanics, a relatively simple contact formulation is employed to describe the interaction of skeletal muscles and bones. Within this work, the contact formulation of Chung (2008) is used. The assumptions for the contact formulation are:

(i) A quasi-static formulation is chosen for both the standard continuum-mechanical framework as well as for the contact formulation.

(ii) Since bones (Section 2.1) are much stiffer than skeletal muscles (Section 7.2.2), bones are considered to be rigid, whereas the skeletal muscles are not.

(iii) An idealised frictionless contact formulation was chosen as frictional forces between bone and muscle are considered to be much smaller than the other acting forces.

It was not part of this thesis to develop and improve existing contact mechanics formulations. Yet, as the contact formulation is numerically quite challenging, a brief introduction into the employed contact mechanics formulation is given in the following chapter. Further information on the specific implementation of contact within CMISS can be found in Chung (2008), Rajagopal et al. (2008), or Saini (2012) and, of course, in standard text books, such as Wriggers (2002) or Laursen (2002).

6.1 Contact Mechanics Theory

For a contact-free formulation, the boundary conditions (displacements or force conditions) and their location of action are known a priori. For a formulation including contact, this is in general not the case, i.e. the locations of possible interactions, the resulting forces, or the subsequent motion of the boundaries need to be determined as a part of the solution itself.

In Figure 6.1, the kinematics for a system of two bodies including contact is shown for the time interval $t \in [t_0, t]$. The first body $\mathcal{B}^M$, which is assumed to be rigid, is called "master", whereas the second, elastic body $\mathcal{B}^S$ is called "slave". Each body has its independent placement function $\boldsymbol{\chi}^i$, $i = \{M, S\}$. Material points in $\mathcal{B}^M$ are denoted by $\mathbf{x}^M$ and material points in $\mathcal{B}^S$ by $\mathbf{x}^S$.

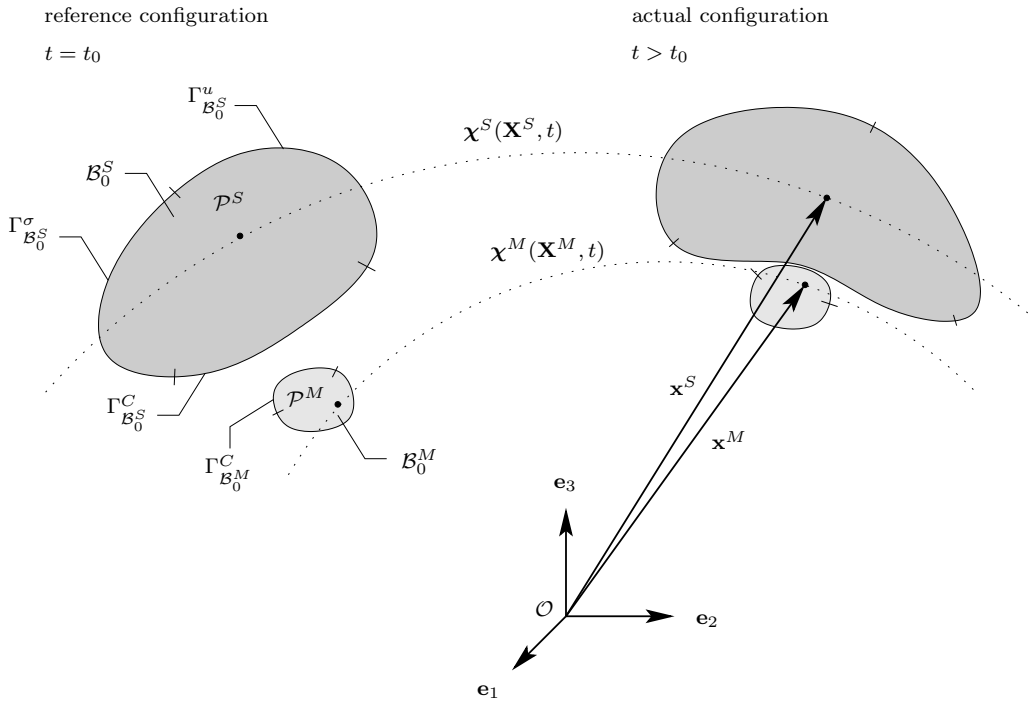

Figure 6.1: *Kinematics of contacting bodies $\mathcal{B}^M$ and $\mathcal{B}^S$, where contact might occur on the predefined boundary is denoted by Γ^C_i, $i = \{M, S\}$.*

While contact is included, a third section Γ^C_i, where possible contact may occur, needs to be introduced. Following the same conventions as for one body, the boundaries' surface sets are mutually exclusive and together constitute the entire surface:

$$\left.\begin{aligned} \Gamma_i &= \Gamma^u_i \cup \Gamma^\sigma_i \cup \Gamma^C_i \\ \emptyset &= \Gamma^u_i \cap \Gamma^\sigma_i \cap \Gamma^C_i \end{aligned}\right\} \quad \text{for} \quad i = \{\mathcal{B}^M, \mathcal{B}^S\}\,. \tag{6.1}$$

The concept of possible contact between the two bodies introduces new constraints that are based on the following physical assumptions:

(i) Any material point of one body cannot occupy the same physical location as any material point of the other body.

(ii) Any force resulting from one body penetrating the other is compressive and acts in contact surface normal direction of the imposing body.

In order to formulate these contact constraints, it is convenient to assign one surface as the one over which contact is parametrised. Here, the master surface is chosen to be monitored with respect to the parametrised slave surface. Therefore, the contact constraints are parametrised by $\mathbf{x}^S \in \Gamma^C_{\mathcal{B}^S}$, while the opposing surface $\Gamma^C_{\mathcal{B}^M}$ needs to provide

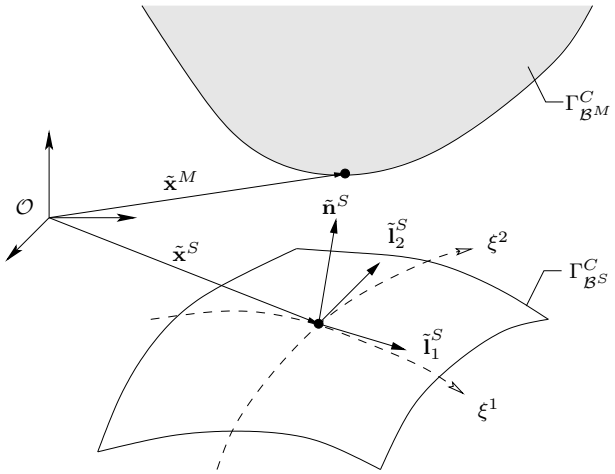

Figure 6.2: *Minimum distance problem for two possibly interacting bodies. The slave surface is discretised by a 2-dimensional, generalised coordinate system $\boldsymbol{\xi}$. The normal vector directs outwards towards the master surface.*

the additional information to complete the definitions. To determine the interaction between the opposing surfaces, first the corresponding points of $\mathbf{x}^M$ on $\Gamma_{\mathcal{B}^S}$ need to be identified.

In general, this is done according to the closest point projection. For a given point $\mathbf{x}^M \in \Gamma^C_{\mathcal{B}^M}$, the closest point on the slave surface can be determined by finding the shortest distance, $\tilde{d}$, between $\mathbf{x}^M$ and a point $\tilde{\mathbf{x}}^S$ at $\Gamma^C_{\mathcal{B}^S}$ by:

$$\tilde{d}^S = \left\|\mathbf{x}^M - \tilde{\mathbf{x}}^S\right\| = \min_{\mathbf{x}^S(\boldsymbol{\xi}) \in \Gamma^C_S} \left\|\mathbf{x}^M - \mathbf{x}^S(\boldsymbol{\xi})\right\| \qquad \forall \quad \mathbf{x}^M \in \Gamma^C_{\mathcal{B}^M}\,, \tag{6.2}$$

where $\boldsymbol{\xi} := \{\xi^1, \xi^2\}$ denotes a parametrisation of the slave surface of a two-dimensional convective coordinate system, which is attached to the surface and therefore changes with the deformation of the body.

The shortest distance can also be used to define the gap or penetration between the two functions. The point $\tilde{\mathbf{x}}^S(\boldsymbol{\xi})$ at $\Gamma^C_{\mathcal{B}^S}$, having the shortest distance to the point $\mathbf{x}^M$ at $\Gamma^C_{\mathcal{B}^M}$ is found by the necessary condition for the minimum of the distance function (6.2), which reads:

$$\frac{\mathrm{d}}{\mathrm{d}\xi^d}\,\tilde{d}^S(\boldsymbol{\xi}) = \frac{\mathbf{x}^M - \tilde{\mathbf{x}}^S(\boldsymbol{\xi})}{\left\|\mathbf{x}^M - \tilde{\mathbf{x}}^S(\boldsymbol{\xi})\right\|} \cdot \frac{\partial \tilde{\mathbf{x}}^S(\boldsymbol{\xi})}{\partial \xi^d} = 0 \quad \text{for} \quad d = 1, 2\,. \tag{6.3}$$

The solution of (6.3) requires orthogonality between the two terms. As the covariant tangent vectors, $\mathbf{l}^S_d$, of the convective coordinates lines, ξ^d, can be determined by,

$$\mathbf{l}^S_d = \frac{\partial \mathbf{x}^S(\boldsymbol{\xi})}{\partial \xi^d} \quad \text{for} \quad d = 1, 2\,, \tag{6.4}$$

which is the second term in (6.3), the first term in (6.3) must be parallel to the normal vector $\mathbf{n}^S$ at $\tilde{\mathbf{x}}^S$, resulting in the location $(\tilde{\xi}^1, \tilde{\xi}^2)$ on $\Gamma^C_{\mathcal{B}^S}$ that exhibits the smallest gap or distance. As a consequence, from (6.3) the condition can be reformulated to

$$-\mathbf{n}^S(\tilde{\boldsymbol{\xi}}) \cdot \tilde{\mathbf{l}}^S_d(\tilde{\boldsymbol{\xi}}) = 0 \quad \text{for} \quad d = 1, 2\,, \tag{6.5}$$

i.e. the current slave point $\mathbf{x}^S(\tilde{\boldsymbol{\xi}})$ is the orthogonal projection of a given master point $\mathbf{x}^M$ onto the current slave surface $\Gamma^C_{\mathcal{B}^S}$. Employing the outward projection of the slave surface at the location of the shortest distance $\tilde{(\cdot)}$, the outward unit normal vector can also be determined by:

$$\tilde{\mathbf{n}}^S = \frac{(\tilde{\mathbf{l}}^S_1 \times \tilde{\mathbf{l}}^S_2)}{\left\|\tilde{\mathbf{l}}^S_1 \times \tilde{\mathbf{l}}^S_2\right\|} \quad \text{or} \quad \tilde{\mathbf{n}}^S = \frac{\mathbf{x}^M - \tilde{\mathbf{x}}^S(\tilde{\boldsymbol{\xi}})}{\left\|\mathbf{x}^M - \tilde{\mathbf{x}}^S(\tilde{\boldsymbol{\xi}})\right\|} \,. \tag{6.6}$$

Both relations can be used to determine the normal vector, $\tilde{\mathbf{n}}^S$. The second alternative is a consequence from Equation (6.3) and (6.5). This alternative may be more convenient for a penalty method, however it has the drawback that the outward unit normal vector is not defined for $\tilde{d} = 0$, cf. Wriggers (2002).

After finding the location $\tilde{\mathbf{x}}^S$ on $\Gamma^C_{\mathcal{B}^S}$, the gap function g_N is defined by:

$$g_N = \tilde{\mathbf{n}}^S \cdot (\mathbf{x}^M - \tilde{\mathbf{x}}^S) \,. \tag{6.7}$$

Note that a positive value of g_N denotes penetration as $\mathbf{n}^S$ is the unit outward normal vector, defined on the slave surface $\Gamma^C_{\mathcal{B}^S}$.

With the gap function at hand, the unregularised description of the frictionless contact formulation, also know as the *Kuhn-Tucker* conditions,

$$\begin{aligned} g_N &\leq 0 \,, \\ t_N &\geq 0 \,, \\ t_N\, g_N &= 0 \,. \end{aligned} \tag{6.8}$$

are defined. The first condition states that the gap function is always smaller than zero, i.e. no penetration is allowed ($\rightarrow$ impenetrability condition). The second condition states that the emerging contact pressure, t_N, is always positive and compressive. The last condition is called complementary condition and states that there should be only a contact compression pressure, when contact really occurs. The conditions are visualised in Figure 6.3. The first condition states that the red line is only on the negative wing of the axis. The second condition states that the contact pressure rises vertically in the positive direction. The third condition states the fact, that, for the unregularised description, a contact pressure only arises if $g_N = 0$.

6.1.1 Weak formulation of the Contact Problem

First, recall that Equation (5.5) defines the principle of virtual work for one elastic body, i.e.

$$\begin{aligned} \mathcal{G}^\chi &= \int_{\mathcal{B}_0} \mathbf{P} \cdot \operatorname{Grad} \delta\boldsymbol{\chi} \, \mathrm{d}V - \int_{\Gamma_{\mathcal{B}_0}} \mathbf{t}_0 \cdot \delta\boldsymbol{\chi} \, \mathrm{d}A \,, \\ \mathbf{X} &= \tilde{\mathbf{X}} \quad \text{on} \quad \Gamma^u \,, \\ \mathbf{t}_0 &= \tilde{\mathbf{t}}_0 \quad \text{on} \quad \Gamma^\sigma \,. \end{aligned} \tag{6.9}$$

Considering contact mechanics between two bodies, a master $\mathcal{B}^M$ and a slave $\mathcal{B}^S$, the overall virtual work $\mathcal{G}^{\text{coupled}}$ is defined by:

$$\mathcal{G}^{\text{coupled}} = \mathcal{G}^{M_\chi} + \mathcal{G}^{S_\chi} + \mathcal{G}^C \,, \tag{6.10}$$

where $\mathcal{G}^{M_\chi}$ and $\mathcal{G}^{S_\chi}$ are the virtual work of the master and the slave, respectively, and $\mathcal{G}^C$ is the contact residual which couples the two bodies, and completes the overall virtual work for the contact problem. According to Laursen (2002), the contact residual $\mathcal{G}^C$ for the frictionless case is defined by

$$\mathcal{G}^C = \int_{\Gamma^C_{\mathcal{B}^S}} t_N \, \delta g_N \, \mathrm{d}A \,, \tag{6.11}$$

where δg_N is the variation of the gap function. The variation of the gap function δg_N is defined similarly to Equation (6.7) by

$$\delta g_N = \tilde{\mathbf{n}}^S \cdot (\delta \boldsymbol{\chi}^M - \delta \tilde{\boldsymbol{\chi}}^S) \,, \tag{6.12}$$

where $\delta \boldsymbol{\chi}$ is each body's virtual displacements. The integral of Equation (6.11) is formulated on the slave surface $\Gamma^C_{\mathcal{B}^S}$, as the contact points are defined within that face.

6.1.2 Regularisation

The regularisation of a frictionless contact description (Kuhn-Tucker condition) is conducted employing the penalty method. Following Chung et al. (2008), a penalty method is chosen, which, compared to an augmented *Lagrange*an method, provides sufficient enough accuracy while reducing calculation effort. The regularised contact pressure is:

$$t_N = \begin{cases} \epsilon_N \, g_N & \text{if} \quad g_N \geq 0 \\ 0 & \text{else} \,, \end{cases} \tag{6.13}$$

where ϵ_N is a penalty factor. Note, for $\epsilon_N \to \infty$, the exact solution would be achieved. An ϵ_N that is chosen too small in comparison to the acting forces might allow the bodies to penetrate. A too large ϵ_N might lead to a system that reacts too stiff and convergence might fail.

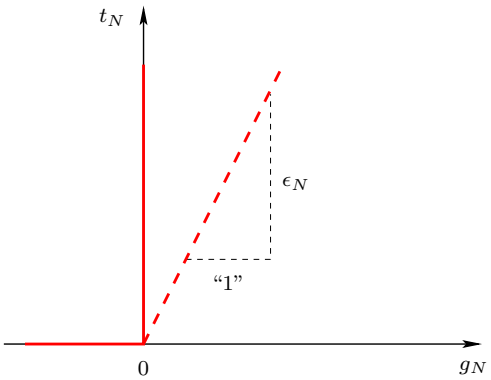

Figure 6.3: *Regularisation of the penalty contact problem by a penalty approximation.*

6.1.3 Linearisation

As the resulting system is nonlinear, it can be solved like before using the *Newton-Raphson* method. Therefore, the directional derivative of Equation (6.11) for the frictionless contact formulation, using the penalty method for regularisation, needs to be defined. In contrast to the non-contact contributions, the contact contribution is linearised by deriving the analytical tangent according to Laursen (2002). The linearised term, Δt_N, for the contact pressure, t_N is defined by:

$$\Delta t_N = \epsilon_N \, H(g_N) \, \Delta g_N \,, \tag{6.14}$$

where H is the *Heaviside* step function.

6.2 Numerical Implementation within CMISS

According to Chung (2008), the numerical contact implementation within CMISS is based on the node-to-face approach derived by Laursen (2002) which is identical to the closest point projection. The discretisation of the contact surfaces is defined similarly to the discretisation of the volume. The only difference is obviously the reduction of one dimension, as surfaces are 2-dimensional objects.

Within the contact face of the master, N_e^C contact points (including the nodes) are defined for each element. The contact points are equally spaced with respect to the local $\boldsymbol{\xi}$-coordinates. These contact points are projected onto the discretised face of the slave to evaluate the gap function. Furthermore, the contact points serve as integration points over which the contact residuals for each element face $\mathbf{R}_e^C$ are evaluated.

Note that for this work, the order of geometric discretisation is chosen to be quadratic. The elements are 27-node (tri-quadratic) hexahedrons, see Section 5.2. The face of such an element contains 9 nodes. To allow an equally spaced number of contact points within that face, the number of contact points need to be odd. The number of contact points, N_e^C, is chosen to be $N_e^C = 7 \cdot 7 = 49$.

The local coordinates are chosen to coincide with the convective coordinate system. The location of the nodes at the master face of one element is described with respect to the $\boldsymbol{\chi}$-coordinate and defined by

$$\mathbf{x}_e^M(\boldsymbol{\xi}) = \sum_{i=1}^{9} N_i(\boldsymbol{\xi}) \, \mathbf{x}_{ei}^M \,. \tag{6.15}$$

Herein, $\mathbf{x}_e$ is similarly defined to $\mathbf{X}_e$ namely consisting of the set of nodes belonging to element's surface.

Using the closest projection algorithm, the surface contact points of the master are projected onto the slave surface. The location of the projected nodes are defined identically to the nodes on the master surface. To distinguish the coordinates of the master and the slave, the coordinate of the slave are denoted by $\tilde{\boldsymbol{\xi}}$ to emphasise that the projected contact points are not pre-determined and equally spaced but determined by the projection Equation (6.2). The discretisation is defined by

$$\mathbf{x}_e^S(\tilde{\boldsymbol{\xi}}) = \sum_{i=1}^{9} N_i(\tilde{\boldsymbol{\xi}}) \, \mathbf{x}_{ei}^S \,. \tag{6.16}$$

The tangent vectors at the projected points (on the slave surface) are computed using the discretisation scheme:

$$\mathbf{l}_d^S = \frac{\partial \mathbf{x}^S}{\partial \tilde{\xi}^d} = \sum_{i=1}^{N_e^C} \frac{\partial N_i(\tilde{\boldsymbol{\xi}})}{\partial \tilde{\xi}^d} \mathbf{x}_{ei}^S \quad \text{for} \quad d = 1, 2\,. \tag{6.17}$$

These formulations are sufficient to compute for each contact point on the master surface the unit normal vector, $\tilde{\mathbf{n}}$, which derives by (6.6), the coordinates of the projected point at the slave surface $\mathbf{x}^S(\tilde{\boldsymbol{\xi}})$, and the gap function, using Equation (6.7).

Further, for the non-contact contributions, also the virtual displacement for including contact is discretised by

$$\delta\boldsymbol{\chi}_e^j(\boldsymbol{\xi}) = \sum_{i=1}^{9} N_i(\boldsymbol{\xi})\, \delta\boldsymbol{\chi}_{ei}^j \quad \text{for} \quad j = \{M, S\}\,. \tag{6.18}$$

Inserting (6.18) into (6.12), δg_N can be computed by

$$\begin{aligned} \delta g_N(\boldsymbol{\xi}) &= \mathbf{n} \cdot \left(\sum_{n=1}^{9} N_i(\boldsymbol{\xi})\ \delta\boldsymbol{\chi}_{ei}^M - \sum_{n=1}^{9} N_i(\tilde{\boldsymbol{\xi}})\ \delta\boldsymbol{\chi}_{ei}^S \right) \\ &= -\delta\boldsymbol{\chi}^C \cdot \boldsymbol{\phi}^C\,, \end{aligned} \tag{6.19}$$

where $\boldsymbol{\chi}^C$ and $\boldsymbol{\phi}^{C,h}$ are introduced by

$$\begin{aligned} \delta\boldsymbol{\chi}_e^C &= \left[\delta\boldsymbol{\chi}_{e1}^S, \ldots, \delta\boldsymbol{\chi}_{e9}^S, \delta\boldsymbol{\chi}_{e1}^S, \ldots, \delta\boldsymbol{\chi}_{e9}^S\right]^T\,, \\ \boldsymbol{\phi}_e^C &= \left[N_1^M\,\mathbf{n}, \ldots, N_9^M\,\mathbf{n}, -N_1^S\,\mathbf{n}, \ldots, -N_9^S\,\mathbf{n}\right]^T\,, \end{aligned} \tag{6.20}$$

to enable a compact formulation of Equation (6.19).

Using the introduced measures, the contact residual can be introduced via the contact contribution of the virtual work:

$$\begin{aligned} \mathcal{G}^C &= \int_{\Gamma_{\mathcal{B}^S}^C} t_N\, \delta g_N \,\mathrm{d}A \\ &= \delta\boldsymbol{\chi}^C \int_{\Gamma_{\mathcal{B}^S}^C} t_N\, \boldsymbol{\phi}^C \,\mathrm{d}A \\ &= \delta\boldsymbol{\chi}^C\, \mathbf{R}^C\,. \end{aligned} \tag{6.21}$$

Whereas the contact residual is defined as,

$$\mathbf{R}^C = \int_{\Gamma_{\mathcal{B}^S}^C} t_N\, \boldsymbol{\phi}^C \,\mathrm{d}A\,. \tag{6.22}$$

6.2.1 Linearisation

Section 6.1.3 introduces in Equation (6.14) the linearised term of the contact stress. It requires the computation of the linearised gap function, Δg_N, that is similarly defined as the variation of the gap function, δg_N, i.e.

$$\begin{aligned} \Delta g_N &= \tilde{\mathbf{n}}^S \cdot (\Delta \boldsymbol{\chi}^M - \Delta \boldsymbol{\chi}^S) \\ &= \tilde{\mathbf{n}}^S \cdot \left(\sum_{i=1}^{9} N_i^M(\boldsymbol{\xi})\, \Delta \boldsymbol{\chi}_{ei}^M - \sum_{i=1}^{9} N_i^S(\tilde{\boldsymbol{\xi}})\, \Delta \boldsymbol{\chi}_{ei}^S \right) \\ &= (\Delta \boldsymbol{\chi}^C)^T \boldsymbol{\phi}^C \,, \end{aligned} \tag{6.23}$$

with

$$\Delta \boldsymbol{\chi}^C = \left[\Delta \boldsymbol{\chi}_{e1}^M, \ldots, \Delta \boldsymbol{\chi}_{e9}^M, \Delta \boldsymbol{\chi}_{e1}^S, \ldots, \Delta \boldsymbol{\chi}_{e9}^S \right]^T \,. \tag{6.24}$$

After defining the variation of the gap function, the linearised contact residual can be introduced using Equation (6.14) and Equation (6.23) by

$$\begin{aligned} \Delta t_N\, \delta g_N &= \epsilon_N\, H(g_N)\, \Delta g_N\, \delta g_N \\ &= \epsilon_N\, H(g_N)\, (\delta \boldsymbol{\chi}^C)^T\, \boldsymbol{\phi}^C\, (\boldsymbol{\phi}^C)^T\, \Delta \boldsymbol{\chi}^C \\ &= (\delta \boldsymbol{\chi}^C)^T\, \mathbf{K}^C \Delta \boldsymbol{\chi}^C \,. \end{aligned} \tag{6.25}$$

This relation is used to introduce the discretised form of contact stiffness matrix $\mathbf{K}^C$,

$$\mathbf{K}^C = \epsilon_N\, H(g_N)\ \boldsymbol{\phi}^C\, (\boldsymbol{\phi}^C)^T \,. \tag{6.26}$$

In summary, the linearised contact residual is

$$\Delta \mathcal{G}^C = \int_{\Gamma_{\mathcal{B}^S}^C} (\delta \boldsymbol{\chi}^C)^T \mathbf{K}^C\, \delta \boldsymbol{\chi}^C \, \mathrm{d}A^S \,. \tag{6.27}$$

Note that the relation only holds for the penalty method without friction between the interacting bodies.

6.2.2 Surface Integration

The evaluation of the tangent stiffness matrix and the contact residuals surface integrals over the slave contact face are required. In contrast to the volume integrals, a rectangular integration rule is used for the surface contact integrals. The quadrature scheme is preferred for the contact mechanics as it captures well the sharp gradients of the contact pressure fields for the fine grids of contact points (Chung, 2008). The contact points are used as integration points. For more details, see Chung (2008).

6.2.3 Solution Procedure

Recalling Equation (6.10) and (6.11), the overall virtual work, $\mathcal{G}^{\text{coupled}}$ consists of contributions of the master $\mathcal{G}^S$, of the slave $\mathcal{G}^S$, and the interaction of both bodies. The element

residual vectors and linearised stiffness matrices for each elastic body are combined to $\mathbf{R}^{\text{coupled}}$ and $\mathbf{K}^{\text{coupled}}$. The virtual work, due to contact, is determined with respect to the slave surface. This decision is however arbitrary. The element residual vectors and linearised stiffness matrices, resulting from the contact formulation are denoted by $\mathbf{R}^C$ and $\mathbf{K}^C$. If penetration occurs, contributions of $\mathbf{R}^C$ and $\mathbf{K}^C$ arise at these nodes location within the matrices. As the size of $\mathbf{R}^C$ and $\mathbf{R}^{\text{coupled}}$ are the same, all nodes, which are not contributing to contact, are zero. Hence, $(\cdot)^{\text{coupled}}$ and $(\cdot)^C$ are of the same size and the global system can be written as

$$\left(\mathbf{K}^{\text{coupled}} + \mathbf{K}^C\right) \Delta \boldsymbol{w}^{\text{coupled}} = - \left(\mathbf{R}^{\text{coupled}} + \mathbf{R}^C\right) . \tag{6.28}$$

Using vector and matrix notation, the contributors can be written in a compact form:

$$\mathbf{K}^{\text{coupled}} = \begin{bmatrix} \mathbf{K}^S & \mathbf{0} \\ \mathbf{0} & \mathbf{K}^M \end{bmatrix} , \quad \mathbf{K}^C = \begin{bmatrix} \mathbf{K}^{C^S} & \mathbf{0} \\ \mathbf{0} & \mathbf{K}^{C^M} \end{bmatrix} , \tag{6.29}$$

where the size of $\mathbf{K}^S$ and $\mathbf{K}^M$ depend on the mesh of each body.

The coupled solution update vectors $\Delta \boldsymbol{w}^{\text{coupled}}$, coupled residual vector $\mathbf{R}^{\text{coupled}}$, and the contact residual vector $\mathbf{R}^C$ are

$$\Delta \boldsymbol{w}^{\text{coupled}} = \begin{bmatrix} \Delta \boldsymbol{w}^S \\ \Delta \boldsymbol{w}^M \end{bmatrix} , \quad \mathbf{R}^{\text{coupled}} = \begin{bmatrix} \mathbf{R}^S \\ \mathbf{R}^M \end{bmatrix} , \text{and} \quad \mathbf{R}^C = \begin{bmatrix} \mathbf{R}^{C^S} \\ \mathbf{R}^{C^M} \end{bmatrix} . \tag{6.30}$$

Note that if one of the bodies is assumed to be rigid, its contribution is zero and the size of the overall matrix reduces to the size of the elastic body.

The whole solution procedure is visualised in Figure 6.4 as a flow chart.

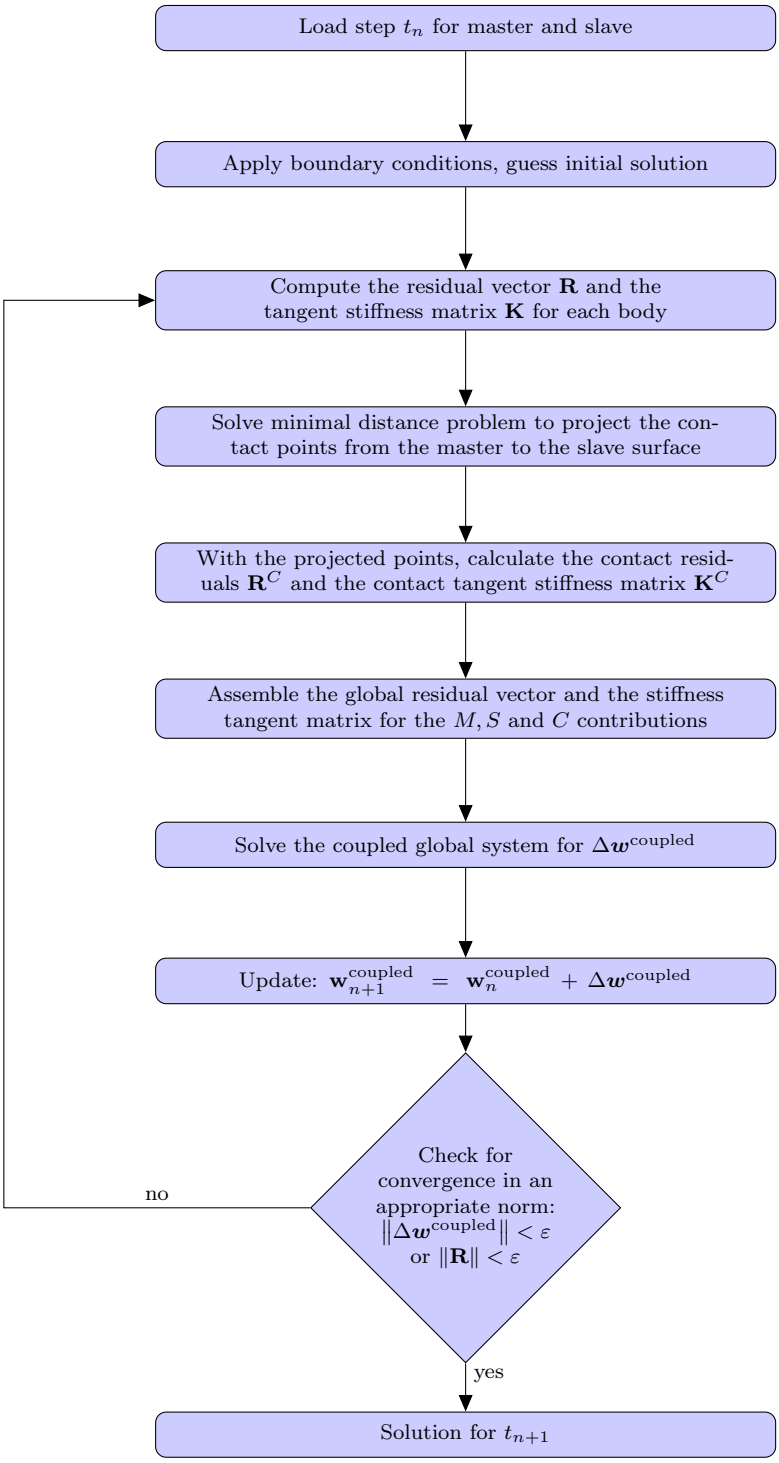

Figure 6.4: *Overall solution procedure including contact.*

7 Upper Limb Model

The goal of this thesis is to introduce a novel multi-muscle musculoskeletal system framework, in which the bodies are modelled as 3-dimensional continuum-mechanical objects and discretised using the finite element method.

Within this chapter, a carefully chosen model of a fraction of the musculoskeletal system is chosen such that it is possible to perform simulations of a continuum-mechanical musculoskeletal system. To start off, the upper limb is chosen as a 2-muscle musculoskeletal system. It consists of the triceps brachii, the biceps brachii, and the elbow joint as hinge joint. The system is fixed by clamping the humerus in the shoulder.

First, the anatomy of the upper limb is introduced. Hereby, the fundamentals of Chapter 2, where generalised definitions of the anatomy were introduced, are specified for the upper limb. Section 7.2 combines all information and introduces model assumptions to facilitate in silico experiments on the Upper Limb Model. In Chapter 7.3, a simple equivalent static system is introduced to define the kinematics of the model and to balance the momentum of the Upper Limb Model. In Section 7.4, a simple analytical example of a system similar to the Upper Limb Model is used to estimate the kinematic and kinetic conditions in an elbow joint. In Section 7.5, the force wrench is introduced to investigate the muscle's mechanical characteristic.

7.1 Anatomy of the Upper Limb

The upper extremity or the upper limb is the region extending from the deltoid region to the hand. The term "upper arm" officially only refers to the structures from the shoulder to the elbow. However, in causal usage, the term upper arm is often used interchangeably.

Depending on the later need, the anatomical structures are introduced using a different degree of detailing, where the order of introduction follows the mechanical chain from the shoulder to the hand. The chain is composed of the shoulder girdle, the shoulder joint, the upper arm, the elbow joint, the forearm, and finally the hand. Figure 7.1 depicts the most important bony components of the upper limb that are mentioned in the following description.

The **shoulder girdle** consists of the clavicle and the scapula and connects the upper limb to the trunk through the sternoclavicular joint, a ball-socket joint which is located at the front side at the top of the sternum. This joint is the only bony connection from the upper limb to the trunk. The clavicle can move in the coronal plane and the transverse plane and is able to rotate around its own axis. It is stabilised by several ligaments. The junction between clavicle and scapula is called acromioclavicular joint. It is also strengthened by strong ligaments, which prevent large lateral and medial movements. Together, these two joints allow the shoulder girdle a wide range of movement. This is largely attributed to the lack of a bone-to-bone contact between the scapula and the trunk. The mobility of the shoulder girdle is supported by a large number of muscles. The

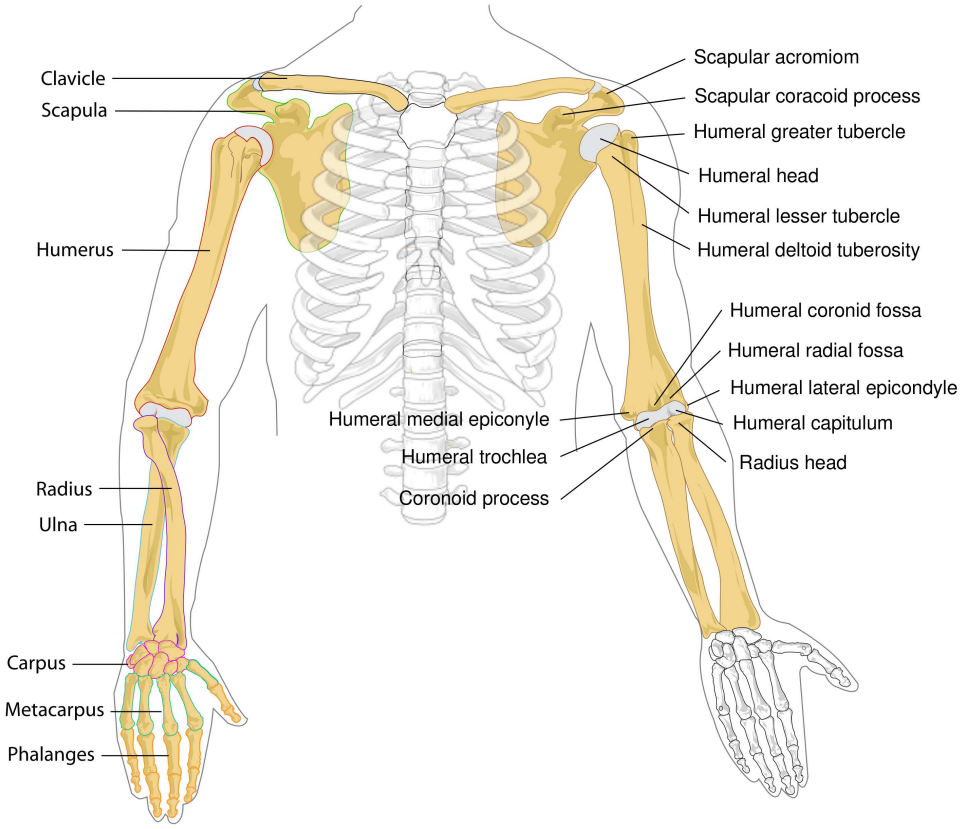

Figure 7.1: *Anatomical features of the upper limb. Source: adapted from Mariana Ruiz Villarreal, Wiki Commons.*

most important of these muscles are muscular sheets rather than fusiform or strap-shaped muscles. Therefore, these muscles never act in isolation but with some fibres acting in coordination with fibres in other muscles. The basic muscles acting on the shoulder girdle are the trapezius, sternocleidomastoideus, omohyoideus rhomboideus major, rhomboideus minor, levator scapulae subclavius, pectoralis minor, and serratus anterior.

The **shoulder joint**, which is anatomically called the glenohumeral joint, is a highly mobile ball and socket joint connecting the glenoid cavity of the scapula and the proximal head of the humerus. The shoulder joint is the ball and socket joint with the largest mobility because it is not stabilised like most other joints. Typically, they are connected to a large extent by ligaments or bony structures but also by skeletal muscles. The large muscles acting at this joint perform multiple actions and seemingly simple movements are often the result of composite antagonist and agonist actions from several muscles. The acting muscles, again, are just named for the sake of completeness without going into further detail: supraspinatus, infraspinatus, teres minor, subscapularis, deltoideus, latissimus dorsi, teres major, pectoralis major, and coracobrachialis.

The next part in the mechanical chain is the upper arm, consisting of the structures between the shoulder joint and the elbow joint. The only bone in this section is **Os humerus**, see Figure 7.1, which is connected at its proximal end to the scapula within the shoulder joint. The distal part joins the elbow with radius and ulna. The humerus is one of the largest and strongest long bones in the human body. It can be divided into

three sections: a rounded head, a long shaft, and the distal head. The smooth, dome-shaped head of the bone lies at an angle to the shaft and fits into a shallow socket of the scapula (shoulder blade) to form the shoulder joint. Below the head, the bone narrows to form a cylindrical shaft. It flattens and widens at the lower end and, at its base, it joins with the bones of the lower arm (the ulna and radius) to unite the elbow.

The **elbow joint** is a complex hinge joint that connects the distal end of the humerus and the proximal ends of the ulna and radius in the forearm. The distal head of the humerus is divided into two joint processes: the trochlea on the medial side and the capitulum on the lateral side. The pulley-shaped trochlea forms a tight hinge joint with the trochlea concave dent of the ulna surrounding it, called humeroulna joint. On the lateral side, the concave end of the head of the radius meets the rounded, convex capitulum to complete the elbow, resulting in a ball and socket joint, called humeroradial joint. The loose union of the capitulum of the humerus and the head of the radius allows the radius to pivot as well as flex and extend. The pivoting of the radius allows for the supination and pronation of the hand at the wrist. Therefore, ulna and radius form a third joint (next to the hinge joint between humerus and ulna and the ball and socket joint between humerus and radius) a pivot joint with the humerus (proximal) and the carpus (distal) to allow rotation of the forearm and the wrist. This pivot joint at the elbow is called superior radioulnar joint. The hinge joint of the elbow allows a flexion and extension of the forearm relative to the humerus or the upper arm. The range of motion of the elbow is limited by the olecranon, the posterior process of the ulna. Flexion is only limited by the soft tissue which is clamped between the forearm and the upper arm; hence the range of motion for active flexion is smaller due to the hardened muscle tissue. In general, the range of flexion can be assumed to be around 140°.

An extensive network of ligaments, surrounding the joint capsule, helps the elbow joint to maintain its stability, while resisting dislocation of the bones, and accommodating for mechanical stresses. The ligaments on either side of the elbow are triangular bands which also participate in forming the elbow joint capsule. Due to their important role of forming the joint capsule, the capsule is strongly structured on the sides whereas it is comparatively weak on the front and back. The radial and ulnar collateral ligaments (medial and lateral ligament) connect and maintain the position of the radius and ulna relative to the epicondyles of the humerus. The annular ligament of the elbow extends from the ulna around the head of the radius to maintain contact between the radius and the humerus. These ligaments lie across the transverse joint axis and are, therefore, always relatively tense and impose strict limitations on abduction, adduction, and axial rotation at the elbow.

Following the same structure, only the skeletal muscles involved in acting on the elbow joint are mentioned in this paragraph.

The **triceps brachii**, has, as the name indicates, three muscle heads – a long, a lateral, and a medial head. The long head arises from the scapula. The lateral head arises high up on the lateral side of the posterior humerus. The medial head arises from a broad area lower down and more medially at the humerus. Each of the three heads has its own motor neuron sub-nucleus in the motor column in the spinal cord. The medial head is formed predominantly by small type I fibres and small motor units, the lateral head of large type IIB fibres and large motor units and the long head of a mixture of fibre types and motor units. The three heads unite and towards the end they build one broad tendon

which inserts at the olecranon process at the back of the ulna. The three heads are the main extensor of the elbow. But with its origin on the scapula, the long head also acts on the shoulder joint and is also involved in retroversion and adduction of the arm. While precisely coordinated forearm or hand movement need to be performed the triceps brachii contracts to fixate the elbow joint (co-contraction).

The **anconeus** is a very minor elbow extensor and ulna abductor. It originates at the lateral epicondyle and inserts at the lateral aspect of the proximal ulna. Some anatomists consider it just as a continuation of the triceps brachii. It forms the joint capsule at the olecranon fossa during extension.

Biceps brachii, as the name already indicates has two muscle heads. The long head arises from the supraglenoid tubercle (directly superior to the glenoid cavity) while the second, called the short head, arises from the coracoid process (a small hook-like structure on the lateral edge of the superior anterior portion of the scapula). I.e. both heads originate at the shoulder blade and travel down the arm, lying in front of the brachialis. Both heads cross the elbow joint, join, and together insert on the radial tuberiosity, which is a protuberance below the radius neck. Actually, the biceps brachii is a tri-articulated muscle; acting across three joints: (i) the shoulder, (ii) the elbow, and (iii) the proximal radioulnar joint. While the biceps also crosses the shoulder, its main function is flexing the elbow and to supinate the forearm. The functionality of the biceps brachii on the shoulder movement is various (the long head: forward flexion, abduction, external rotation. The short head: adduction, stabilisation by carrying high loads).
The biceps brachii has a fusiform-like fibre orientation with around 50% of the muscle fibres being fast-twitch and slow-twitch fibres.

The **brachialis** arises from this broad area on the anterior lower half of the humerus and inserts on the coronoid process, which is the front bony profusion of the ulna. The fibres converge from the wide origin towards the thick tendon inserting at the ulna. As the brachialis inserts at the ulna, it only acts as elbow flexor and does not participate in supination and pronation. The muscle is a strong elbow flexor when the palm is pronated.

The **brachioradialis** originates at the most distal third of the humerus, just below the deltoid tuberosity, crosses the elbow and inserts at the distal end of the radius. The muscle belly is mostly positioned at the forearm, while only a small excerpt crosses the elbow. Its job is to flex the elbow and aid pronation and supination. When the forearm is pronated, the brachioradialis tends to supinate as it flexes. In a supinated position, it tends to pronate as it flexes. This also assists the biceps brachii. The brachioradialis is a stronger elbow flexor when the forearm is at 90° between supination and pronation at the radioulnar joint. When pronated, the brachioradialis is more active during elbow flexion since the biceps brachii is in a mechanical disadvantage. With the insertion comparatively close to the fulcrum of the elbow, the brachioradialis does not generate as much joint torque as the brachialis or the biceps. It is mainly effective when those muscles have already partially flexed the elbow. The action of the brachioradialis is especially in demand when quick movements are required due to the distribution of fulcrum, effort and load (class 3 lever system) and when a weight is lifted during slow flexion of the forearm.

Pronator teres is a small muscle with two heads. The larger one originates just above the medial epicondyle of the humerus. The second originates from the medial side of the coronoid process of the ulna. The muscle ends in a flat tendon and inserts at the middle on the medial surface of the radius. Its main action is pronating the forearm. It is only

weakly participating in flexing the elbow.

Extensor carpi radialis longus and – brevis arise from the lateral epicondyle of the humerus and insert on the third metacarpal of the hand. Although they cross the elbow, they are not considered to participate in elbow flexion. They act on extending and abducting the wrist joint and the hand.

The forearm consists of the two bones **Os ulna and Os radius**, where the ulna is the larger of the two bones. As mentioned already in the elbow description, the radius pivots around the ulna. Most muscles passing along the forearm originate lateral or medial at the epicondyle of the humerus and insert either at the wrist, hand, or fingers. As their origin is so close to the fulcrum of the humerus, they are practically not participating in acting on the elbow joint. Due to the high number of muscles acting on the sophisticated hand and the fact that these muscles are not of concern for this thesis, the muscles are not mentioned and discussed in further detail.

Ulna and radius join at the **carpus** or wrist. The hand consists of 27 bones, 8 of those bones belong to the carpus. The rest of the bones form the palm (metacarpus) and the fingers (phalanges). All bones intersect in joints. As it is not of interest for this thesis, the complex anatomy of the hand is not discussed any further.

7.2 Upper Limb Model Assumptions

Section 7.1 pointed out how complex and interwoven the real musculoskeletal system of the upper limb is. As it is impossible to incorporate all natural phenomena in one model, model assumptions need to be made in order to facilitate simulations of a multi-muscle musculoskeletal system using spatially a volumetric discretisation. In other words, a radical reduction of complexity needs to be introduced.

The Upper Limb Model, as it is shown in Figure 7.2 consists of three bones: Os humerus, Os ulna, and Os radius. The three bones form the elbow joint, which is considered to be an ideal hinge joint. The bones of the hand are not necessarily required for investigating elbow movements and are therefore not considered. As the Upper Limb Model does not account for supination and pronation, the ulna and the radius can be united to build the forearm. For two reasons the bones are considered to be rigid without causing severe model errors: (i) The bones are much stiffer than the rest of the soft tissue. (ii) In this study, only naturally occurring loads rather than high accelerations, as they may result e.g. in accidents, are considered.

Gravitational forces need not to be considered, as the upper limb position is such that the flexing elbow movement is in a horizontal plane. Therefore, the dead weight of the contributing objects is not of interest.

Without involving synergetic muscle effects, at least one single antagonistic muscle pair needs to be chosen to enable the movement of an idealised elbow joint.

The choice for the single extensor muscle is simple. In the Upper Limb Model, the three triceps heads – long, lateral, and medial – are united to build one homogenised skeletal muscle. It is by far the most powerful elbow extensor. Unfortunately, no information about the real fibre orientation was available from the visible human data set. However, to introduce a more realistic fibre structure, the fibres of the triceps brachii are imitated to arrange bipennate. To establish the fibre structure within the model, first the fibre orientation was determined to be fusiform, i.e. the fibre are aligned along the longitudinal

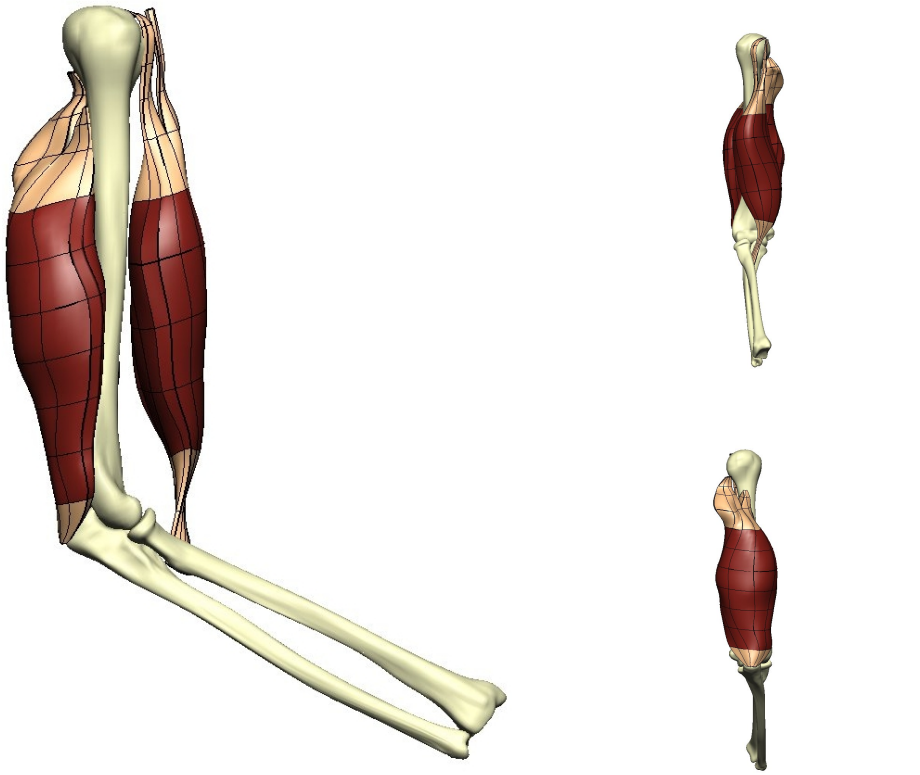

(a) *side view* **(b)** *front and back view*

Figure 7.2: *The upper limb model consists of the bones Os humerus, Os ulna and Os radius, which are considered to be rigid and of the antagonistic muscle pair, triceps brachii and biceps brachii. The muscle tissue is coloured dark red and the tendon tissue beige. The geometry is established using the virtual human male's data set (Spitzer et al., 1996).*

boarders of the finite elements. The finite elements in the middle are chosen to be the central line with a parallel fibre orientation, see Figure 7.3a. Elements to the left and right are rotated by 15° to the left and right, respectively.

The elbow flexor's choice is more problematic as there are several synergetic acting muscles. Some elbow flexors are not only responsible for elbow flexion but also for forearm supination and pronation. Furthermore, their ability to generate an elbow moment depends on the posture of the hand. Possible candidates are the biceps brachii, the brachialis, the brachioradialis, extensor carpi radialis longus, and the pronator teres. Murray et al. (2000) identified the isometric moment-generating capacity building the product of the physiological cross-section area ([m^2]), the average moment arm ([m]), and the cosine pennation angle ([-]) of the muscles acting on the elbow joint. They pointed out that biceps brachii produces the largest moment capacity (20 cm^3), followed by brachialis (11.5 cm^3), brachioradialis (6.8 cm^3), extensor carpi radialis longus (3.2 cm^3), and pronator teres (3.1 cm^3). Thus, the biceps brachii is chosen as the flexor in this Upper Limb Model due to its highest moment-generating capacity. As well as for the triceps brachii, the two heads of the biceps brachii are homogenised to a fusiform muscle belly, see Figure 7.3b.

The geometry of the upper limb is established using the *virtual human male*'s data set (Spitzer et al., 1996). The data of the virtual human male was acquired in a supine

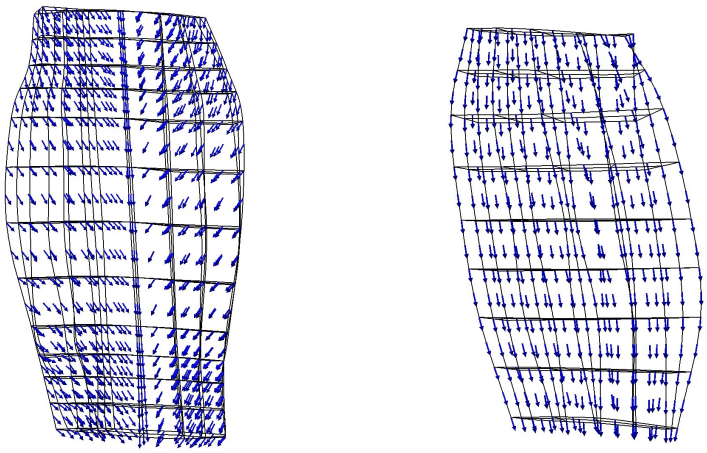

(a) *triceps brachii* **(b)** *biceps brachii*

Figure 7.3: *The triceps brachii's bipennate fibre architecture is established by assuming the middle column of the elements as parallel and the elements to the left and right to be pennated by 15° to opposite directions. The biceps brachii is assumed to have a fusiform fibre architecture.*

position. The arm was resting on the abdominal belt, where the arms had an elbow flexion angle of approximately 60°. The origin of the chosen coordinate system is the intersection between the mid sagittal and mid coronal plane at the most inferior position, where the x-axis points to the right, the y-axis anteriorly, and the z-axis superiorly.

The mesh is generated by a least-square fit introduced by Bradley et al. (1997) using the finite element software package CMISS (for more information about CMISS cf. Section 5.1). The surface fitting procedure has been extensively applied to muscular organ modelling, e.g. in Nash and Hunter (2000) and Röhrle and Pullan (2007). The preliminary mesh was discretised using *Hermite* ansatz functions and converted to quadratic *Lagrange*an shape functions.

Using a continuum-mechanical approach for the musculoskeletal system, the choice of the muscle's stretch state, has a strong influence on the mechanical behaviour. As there are no comparable continuum-mechanical models available, no experience exists on what to choose best. As the choice of the muscle's prestretch is not uniquely defined, the muscle length is chosen in such a way that the passive muscle does not cause a compressive force for the shortest possible length. Therefore, the muscles' geometry is shortened by removing a few centimetres from both the proximal and the distal ends of each muscle. Within the prestretch phase, the muscles are stretched to the original length. The disadvantage of that choice is that the original volume of the muscle reduces depending on the amount of prestretch, and hereby the maximal reachable muscle force.

The skeletal muscles are represented in two evolution steps. The first one assumes the tendon tissue to be rigid. As a consequence, the tendon tissue is not considered within the finite element simulation and just visualised by a rigid mesh. In the second evolution step, the tendons are considered to behave as a strong, transversely isotropic material, see Section 4.4.

7.2.1 Rigid-Tendon Model

The skeletal muscle material parameters used for the model, are taken from literature and listed in Table 7.1. In case of the active muscle parameters, parameter set in Günther et al. (2007) is chosen as an initial guess and adapted for a continuum-mechanical approach. As their parameter set is determined for a *Hill*-type muscle, the data needed to be adjusted to fit into the continuum-mechanical framework. Adjustments are conducted manually until an adequate force response was achieved. Material parameters for the isotropic and passive material behaviour are determined using a least-square fit to experimental data (Hawkins and Bey, 1994; Zheng and Mak, 1999). For the maximum active stress, $\sigma_{\max}$, the values vary in the literature from 100-500 kPa (Woittiez et al. (1984); Fitts et al. (1991); Van Leeuwen and Spoor (1992)). Here, a value of $\sigma_{\max} = 300\,\text{kPa}$ is assumed.

Table 7.1: *Skeletal muscle tissue parameter set, as introduced in* Section *4.3, for triceps and biceps brachii when the tendons are considered to be rigid.*

contribution	parameter	triceps	biceps	source
isotropic	c_{1M}	$3.56 \cdot 10^{-2}$ MPa	$3.56 \cdot 10^{-2}$ MPa	Hawkins and Bey (1994)
	c_{2M}	$3.86 \cdot 10^{-3}$ MPa	$3.86 \cdot 10^{-3}$ MPa	
passive	c_{3M}	$0.2939 \cdot 10^{-8}$ MPa	$3.5686433 \cdot 10^{-8}$ MPa	Zheng and Mak (1999)
	c_{4M}	34.042 [-]	42.6 [-]	
active	ΔW_{asc}	0.20 [-]	0.25 [-]	adapted from Günther et al. (2007)
	ΔW_{desc}	0.10 [-]	0.15 [-]	
	ν_{asc}	3.00 [-]	3.00 [-]	
	ν_{desc}	4.00 [-]	4.00 [-]	
	λ_f^{opt}	1.13 [-]	1.35 [-]	-
	$\sigma_{\max}$	0.30 MPa	0.30 MPa	-

The choices of the boundary conditions are delicate, especially at the proximal end of the muscle. All nodes at these faces are fixed in the longitudinal muscle direction (z-direction). Some nodes in the centre of these faces are fixed in all three space-coordinates to maintain sufficient restrictions, see Figure 7.4. As the muscles are at their proximal ends in direct contact to the humerus, one has to balance between the restriction and the compliancy of the muscles' face. By adapting the number and location of the fixed nodes, the restriction can be locally increased or decreased. It needs to be balanced between an acceptable shape and numerical robustness.

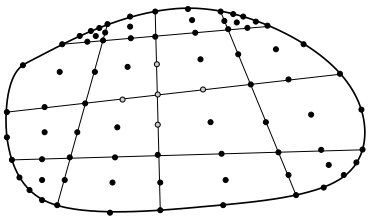

Figure 7.4: *Nodal choice of the boundary conditions at the distal and proximal ends of the muscle mesh. The black nodes are fixed longitudinally whereas the grey nodes are fixed in in all directions.*

7.2.2 Muscle-Tendon-Complex Model

In a second evolution step, muscle and tendon tissue is considered. The centre or belly was defined as muscle tissue, the tapering area is defined as a transition zone and the slender ends as tendon tissue. As the constitutive relation of Section 4.4 is purely elastic, all viscoelastic effects of the tendon tissue are neglected. During the discretisation process, the two muscle heads part at the proximal end of the muscle belly. Furthermore, the simulations were more robust when tendon ends were split in a U-shape and not a V-shape and when filling the gap with isotropic soft tissue. Figure 7.5 depicts the different zones by different colours.

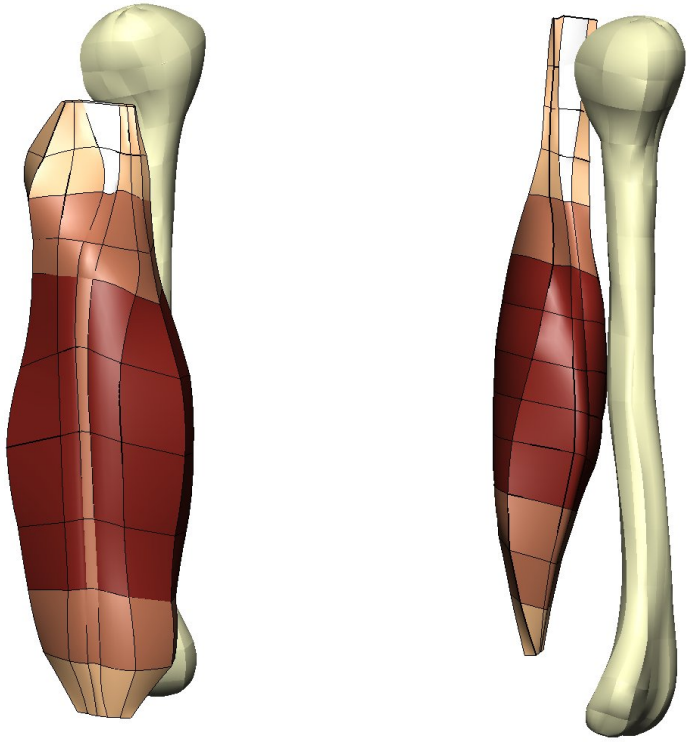

(a) *anterior view of triceps brachii* **(b)** *lateral view of biceps brachii*

Figure 7.5: *The muscle tissue is coloured in dark red. Tendon tissue is shown in beige and other soft tissue in white. The transition zone from tendon to muscle tissue is indicated by a colour between dark red and beige. Standard quadratic Lagrange finite elements are used to represent the separating muscle heads and the soft tissue between the heads to circumvent alternatives as e.g. hanging nodes and to reduce and avoid numerical problems. Between the muscle heads, the elements are tapering towards the muscle's belly to reflect the V-shape best possible. In the middle of the triceps along the longitudinal axis, one row of elements has an increased tendon tissue ratio to represent the aponeurosis sheet of a bipennate muscle.*

In the model, the triceps' origin combines the two most lateral heads to one strong united head while the most medial head is separated from the two others. The resulting gap is filled by isotropic soft tissue. The triceps' insertion unites into one wide tendon at the olecranon process.
For the model of the biceps brachii, its two heads are also combined to form one fusiform

muscle belly with two separate proximal tendons. The gap between the two tendon heads is filled with isotropic soft tissue. The fibre direction in the tendon tissue zone is assumed to behave fusiform-like.

The cross-section at the ends of the muscles is much smaller compared to the ends of the muscle tissue with rigid tendons. Furthermore, the tendons have to withstand relatively small deformations, hence, at the distal surfaces, all nodes were fixed in all spatial directions.

Bipennate muscles have a slim aponeurotic tissue layer which deeply penetrates into the muscle belly, see Figure 2.12c. The aponeurosis is a very fine and slim tissue layer which has a strong impact on the mechanical behaviour of the overall muscle-tendon complex. To represent the triceps more realistically, a central line of elements is defined as aponeurotic tissue layer, which connects the proximal and distal ends of the muscle. Compared to the thickness of the aponeurosis, the size of the element is large. Therefore, the mechanical behaviour of the aponeurotic tissue layer is homogenised using the material variable γ^M which is chosen to be $\gamma^M = 0.99$. As the tendon is approximately 1000 times stronger than muscle tissue, a linear interpolation is not constructive. Imagine a tissue composition of 10% tendon and 90% muscle where muscle has the stiffness of 1 and tendon of 1000. The interpolated bulk has a stiffness of 100.9 which is still 100 times stiffer than muscle. A tissue consisting of 1% tendon and 99% muscle is still eleven times stiffer than pure muscle tissue. Hence, the chosen material parameter γ^M is chosen to be $\gamma^M = 0.99$.

Table 7.2: *Skeletal muscle material parameter set, as introduced in* Section *4.4, for triceps and biceps brachii when the muscles are considered as a muscle-tendon complex.*

tissue	contribution	parameter	triceps	biceps	source
muscle	isometric	c_{1M}	$3.56 \cdot 10^{-2}$ MPa	$3.56 \cdot 10^{-2}$ MPa	Hawkins and Bey (1994)
		c_{2M}	$3.86 \cdot 10^{-3}$ MPa	$3.86 \cdot 10^{-3}$ MPa	
	passive	c_{3M}	$4.02 \cdot 10^{-7}$ MPa	$3.57 \cdot 10^{-8}$ MPa	Zheng and Mak (1999)
		c_{4M}	38.5 [-]	42.6 [-]	
	active	ΔW_{asc}	0.30 [-]	0.25 [-]	adapted from Günther et al. (2007)
		ΔW_{desc}	0.10 [-]	0.15 [-]	
		ν_{asc}	4.00 [-]	3.00 [-]	
		ν_{desc}	4.00 [-]	4.00 [-]	
		λ_f^{opt}	1.3 [-]	1.35 [-]	-
		$\sigma_{\max}$	0.30 MPa	0.30 MPa	-
tendon	isotropic	c_{1T}	2.31 MPa	2.31 MPa	Weiss and Gardiner (2001)
		c_{2T}	$1.15 \cdot 10^{-6}$ MPa	$1.15 \cdot 10^{-6}$ MPa	
	passive	c_{3T}	7.99 MPa	7.99 MPa	Weiss and Gardiner (2001)
		c_{4T}	16.6 [-]	16.6 [-]	

7.3 Equivalent Static System

In order to investigate equilibrium positions of the Upper Limb Model, and to avoid a large and complex system, in which all components are considered to be deformable and in contact, e.g. bone-bone contact within the joint, a reduced equivalent static system is introduced to investigate equilibrium positions of the Upper Limb Model, see Figure 7.7a.

It consists of the humerus, the forearm, the antagonistic muscle pair, and an external force F to increase the DoFs of the system by one. The angle between the humerus and the forearm is defined as the elbow flexion angle θ and defines the position of the forearm. The humerus is supported in all spatial directions and the forearm rotates around the fulcrum of the elbow joint. The forearm is represented including a rigid, bend-resistant corner at the fulcrum to represent the location of the olecranon. The muscle attachment points coincide with the volumetric model. The forearm's rotation matrix is defined by an axis and an angle. The rotation angle is defined to be the elbow flexion angle and the rotation axis is defined by a vector product of a vector along the humerus and the orientation of a vector from the fulcrum and to the distal end of the forearm.

As both muscles insert at the forearm, the position of the forearm defines the muscles' lengths and lever arms, i.e. the muscles' kinematics only depend on the elbow angle.

As one only considers an equivalent static system and assumes rigid bones, it is sufficient to identify, for each insertion or origin, one node on each mesh of the ulna and radius as the muscles' insertion points. The muscles' length are defined by the linear distance between the origin and insertion points. The origin is fixed whereas the location of the insertion point varies depending on the elbow flexion angle. The chosen nodes on the bone are tracked for the physiologically reasonable range of motion of the forearm, i.e. $10° < \theta < 150°$. The muscle length is defined as change of the distance between origin and insertion relative to its initial position at $\theta_0 = 60°$. Then, for each of the muscle lengths relative to the initial position, a separate third-order polynomial has been obtained using MATLAB (2014)'s least-squares fitting functionality. The respective relative muscle lengths are depicted in Figure 7.6a and Figure 7.6b.

Compared to the triceps brachii, the biceps brachii has a much larger change of length. The reason is that the location of the attachments' site is further away from the elbow's fulcrum.

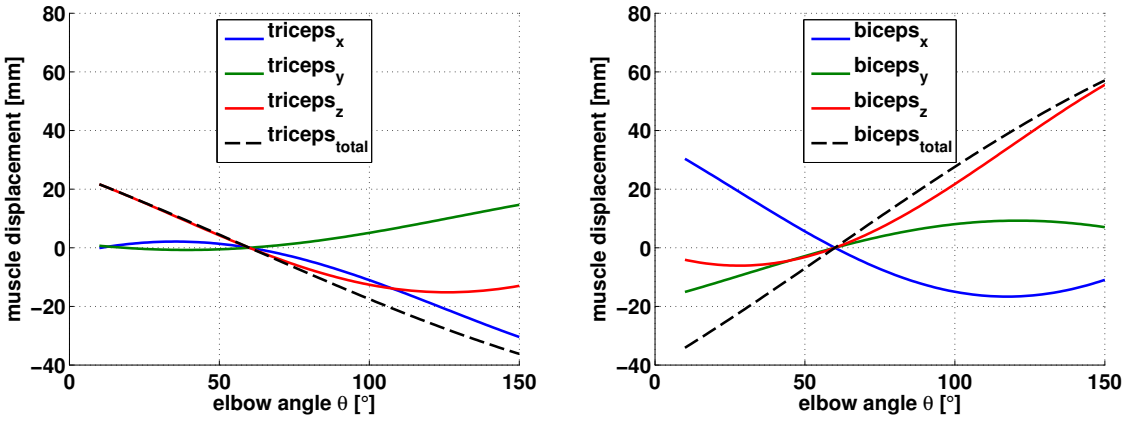

(a) *triceps brachii* **(b)** *biceps brachii*

Figure 7.6: *Relative change of muscle length is determined by subtracting the muscle length at $\theta_0 = 60°$ from the current muscle length. As the z-direction is close to parallel to the longitudinal axis of the muscle, it is dominating the mechanical behaviour of the muscle.*

The muscle lever arms are determined using two different methods. The first method, introduced by An et al. (1984), is widely used and its related errors are considered to

be small. It is also known as the tendon-displacement method and is derived using the principle of virtual work and basic geometry and defines the moment arm as the derivative of the muscle length with respect to the joint angle. The idea basically is that the change of length of a string fixed at two ends which is wrapped around a pulley is caused only by that part of the string which wraps around the pulley with a diameter l. Hence, the lever arms can be defined by:

$$l_m = \frac{\mathrm{d}L_m}{\mathrm{d}\theta} \quad \text{as} \quad \Delta L_m = 2\,\pi\,l_m\,\frac{\Delta\theta}{2\,\pi}\,, \qquad \forall \quad m = \{T, B\}\,, \tag{7.1}$$

where L_m is the muscle's length and l_m is the distance from the joint centre, or the pulley to the tendon or string. The second part of (7.1) exactly describes the part of the string which is wrapped around the pulley.

Within the first method, the lever arm is a scalar-valued parameter lacking all information of the actual location and orientation of the acting members. Unlike rigid-body simulations, where the muscle force direction is an assumed parameter derivable from the kinematics, the volumetric model enables to introduce a second method which determines the lever arm by considering the force direction depending on the muscle activation, the muscle geometry, the fibre orientation, and the restricting neighbours.

As the muscle force orientation can change dramatically within the range of a possible acting situation and a new point of action can be derived in order to respect the mechanical situation of the muscle (see Chapter 7.5), a more detailed description of the lever arm is required to advantageously use this results.

The lever arm resulting from the vector-resulting description is determined by the shortest distance between the muscle reaction force, $\mathbf{F}_m$, and the location of the elbow's fulcrum, $\mathbf{x}_f$ and can to be determined by basic geometry. To determine the vector-resulting lever arm, firstly, a plane is defined using a support point and a vector that is normal to the plane. The fulcrum of the elbow is chosen to be the support point while the normal direction of the plane is defined by the muscle reaction force. Secondly, a line is defined by a point and a vector defining its orientation. The line's support point is the point of action of the muscle's insertion face while the orientation of the line is also defined by the muscle reaction force. As the plane and the line are perpendicular to each other, they always have one intersection which can be derived by:

$$\mathbf{l}_m = \frac{(\mathbf{x}_f - \mathbf{x}_m) \times \mathbf{F}_m}{\|\mathbf{F}_m\|}\,, \qquad \forall \quad m = \{T, B\}\,. \tag{7.2}$$

Herein, $\mathbf{l}_m$ is the vector representing the shortest distance between the line and the elbow fulcrum, $\mathbf{x}_f$.

The resulting scalar-valued moment can be determined by the norm of the vector product or by the product of the norm of the lever arm and the force, as the two vectors are, by definition, perpendicular to each other, i.e.

$$M_m = \|\mathbf{l}_m \times \mathbf{F}_m\| = \|\mathbf{l}_m\| \cdot \|\mathbf{F}_m\| = l_m \cdot F_m\,, \qquad \forall \quad m = \{T, B\}\,. \tag{7.3}$$

Herein, the scalar-valued lever arm and muscle reaction force are defined by $l_m = \|\mathbf{l}_m\|$ and $F_m = \|\mathbf{F}_m\|$, respectively.

To investigate the static equilibrium of the upper limb, the equivalent static system is introduced (Figure 7.7a). A free body diagram of the forearm is defined by the black

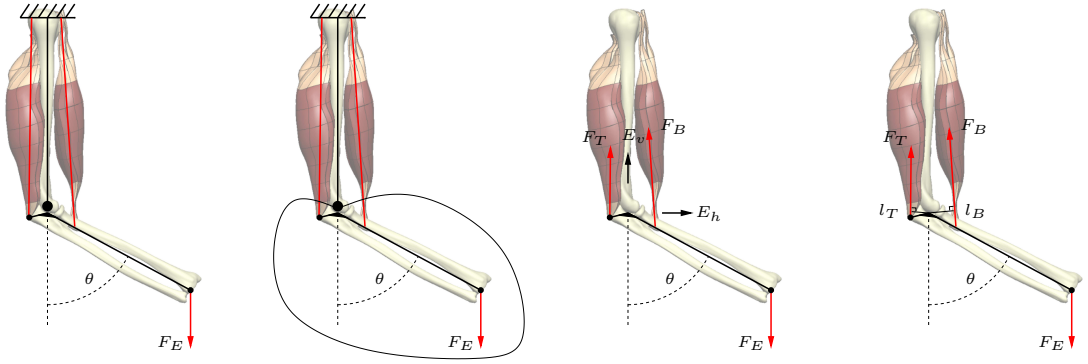

(a) *equivalent static system* **(b)** *area of interest* **(c)** *acting forces on the forearm* **(d)** *moment equilibrium of the forearm*

Figure 7.7: *Employing the Upper Limb Model to introduce the equivalent static system of the forearm. By defining a free body diagram of the forearm, a static equilibrium can be defined for the forearm. The rotation axis is positioned in the fulcrum and points upwards, perpendicular to the paper normal.*

loop indicated in Figure 7.7b. The acting forces (Figure 7.7c) are the muscle reaction forces, the elbow contact forces, and an arbitrarily chosen external load F_E, which acts as a perturbing moment to the system. A moment balance can be formulated for the forearm with respect to the fulcrum of the elbow. Hereby, one obtains

$$F_T(\theta, \alpha_T)\, l_T(\theta) + F_E\, l_E(\theta) - F_B(\theta, \alpha_B)\, l_B(\theta) = 0\,, \tag{7.4}$$

where F_T and F_B are the muscle reaction forces determined by the FE simulation, which are a function of the elbow flexion angle and the muscle activation, F_E is the introduced external force and l_m are the scalar-valued lever arms for triceps, biceps and the external force, respectively.

As the lever arms of the elbow contact forces E_h and E_v are zero, those forces do not have an impact on the defined momentum balance.

A penalty contact formulation is incorporated as introduced in Chapter 6. Since there is no direct contact between the muscles, the only contact occurring is between each muscle tissue and the rigid humerus.

The muscle forces are determined by the continuum mechanical model. The evolving system of partial differential equations is solved using the finite element software package CMISS as it was introduced in the previous chapters. The muscle reaction forces are determined by summing the nodal residuals (cf. Section 5.2) at the muscle's end cross-section.

7.4 Calculation Example of the Upper Limb

To develop a feeling for the magnitude of the acting muscle forces a simple arithmetic sample calculation is derived in the this section.

Imagine the following scenario: A dead load acting in the hand is sought to extend the forearm. The biceps brachii is the only flexor muscle acting on the upper limb. The equivalent static system is depicted in Figure 7.8.

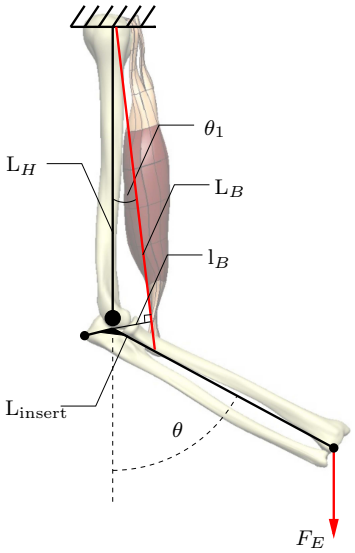

Figure 7.8: *Upper Limb Model calculation example: adapting* Figure *7.7a by neglecting triceps brachii and introducing* θ_1 *and* L_{insert}*, the distance between the elbow's fulcrum and the biceps' insertion.*

The length of the humerus is $L_H = 32\,\text{cm}$, the distance from the elbow's fulcrum to the location where the external force acts is $L_E = 34\,\text{cm}$, and the distance from the elbow's fulcrum to the biceps's insertion is $L_{\text{insert}} = 9\,\text{cm}$. In addition to the elbow angle, an angle θ_1 is needed to define the angle between the humerus and the biceps. Further, it is assumed that the biceps is attached to the top end of the humerus. The necessary muscle force to maintain the arm in a static position can be calculated using trigonometry and algebra.

The first step is to sum the moments applied to the fulcrum of the elbow, where the only two acting forces are the biceps muscle force and the external dead load:

$$F_E\, l_E(\theta) - F_B(\theta)\, l_B(\theta) = 0 \tag{7.5}$$

$$\Leftrightarrow F_B(\theta) = \frac{F_E\, l_E(\theta)}{l_B(\theta)}\,. \tag{7.6}$$

With the help of the law of cosines, the biceps's length can be determined to:

$$L_B = \sqrt{L_H^2 + L_{\text{insert}}^2 + 2\, L_H\, L_{\text{insert}}\, \cos(180° - \theta)}\,. \tag{7.7}$$

Using Equation (7.1) to determine the lever arm:

$$l_B = \frac{\partial L_B}{\partial \theta} = \frac{L_H\, L_{\text{insert}}\, \sin(\theta)}{2\, L_B}\,. \tag{7.8}$$

Alternatively, l_B can be geometrically deduced by:

$$l_B = L_H \sin(\theta_1), \tag{7.9}$$

$$L_{\text{insert}} = \sqrt{L_H^2 + L_B^2 + 2\, L_H\, L_B \cos(180° - \theta_1)}, \tag{7.10}$$

$$\sin(\theta_1) = \sqrt{1 - \cos^2(\theta_1)}, \tag{7.11}$$

where (7.10) is the law of cosines and (7.11) is the *Pythagor*ean identity. By inserting (7.10) and (7.11) into (7.9) the lever arm can be deduced to:

$$l_B = \frac{1}{2\, L_B} \sqrt{4\, L_H^2\, L_B^2 - (L_H^2 + L_B^2 - L_{\text{insert}}^2)^2}. \tag{7.12}$$

The graphs of Equation (7.8) and (7.12) coincide and demonstrate the applicability of Equation (7.1).

Having a closer look at the derived relations, one can see that the influence of the ratio of the lever arms, $l_B(\theta)$ and $l_E(\theta)$, on the demanded muscle force. Furthermore, the resulting muscle force increases linearly with the dead load, cf. Figure 7.9, which depicts the result for Equation (7.5) for a dead load of $1\,\text{kg} \leq F \leq 12\,\text{kg}$ and an elbow angle ranging from $0° \leq \theta \leq 180°$. Due to the lever class 3, where the effort lies between the fulcrum and the load, the demand in biceps force is quite high and can be up to several hundred *Newton*. The advantage of such an order of fulcrum, load, and effort is, as already mentioned in Section 2.4.5, that fast movements are feasible.

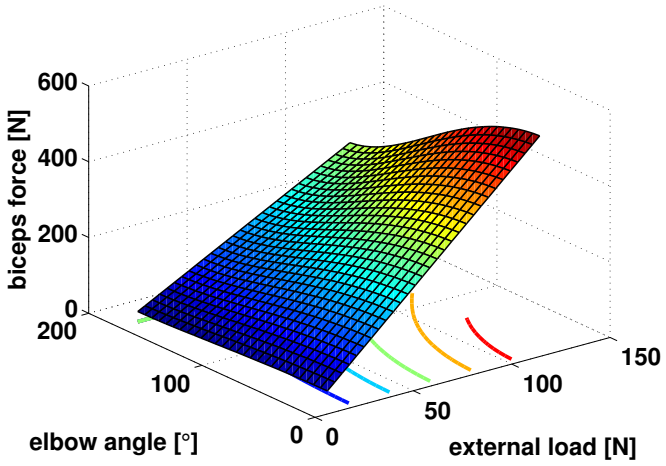

Figure 7.9: *The biceps force resulting from the analytical investigation:* Equation *(7.5) is evaluated for an external dead weight ranging from 1 to 12 kg and an elbow angle* $0° < \theta < 180°$.

Further information can be found in standard biomechanics books as, for example, in Tözeren (2000) or Freivalds (2011).

7.5 Muscle Force Dyname

In contrast to rigid-body models, continuum-mechanical models have the advantage of spatially distributing mechanical measures. Hence, a continuum-mechanical model can

be applied to investigate the muscle force flowing through the muscle from origin to insertion. The muscle force's orientation changes due to muscle-intrinsic phenomena such as the complex geometry, local distributed material parameters, or the fibre structure.

In the modelling world, skeletal muscle are very often attached to bones at one point or node. In nature, the attachment areas can be small or wide. This feature, might be represented in continuum-mechanical approaches by distributing the muscle attachment site to several nodes of the bone. Yet in rigid-body systems, geometrically everything is reduced to points and lines. To compensate, very often big muscles are represented by several representatives to improve the representation of the muscle length and lever arm.

An alternative idea might be, when continuum-mechanical approaches are coupled to rigid-body systems. Continuum-mechanical models might improve the solution of rigid-body systems by returning altered muscle reaction force directions or lever arms to rigid-body models.

Therefore, when skeletal muscle forces need to be exchanged to other frameworks or insert to the bone, mostly one vectorial force value and on point of action is used to apply the muscle force. Due to the finite element discretisation, a traction vector can be defined for each muscle's node at an muscle insertion face. Hence, to transfer the force from one of the muscle's end face to a particular location of the bone, either one from all possible face nodes needs to be selected or one needs to come up with a method to reduce the end face traction vectors to a unified value acting at a particular location.

This section presents a method to investigate the mechanical state of the muscle by condensing the nodal traction vectors at a face to a unique pair of three-dimensional vectors.

To investigate the mechanical behaviour of the muscle, the screw theory, introduced by Ball (1900), is used. A screw is a pair of three-dimensional vectors, such as linear and angular velocities for kinematical systems and forces and torques for statical systems. The mechanical description of a statical system, where an arbitrary amount of forces act upon, can be described after choosing a point of reference by only a resulting force and a resulting torque, i.e. by

$$\boldsymbol{\mathcal{W}} = \sum_{i}^{N_F} \{\mathbf{F}_i, \mathbf{F}_i \times \mathbf{l}_{\mathbf{F}_i}\} = \{\mathbf{F}, \mathbf{M}_{\mathbf{X}}\}\,, \quad i = 1, .., N_F\,. \tag{7.13}$$

Herein, $\boldsymbol{\mathcal{W}}$ is the force wrench which is the screw for a static situation, $\mathbf{F}_i, i \in \mathbb{N}$ is one of N_F forces acting on the system, $\mathbf{l}_{\mathbf{F}_i}$ is the lever arm of the acting force i from its original point of action to the chosen reference point, $\mathbf{F}$ is the resulting force, and $\mathbf{M}_{\mathbf{X}}$ is the resulting moment with respect to an arbitrary location $\mathbf{x}$.

The reason for obtaining besides the resulting force also a resulting moment is the fact that when the point of action of the force is relocated other than along its line of action, the force generates a torque. Hence, for uniting N_F forces in an arbitrary point of action, the perpendicular distance $\mathbf{l}_i$ and the magnitude of the force define the emerging torque for each force $\mathbf{F}_i$.

Assuming one considers the proximal or distal face, denoted by Γ as depicted in Figure 7.10a, the IVBP determines the stress at Γ. The resulting force, $\mathbf{F}$, on the cross-

sectional area, Γ_{int}, is determined by

$$\mathbf{F} = \int_{\Gamma_{int}} \mathbf{S}\ \mathbf{n}_0 \, \mathrm{d}A = \int_{\Gamma_{int}} \mathbf{t}_0 \ \mathrm{d}A \,. \tag{7.14}$$

The location where the wrench is defined is somehow arbitrary. Yet, often times the surface's barycentre, $\mathbf{x}_s$ is chosen as point of action. The resulting moment with respect to the barycentre of the face is obtained by

$$\mathbf{M}_{\mathbf{X}_s} = \int_{\Gamma_{int}} (\mathbf{x}_{\mathbf{X}_i} - \mathbf{x}_s) \times \mathbf{t}_0 \ \mathrm{d}A \,, \tag{7.15}$$

where $\mathbf{x}_{\mathbf{X}_i}$ is the coordinate of any node at the surface Γ and $\mathrm{d}A$ is the referential cross-sectional area of interface Γ_{int}.

Numerically, the integral is computed by summing the nodal traction vectors at the interface using a *Riemann* sum. The nodal traction vectors are determined by multiplying the stress, determined at the *Gauss* points, by their appropriate face increment $\mathrm{d}A$ and reduces to Equation (7.13).

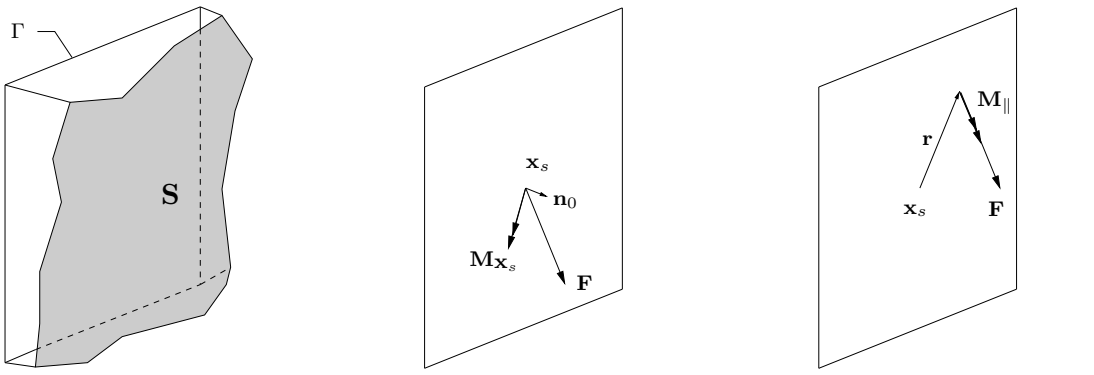

(a) *surface stress distribution* **(b)** *resulting screw* $\boldsymbol{\mathcal{W}}$ **(c)** *replacing the point of action*

Figure 7.10: *The force wrench is establish in two steps: First the surface stress distribution is unified at the surface's barycentre,* $\mathbf{x}_s$ *to a resulting force,* $\mathbf{F}$*, and moment,* $\mathbf{M}_{\mathbf{X}_s}$*. Second, the initial point of action,* $\mathbf{x}_s$*, can be relocated by* $\mathbf{r}$ *such that total moment* $\mathbf{M}$ *can be minimised by getting rid of* $\mathbf{M}_{\perp}$*. Thereby,* $\mathbf{M}$ *is reduced to* $\mathbf{M}_{\|}$*, which is the torsional fraction of the moment.*

The advantage of the force wrench is that the resulting moment can be reduced by relocating the force's point of action. Therefor, first the moment $\mathbf{M}_{\mathbf{x}_s}$ is split into two components: $\mathbf{M}_{\|}$ and $\mathbf{M}_{\perp}$. The component $\mathbf{M}_{\|}$ points parallel, while $\mathbf{M}_{\perp}$ points perpendicular to $\mathbf{F}$. Hence,

$$\mathbf{M}_{\mathbf{x}_s} = \mathbf{M}_{\|} + \mathbf{M}_{\perp} \,. \tag{7.16}$$

The point of action of $\mathbf{F}$ can be moved along a direction $\mathbf{r} = \mathbf{F} \times \mathbf{M}_{\mathbf{x}_s}$ such that $\mathbf{M}_\perp \equiv \mathbf{0}$. In order to determine the length of $\mathbf{r}$, Equation (7.16) is multiplied by $\mathbf{F}$.

$$\mathbf{M}_{\mathbf{x}_s} \times \mathbf{F} = \underbrace{\mathbf{M}_\parallel \times \mathbf{F}}_{=\mathbf{0}} + \mathbf{M}_\perp \times \mathbf{F} \,. \tag{7.17}$$

By inserting $\mathbf{M}_\perp = \mathbf{r} \times \mathbf{F}$ in (7.17), one obtains

$$\mathbf{M}_{\mathbf{x}_s} \times \mathbf{F} = (\mathbf{r} \times \mathbf{F}) \times \mathbf{F} \,. \tag{7.18}$$

as $\mathbf{r} \perp \mathbf{F}$. By using index notation and the permutation symbol for the cross product, Equation (7.17) can be rearranged to

$$\mathbf{M}_{\mathbf{x}_s} \times \mathbf{F} = \mathbf{F}^2\,\mathbf{r} - \mathbf{F}\underbrace{(\,\mathbf{r} \cdot \mathbf{F}\,)}_{=\mathbf{0}} \,. \tag{7.19}$$

Herein, $\mathbf{F}^2$ denotes the inner product of the force, i.e. $\mathbf{F}^2 = \mathbf{F} \cdot \mathbf{F}$. Equation (7.19) can be solved for $\mathbf{r}$ and yields

$$\mathbf{r} = \frac{\mathbf{M}_{\mathbf{x}_s} \times \mathbf{F}}{\mathbf{F}^2} \,. \tag{7.20}$$

At the eccentric point of action, the original wrench $\{\mathbf{F},\, \mathbf{M}_{\mathbf{x}_s}\}$ reduces to $\{\mathbf{F},\, \mathbf{M}_\parallel\}$, i.e. the resulting moment is just the torsional part of the initial resulting moment. The bending part is taken care by the new eccentric location of the forces point of action.

Note, this procedure applies not only for the proximal or distal attachment area, but for any cut within the muscle. By cutting the muscle perpendicular to its longitudinal axis at arbitrary locations along that line, a sequence of resulting forces on these incremental cross-sections along the longitudinal axis of the muscle can be considered as a line of action (Sprenger et al., 2011). The sequential location of the point of action and the magnitude and orientation of the resulting force can be used to investigate the mechanical exposure of the muscle as it is depicted for example in Figure 10.1.

8 Multi-Muscle Forward-Dynamics Simulations

This section introduces three possible options for continuum-mechanical based musculoskeletal system simulations.

In the first option, the muscle activations for the two acting muscles of the Upper Limb Model are prescribed. The purpose of these simulations is to investigate whether the musculoskeletal system, as it is defined, can find a static equilibrium.

In the second option, a forward-inverse model is employed to convert experimental data into muscle activations. The evaluated muscle activations are applied to the Upper Limb Model and the resulting equilibrium position is compared to the isometric trials of the experiments.

The last option sketches how volumetric skeletal muscle simulations can be coupled with rigid-body simulations.

8.1 Prescribed Forward-Dynamics Model

Equation (7.4) describes the moment equilibrium of the elbow:

$$F_T(\theta,\, \alpha_T)\; l_T(\theta) + F_E\; l_E(\theta) - F_B(\theta,\, \alpha_B)\; l_B(\theta) = 0\,. \tag{8.1}$$

The equation includes four DoFs: the elbow angle, θ, the muscle activations, α_T and α_B, and the external force, F_E. The muscle reaction forces are a result of the finite element simulation and depend on the elbow angle and the muscle activation. They are determined by summing the nodal residuals at the muscle insertion cross-section and taking the absolute value of the resulting reaction force.

To investigate the Upper Limb Model, a two step procedure is installed. Within the first step, a reference solution is determined. This solution will be used to observe, if a perturbed initial state can find the correct equilibrium condition.

To find a static equilibrium position of the upper limb in the first step, three out of four DoFs are prescribed: $\theta = \bar{\theta}$, $\alpha_T = \bar{\alpha}_T$, and $\alpha_B = \bar{\alpha}_B$. Note, the exerted muscle forces are completely based on the results of the finite element simulations. By rearranging (8.1), an external force $\bar{F}$ can be determined, where the system is in equilibrium:

$$\bar{F_E}(\bar{\theta}) = \frac{F_B(\bar{\theta},\, \bar{\alpha}_B)\; l_B(\bar{\theta}) - F_T(\bar{\theta},\, \bar{\alpha}_T)\; l_T(\bar{\theta})}{l_E(\bar{\theta})}\,. \tag{8.2}$$

The four DoFs, marked with $\bar{(\cdot)}$, build the reference solution. Subsequently, the system is disturbed by starting the convergence process by prescribing one of the four DoF with a different value as the ones prescribed in the reference. Only one DoF is changed, as for two DoFs an optimisation problem would have to be solved.

After the perturbation, it is determined whether the Upper Limb Model can converge towards the known equilibrium state. If Equation (8.1) is not in equilibrium, the moment equilibrium exhibits a residual moment,

$$F_T(\theta,\, \alpha_T)\; l_T(\theta) + F_E\; l_E(\theta) - F_B(\theta,\, \alpha_B)\; l_B(\theta) = M\,. \tag{8.3}$$

Convergence is monitored by considering the resulting elbow moment as the system error. Depending on the perturbed DoF, the investigation of the Upper Limb Model can be categorised into three scenarios: (i) position-driven, (ii) activation-driven, or (iii) force-driven forward model.

8.1.1 Position-Driven Scenario

In case of the position-driven scenario, a desired angle θ – and therefore the position of the forearm – is predescribed and one seeks the level of activation for one muscle, e.g. the level of activation of the triceps. Prescribing all DoFs and a random $\alpha_T \in [0, 1]$ leads to a non-equilibrium (unless α_T has accidentally be chosen such the system would be in equilibrium) and produces a resulting elbow moment.

For the solution process, in which the external force, the biceps' level of activation, and the elbow angle are kept constant, a *Newton-Raphson*-iteration scheme is employed to determine an improved approximation for the triceps' level of activation, i.e. the next iteration step $i + 1$ is given by

$$\alpha_T^{(i+1)} = \alpha_T^{(i)} - \frac{M^{(i)}}{\frac{\partial M^{(i)}}{\partial \alpha_T}}\,, \quad \text{i=1,...,n}\,, \tag{8.4}$$

where, $n \in \mathbb{N}$. For practical purposes, the *Newton*'s method is replaced with the secant method, i.e. by approximating $\frac{\partial M^{(i)}}{\partial \alpha_T}$ with the differential quotient

$$\frac{\partial M^{(i)}}{\partial \alpha_T} \approx \frac{\Delta M^{(i)}}{\Delta \alpha_T^{(i)}} = \frac{M^{(i)} - M^{(i-1)}}{\alpha_T^{(i)} - \alpha_T^{(i-1)}} = \frac{F_T^{(i)} - F_T^{(i-1)}}{\alpha_T^{(i)} - \alpha_T^{(i-1)}}\,. \tag{8.5}$$

The last part of the equation is only valid for determining the lever arm with the tendon displacement method. If the vector resulting lever arm is used, the lever arm also depends on the muscle activation and cannot be cancelled from the ratio.

To determine the differential quotient for $i = 1$, the residual moement is set to greater than the ε, the muscle activation, $\alpha_T^{(0)}$, is defined as $\alpha_T^{(0)} = |\alpha_T^{(1)} - 0.01|$. Note, $F_T^{(0)}$ needs to be computed based on $\alpha_T^{(0)}$.

8.1.2 Activation-Driven Scenario

For the activation-driven scenario, one seeks the resulting elbow angle for prescribed activation levels and a given external force. Based on an initial $\theta^{(0)}$, Equation (8.4) is adapted in the following way

$$\theta^{(i+1)} = \theta^{(i)} - \frac{M^{(i)}}{\frac{\partial M^{(i)}}{\partial \theta}}\,, \quad \text{i=1,...,n}\,, \tag{8.6}$$

to determine the next iterate for the elbow angle. Should $\theta^{(i+1)}$ be outside the physiological range, i.e. $\theta^{(i+1)} < 10^\circ$ or $\theta^{(i+1)} > 150^\circ$, then the minimal or maximal physiological range value are prescribed. Like before, $\frac{\partial M^{(i)}}{\partial \theta}$ is approximated by the following differential quotient,

$$\frac{\partial M^{(i)}}{\partial \theta} \approx \frac{\Delta M^{(i)}}{\Delta \theta^{(i)}} = \frac{M^{(i)} - M^{(i-1)}}{\theta^{(i)} - \theta^{(i-1)}} \,. \tag{8.7}$$

For $i = 0$, the initial elbow angle is chosen to be $\theta^{(0)} = 60^\circ$. The angle $\theta^{(1)}$ represents an initial starting value to the iteration procedure. Note, the angle should be within the physiological range of $10^\circ \leq \theta \leq 150^\circ$.

8.1.3 Force-Driven Scenario

By prescribing realistic time-dependent constraints, one needs to solve at each time step the equilibrium equations to obtain depending on the chosen scenario a movement in a forward-dynamics fashion.

Within the force-driven scenario, one assumes that the level of activation for the biceps and triceps remains constant. Now varying the external force applied at the distal end of the forearm results in a change of elbow angle, i.e. an increase in F leads to a forearm extension while a decrease in F leads the forearm to flex. The change of elbow angle resulting due to such a force perturbation can be solved in the same way as described in the two previous sections.

Note that this methodology of achieving forward-dynamics simulations through one of these scenarios only holds for relative slow movements, in particular for movements, in which the inertia terms can be neglected.

8.1.4 Simulation Procedure

All the above described iterations aim to find the moment equilibrium of the system. The system is considered to be in equilibrium, if the remaining moment of the system after the iteration is less than ε, i.e.,

$$|M^{(i+1)}| \leq \varepsilon \,, \qquad \text{with} \quad \varepsilon > 0 \,. \tag{8.8}$$

Unless otherwise stated, ε is chosen to be 10^{-9} Nmm.

Figure 8.1 shows the solution procedure of the simulation for the activation-driven procedure. As explained in Section 7.2, the muscle needs to be brought into the initial position at $\theta_0 = 60^\circ$. Hence, in the prestretch phase (green box), the muscle simulations are started simultaneously and the muscles are pre-stretched to their initial position at $\theta_0 = 60^\circ$.

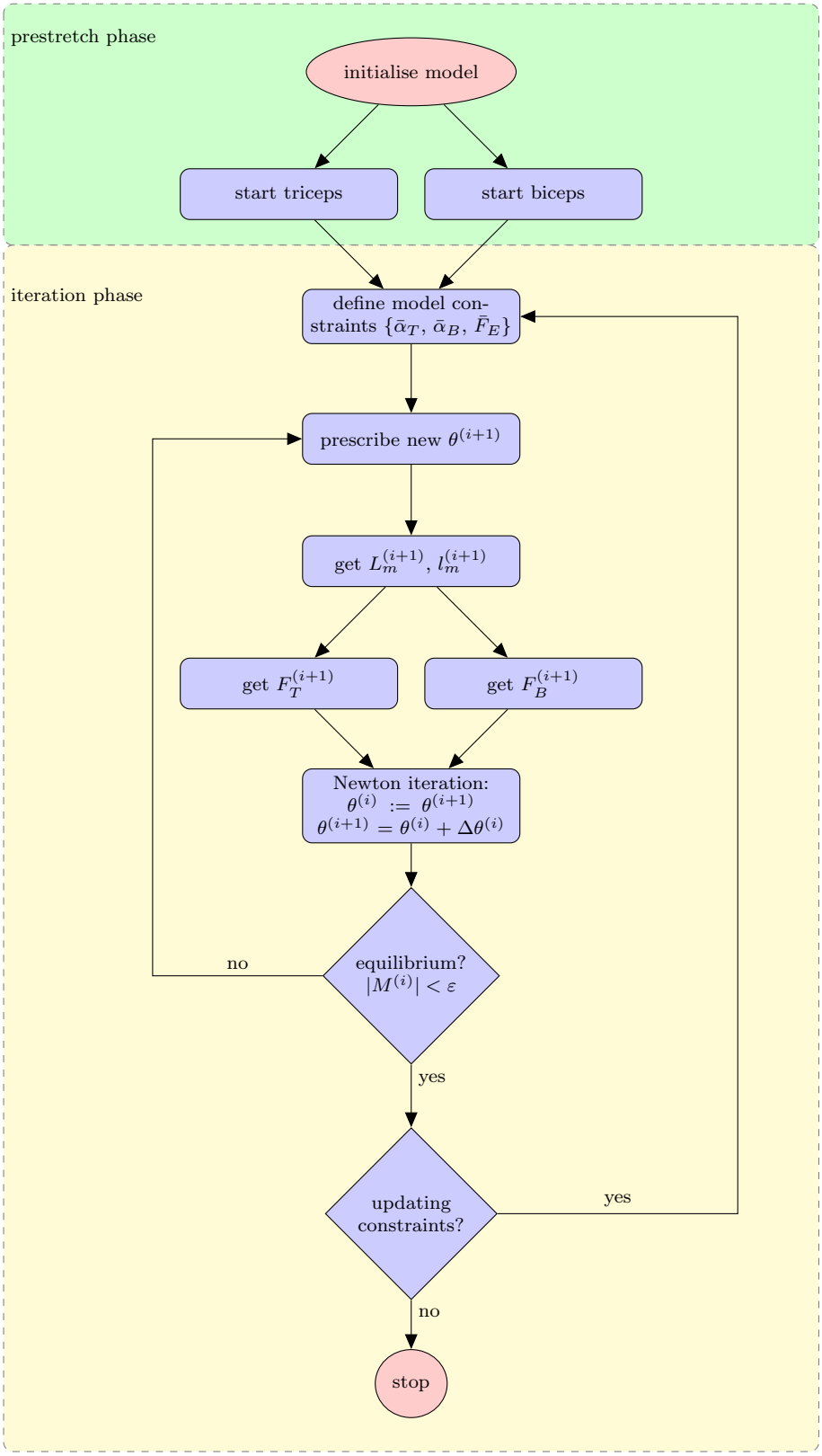

Figure 8.1: *Iteration flow chart of the Upper Limb Model: The green box indicates the prestretch phase of the skeletal muscles. Within the iteration process, the elbow angle changes until the muscle reaction forces converges to a static equilibrium. The variation of θ is employed by a secant method.*

When they reach that position, the iteration phase (yellow box) starts. Herein, the algorithm prescribes the constraints defined in one of the three introduced scenarios. When the new position is set, first the new boundary conditions (consisting of the location of the muscles' distal end and its activation) for the FE simulations need to be determined; i.e. by evaluating the muscle length to the given elbow angle, the FE boundary conditions can be prescribed. After both FE simulations converged, the muscle reaction forces are determined by exploiting the FE simulations' results. Additionally, the lever arms are determined by either evaluating the tendon-displacement method or the vector-resulting lever arm method. After the moment balance is solved and the successive iteration state, $(i+1)$, is determined, within the equilibrium rhombus it is checked whether the equilibrium criterion is met.

If it is met, it is checked whether a second updating criteria is defined. By defining e.g. successive different constraints a successive change of the position can be established, see Section 8.1.3. For example, for a constant external load F_E and a constant biceps activation α_B and a successively increasing α_T, the forearm has to extend. For a successively increasing α_B while α_T and F_E are constant, the forearm has to flex. The same can be observed for successively increasing or decreasing the external load F, while keeping the muscle activations fixed.

8.2 EMG-driven Forward-Dynamics Model: Employing a Forward-Inverse Model

The wide field of biomechanics has at least one thing in common: the problem validating their models, see e.g. Lewandowski (1982) or Anderson et al. (2007). In Section 9.2, it is shown, that the presented model of the upper limb is able to find an equilibrium position. Yet, the question whether that position is realistic or not is still not touched.

Together with experimental data, the forward-inverse model, introduced by Buchanan et al. (2004), is employed to solve the muscle redundancy problem, to extract muscle activation (see Section 9.3.1), and last but not least to compare the Upper Limb Model model results to the one determined by the forward-inverse model (see Section 9.3.2). The model was provided by courtesy of Prof. David Lloyd, who gave the author the chance to get acquainted to the model and perform the experiments at the Gold Coast Campus of the Musculoskeletal Research Group, Griffith Health Institute at the Griffith University in Australia.

In Figure 8.6, the forward-inverse model is depicted in its hole complexity trying to sketch the interaction of the different parts. The different parts of the model are:

- conducting experiments for collecting EMG data, position data, and elbow joint torques,
- processing the raw data,
- developing an upper limb OpenSim model, that provides the rigid-body and muscle kinematics, see Holzbaur et al. (2005),
- muscle-tendon-complex model to determine the muscle forces, and
- the solution processes for
  - the forward-dynamics rigid-body model,

- the inverse-dynamics rigid-body model, and
- the optimisation process that minimises the least squared difference to calibrate model parameters.

Each part includes its own complexities and by coupling them to a single unit, a rather complex framework develops. Within the next sections, each step will be introduced.

8.2.1 Experiments

The first step was the process of acquiring experimental data. Therefore, a voluntary subject, age 31, height 182 cm, and weight 75 kg, was sat in a BIODEX MULTI-JOINT SYSTEM-PRO, Figure 8.2. The Biodex is a dynamometer used, for example, in sports and orthopaedics medicine, in pediatric medicine, and in neurorehabilitation. The measurement device can perform isometric, isokinetic and isotonic motions. The experimental setup was adjusted from the machine's manual, Biodex Medical Systems (2006), for *measuring the elbow: extension/flexion (seated)*. The most important attributes for the best position, while performing the subscribed motions, are: that the elbow joint is in the same centre of rotation as the shaft of the Biodex, that the subject sits straight and the trunk is as tightly fixed as possible to the chair, and that the forearm is in a supinated position to increase the potential impact of the biceps brachii on flexing the elbow. The Biodex acquires torque in [Nm], velocity in [deg/s], and position data in [deg] at a rate of 2000 Hz. For calibrating purposes, the range of motion was defined as well as the reference angle.

Figure 8.2: *Biodex's dynameter System 4 Pro^{TM} is used for measuring the elbow torque. Source: Biodex Medical Systems (2006)*

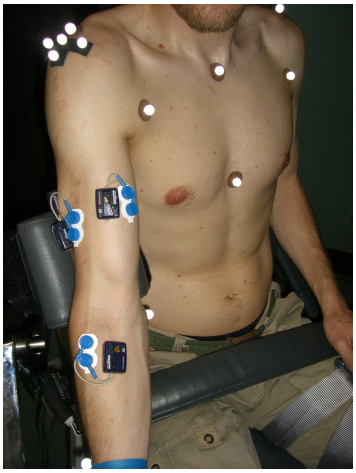

Figure 8.3: *The subject is positioned on the Biodex. Wireless EMG dipole electrodes are fixated on right arm of the subject. Furthermore, positioning markers are placed on his upper body.*

The muscle activation was measured using a wireless, dipole-surface electrode placed on triceps brachii, brachialis, brachioradialis, and biceps brachii on four different channels. The distance between the dipole electrodes is 2 cm. The motion data were recorded with a rate of 1000 Hz using a Vicon motion capturing system. The white spheres depicted in Figure 8.3 are the strongly reflective position markers for the Vicon motion capturing

system. The Vicon system consists of, in this case, 5 cameras, which were positioned around the subject. The system is calibrated, using a special tripod, to identify the subject uniquely in space. Additionally, before the data acquisition, the subjects' markers were registered and named to make them uniquely recognisable by the system later in the trials.

Three different classes of trials were conducted: isometric, isokinetic and passive. The passive motion was done for both calibrating the Biodex system as well as for determining the passive muscle forces. Three different isokinetic trials were done with a velocity of 60, 120, and 180 deg/s. In case of the isometric trials, the elbow angle was positioned by the Biodex from 1° to 140° in 10° steps. Each trial was conducted for 50% and 100% effort. Between each trial, a break of about 2-3 min was met to give the muscle a chance to recover.

8.2.2 EMG-Data Processing

The purpose of using EMG signals is to solve the muscle redundancy problem by processing the EMG signals to determine muscle activation. A raw EMG-signal train is a voltage that is both negative and positive in a scale of [mV]. The muscle activation is by definition a value $\alpha \in [0, 1]$. Therefore, the raw data need to be normalised, smoothed, and filtered in order to be used to estimate the muscle force.

The transformation of EMG data into muscle activation is not trivial. In the literature, there is a wide range of methods, ranging from assuming a linear transformation of EMG to muscle activation to a complex multi-step nonlinear relation transforming EMG to muscle activation. The procedure introduced in Buchanan et al. (2004), is one of the more complex ones, including various nonlinear relations. In the following section, these steps will be briefly introduced.

The process of transforming raw data into the muscle activation is indicated in Figure 8.3 by the big black arrow pointing from the raw EMG signal to the processed signal train. It is possible to classify the EMG signal processing into three steps:

- EMG processing,
- activation dynamics, and
- relating neural activation to muscle activation.

The first step of processing the raw EMG data is rather standard and starts with removing a DC offset or low frequency noise. This is accomplished by a fourth-order *Butterworth* high-pass filter of 6 Hz. After high pass filtering, the data need to be rectified. The next important step is to normalise the signal train. The question how to normalise is controversially debated. Commonly, the maximum voluntary contraction (MVC) is chosen for normalisation. Yet, it is also not clear, how to define MVC: at maximal force for each muscle, at maximal joint torque, under dynamic or static conditions, or at the peak of its force-length curve? Here, for each muscle the maximal rectified value is chosen to normalise the signal train. This leads to the fact that the final activation is within zero and one, see Kendall et al. (1993). The last step in signal processing is to remove high-frequency noise. Naturally, skeletal muscles act as a low-pass filter, i.e. the resulting force is smooth and high-frequency signals passing through the muscle initialise slower

processes such as calcium dynamics which, in turn, lead to force production. Therefore, frequencies higher than 3-10 Hz (here 6 Hz are chosen), typically are cut off.

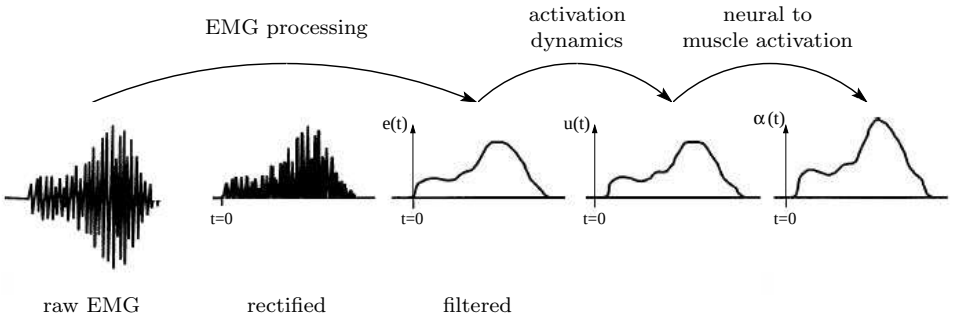

Figure 8.4: *Processing EMG signal trains to neural activation, adapted from Buchanan et al. (2004).*

The question whether normalised, rectified, and filtered EMG signals, $e(t)$, are appropriate to be directly related to skeletal muscle force can be answered positively under static conditions. In general, however, it takes time for the action potential to spread along the bulk of the muscle and to initiate the muscle contraction processes. Therefore, the second step, which transforms EMG signals $e(t)$ into neural activation $u(t)$, is called activation dynamics.

Zajac (1989) introduced a first-order linear ordinary differential equation to address the transformation of $e(t)$ to $u(t)$. Buchanan et al. (2004) presented a second-order linear differential equation which is superior for discrete data. The discretisation is conducted by using a backward *Euler* scheme. Hereby, the second-order linear differential equation can be approximated by the following discrete equation,

$$u(t_n) = \beta_1\, e(t_n - d) - \beta_2\, u(t_{n-1}) - \beta_3\, u(t_{n-2})\,. \tag{8.9}$$

Equation (8.9) is a recursive formulation, because $u(t)$ depends on the current EMG signal and two history neural activation values. Furthermore, d is the electromechanical delay. It is in the range of 10-100 ms (Corcos et al. (1992)) and reflect the time delay due to the calcium transport across the sarcolemma and the time delay the muscle needs to polarise and contract to macroscopically produce force. The three parameters β_1, β_2, and β_3 are coefficients that define the second-order activation dynamics. The three parameters are not independent from each other but have the following relations

$$\begin{aligned} \beta_1 &= \gamma_1 + \gamma_2\,, \\ \beta_2 &= \gamma_1 \cdot \gamma_2\,, \\ |\gamma_1| &< 1\,, \\ |\gamma_2| &< 1\,, \\ 1 &= \beta_1 - \beta_2 - \beta_3\,. \end{aligned} \tag{8.10}$$

When the parameters γ_1 and γ_2 are known, the relations can be solved for β_1, β_2, and β_3. The constraints given by (8.10) are the result of the requirement that Equation (8.9) produces a stable relation. If the relations, which are used as a filter, are not stable, the resulting neural activation oscillates at the natural frequency of the filter or even diverges

towards infinity. For further details, the reader is referred to Buchanan et al. (2004) and the citations therein.

The third and last transformation step is performed by converting the neural activation, $u(t)$, into muscle activation $\alpha(t)$. Heckathorne and Childress (1981), Woods and Bigland-Ritchie (1983), or Zuniga and Simons (1969) have shown that isometric EMG, and therefore neural activation, is not necessary linearly related to muscle force. Remembering Figure 2.10, one stimulation pulse will create a twitch response and multiple stimulation pulses will cause multiple twitch responses. If the stimulation frequency increases, the twitches will start to fuse and the average force produced by the motor unit will steadily increase. However, for a further increasing stimulation frequency, the behaviour of the resulting curve converges more and more towards the tetanus behaviour, where no further force can be produced by the muscle even if the stimulation frequency increases. This phenomena leads to the conclusion, that there is a nonlinear relationship between stimulation frequency and force for single motor units. Which is not covered by the neural activation. This nonlinearity can further be increased by other factors such as the size effect, where small motor units are recruited at low intensity levels and larger ones at higher intensity levels. Manal and Buchanan (2003) came up with a logarithmic function relating $u(t)$ to $\alpha(t)$ including four parameters. Manal et al. (2002) and Lloyd and Besier (2003b) further extended the before mentioned relation by an alternative formulation which yields adequate solutions:

$$\alpha(t) = \frac{e^{A\,u(t)} - 1}{e^{A} - 1}\,, \tag{8.11}$$

where A is the shape factor, condensing the information of the four parameters to a single value. The shape factor's value is ranging from $[-3, 0)$, where for the $\lim_{A\to 0}$ the relation simplifies to a linear relation and for $A = -3$ the relation behaves highly exponential.

The values for d, γ_1, γ_2 and A are preset to $d = 40\,\text{ms}$, $\gamma_1 = \gamma_2 = 0.5$, and $A = -0.1$, respectively, cf. Buchanan et al. (2004). During the calibration process, these values are adapted to find a minimum in the objective function, see Section 8.2.5.

8.2.3 Muscle-Tendon-Complex Mechanics

Within forward-dynamics and inverse-dynamics rigid-body models, the muscle contraction dynamics is determined by a *Hill*-type muscle model.

The muscle model of Figure 1.1b, like the muscle model employed here, consists of a contractile element, a parallel elastic element, and a serial elastic element to describe the tendon. One significant advantage of this type of muscle model is that it is, in most cases, governed by one ODE for the resulting MTC force

$$F_m(t) = f(\dot{L}_m)\, f(L_m)\, \alpha_m(t) F_m^0\,. \tag{8.12}$$

Herein, $f(\dot{L}_m)$ is the dimensionless force-velocity relation, $f(L_m)$ is the dimensionless force-length relation, and F_m^0 is the maximum isometric muscle force. The force-velocity relation, $f(v_m)$, is an adaption of Hill (1938) and is similar to Figure 1.1a. The difference of this muscle fibre represented by a 3-element-*Hill*-type muscle model to the one of Figure 1.1b is that CE and SEE are connected in parallel and that both are connected in series to SEE.

The active part of the force-length relation used within the forward-inverse model is also based on Figure 2.10 and is similar to the one introduced for the continuum-mechanical model in Section 4.3. Yet, the force-length relation is defined by a cubic spline interpolating the curve developed by Gordon et al. (1966). Additionally, the relation is coupled to the muscle activation, i.e. the force is not scaled linearly with the activation but following a nonlinear relation introduced by Lloyd and Besier (2003a). The passive part of the force-length relation is an exponential dimensionless relation.

The tendon or SEE is also modelled using a dimensionless relation which is defined for three different regions. In the first region, the tendon force is zero when the tendon strain is less than the tendon slack length. Above that, it is similar as introduced in Section 2.4.4. In the second region, a quadratic relation reflects the toe region. In the third region, a linear relation is used with an elastic modulus of 1.200 MPa.

The muscle fibre pennation angle is included by using a trigonometric relation. It determines the time dependent pennation angle by scaling the constant measured angle by a ratio of optimal-to-current fibre length.

For more details, the reader is referred to Buchanan et al. (2004) and the references therein.

8.2.4 OpenSim Model

One of the most important input parameters for the muscle-tendon complex (MTC) mechanics is the MTC-length. The MTC kinematics, including MTC length and the thereof derived MTC lever arm, is provided by the open-source multi-body system model *arm26*, which is introduced by Holzbaur et al. (2005) and includes anatomical observations by Murray et al. (1995). The *arm26*-model is adapted (simplified) by the author to an appropriate degree. In the here discussed version, it consists of seven MTCs (three triceps brachii heads, two biceps brachii heads, brachialis, and brachioradialis) and a single free movable joint, the elbow joint, which is considered to be a hinge joint. The lever arms are derived using the tendon displacement method, see the derivation of Equation (7.1).

OpenSim is a rather advanced multi-body system model which also includes bone geometries. This has an impact on

(i) muscle-tendon complexes: They do not follow straight lines, from their origin to their insertion, but are reorientated on defined wrapping surfaces and via-points.

(ii) joint motions: They are not represented as idealised joints but allow complex motion patterns of moving joint centres, leading to rotational and translational DoFs.

(iii) lever arms: They depend on the complex geometric muscle kinematics as, for example, the wrapping surfaces, the via-points and the changing centre of rotation.

For each included muscle, several via-points and wrapping surfaces are defined. More details on the model itself can be found on the SimTK web page[1]. There, the model can also be downloaded.

In order to make the rigid-body system model applicable for the forward-inverse model, the out-of-the box OpenSim model needs to be scaled to fit the size of the subject. Therefore, landmark markers are defined within the model, see Figure 8.5. Those markers

[1] `https://simtk.org/home/up-ext-model`

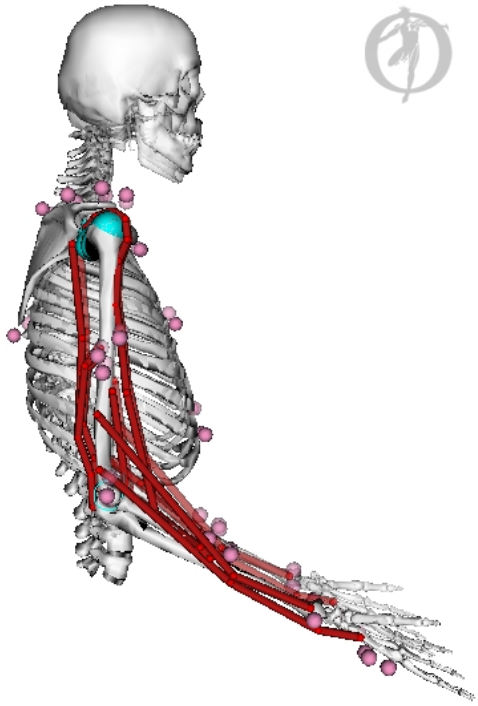

Figure 8.5: *OpenSim multi-body model. The model consists of seven muscles (three for the triceps, two for the biceps and one for the brachialis and brachioradialis). The cyan coloured objects are wrapping surfaces and the magenta spheres are representing the position of the markers. The original model is transparent while the scaled subject-specified model is opaque.*

are positioned at the same predefined locations on the subject and specified using the Vicon camera system and software. Within the OpenSim software package, it was possible to scale the initial model to the subject, yielding a subject specific rigid-body model.

8.2.5 Forward-Inverse-Dynamics Model and Optimisation

The heart of the forward-inverse model is the interaction of the forward- and the inverse-dynamics models by optimisation.

The forward-dynamics rigid-body model receives as model inputs the muscle activations from the EMG-data processing, the kinematics from OpenSim, and the muscle contraction dynamics to determine the MTC reaction forces, to finally determine the joint torques, M_{FD}; in this case the elbow torque, see Figure 8.6.

On the other hand, the inverse-dynamics rigid-body model uses the experimental torque data to determine the joint torque to solve the rigid-body model. The mechanical rigid-body chain for solving the elbow torque is trivial as the elbow torque is measured directly with the Biodex. Hence, the inverse-dynamics model reduces to the measured elbow torques, M_{ID}.

Within the optimisation process, the sum of the squared difference of the elbow torques

over all N sample points is minimised, i.e.

$$\min \sum_{i=1}^{N} (M_{FD}^{i} - M_{ID}^{i})^2 \,, \tag{8.13}$$

by adjusting selected model parameters which is indicated in Figure 8.6 by the red arrows. The red arrows point on the activation dynamics and on the MTC model. Within the activation dynamics, as mentioned already in Section 8.2.2, the model parameters are γ_1, γ_2, and A to adjust the resulting muscle activation. Within MTC mechanics, the tendon slack length and the maximal isometric force adjust the resulting muscle force. The material parameters are adjusted plus-minus a selectable variation around the initial value. The optimisation uses an simulated annealing scheme. This scheme is a probabilistic, heuristic optimiser appropriate for a discrete space. The parameters are adjusted within an off-line phase, called calibration.

The number of adjustable parameters should be large enough to fit the experimental torque well, but should not be too large to loose its predictability, cf. Buchanan et al. (2004). Too many adjustable parameters reduce the convincing power of a model and will be suspected to be a mathematical exercise in curve fitting (Heine et al. (2003)).

Once the optimal solution is found for one subject, the trials can be investigated for the distribution of muscle reaction forces acting on a joint.

8.3 Multi-Body Simulation-Driven Multi-Muscle Model

A further approach to achieve forward-dynamics simulations using three-dimensional continuum-mechanical skeletal muscle models is by using the idea of nested models. Nested models in this context are two models that are compatible and describe the same physical effects using different underlying physical models. For example, in skeletal muscle mechanics, the force exerted by a skeletal muscle can be either modelled by a one-dimensional Hill-type skeletal muscle model or by a (chemo-electro) mechanical three-dimensional continuum model. Both models describe, up to the respective modelling error, the same physical phenomena, e.g. muscle force exertion. However, the musculoskeletal system appealing to one-dimensional Hill-type muscle models can be solved much faster than the system that appeals to three-dimensional continuum-mechanical based skeletal muscle models.

Hence, it is possible to use the computational less expensive model to solve the forward-dynamics problem to obtain for a particular point in time the respective activation levels and joint positions. The less expensive model is indicated by the blue box in Figure 8.7 and is called a discrete model. These are mostly rigid-body models. Then, in a subsequent step, the levels of activation and the position of the joint are used as input to the continuum-mechanical model (yellow box) as initial guess for the continuum-mechanical model. Now presuming, that the modelling error of the one-dimensional skeletal muscle model is small, one should have an excellent initial guess for the continuum-mechanical model.

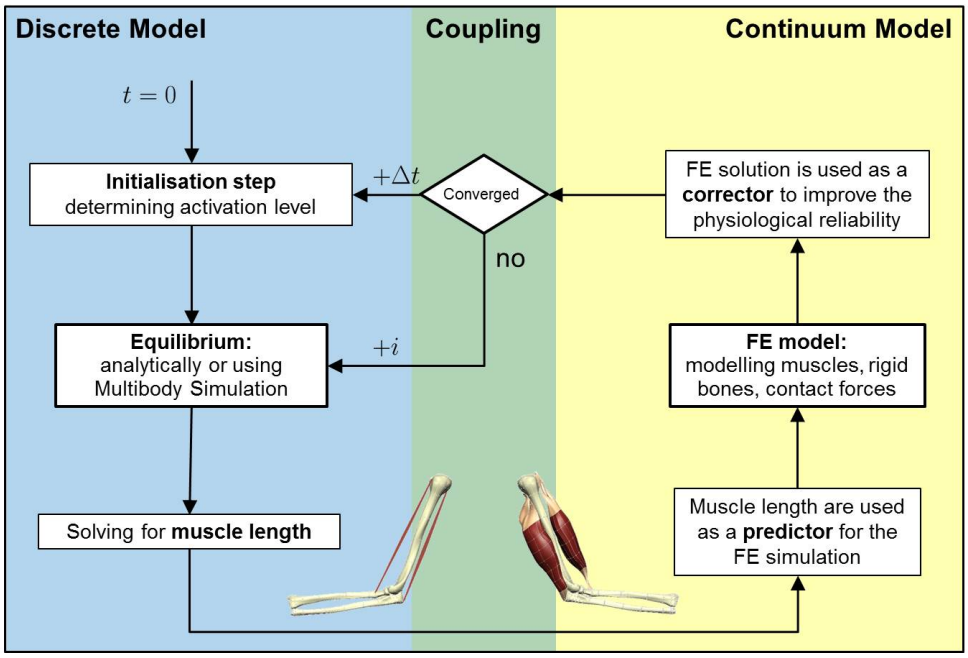

Figure 8.7: *A possible approach to facilitate forward-dynamics simulation of musculoskeletal systems by coupling two modelling approaches. The left, blue box is representing rigid-body simulations, which are mostly used for the discrete modelling approach, the opposing right, yellow box, represents the continuum-mechanical modelling approach. Both models are linked to each other by a coupling procedure, indicated by the green overlapping area.*

As a result, just like with a close initial guess for *Newton*s method (Kim et al., 2006), one would expect only a few iterations of the more complex model, e.g. the musculoskeletal system appealing to continuum-mechanical models, in order to achieve (moment) equilibrium.

Presuming that the modelling error is smaller for the musculoskeletal system model appealing to continuum-mechanical muscle models than for the system appealing to one-dimensional models, one could also subsequently compute the resulting muscle forces (including their magnitude and orientation), the varying lever arm, and small changes in the elbow angle determined within the three-dimensional skeletal muscle models to update the respective quantities within the discrete model.

As long as there is a significant difference between the two modelling approaches, the two models will iterate until common quantities can be found. If that should be the case, the next time step can proceed using again the discrete model as a predictor.

A possible tool to exchange data between the to models could be a web-service linking the simulation packages from both modelling worlds. Hereby, both simulation tools only need slight adjustments, while the effort and brain work is in the web-service. A wrapper, the web-service, and an orchestration application are needed to make the green box work exchanging the necessary data while keeping track of the simulation.

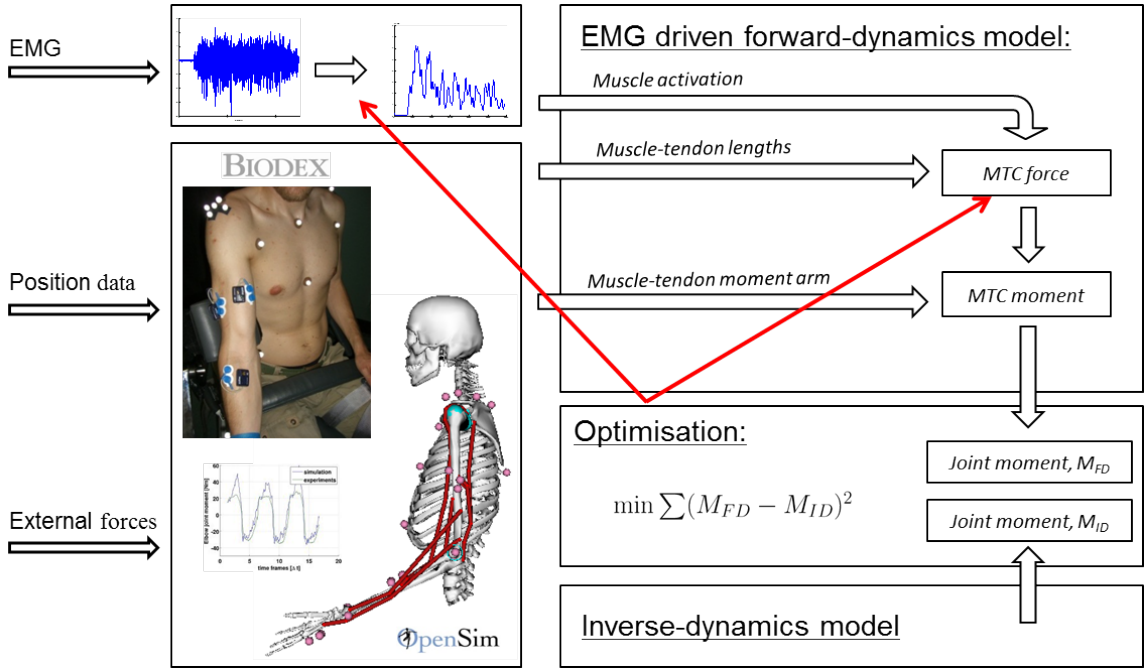

Figure 8.6: *The forward-inverse model consist of several components. The three arrays on the left represent the data acquisition, consisting of measuring the muscle activity with EMG electrodes, the arm position using either a motion capturing system or the intrinsic position data of the Biodex, and the elbow torque using the Biodex.*
The top left box represents the activation dynamics, i.e. , the data processing from raw EMG to muscle activation.
The bottom left box provides the OpenSim model to prepare the kinematics of the musculoskeletal system and the Biodex data precessing.
The top right box represents the forward-dynamics rigid-body model including the muscle contraction dynamics. Herein, the model inputs are the muscle activation from the activation dynamics and the muscle kinematics from the OpenSim model. The resulting rigid-body model is solved for the time sequence of the elbow moment.
The bottom right box represents the inverse-dynamics model. In general, the model inputs are muscle activation, the muscle kinematics, and the external loads to solve the resulting rigid-body system for the joint moment. In this particularly simple example, the inverse-dynamics model is not required, as the elbow moment can be measured directly.
The middle-right box is representing the optimisation procedure. The inputs are the time transient elbow moment from both, the forward-dynamics and inverse-dynamics, model and computes the summed least square which are reduced by adapting parameters of the activation dynamics and the muscle contraction dynamics, which is indicated by the red arrow.

9 Results

9.1 Single Muscle

Hill-type muscles are popular within MBS investigating the kinetics of movements. In contrast finite element simulations can produce spatially varying output. This property offers the possibility to investigate heterogeneities, diseases, or disorders. Using this advantage, the next two sections investigate for the rigid-tendon model and for the muscle-tendon-complex model the advantages of the continuum-mechanical approach.

First the ability of the continuum-mechanical muscles to reproduce the upper limbs range of motion is investigated. Therefore, no moment equilibrium is determined. The muscles are not coupled to the static equilibrium system. The muscles are tested independently from each other if the full range of mechanical states, using the constraints given by the Upper Limb Model, is achievable.

The motion of the forearm is mainly define by the position of the insertion points of the skeletal muscles. For the finite element simulation, the forearm position imposes the boundary constraints at the distal end of the skeletal muscles. The solution space is restricted by:

- the forearm's range of motion, which is $10° \leq \theta \leq 150°$,
- the level of muscle activation, which is $0 \leq \alpha \leq 1$, and
- whether the effects of contact are considered or not.

To test the full range of motion, increments of $\Delta\theta = 1°$ and $\Delta\alpha = 0.1$ are tested. In a first model evolution step, the tendons are assumed to be rigid, see Section 7.2.1. The corresponding muscle tissue constitutive law is based on the formulation given in Section 4.3.

In a second evolution step, the whole muscle-tendon complex is considered to be deformable as introduced in Section 4.4 and Section 7.2.2.

9.1.1 Rigid-Tendon Model

In this section, the model assumptions of Section 7.2.1 are employed. Herein, only muscle tissue is considered to be an elastic material. The tendons are visualised but not considered as an elastic material. Their shape and length is included for visualising purposes only.

The results are split into four sections: visualising the raising arm movement, the resulting muscle reaction forces, the fibre stretch distribution, and the results from the force wrench.

Raising Arm

Figure 9.1 visualises the upper limb for $\theta = 10°, 45°, 80°, 115°$, and $150°$. It might be worth repeating, that the shown situations do not represent physiological situations, as the elbow moment balance is not considered. The figures show two muscles at the same joint position with the same (random) activation. The top row shows the resulting deformations for the fully activated muscles while considering contact. The bottom row shows the difference between considering contact and not considering contact.

To compare the different FE solutions in the bottom row of Figure 9.1, a new version of the *Green-Lagrange*an strain tensor is introduced. The *Green-Lagrange*an strain tensor of (3.13) compares the current configuration with the reference configuration. Therefore, the current nodal coordinates without contact are defined as the "new" reference configuration whereas the current nodal coordinates with contact are defined as the "new" actual configuration. With these two new configurations at hand, a "new version" of the deformation gradient, as introduced in Equation (3.4), a "new version" of the right *Cauchy-Green* deformation tensor, as introduced in Equation (3.10), and finally a "new version" of the *Green-Lagrange*an strain tensor, $\mathbf{E}^{\text{new}}$, can be determined. To be able to plot a strain tensor, either a special tensor visualisation procedure is needed or the tensor needs to be converted to a scalar value (Wünsche, 1999). Following the idea of Zhe et al. (2004), who defined an effective strain measure similar to the *von Mises* stress, the following effective strain is introduced

$$E_{\text{eff}} = \frac{2}{3}\sqrt{\frac{1}{2}\left[(E_{11}^{\text{new}} - E_{22}^{\text{new}})^2 + (E_{22}^{\text{new}} - E_{33}^{\text{new}})^2 + (E_{11}^{\text{new}} - E_{33}^{\text{new}})^2 + \right.} \\ \left. + \frac{3}{2}\left(E_{12}^{\text{new}\,2} + E_{23}^{\text{new}\,2} + E_{13}^{\text{new}\,2}\right)\right]. \tag{9.1}$$

For a fully extended forearm, the biceps is slender and slim whereas the triceps is short and compact, see Figure 9.1a. In Figure 9.1e where the forearm is fully flexed, the triceps gets stretched and the biceps becomes bulged. While the Figures 9.1a-9.1e show the shape of the muscle tissue, Figures 9.1f-9.1j highlight the effect of considering contact. The black grid lines represents the FE mesh including contact while the coloured, contoured muscle represents the solution without contact. The contour plot visualises the effective strain – the difference between the two solutions – where red denotes a high deviation (0.5) and blue a small one (0.0). The red arrow at the osteotendinous junction represents the muscle reaction force acting at the point of action determined by the methodology introduced in Section 7.5. Depending on the constraints, the force's offset of the point of action and the deviation of the orientation changes. The length of the arrow is proportional to its absolute value.

For the fully extended forearm, the grid and contour plot deviate for both muscles. The triceps deviates only slightly. But, the triceps' offset from the point of action is, compared to the biceps, already significant. At the proximal or myotendinous junction, both solutions are deviating about 6.0 mm where contact pushed the whole proximal surface posteriorly. This offset reduces proximally and is totally vanished at the distal, posterior junction. Furthermore, at the distal, anterior end of the junction, the muscle is compressed by the humerus by about 3 mm.

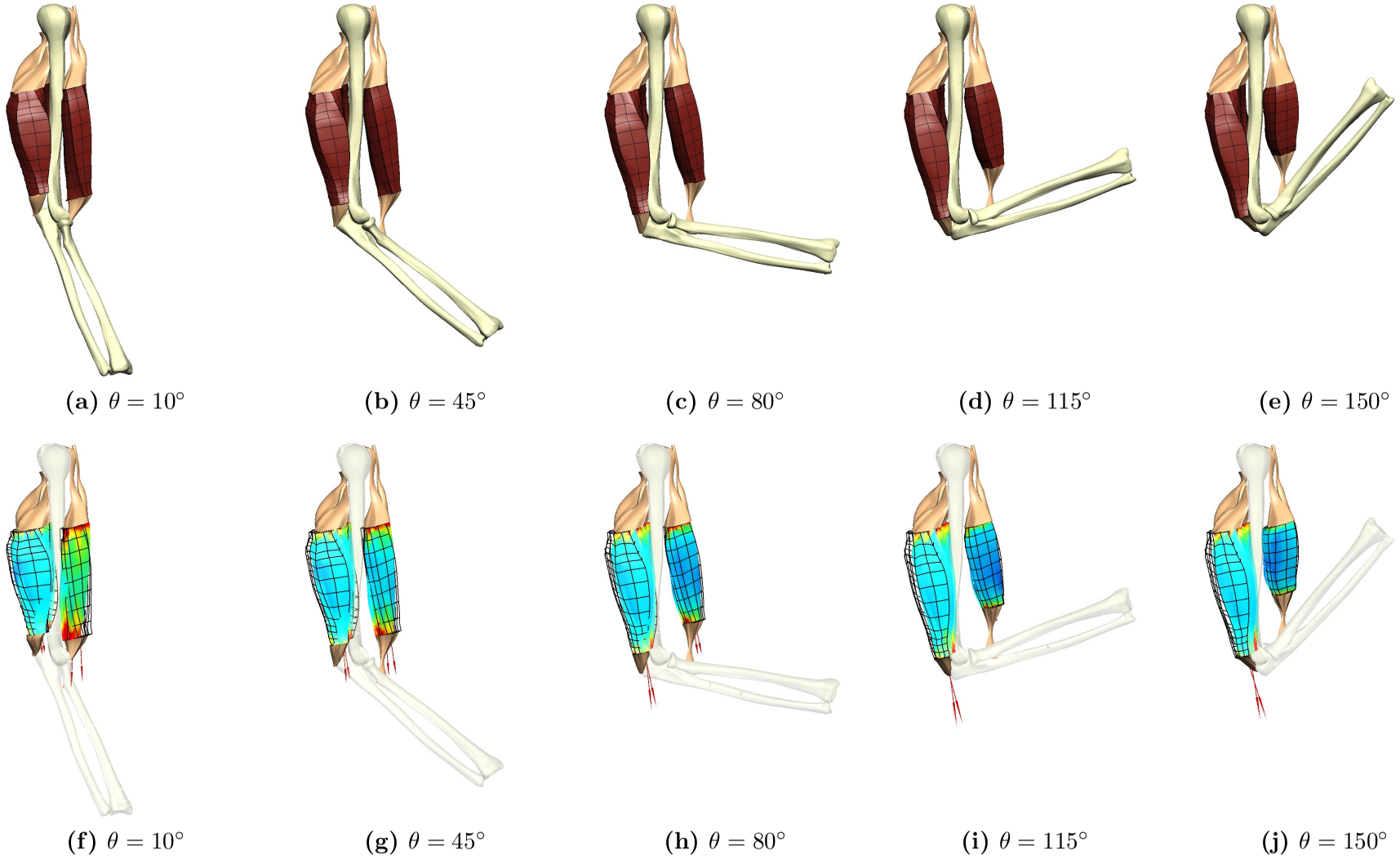

(a) $\theta = 10°$ **(b)** $\theta = 45°$ **(c)** $\theta = 80°$ **(d)** $\theta = 115°$ **(e)** $\theta = 150°$

(f) $\theta = 10°$ **(g)** $\theta = 45°$ **(h)** $\theta = 80°$ **(i)** $\theta = 115°$ **(j)** $\theta = 150°$

Figure 9.1: *The raising arm movement depicted at five distinct positions with fully activated muscles. The upper row depicts the deformation if contact is considered, the lower row depicts the newly defined deformation measure in order to compare the deformations with the effects of contact or without contact. The effective strain is scaled from* $E_{\text{eff}} \in [0, 0.5]$*, where small differences are blue and high are red.*

The biceps' solution deviates more – especially at the proximal end. Here, the solution of the mesh is deviating by 9.1 mm anteriorly and by only 7.0 mm posteriorly. At the proximal end, the offset reverses and the mesh is anteriorly pushed by 8.2 mm . On the other hand, the difference of the biceps' resulting reaction force is small.

For flexing the elbow, the distance between the biceps' belly and the humerus increases and contact does not play a crucial role anymore. It is not until the forearm is fully flexed, when the bulged biceps comes in contact with the humerus. As contact plays only a minor role, the solution's meshes almost coincide. On the other hand, the triceps elongates for flexing the forearm and the difference between the two solutions (with and without contact) increases. The difference is especially large at the distal end, where the triceps is pushed against the humerus. At $\theta = 150°$, the triceps penetrates the humerus by 11.5 mm. With contact, the distal end of the triceps wraps around the distal head of the humerus. Proximal, the surface's offset is 10.9 mm.

Resulting Muscle Reaction Forces

Probably, the most fundamental and straight forward results of the FE simulations are the absolute values of the muscle reaction forces. Considering contact, three different reaction forces can be observed: (i) the resulting muscle reaction force, (ii) the active part of the resulting muscle reaction force, and (iii) the contact force between muscle and bone. The muscle reaction forces depend on the material description, the geometry, the fibre orientation, the contact formulation, and the boundary conditions.

Figure 9.2 depicts the absolute values of the muscle reaction forces for the biceps and triceps brachii for different activation levels throughout the full range of motion. The blue curves always denote the triceps' curve while the biceps' curve are denoted by red curves. The bold curve include the effects of contact whereas the thin curves do not. The highest curve represents the resulting muscle reaction force for a fully activated muscle while the lowest curve represents the purely passive mechanical behaviour of the muscle.

The muscle reaction forces are a result of the finite element simulation and depend on the elbow angle as well as on the muscle activation. They are determined by taking the *Euclid*ean norm after summing the nodal residual vectors at the muscle's osteotendinous junction.

As the activation is proportional to the active stress contribution (see Equation (4.30)), the resulting reaction forces are almost linearly distributed between the curve resulting from the fully activated muscle and the curve resulting form the passive muscle.

For the interpretation of the triceps reaction forces, the muscle length has to considered, cf. Figure 7.6a, as it has the strongest impact. As the muscle insertion point, which defines the fixed nodes, is tracking the motion of the olecranon of the ulna, the muscle insertion point does not only change its length but also does a translational movement. Although the overall triceps length is increasing, the z-component does decrease for flexing the forearm. The z-direction is nearly coinciding with the longitudinal direction of the muscles and hence has the strongest impact on the length of the muscle. The other two direction cause, depending on their magnitude, only a shear-like movement. Hence, the maximum triceps reaction force is reached between 126° and 128° depending on the level of activation. For the fully activated triceps, the maximal value is $F_T(\theta = 128°, \alpha_T = 1.0) = 1026\,\mathrm{N}$, while the maximal value for the purely passive behaviour is $T(128°, 0.0) = 365\,\mathrm{N}$.

As the biceps is the antagonist of the triceps, its length changes in the opposite direction.

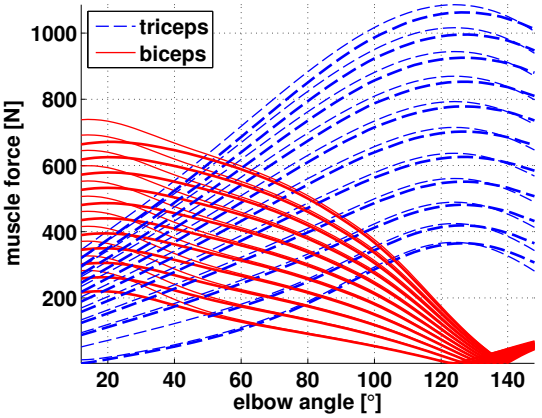

Figure 9.2: *The muscle reaction forces for triceps and biceps brachii for activations* $\alpha = 0.1\,i$ *with* $i = 0..10$. *The lowest curve is determined by* $\alpha = 0$ *and the highest by* $\alpha = 1$. *The aim to prestretch the muscles such that no compression occurs is not achieved for the biceps brachii.*

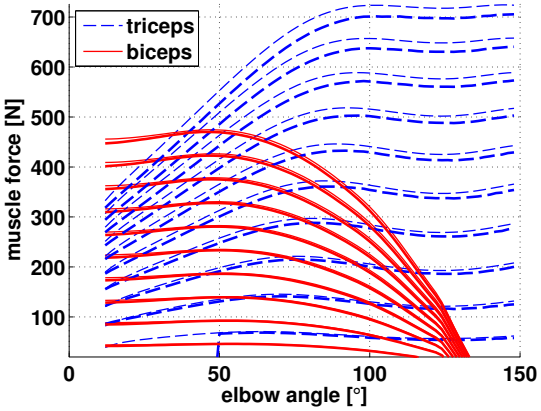

Figure 9.3: *The active part of the muscle reaction forces is determined by subtracting the passive muscle reaction force from the muscle reaction forces for* $\alpha = 0.1\,i$ *with* $i = 1..10$

After reaching the peak at $\theta = 20°$, the biceps' resulting curve is monotonically decreasing, as the length of the biceps is decreasing, see Figure 7.6b. Unfortunately, due to numerical issues, the biceps' prestretch could not be chosen such that no compressive force is required for the whole range of motion. Hence, the resulting curves have depending on the degree of activation a kink at $\theta \approx 130°$. The biceps reaction force reaches its maximal force values for $F_B(\theta = 22°, \alpha_B = 1.0) = 671.2\,\mathrm{N}$ and $F_B(18°, 0.0) = 220.1\,\mathrm{N}$. For the triceps, the influence of contact on the reaction force is close to a constant offset of about 30 N. At $\theta \approx 130°$, the difference between the solutions reduces and, depending on the activation, also changes the effect, i.e. the solution including contact is larger than the solution without contact. For the biceps, contact has a stronger influence on the reaction force at $\theta < 50°$. The difference is maximal with 74.6 N at $\theta = 10°$.

The purely active force contribution of a muscle is obtained by subtracting the passive muscle force from the reaction force where the level of activation is larger than one. The resulting force is depicted in Figure 9.3.

The maximal active triceps forces is $F_T^{\mathrm{act}}(100°, 1.0) = 723.4\,\mathrm{N}$. After an elbow angle of about 100°, the force remains roughly constant up to $\theta = 150°$. The maximal active biceps force is $F_B^{\mathrm{act}}(46°, 1.0) = 470.1\,\mathrm{N}$, The active biceps force slightly reduces when the biceps is further stretched to its limit at $\theta = 10°$. The influence of the effect of contact are rather small. The muscle reaction forces are only slightly larger if no contact is considered. The reason might be due to numerical issues. If no contact is included, it was necessary to fix more nodes at the osteotendinous junction in all three spatial dimensions. Higher restrictions at the boundary cause higher reaction forces.

Depending on the elbow angle, the contact forces between the muscle and the bone can be significant. Figure 9.14 depicts the normalised exerted muscle forces of the biceps and triceps brachii and its contact forces with respect to the bone. For better comparison, the

exerted muscle forces have been normalised with respect to the maximal exerted muscle force of the respective muscle. Further, the contact force is depicted as a percentage of the exerted muscle force at a particular elbow angle. The normalised forces for the passive muscles are depicted in Figure 9.4a and for the fully activated muscles in Figure 9.4b.

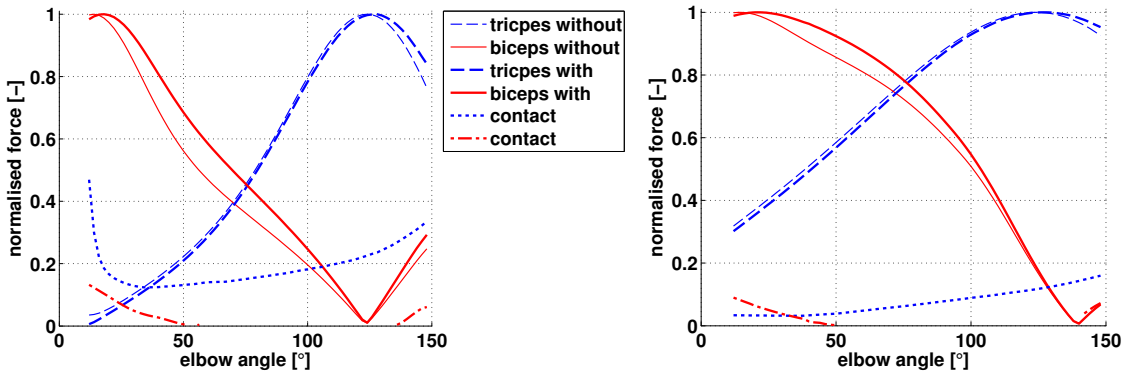

(a) $\alpha = 0$ **(b)** $\alpha = 1$

Figure 9.4: *The exerted muscle force is normalised by the maximal muscle force, whereas the contact force is normalised with muscle reaction force, determined at the same angle and activation, and plotted for the entire range of motion.*

For the passively stretched triceps, the two normalised resulting reaction forces almost coincide throughout the range of movement. The reaction force without contact reduces faster only for $\theta > 126°$. However, the difference is limited to a maximum of 7.6% at $\theta = 150°$. For the biceps, the relative reaction force including contact is always higher. The reason for that is that the curve of the absolute force, which does not include contact, is steeper and hence is divided throughout the range of movement by a larger maximal value. Interestingly, the contact force of the triceps is larger than the one of the biceps, even though the reaction forces for the biceps is deviating more than that of the triceps. For the passively stretched triceps, the contact force reaches its maximum with 47% of the respective triceps reaction force at $\theta = 10°$, reduces to 12.4% at $\theta = 42°$ before it raises again to 33.6% at $\theta = 150°$. For the fully activated triceps, the relative contact force is much smaller and increases from close to zero at $\theta = 10°$ to 16% of the respective triceps reaction force at $\theta = 150°$. The contact force for the biceps are only present for $\theta < 50°$ and $\theta > 140°$. For the passive biceps, the contact force reaches 13.2% at $\theta = 10°$ and 6.1% at $\theta = 150°$. For the fully activated biceps, the contact force reaches 8.4% at $\theta = 10°$ and 7.2% at $\theta = 150°$.

Muscle Fibre Stretch Distribution

Hill-type skeletal muscle models cannot take into account the heterogeneity of the fibre direction within a muscle. Yet, the fibre distribution has a strong influence on the mechanical response of a muscle. Hence, the mechanical state of the muscles can be investigated by having a closer look at the muscle's stretch distribution.

During the solution process of the FE simulation, the fibre stretch is determined at each *Gauss* point. For the tri-quadratic shape functions, 27 *Gauss* points per element

have been used within this work.

To visualise these enormous data, the evaluated fibre stretches are categorised into 0.1-wide spaced bins ranging from $0 \leq \lambda_f \leq 2$ and normalised with respect to the overall number of Gauss points. Independent of the element's volume, each fibre stretch value is considered equal. The resulting fibre stretch distributions are depicted in Figure 9.5. Red denotes a high occurrence (20%) and blue a low occurrence. White space denotes that this event never occured.

The distribution is plotted with the fibre stretch on the abscissa (x-axes) and the elbow flexion angle on the ordinate (y-axis). Hence, a fibre stretch distribution, for a particular elbow position, is obtained by following a horizontal line in each subfigure. The plots show the fibre stretch distribution including the effects of contact. As contact occurs and as the resulting fibre distribution is quite complex, it does not make much sense to compare the fibre stretch distribution with and without contact by comparing figures similar to 9.5.

For the triceps, the muscle is shortest at $\theta = 10°$ and increases its length with increasing θ. The biceps brachii behaves vice versa. It can be said that the fibre distribution is more compact for the short and unactivated muscle. The distribution becomes wider and more complex for increasing muscle length and muscle activation. In general, it can be observed that at $\lambda_f \approx 1.4$ the distribution accumulates. The reason for this phenomenon is that the passive fibre contribution starts to dominate around $\lambda_f = 1.4$ preventing through its stiffness further stretching.

Due to the bipennate fibre architecture of the triceps, a wider stretch spectra can be observed than for the fusiform biceps. The triceps' main accumulation is dominated by the cross-section's centre, where the fibres are orientated along the longitudinal axes of the muscle. When the activation of the triceps increases, the fanning of the fibres increases and the fibre stretch spectra becomes wider and less distinct.

The biceps, depicted on the right side of Figure 9.5, is a fusiform muscle and therefore has a more distinct fibre stretch distribution. When increasing the muscle activation, the contact between the biceps and the humerus increases and, hence bulges. Therefore, the angle between the longitudinal axis of the muscle and the fibre increases. Yet, with increasing muscle length, the distribution becomes wider.

In Figure 9.6, the muscle's mean fibre stretch is determined and depicted for $\alpha = 0.0$, 0.5 and 1.0 vs. θ. The bold curves denote the mean fibre average including contact whereas the thin curves do not include contact.

The triceps' mean fibre stretch ranges from $\lambda_f(\theta = 10°, \alpha_T = 1) = 0.933$ to $\lambda_f(\theta = 124°, \alpha_T = 0) = 1.177$ and each mean curve increases with increasing muscle activation. The biceps' mean fibre stretch covers a larger area, ranging from $\lambda_f(\theta = 150°, \alpha_B = 1) = \lambda_f = 0.87$ to $\lambda_f(\theta = 10°, \alpha_B = 0) = 1.4$ and is close to independent from the muscle activation. While the triceps' mean fibre stretch is increasing with increasing muscle length the biceps' one is not. The reason for this behaviour is due to the bipennate and fusiform fibre architecture.

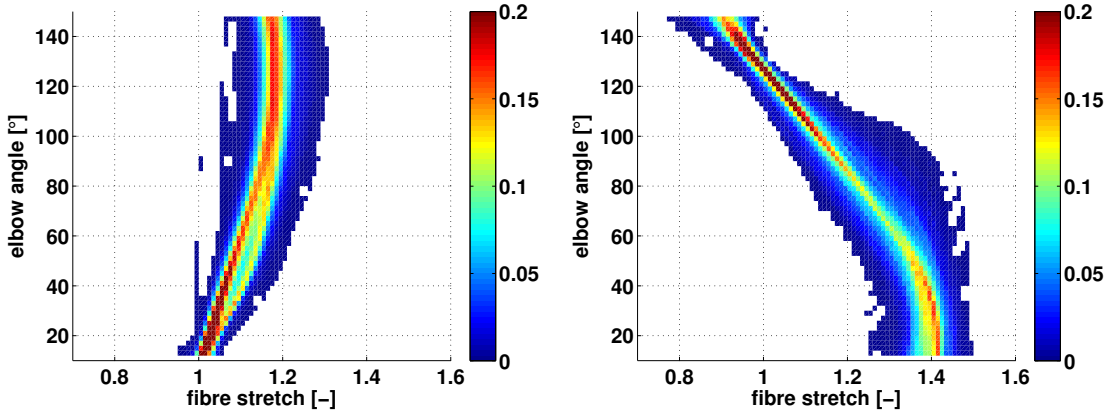

(a) *triceps*, $\alpha = 0.0$ (b) *biceps*, $\alpha = 0.0$

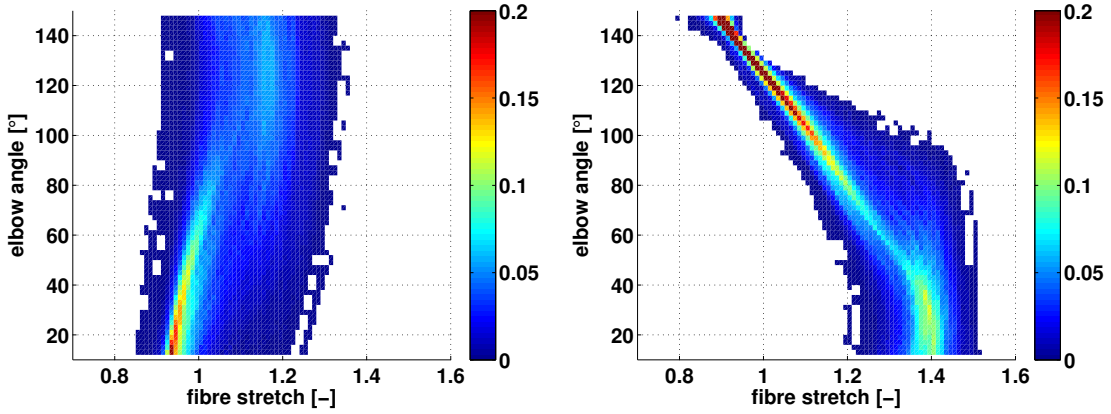

(c) *triceps*, $\alpha = 0.5$ (d) *biceps*, $\alpha = 0.5$

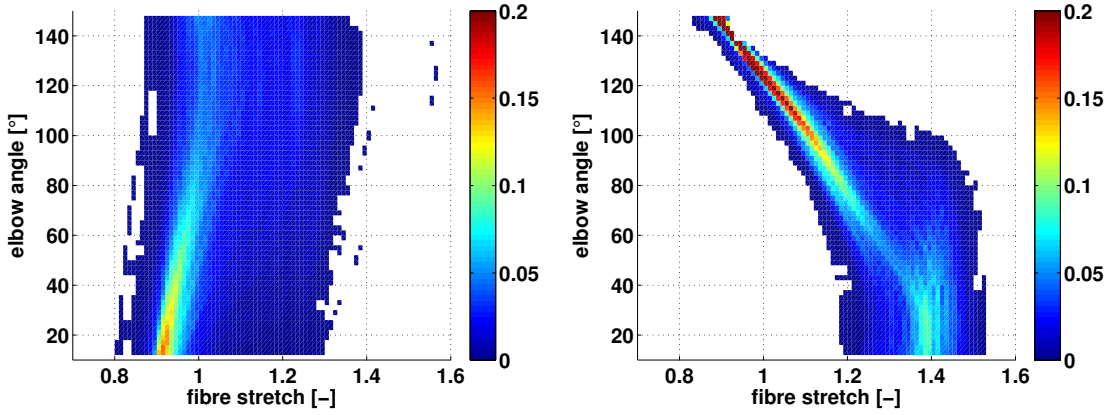

(e) *triceps*, $\alpha = 1.0$ (f) *biceps*, $\alpha = 1.0$

Figure 9.5: *The relative fibre occurrence is plotted vs. the elbow flexion angle θ and the muscle fibre stretch λ_f. The scale for the relative occurrence is limited to 0.2 to resolve also fibres with less frequent fibre stretch occurrences. A horizontal line represents the muscle's fibre distribution for one particular position. Hence the sum of all occurrences on a horizontal line is one.*

The central line along the longitudinal axis of the triceps behaves similar to the fusiform biceps; these fibres are aligned with the longitudinal axis of the muscle and therefore are

directly linked to the muscle length. The triceps fibres in the pennate area can contract as they are not directly coupled to the length of the muscle. When these fibres contract, the shape of the muscle changes and invokes a rotating-like movement. The reason why the biceps covers a wider range is, on the one hand, the larger change in muscle length due to the location of the insertion attachment site and on the other hand due to the fusiform fibre architecture. The influence of the effects of contact on the mean fibre stretch is slightly larger for the triceps but in general rather small.

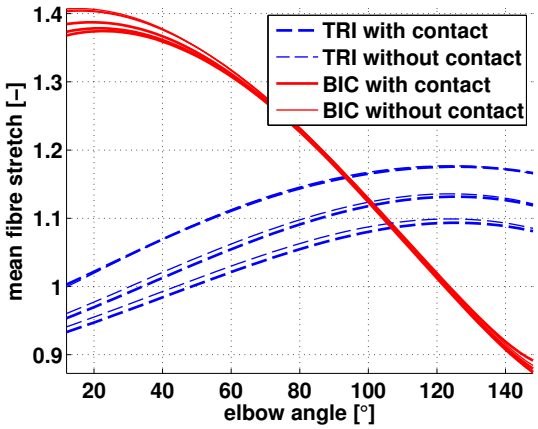

Figure 9.6: *Mean muscle fibre distribution for triceps (red) and biceps (blue) for* $\alpha = 0, 0.5$ *and 1. The curves including contact are bold and the curves without are thin. The triceps is abbreviated by TRI whereas the biceps by BIC. For an increasing level of muscle activation, the mean fibre stretch shortens. Yet, the biceps' mean fibre stretch is rather independent of the activation. The difference of the mean fibre stretch due to contact is not very large.*

Figure 9.6 could lead to the premature conclusion that contact does not have a big influence on the fibres within the continuum. To withdraw that conclusion Figure 9.7 and 9.8 are presented to investigate the impact of the effects of contact on the fibre stretch distribution within the muscles.

For Figure 9.7, the fibre stretch difference between considering the effects of contact and not is evaluated. At each *Gauss* point, the fibre stretch value obtained from simulations that do not consider contact is subtracted from the fibre stretch value of the simulations not considering contact, even though their current position may not coincide. The resulting $\Delta\lambda_f$ is depicted in Figure 9.7 at their actual position when contact is included. The scale of the legends is from blue to red $-3\% \leq \lambda_f \leq 3\%$.

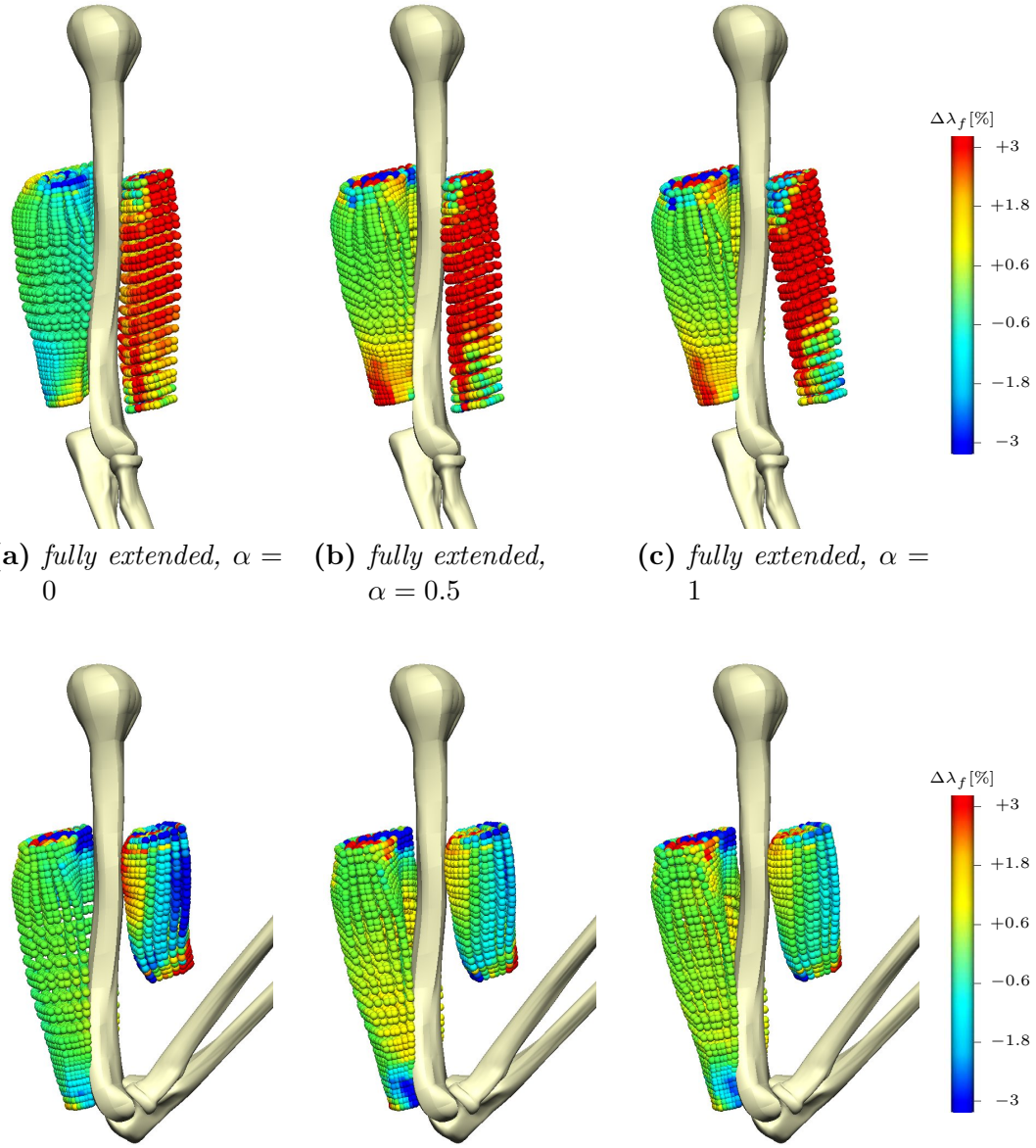

(a) *fully extended,* $\alpha = 0$ **(b)** *fully extended,* $\alpha = 0.5$ **(c)** *fully extended,* $\alpha = 1$

(d) *fully flexed,* $\alpha = 0$ **(e)** *fully flexed,* $\alpha = 0.5$ **(f)** *fully flexed,* $\alpha = 1$

Figure 9.7: *The difference between the fibre stretch resulting from simulations considering contact and not. The difference are computed at each integration point. The fibre stretch difference is negative (blue), when the fibres in simulations are longer without contact and positive (red) when the fibres are longer in simulations with contact.*

For the fully flexed triceps, the fibres close to contact sites at the humerus are shorter while the fibre on the posterior side of the triceps are longer. This effect increases for an increasing level of muscle activation. For the fully extended elbow, the triceps fibres exhibit the same behaviour.

For the fully extended biceps, the difference is quite large. For all three activations, the difference in the fibre stretch is more than 3% at the centre of the belly. Only at the dorsal, distal and at the anterior, proximal end of the biceps, the fibres are longer if no

contact is considered. For the fully flexed elbow, the biceps behaves similar to the triceps, i.e. the fibre difference moves more towards shorter fibre stretches. Yet for the biceps, the difference is more pronounced for the passive muscle.

Figure 9.8 evaluates the spatial difference by classifying the difference of *Gauss*ian fibre stretch of simulations that include contact and such that do not include contact into ten equally spaced groups with $\Delta\lambda_f = 0.5\%$. Hereby, one can investigate how large the deviation of the fibre stretch at the *Gauss* points is and how often it occurs. In the first group, the difference of the fibre stretch between simulations that include contact and such that do not is zero to 0.5%. In the last group, differences larger than 5.0% can be observed.

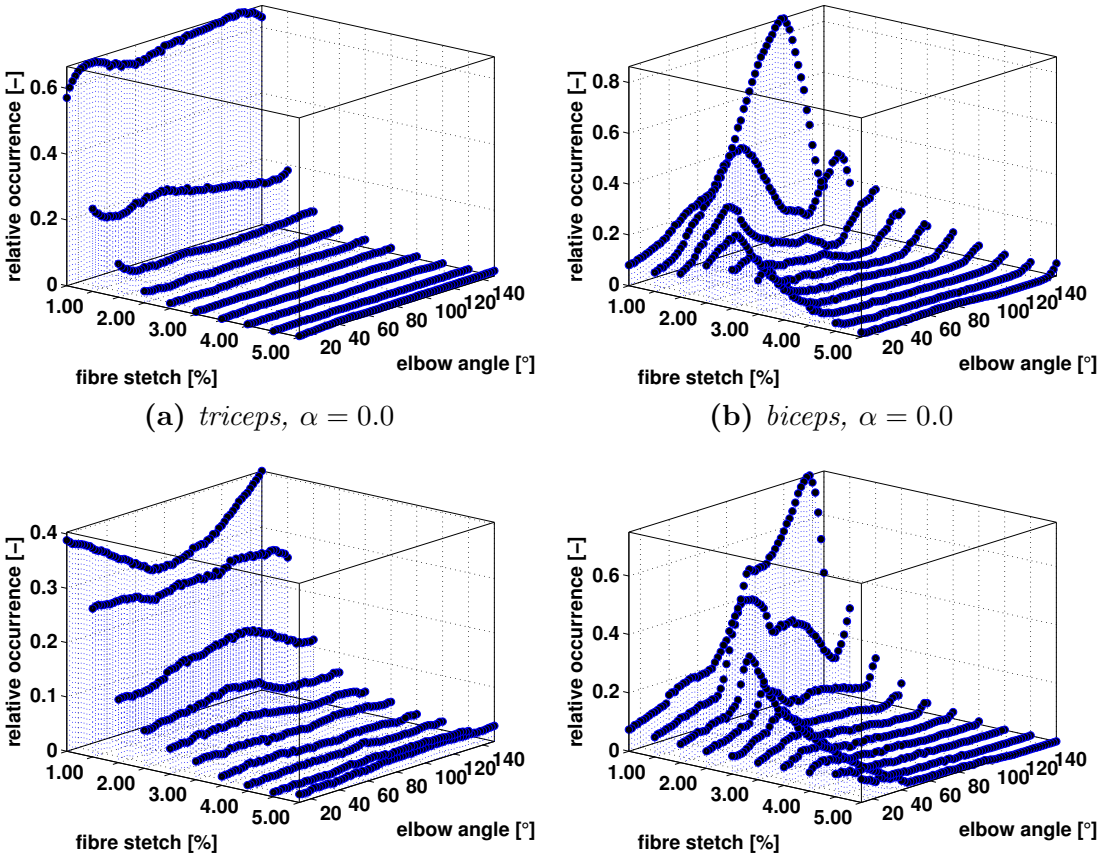

(a) *triceps*, $\alpha = 0.0$ **(b)** *biceps*, $\alpha = 0.0$

(c) *triceps*, $\alpha = 1.0$ **(d)** *biceps*, $\alpha = 1.0$

Figure 9.8: *Relative occurrence of the fibre stretch difference evaluated for* Figure *9.7. I.e. the fibre stretch of a particular location determined by simulations not including contact is subtracted from the fibre stretches determined by simulations including contact. Their absolute difference is categorised into ten equally spaced groups and normalised by the number of integration points. Their relative occurrence is plotted vs. the elbow flexion angle θ and the difference in the muscle fibre stretch $\Delta\lambda_f$. The left side depicts the triceps brachii. The right side depicts the results for biceps brachii. The top row depicts the results of a passively stretched muscle while the bottom row depicts the fully active muscles.*

For the passive triceps, the distribution is rather independent of the elbow angle. Between 60-65% of the muscle fibres deviate less than 0.5%, around 20% deviate less than 1%, around 2% deviate less than 2%, and only about 1% of the *Gauss* points' fibre

stretches deviate more than 5%. For the active triceps, the deviation increases. Around 26% of the fibres have a larger fibre stretch difference than 1%, around 7% deviate more than 2%, and about 2% of the fibres deviate more than 5%.

For the biceps, the fibre stretch distribution is more complex but very similar for the passive and the fully activated muscle. A peak emerges in both activation scenarios. The difference is that the peak appears about 20° towards higher elbow angles for the fully active biceps than for the passive biceps. For elbow angles smaller than 60°, close to none of the fibre stretches are the same. For $\theta = 10°$, only 8% of the fibres of the two scenarios have the same length. A total of 92% of the fibres deviate for at least 1% in their length even though the overall muscle length is not changing.

The Muscle Force Wrench

In contrast to rigid-body models, continuum-mechanical models have the advantage of taking into account spatial heterogeneities. Hence, a continuum-mechanical model can be applied to investigate the muscle force flowing through the muscle from origin to insertion. The muscle force's orientation changes due to muscle-intrinsic phenomena such as the complex geometry, locally distributed material parameters, or the fibre structure.

To study these phenomena, the offset of the point of action of the muscle reaction force is determined using the force wrench procedure introduced in Section 7.5.

Figure 9.9 depicts the amount that the point of action is deflected from the barycentre of the muscle's proximal surface by minimising the orthogonal fraction of the resulting moment at the surface, see Equation (7.20).

For rigid tendons, the deviation of the position of the point of action is small and mostly within 3 mm. The impact of the effects of contact are small as the shape of the muscles' surfaces are similar independent of contact. Yet in case of the triceps, contact influences the displacement of the point of action at $\alpha = 0$ and 1. The biceps' deviation of the position of the point of action has a big dip at about 120°. The cause for this dip is related to the fact that the magnitude of the reaction force is close to zero in that region. Hence, the orientation of the reaction force is more indifferent. Therefore, the nominator of Equation (7.20) becomes dominant and the results are strongly deviating. To summarise, the dip is an effect of the badly defined prestretch. This is also the case at $10° < \theta < 15°$ for $\alpha_T = 0$. Interestingly, for increasing the biceps activation, the point of action is less eccentric, hence the muscle force seems to flow more directly through the centre of the muscle.

To investigate the variance of the orientation of the resulting muscle reaction force, the orientation of the reaction force is compared to the orientation of the line defined by the barycentre of the origin and insertion point, similar to Röhrle and Pullan (2007). The location of the origin and the insertion is determined by the barycentre of the myotendinous junction and the osteotendinous junction, respectively. The deflection angle enclosed by the two muscle reaction force vectors is determined by:

$$\sphericalangle = \arccos \frac{\|\mathbf{F}_1 \cdot \mathbf{F}_2\|}{\|\mathbf{F}_1\| \cdot \|\mathbf{F}_2\|}, \qquad \text{or} \quad \sphericalangle = \arctan \frac{\|\mathbf{F}_1 \times \mathbf{F}_2\|}{\|\mathbf{F}_1\| \cdot \|\mathbf{F}_2\|}. \tag{9.2}$$

where $\mathbf{F}_1$ and $\mathbf{F}_2$ are two reaction forces. They are determined by summing all three components of the nodal residuals at the distal and proximal junctions. The second

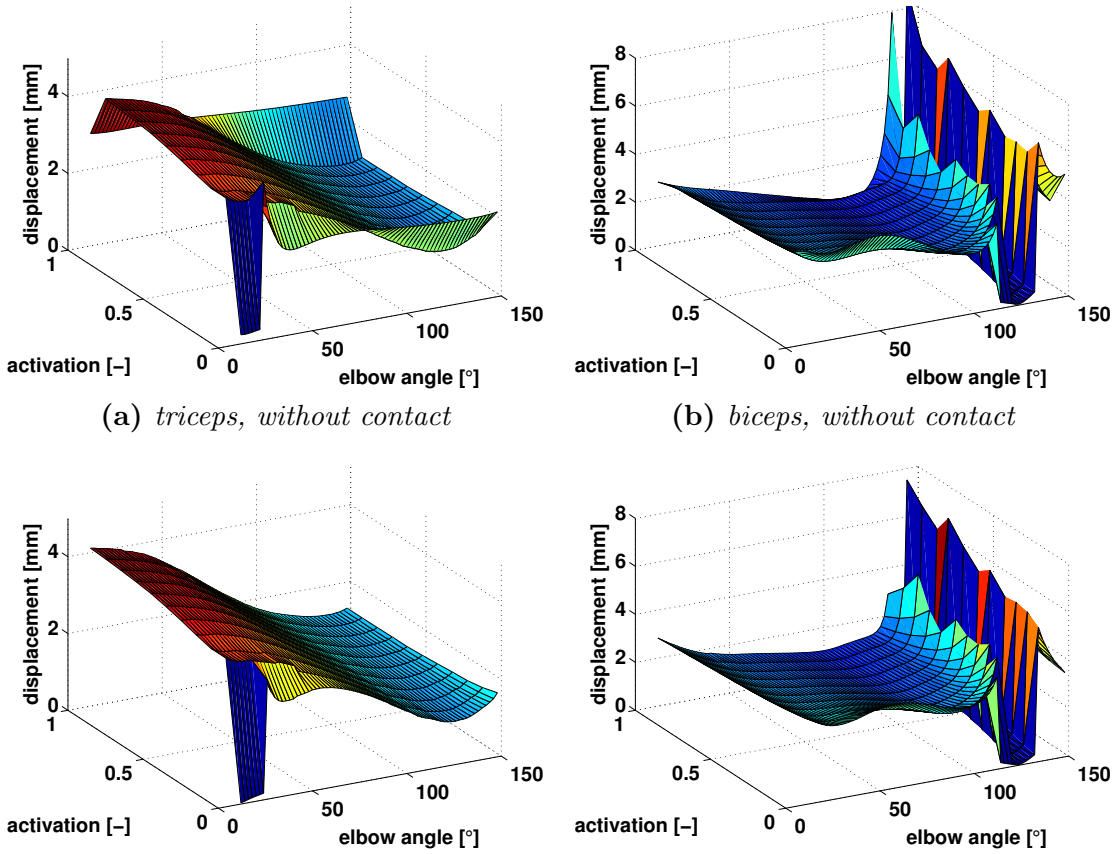

(a) *triceps, without contact* (b) *biceps, without contact*

(c) *triceps, with contact* (d) *biceps, with contact*

Figure 9.9: *The new location of the point of action, that is determined by the force wrench procedure, depends on the elbow angle and the muscle activation. The triceps is depicted on the left and biceps brachii on the right. The top row depicts results of simulations without considering contact and the lower row with contact. In case of the triceps, the contact has a larger impact on the eccentricity of the resulting force. Whereas for the biceps, contact does not have such a big influence. The dip at about 120° is due to the biceps force which tends to be zero in that range.*

option is more accurate, especially if $\mathbf{F}_1$ and $\mathbf{F}_2$ are not unit vectors and that it also encounters any accuracy problems for angles that are near zero or π.

For the triceps, the angular deflection increases with increasing muscle length and decreases with muscle activation. At $\theta = 10°$, the deviation is about 1° and increases to 16° for $\theta = 150°$. The biggest influence of contact can be observed for $\alpha_T = 1$, for which the deviation is not reduced but increased. For the biceps, the angular deviation is small throughout the domain. The surface is concave with its lowest value at 0.75° in the centre. The values are in the range between 0.75°-2°. For $\theta > 100°$, the deviation increases up to 7°, until the reaction force points into the other direction. As the changes are very large in this region, they are removed from the plot. The impact of the contact on biceps and triceps is only recognisable for $\alpha = 0$ and 1 where the deflections are larger if compared to the non-contact framework.

The change of the point of action and the reorientation of the muscle reaction force,

can be seen in a video on the authors website[1] and within the supplemental material to this thesis.

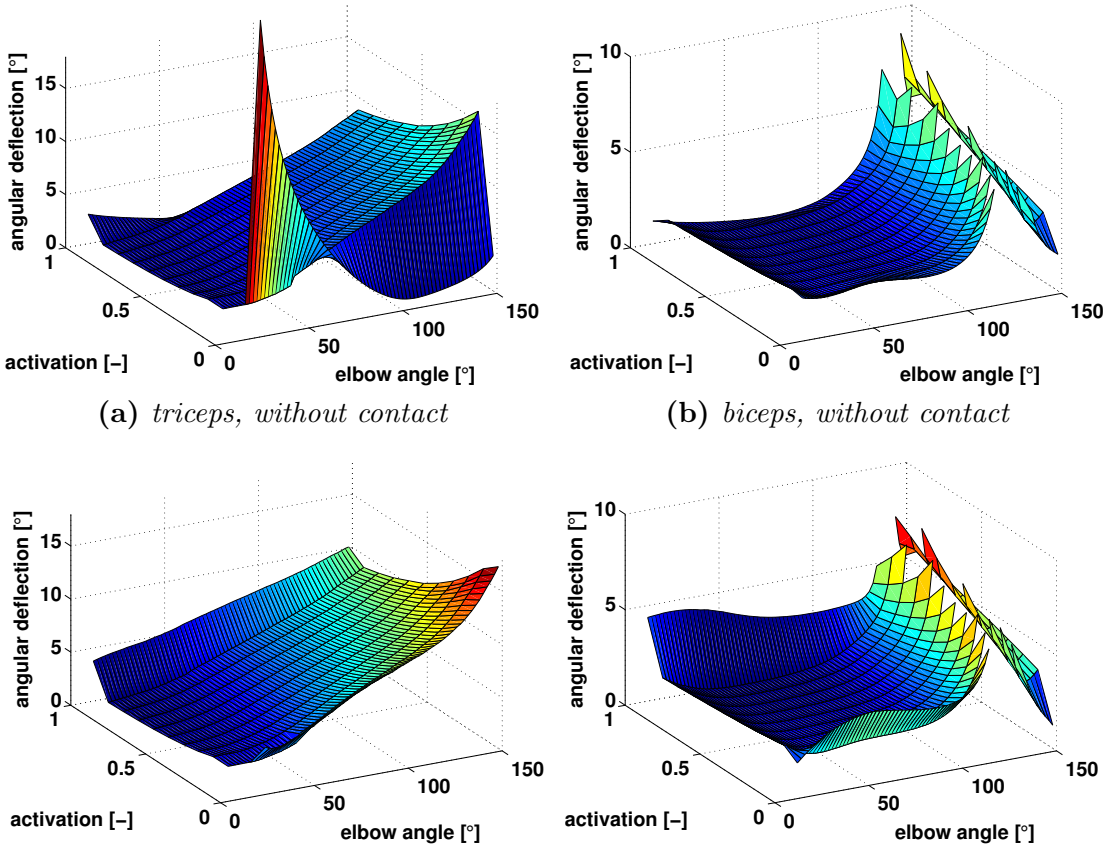

(a) *triceps, without contact* (b) *biceps, without contact*

(c) *triceps, with contact* (d) *biceps, with contact*

Figure 9.10: *Deviation of the orientation of the resulting reaction force compared to a one-dimensional representation defined by the barycentre of the origin and insertion point. The orientation of the muscles' resulting reaction force is weakly depending on the effects of contact.*

[1] `www.mechbau.uni-stuttgart.de/ls2/jrg/people/academic_staff/sprenger/index.html`

9.1.2 Muscle-Tendon-Complex Model

In the second evolution step, the tendon tissue, as it is introduced in Section 7.2.2, is considered. Tendon tissue is much stiffer than muscle tissue, see Section 2.4.4. Yet, due to the tapering, the overall strength is not as much as the mechanical material parameters may suggest. Within this section, the same plots as in the previous section are presented. Again, the results are split into four sections visualising the raising arm movement, the resulting muscle reaction forces, the fibre stretch distribution, and the results from the force wrench.

Raising Arm

Figure 9.11 presents the same sequence of snapshot as in Figure 9.1. Again, the full range of motion of the Upper Limb Model is depicted to discuss the mechanical behaviour of the muscles.

For the fully extended forearm, the triceps closely follows the shape of the humerus. At the distal end of the humerus, the gap between humerus and triceps is slightly larger, as the insertion boundary condition follows the circular movement of the olecranon. Further, there are no boundary constraints defined at the outside of the triceps, which would press the triceps towards the humerus. While the forearm is flexing, the triceps stretches. Without considering contact, the triceps penetrates the humerus about 24 mm, which is more than the full diameter of the humerus. With contact, the triceps wraps around the head of the humerus strongly influencing the triceps reaction force and orientation. This phenomenon is even more pronounced with increasing levels of activation.

Further, for the fully extended forearm, the biceps is fully stretched and forms a long slender muscle. Without contact, the biceps penetrates the humerus at the distal end of its shaft about 20 mm. With contact, the biceps is pushed by the humeral shaft and especially by the epicondyle to increase the muscle length. When flexing the forearm, the biceps shortens and the belly of the biceps forms. Due to the applied circular movement at the insertion, the distance between the humerus and the biceps brachii increases and contact plays a minor role.

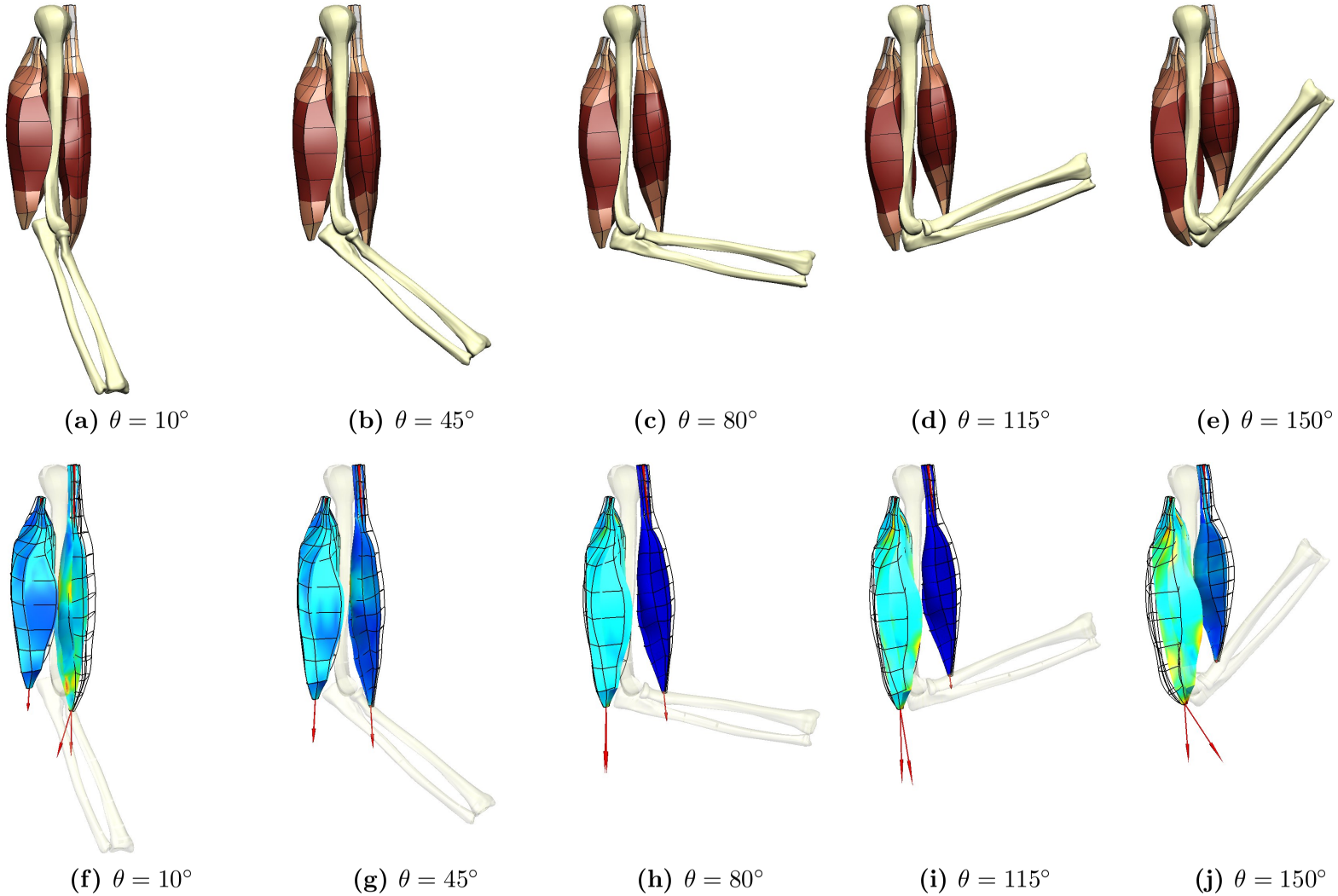

(a) $\theta = 10°$ **(b)** $\theta = 45°$ **(c)** $\theta = 80°$ **(d)** $\theta = 115°$ **(e)** $\theta = 150°$

(f) $\theta = 10°$ **(g)** $\theta = 45°$ **(h)** $\theta = 80°$ **(i)** $\theta = 115°$ **(j)** $\theta = 150°$

Figure 9.11: *Raising the forearm, for different elbow flexion angles at full muscle activation. The upper row depicts the scenario when contact is considered, while the lower row compares the solutions when contact is considered and not. The effective strain is scaled such that* $E_{\text{eff}} \in [0, 0.5]$*, where small differences are depicted in blue and high differences in red.*

The difference between the solutions considering the impact of contact and not is depicted in the lower row of Figure 9.11. The contour plots visualise the strain, defined by Equation (9.1) and the variation of the resulting muscle reaction force. The black grid of the muscle represents the solution considering contact while the coloured, contoured muscle is representing the solution without contact. The contour plot visualises the effective strain, $E_{\text{eff}} \in [0, 0.5]$, – the difference between the two solutions – where red denotes a high deviation and blue a small one. It can be seen that the difference between the solutions is more pronounced for the muscle in its stretched position and in regions close to the attachment sites. The same can be said for the difference of the orientation of the resulting reaction forces. The more the muscles are stretched, the stronger is the contact between the muscle and the bone deflecting the reaction force.

The full range of motion raising the arm can be seen in the video, which is posted on the author's website[2] and within the supplemental material to this thesis.

Resulting Muscle Reaction Forces

The muscle reaction forces are plotted in Figure 9.12. Again, the dashed, blue curves in Figure 9.12 denote the triceps reaction forces while the solid, red curves denote the biceps reaction forces. The highest curve represents the resulting muscle reaction force for a fully activated muscle while the lowest curve represents the purely passive mechanical behaviour of the muscle. While the curves of the resulting muscle forces considering contact are thick, the ones without are thin.

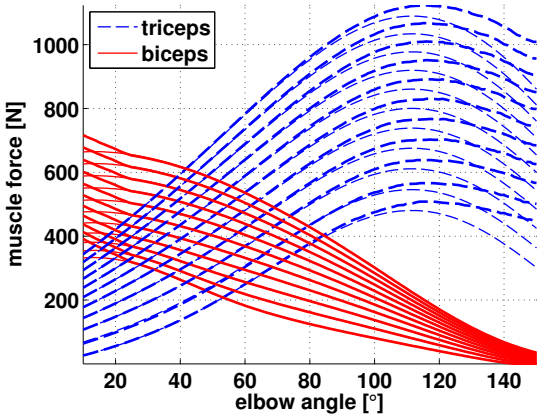

Figure 9.12: *The muscle reaction forces for triceps and biceps brachii for activations $\alpha = 0.1\,i$ with $i = 0..10$. The lowest curve is determined by $\alpha = 0$ and the highest by $\alpha = 1$.*

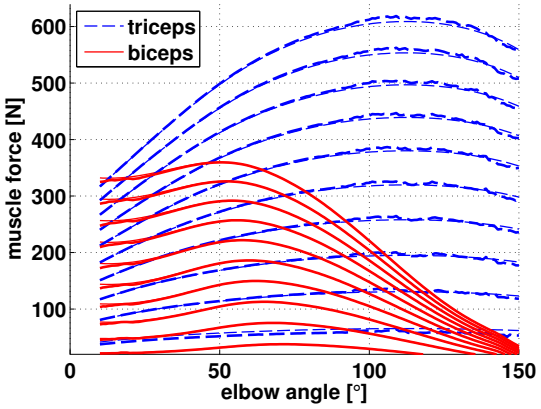

Figure 9.13: *The active part of the muscle reaction forces is determined by subtracting the passive muscle reaction force from the muscle reaction forces for $\alpha = 0.1\,i$ with $i = 1..10$*

The prestretch of the muscle is chosen such that the muscle reaction force is positive for the shortest muscle length. The maximum triceps reaction force is reached between 115° and 120° depending on the level of activation. For the fully activated triceps, the maximal value is $F_T(\theta = 115°, \alpha_T = 1.0) = 1123\,\text{N}$ while the maximal value for the purely passive

[2] `www.mechbau.uni-stuttgart.de/ls2/jrg/people/academic_staff/sprenger/index.html`

behaviour is $F_T(118°, 0.0) = 508.2\,\text{N}$. The triceps reaction force only depends on the effects of contact for $\theta > 90°$ i.e. when the triceps bends around the distal head of the humerus. Here, the reaction force without contact decreases more as the muscle length increases including contact while it does decrease without contact. The difference between the two solutions at $\theta = 150°$ is for the fully activated triceps 148 N. The biceps reaction force is monotonically decreasing and reaches its maximal force values for $B(\theta = 10°, \alpha_B = 1.0) = 716.7\,\text{N}$ and $B(10°, 0.0) = 391.7\,\text{N}$. For the biceps, the reaction force does only depend on the contact for $\theta < 25°$ when the biceps is in contact with the epicondyle. The difference in force between the two solutions is at $\theta = 10°$ for the fully activated biceps 113 N. The triceps reaction force are below 30 N for $F_T(\theta > 145°, \alpha_B = 0)$. The biceps force is negative for $F_B(\theta < 145°, \alpha_B = 0)$ indicating that a larger prestretch should have been defined. A few millimeters larger would have been sufficient.

The purely active force contribution of a muscle is obtained by subtracting the passive muscle force from the activated muscle force. The results are depicted in Figure 9.13.

For the triceps brachii, the active part is maximal, depending on the level of activation, between $\theta = 100°$ and $\theta = 120°$. For the biceps brachii, the active force is maximal for elbow angles between $\theta = 50°$ and 74°. The maximal forces are $F_T^{\text{active}}(106°, 1.0) = 617.8\,\text{N}$ and $F_B^{\text{active}}(51°, 1.0) = 359.6\,\text{N}$.

From Figure 9.13, one can clearly observe that for both muscles the active part of the reaction force does not deviate whether contact is considered or not. Hence, one can conclude that the increase in muscle length, due to contact, just has an impact on the passive muscle force contribution and not on the active one. Furthermore, the muscles act for the largest portion of their physiological range of motion on the ascending limb of the force-length relationship, i.e. the muscle force predominantly increases if the muscle is being stretched. For the biceps, the active part can be zero when the muscle is short enough.

Depending on the elbow angle, the contact forces between the muscle and the bone can be significant. Figure 9.14 depicts the normalised exerted muscle forces of the biceps and triceps brachii and its contact forces with bone. For better comparison, the exerted muscle forces have been normalised with respect to the maximal exerted muscle force of the respective muscle. Further, the contact force is depicted as a percentage of the exerted muscle force at a particular elbow angle.

For the triceps, the contact forces are significant. For $\alpha_T = 0$, the contact force starts to be considerable at $\theta \approx 80°$. It finally reaches 91% of the muscle reaction force at $\theta = 150°$. The spikes at $\theta = 65°$, 143°, 146° are most probably developing due to jumps of the element vertices from one side of the humerus to the other (an numerical phantom which stores the pressure until it reaches a limit where the element vertices slides over on the other side of the humerus curvature). For the active triceps, at a maximal elbow angle of 150°, the contact force is 70.4% of the exerted muscle force at the same angle. Even though, the contact forces for the triceps brachii are quite significant for larger elbow angles, the contact force still measures 23.3% of the exerted muscle force when the maximal muscle force is produced, i.e. at an elbow angle of 115°. Note that the triceps is pushing with more than 200 N against the shaft of the humerus.

Since no surrounding tissue was considered within this work and the biceps is a superficial muscle, the contact forces between the biceps brachii and the humerus are much smaller. Nevertheless, at small and large elbow angles, i.e. at $\theta < 50°$ and at $\theta > 140°$,

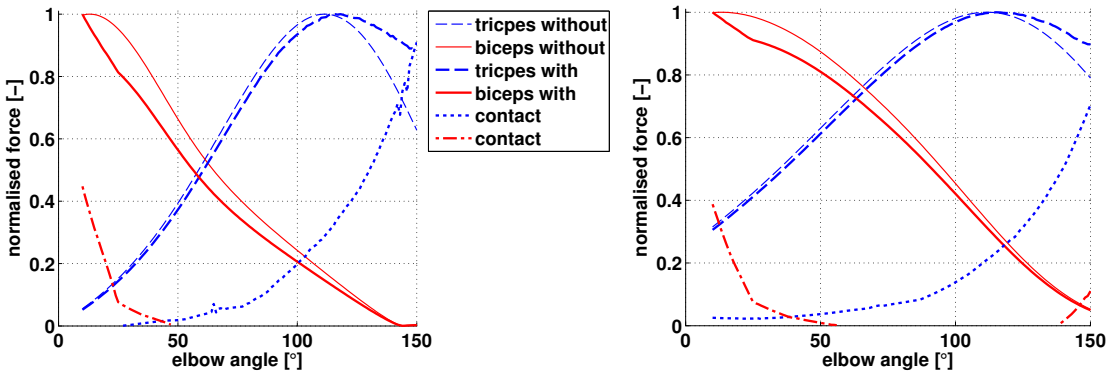

(a) $\alpha = 0$ **(b)** $\alpha = 1$

Figure 9.14: *Normalised exerted muscle forces vs. contact forces for the entire range of motion assuming fully activated muscles.*

the contact forces are still around 40% and 10% of the respective exerted muscle force.

Muscle Fibre Stretch Distribution

The MTC's fibre stretch distribution is shown in Figure 9.15. Both muscles have a narrower stretch distribution when the muscle is shorter and less activated. The fibre stretch is predominantly close to $\lambda_f = 1$ for the passive muscle in its shortest configuration. Because tendon tissue is much stronger than muscle tissue throughout all configurations, there is an occurrence accumulation at $\lambda_f = 1$ which can, for example, be nicely seen in Figure 9.15f or 9.15e. Further, it can be observed that the fibre stretch tends to accumulate at $\lambda_f \approx 1.4$. The reason for this phenomenon is that at around $\lambda_f = 1.4$, the passive stress starts to dominate and the muscle tissue becomes much stiffer. As a result other fibres are stretched first, before these fibres are stretched any further.

Due to the transition zone between tendon tissue and muscle tissue, the stretch distribution scatters and it becomes more difficult to assign areas to specific features. For growing muscle length, the fibre stretch distribution spreads out and becomes more diverse. Due to the bipennate fibre architecture of the triceps, a wider stretch spectrum can be observed compared to the fusiform biceps. The triceps' fibres are agglomerating at $\lambda_f = 1$ at its shortest configuration and slightly increases towards $\lambda_f = 1.2$ at is longest configuration. For an increasing triceps activation, the distribution is less distinct and moves towards shorter fibre stretches. For the biceps, the highest fibre stretch occurrence starts, for the shortest length, with $\lambda_f \approx 1$ and shifts towards $\theta = 40°$ and $\lambda_f = 1.4$. Here, the passive muscle strength starts to dominate and the fibres start to accumulate at $\lambda_f \approx 1.4$. As well as for the triceps, the biceps' distribution becomes less distinct for increasing muscle activation and the fibres stretch moves towards shorter lengths.

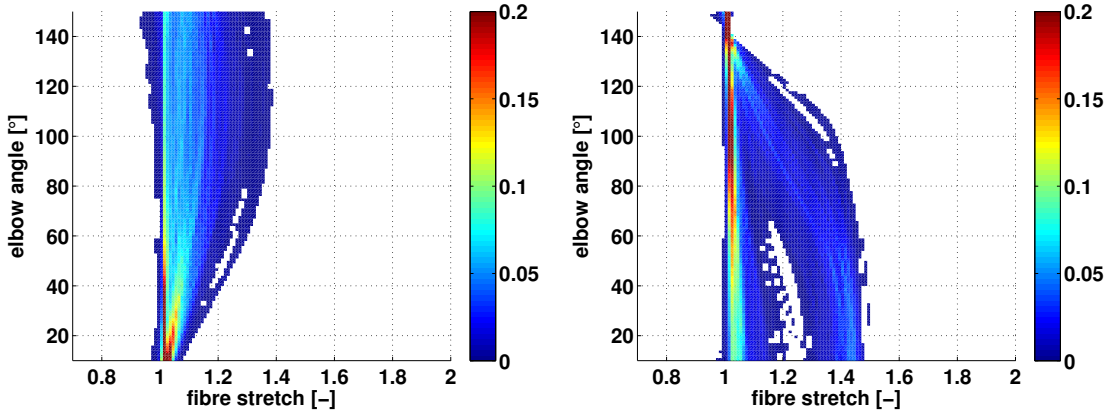

(a) *triceps*, $\alpha = 0.0$ (b) *biceps*, $\alpha = 0.0$

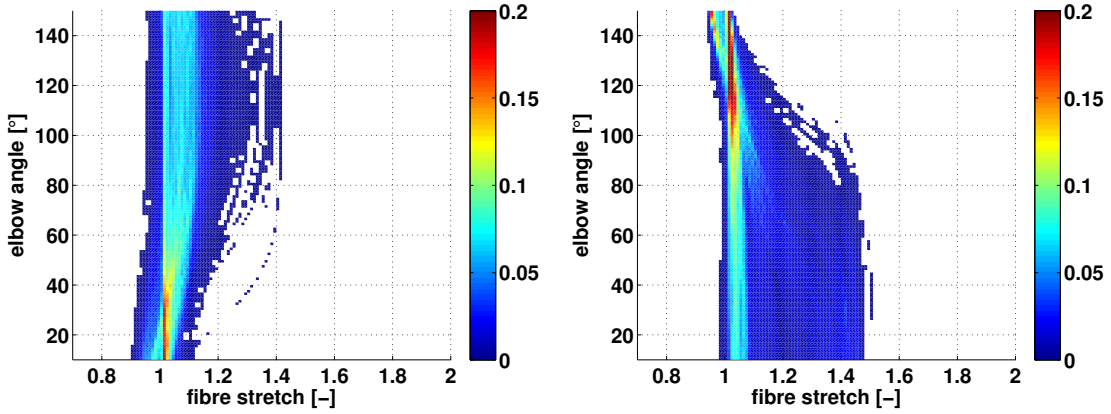

(c) *triceps*, $\alpha = 0.5$ (d) *biceps*, $\alpha = 0.5$

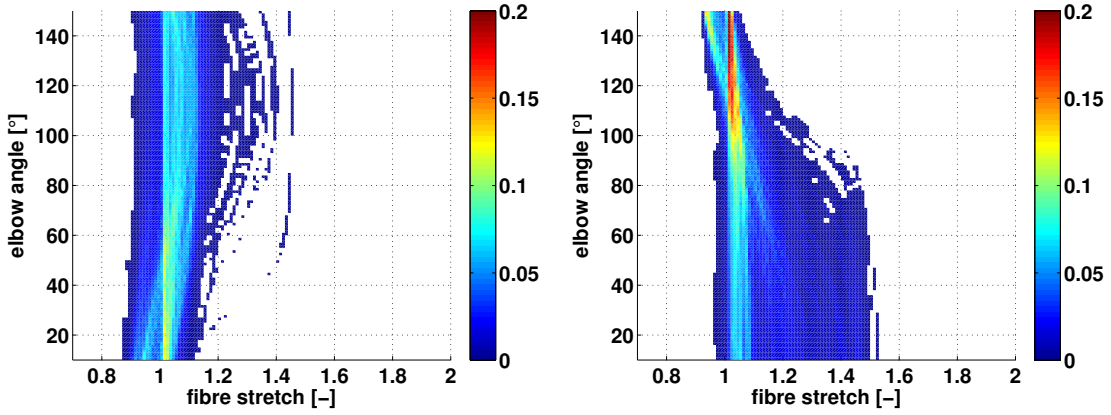

(e) *triceps*, $\alpha = 1.0$ (f) *biceps*, $\alpha = 1.0$

Figure 9.15: *The relative fibre occurrence is plotted vs. the elbow flexion angle θ and the muscle fibre stretch λ_f. The scale for the relative occurrence is limited to 0.2 to resolve also fibres with less frequent fibre stretch occurrences. A horizontal line represents the muscle's fibre distribution for one particular position. Hence the sum of all occurrences on a horizontal line is one.*

The mean triceps and biceps fibre stretch is plotted in Figure 9.16 for $\alpha = 0, 0.5$ and 1. For the passive triceps, the mean fibre stretch covers a range from $\lambda_f = 1.013 - 1.098$.

The shape of the curve does not change with increasing muscle activation. Yet, the mean fibre stretch reduces and the values for the fully activated triceps are shifted about 3.4% towards shorter lengths compared to the passive triceps. The mean fibre stretch for the passive biceps is between $\lambda_f = 0.997$ and $\lambda_f = 1.182$. The shape of the curve changes only slightly with increasing muscle activation. Compared to the passive biceps, the curve of the active biceps is less S-shaped. Yet, the mean fibre stretch reduces and the values for the fully activated biceps are shifted about 2.6% towards shorter lengths compared to the passive biceps. Contact has a larger influence on the triceps especially at higher flexion angles than on the biceps as the curves differ stronger for the triceps than for the biceps. In their shortest configuration and fully activated, both muscles exhibit mean fibres stretches $\lambda_f < 1$.

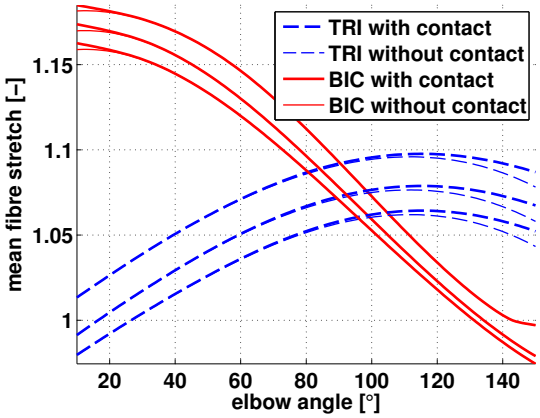

Figure 9.16: *Mean muscle fibre distribution for triceps (red) and biceps (blue) for $\alpha = 0, 0.5$ and 1. The curves including contact are bold and the curves without are thin. For an increasing level of muscle activation, the mean fibre stretch shortens. The difference of the mean fibre stretch due to contact is not very large.*

Figure 9.16 could lead to the premature conclusion that contact does not have a big influence on the fibres within the continuum. To falsify this conclusion, Figure 9.17 and 9.18 are presented to investigate the impact of the effects of contact on the fibre stretch distribution within the muscles.

To compare the impact of the effects of contact on the fibre distribution, the focus is set on the local fibre stretch distribution. By comparing the resulting local fibre stretch distribution including and not including contact, a large spatial deviation can be observed. The difference in fibre stretch between considering the effects of contact and not is depicted in Figure 9.17. At each *Gauss* point, the fibre stretch value of the simulations that considered the effects of contact is subtracted from the fibre stretch value of the simulations that do not consider the effects of contact, even though their current position may not coincide. The deviation of their location varies more or less depending on the elbow angle, the muscle activation, and the location within the muscle. The resulting $\Delta\lambda_f$ is depicted in Figure 9.17 at their actual position determined including contact. The scale of the legends is from blue to red $-3\% \leq \lambda_f \leq 3\%$.

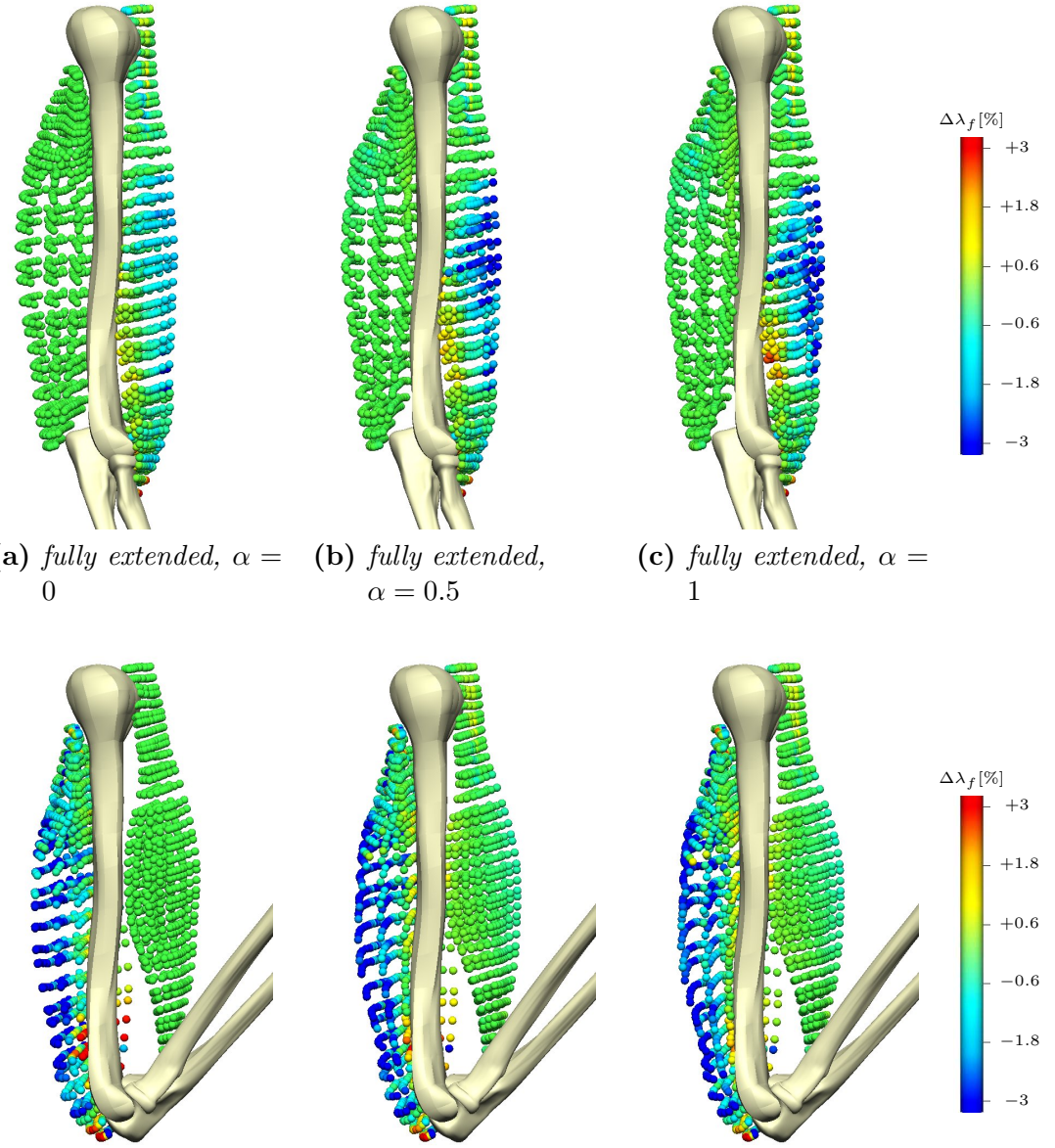

(a) *fully extended,* $\alpha = 0$ **(b)** *fully extended,* $\alpha = 0.5$ **(c)** *fully extended,* $\alpha = 1$

(d) *fully flexed,* $\alpha = 0$ **(e)** *fully flexed,* $\alpha = 0.5$ **(f)** *fully flexed,* $\alpha = 1$

Figure 9.17: *The difference between the fibre stretch resulting from including the effects of contact and not determined at each integration point. The fibre stretch difference is negative (blue), when the fibres without contact are longer, and positive (red), when the fibres including the effects of contact are longer.*

In case of the triceps at the fully extended position, the difference of the fibre stretch is obviously very small as the contact forces are quite small for these positions. This situation significantly changes when the forearm is extended. While the muscle is pushed laterally, the medial fibres are pushed together and the lateral ones are stretched. Hence, there is a large area in which the fibres are further stretched. The area where the fibres are shorter is much smaller as two effects coexist. Firstly, the fibres' length reduces as they are pushed by the bone. Secondly, the fibres are stretched as the muscle elongates

while the humerus forces the muscle to deform. The biceps' behaviour is similar. Yet, contact is most prominent for the fully extended forearm position. But the effect is the same. The medial fibres are shorter, where as the lateral are stretched. For the fully activated biceps, this effect can be seen even for the fully flexed muscle.

To emphasise the phenomena, Figure 9.18 presents the spatial evaluated differences of the classified into ten equal spaced groups. In the first group, the difference between the two cases is less then 0.5%. In the last group, the difference is larger than 5.0%. The distribution is plotted separately for each muscle (the triceps is left and the biceps right) and for the passive (the upper row) and the fully activated muscle (lower row) over the full range of movement.

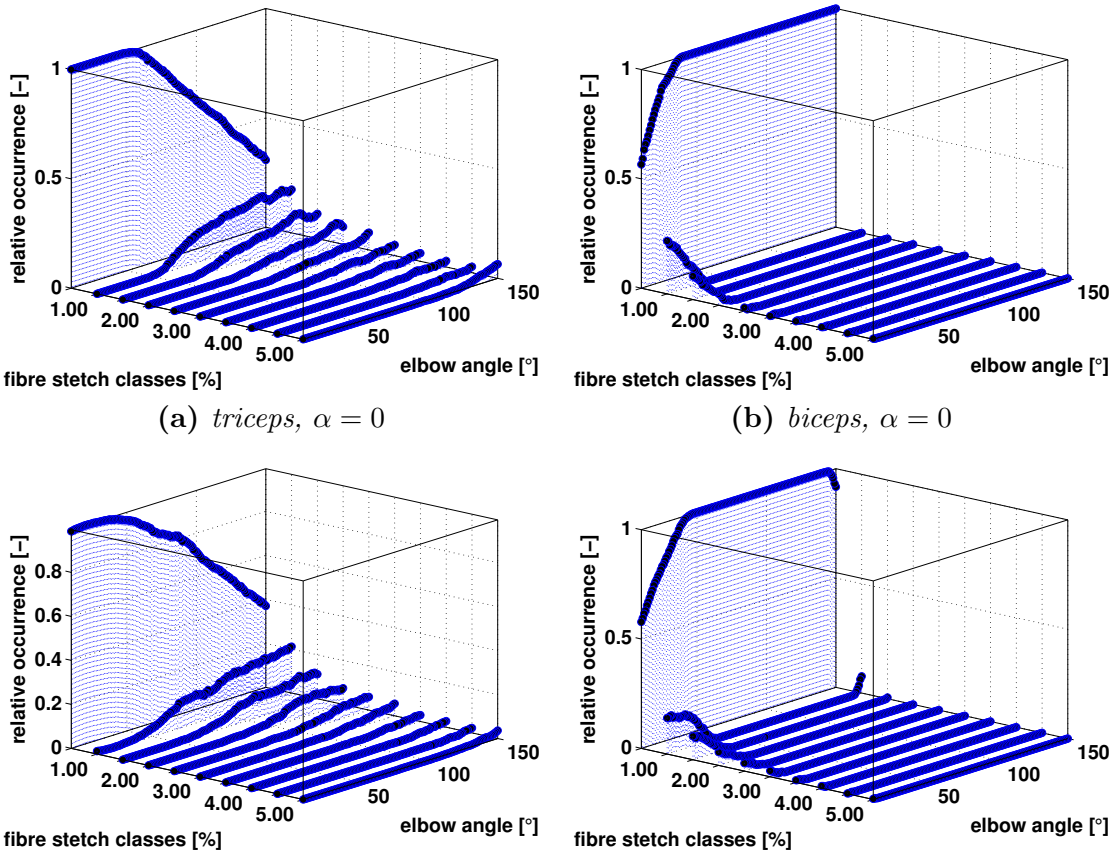

(a) *triceps,* $\alpha = 0$ **(b)** *biceps,* $\alpha = 0$

(c) *triceps,* $\alpha = 1$ **(d)** *biceps,* $\alpha = 1$

Figure 9.18: *Relative occurrence of the fibre stretch difference evaluated for* Figure *9.7. I.e. the fibre stretch of a particular location determined by simulations not including contact is subtracted from the fibre stretches determined by simulations including contact. Their absolute difference is categorised into ten equally spaced groups and normalised by the number of integration points. Their relative occurrence is plotted vs. the elbow flexion angle* θ *and the difference in the muscle fibre stretch* $\Delta\lambda_f$*. On the left is the triceps brachii and on the right for biceps brachii. On the top is the behaviour of the passive muscle and on the bottom the one of the active ones.*

For the fully extended forearm, the deviation of the two solutions is very small. The fibre stretch starts to deviate at $\theta = 52°$. For extending the forearm, the impact of the contact increases and also the deviation of the fibre stretch increases. For the passive

triceps (Figure 9.18a), for example, at $\theta = 56°$ the difference is for 98.4% of the fibres less than 0.5%. On the other hand, at $\theta = 150°$ the difference is for 68.3% of the fibres larger than 0.5% and for 6.6% of the fibres larger than 5.0%. For the fully flexed forearm, the biceps is only slightly pressed against the humerus. Hence, the difference of the fibre stretch is smaller compared to the one of the triceps. The deviation of the fibres is occurring until $\theta = 40°$ and increases towards fully extending the forearm. For the fully activated biceps (Figure 9.18d), for example at $\theta = 10°$, the difference is for 70.6% of the fibres less than 0.5%, for 2.8% of the fibres less than 2.5%, and for 1.2% of the fibres less than 3%.

The Muscle Force Wrench

In Figure 9.19, the amount the point of action is deflected from the barycentre of the muscle's proximal surface is determined by minimising the orthogonal fraction of the resulting moment at the surface, see Equation (7.20).

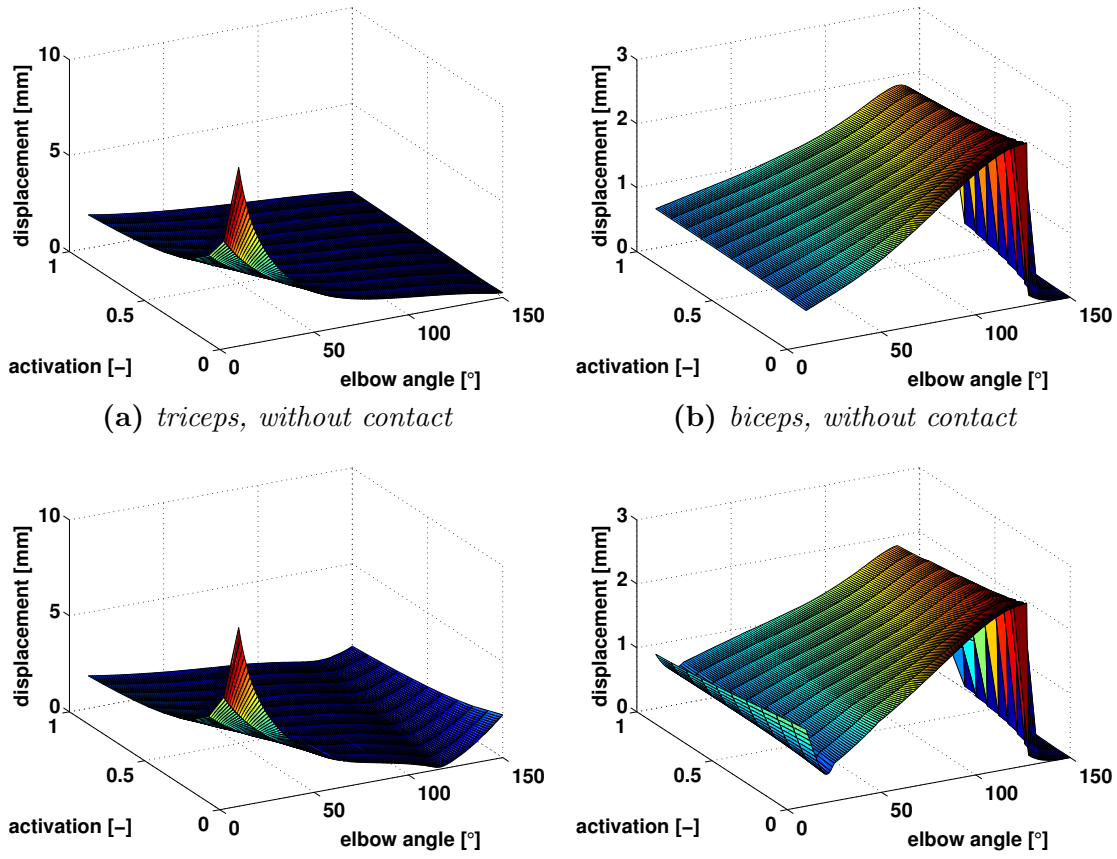

(a) *triceps, without contact* **(b)** *biceps, without contact*

(c) *triceps, with contact* **(d)** *biceps, with contact*

Figure 9.19: *The new location of the point of action, that is determined by the force wrench procedure, depends on the elbow angle and the muscle activation. In case of the triceps, the contact has a larger impact on the eccentricity of the resulting force. Whereas for the biceps, contact does not have much of an influence.*

The triceps' deflection of the point of action (Figure 9.19a and 9.19c) is in the widest range of θ and α a smooth and slightly increasing surface. For a reducing elbow angle and

an increasing activation, the maximal value is about 2 mm. Yet, for a very short triceps ($\theta < 50°$) and a low activation ($\alpha_T < 0.5$) the amount of deflection rises strongly up to 10 mm. In case of considering contact, the deflection increases from the non-contact results only for the long triceps ($\theta > 130°$, depending on the level of activation) as the triceps has to bend around the olecranon by an increase of only a few millimeters. The maximal deflection of the point of action is 2.1 mm at $\theta = 150°$ and $\alpha_T = 0$. The biceps' deflection of the point of action is a slightly increasing for the decreasing biceps length, while it is close to independent of the muscle activation. The maximal deflection is around 3 mm. The difference between contact and non-contact is marginal. There is only an additional small dent at $\theta = 0.24°$ where the deflection increases for less than one millimeter.

In Figure 9.20, the deviation of the orientation of the resulting muscle reaction force is compared to the orientation of the line defined by the barycentre of the muscle's origin and insertion.

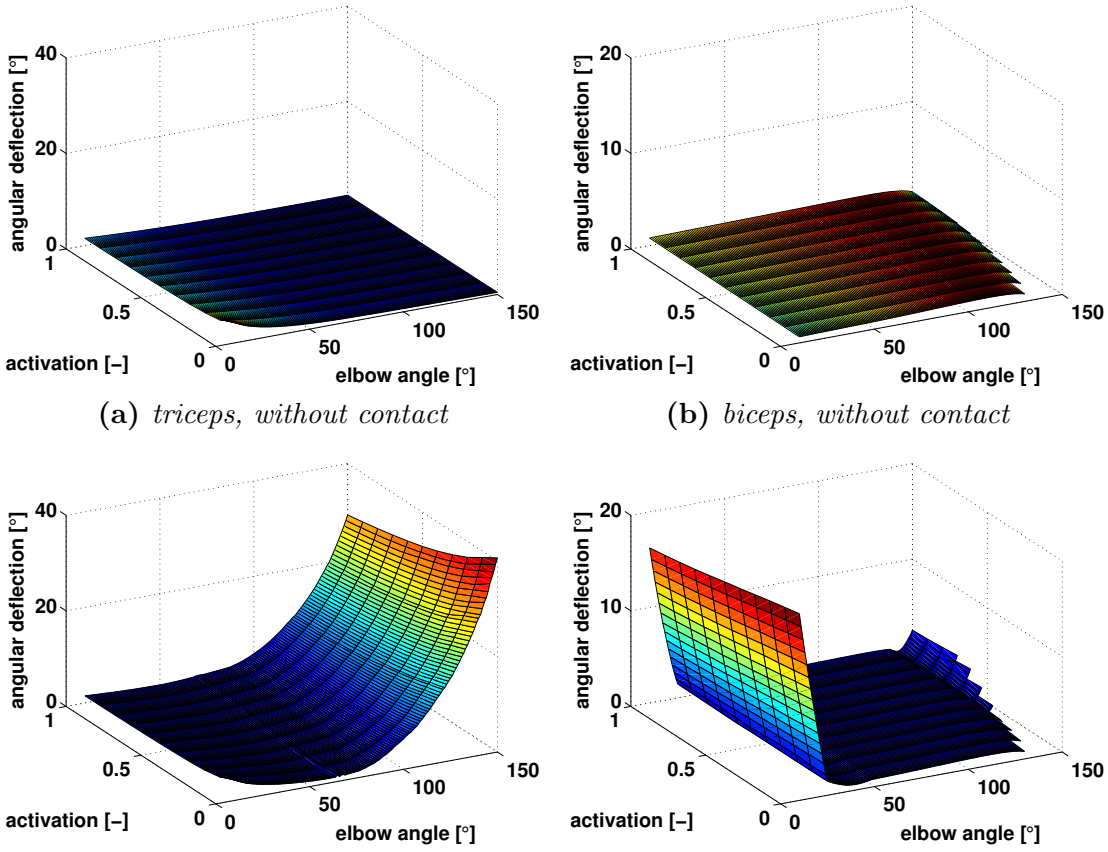

(a) *triceps, without contact* **(b)** *biceps, without contact*

(c) *triceps, with contact* **(d)** *biceps, with contact*

Figure 9.20: *Deviation of the orientation of the resulting reaction force compared to a one-dimensional representation line defined by the barycentre of the origin and insertion point. The orientation of the muscles' resulting reaction force is strongly depending on the effects of contact.*

For the triceps, the deflection of the orientation of the reaction force increases without considering the effects of contact (see Figure 9.20a) slightly towards a short and low activated triceps with a maximal deviation of around 4.5°. Including contact, the behaviour of Figure 9.20a is superposed with the strong influence of the triceps wrapping

around the olecranon. Hence, for increasing the triceps length, the triceps' orientation deviates from the orientation of the line by up to 40°. The biceps' deflection of the reaction force is without contact mostly less than 1 mm, i.e. very small and negligible. With contact, the biceps' deflection superposes for a long biceps the impact of the contact. For a very extended forearm, the biceps touches the humerus, hence, the deflection increases to approximately 20°.

For the results of the MTC depicted in Figure 9.19 and 9.20, less artifacts are arising as the muscle reaction forces are not reducing to zero or changing the sign as they do if rigid tendons are assumed.

9.1.3 Muscle Resulting Elbow Moment

As a joint moment is a product of a lever arm and a force acting on the joint, not only the muscle's force but also the muscle's lever arm have an impact on the generated joint moment. Hence, for the determination of an elbow equilibrium, also the two different methods to determine the lever arm have to be considered within this investigation. So before convergence studies of the Upper Limb Model are presented, the lever arms and the resulting muscle elbow moment are shown for the whole variability space.

As the convergence behaviour of the system for rigid and compliant tendons does not conceptionally change, it is not differentiated between the results of the two evolution steps. The results, shown here, are produced using the full MTC model.

Employing the Tendon-Displacement Method

Figure 9.21 shows the lever arm resulting from using the tendon-displacement method (TDM). Due to the fact that the muscles' length relation is smooth, the derivatives are well behaving and the curves are continuous. As the triceps is an extensor muscle and the biceps a flexor muscle, the lever arms are of opposite sign. The triceps lever arm is mostly close to -20 mm. The biceps lever arm is in the fully flexed state close to 37 mm, reaches its maximum of 41 mm at 60°, and declines to 27 mm at full extension.

The elbow joint moments resulting from the TDM are shown in Figure 9.22. The elbow moment is a function of the elbow angle and the muscle activation, while the dependency on contact is small. For the triceps, the maximal moment is $M_T(\theta = 100°, \alpha_T = 1) = -26.1\,\text{kNmm}$ and the minimum is $M_T(\theta = 10°, \alpha_T = 0) = -0.85\,\text{kNmm}$. As the triceps acts as an extensor, the moment is defined to be negative and even though the value of $M_T(\theta = 100°, \alpha_T = 1)$ is smaller than the value of $M_T(\theta = 10°, \alpha_T = 0)$, the absolute value is larger. For the biceps, the maximal moment is $M_B(\theta = 28°, \alpha_B = 1) = 25.2\,\text{kNmm}$ and the minimal is $M_B(\theta = 150°, \alpha_B = 0) = -0.13\,\text{kNmm}$. The last moment is negative as for $T_B(\theta > 146°, \alpha_B = 0)$ the reaction forces are negative, i.e. the prestretch should be defined a few millimeters larger.

Vector-Resulting Lever Arm

For the determination of the vector-resulting lever arm (VRLA), Equation (7.2) is solved and plotted as surface vs. muscle activation and elbow angle as it points out, that the lever arm is not only a function of the elbow angle but also of the muscle activation. The reason for the muscle activation dependency is that the muscle force orientation varies with the

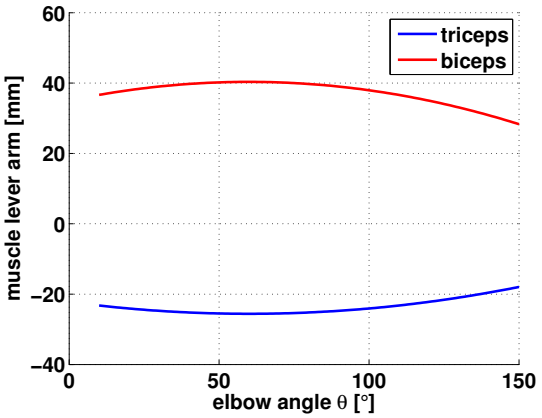

Figure 9.21: *The lever arms for triceps and biceps brachii for the TDM are determined by taking the derivative of the muscle lengths with respect to θ.*

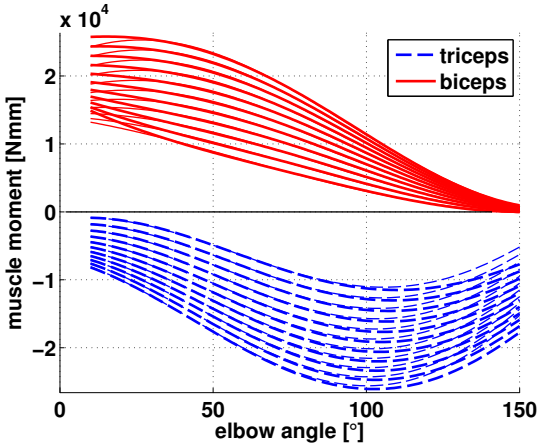

Figure 9.22: *The product of lever arm and muscle force yields the resulting elbow joint moment which depends on θ and α. The thick curves consider contact whereas the thin curves do not. The curve with the lowest absolute value belongs to $\alpha = 0$ and raises in $\Delta\alpha = 0.1$ steps up to $\alpha = 1$ to build 11 curves for each muscle.*

muscle activation and has an impact on the vector-resulting lever arm. Furthermore, the contact formulation has an influence on the vector-resulting lever arm as it influences the orientation of the reaction force strongly.

For the triceps, see Figure 9.23a and b, the lever arm is, for a flexing elbow, a monotonically decreasing surface. Not considering contact, the lever arm is between -8 mm, for large elbow angles, and -30 mm, for small elbow angles. While the muscle activation's dependency is mostly only weak, it has a strong influence on a fully extended forearm. Towards a passive muscle, the lever arm drops. Considering contact, the overall muscle activation's dependency is stronger. Rather significant is the fact, that the lever arm including contact is less linear. Contact causes a concave bend for the elbow angle dependency. For an extended elbow, the lever arm including contact even becomes positive. Furthermore, the distinct kink at the extended elbow towards a passive muscle state is not existing.

For the biceps, see Figure 9.23b and d, the lever arm values are mostly between 10 and 15 mm. For the passive, fully flexed muscle, the muscle reaction force is very close to zero. Hence, its orientation is not clearly defined anymore and therefore, the resulting biceps reaction force and moment, respectively, are not well defined anymore. When contact is also considered, the slight decrease towards the fully extended elbow vanishes and the biceps lever arm is about 13.5 mm and very close to constant.

As the lever arms are determined using the exact vectorial locations, it is possible now to incorporate the change of the location of the point of action and the different orientations of the muscle reaction force. To point out the impact of the change of location, in Figure 9.24 the difference between the results of Figure 9.23 are subtracted

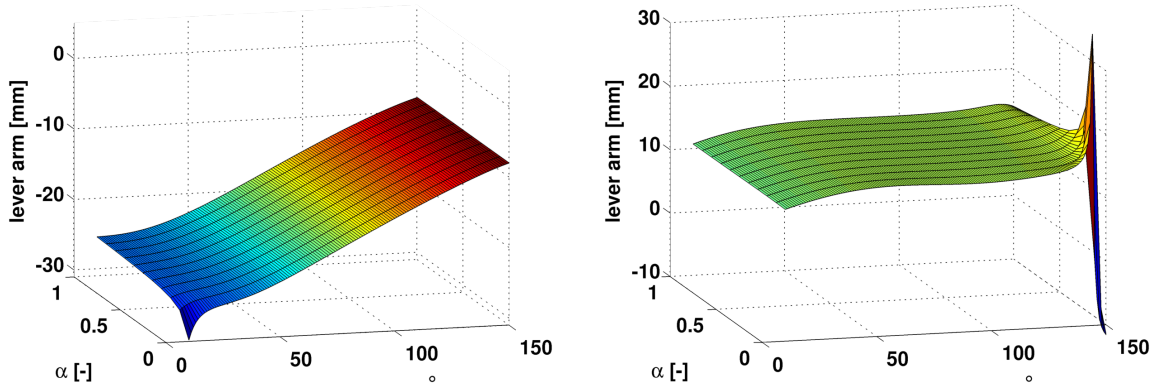

(a) *triceps, without contact*

(b) *biceps, without contact*

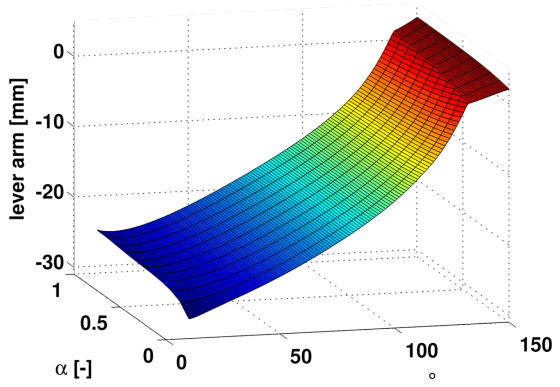

(c) *triceps, with contact*

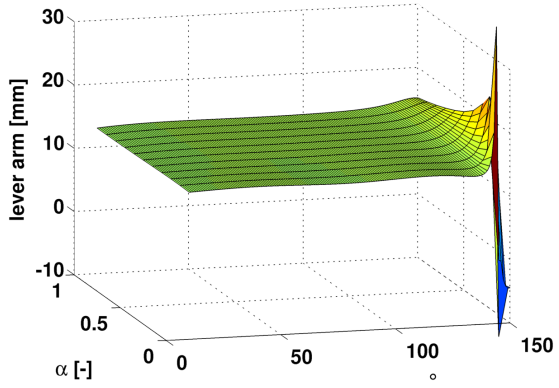

(d) *biceps, with contact*

Figure 9.23: *The VRLA lever arms are a function of the muscle activation, the elbow angle, and the effects of contact. For the few simulations, where the biceps reaction force becomes very small and negative, the algorithm fails to predict a reasonable lever arm.*

from the results considering the change of the point of action.

For the triceps, Figure 9.24a shows that the influence of the change of the point of action on the lever arm is not very large. It is smaller than 1 mm. The results of Figure 9.24c show that the behaviour of the lever arm is not considerable influenced by the effects of contact. Only for $\theta > 120°$, the influence of contact increases and the lever arm raises up to 1 mm. For the biceps (Figure 9.24b), the values are even smaller and within 0.4 mm. The area, in where the biceps reaction forces become very small, the lever arm is indifferent and less significant. The results of the lever arm appear not to be significantly influenced by the effects of contact as the surface in Figure 9.24d is very similar to the one in Figure 9.24b.

In Figure 9.25, the elbow moment resulting from using the tendon-displacement method (TDM) is compared to the results using the vector-resulting lever arm (VRLA) method. If the moment using the VRLA method is plotted similar to Figure 9.22 using lines, the results would be hardly recognisable as the resulting lines are intersecting each other. To improve the comparability of the results, the following plots are visualised using surface plots and Figure 9.25c and 9.25d repeat the results of Figure 9.22 as surface plots.

In Figure 9.25, the triceps' elbow moment can be seen on the left and the biceps' elbow moment on the right. The four figures, Figure 9.25c-f, show the resulting moment for using

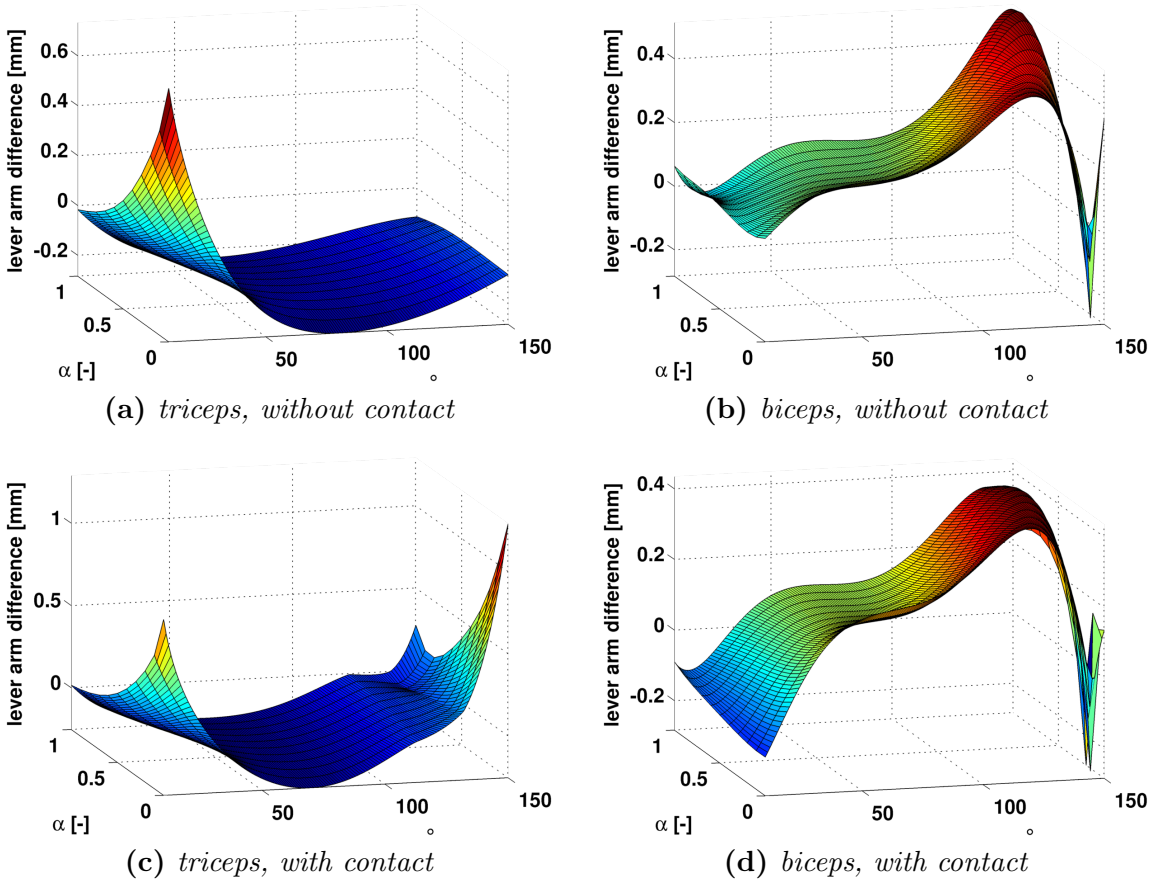

Figure 9.24: *Investigates the impact of the change of location of the point of action on the VRLA, i.e. the solution of VRLA is subtracted from VRLA+.*

the TDM (second row) and the VRLA (third row). The first and the fourth row show the impact of the effects of contact on the resulting moment using the TDM resulting moment and on the VRLA method resulting moment, respectively. This is done by subtracting the moment including the effects on contact from the moment not including contact. The second row shows the moment resulting from using the TDM and the third row the moment from using the VRLA method. All four plot include contact.

For the resulting moment using the TDM without contact, the triceps takes its maximum absolute value at $|M_T(\theta = 100°, \alpha = 1)| = |-25.59|$ kNmm and $|M_T(\theta = 102°, \alpha = 1)| = |-26.07|$ kNmm if contact is considered. For the VRLA method, the triceps induced elbow moment is significantly weaker. The triceps exhibits its largest absolute moment with $|M_T(\theta = 73°, \alpha = 1)| = |-17.53|$ kNmm for not taking into account contact and $|M_T(\theta = 73°, \alpha = 1)| = |-16.89|$ kNmm if contact is considered. Using the VRLA method, the triceps' moment passes the neutral line for a fully flexed elbow, as the value of the lever arm changes its sign. I.e. for $\theta > 130°$, the triceps acts as an elbow flexor throughout all levels of activations! As the biceps' VRLA is roughly 2.5 times smaller than the one determined by the TDM, the resulting elbow moment is also smaller. While the maximum value for the TDM is $M_B(\theta = 10°, \alpha = 1) = 24.28$ kNmm without contact, the absolute maximal value for contact is $M_B(\theta = 10°, \alpha = 1)$ is 22.22 kNmm.

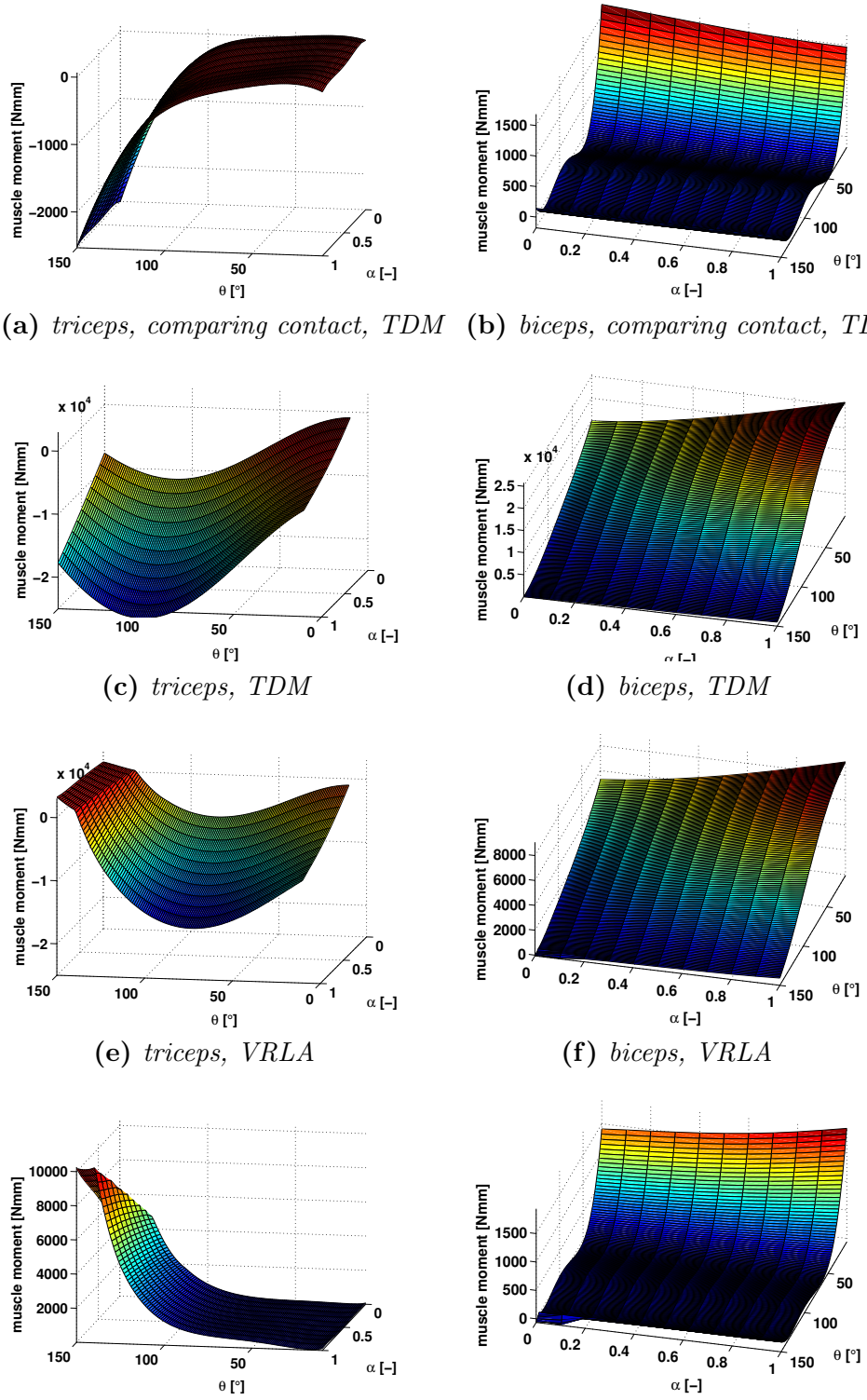

(a) *triceps, comparing contact, TDM* **(b)** *biceps, comparing contact, TDM*

(c) *triceps, TDM* **(d)** *biceps, TDM*

(e) *triceps, VRLA* **(f)** *biceps, VRLA*

(g) *triceps, comparing contact, VRLA* **(h)** *biceps, comparing contact, VRLA*

Figure 9.25: *The resulting triceps moment is plotted versus the muscle activation and elbow angle. The first two rows are determined using the TDM. The lower two rows are determined using the VRLA in addition to considering a changing point of action. For the upper and the lower row, the moment resulting from considering contact is subtracted from the moment resulting from not considering contact to highlight the influence of contact on the resulting moment.*

The moment using the vector-resulting lever arm is $M_B(\theta = 10°, \alpha = 1) = 7.134\,\text{kNmm}$ without contact and $M_B(\theta = 10°, \alpha = 1) = 8.532\,\text{kNmm}$ with contact. As the VRLAis close to constant, the resulting elbow moment is very much resembling the biceps reaction force.

Depending whether the TDM or the VRLA method is used, the influence of the contact formulation on the resulting triceps moment is very different. While the TDM increases the extension potential of the triceps at high flexion angles for 2.5 kNmm, the VRLA acts exactly the opposite and the extension potential reduces up to 10 kNmm for high flexion angles.

The influence of the contact formulation on the resulting biceps moment is quite similar, both in shape and magnitude, for using the TDM and the VRLA.

9.2 Prescribed Forward-Dynamics Model

To analyse the performance of the Upper Limb Model, the two step approach of Section 8.1 is considered. Therefor, in a first step a reference solution is determined. In a second step, one of the four DoFs will be perturbed and the task will be to investigate whether the algorithm converges to the correct equilibrium solution (reference solution). If not stated otherwise, the full MTC muscle model including muscle-bone contact and the lever arms resulting from the tendon-displacement method are used.

First, the equilibrium solution for a particular set of activation parameters α_T and α_B, initial angle θ and applied force F_E is determined. This equilibrium solution shall serve in the following as reference solution. By defining $\theta = \bar{\theta}$, $\alpha_T = \bar{\alpha}_T$, and $\alpha_B = \bar{\alpha}_B$, one can solve Equation (8.2) for the fourth DoF, the external force, $\bar{F}_E$. By choosing $\bar{\alpha}_T = 0.29$, $\bar{\alpha}_B = 0.95$, and $\bar{\theta} = 71.016°$, one obtains with $l_T(\bar{\theta}) = -17.954\,\text{mm}$, $l_B(\bar{\theta}) = 28.311\,\text{mm}$, $l_E(\bar{\theta}) = -141.25\,\text{mm}$, and the resulting muscle forces $F_T(\bar{\theta}, \bar{\alpha}_T) = 503.4\,\text{N}$ and $F_B(\bar{\theta}, \bar{\alpha}_B) = 465.6\,\text{N}$ the external force of $\bar{F}_E = 22.0013\,\text{N}$. Note, the four DoFs marked with $(\bar{\cdot})$ build the reference solution for the subsequent simulations.

Within the next three sections, the numerical tests aim to solve for equilibrium after perturbing individual values for one time step. The perturbation within the different scenarios lead to a non-zero resulting moment. The numerical tests investigate the behaviour of the proposed iteration procedure described in Section 8.1, to find the reference solution, in which the musculoskeletal system is in equilibrium.

To do so, Section 9.2.1 investigates the perturbation of one level of activation for one of the muscles (e.g. the triceps). The initial values for the other DoFs ($\bar{\theta}$, $\bar{\alpha}_B$, and $\bar{F}_E$) are prescribed as determined for the reference solution, cf. Section 8.1.1. Similarly, Section 9.2.2 investigates the perturbation of the elbow angle while the other DoFs are fixed, cf. Section 8.1.2. Section 9.2.3 aims to describe input for successive time steps in order to obtain successive equilibrium positions. The results of the successive steps lead to a "quasi-static" movement. Depending on how the input was evaluated, one can speak of a forward-dynamics simulation.

The results presented within this section will particularly focus on convergence studies within each time step in order to demonstrate that only a few (typically less than 6) iterations are necessary to achieve equilibrium with respect to a certain threshold. As one needs to solve for each time step the governing equations of finite elasticity for the two muscles as well as to take into account the muscle-bone interaction, a low number of

iterations is desired to ensure reasonable computational costs for the overall method.

9.2.1 Position-Driven Scenario

To investigate the numerical behaviour of the position-driven approach, either the triceps or biceps brachii muscle activation is varied. The goal is to investigate if and how quickly Equation (8.1) can be recovered. First, α_T is (randomly) chosen to be 0.20 (instead of $\bar{\alpha}_T = 0.29$, which would provide equilibrium as pre-computed for our reference solution). The results of the iteration process proposed Section 8.1.1 are shown in Table 9.1.

Table 9.1: *Iterative procedure for perturbing α_T from 0.29 to 0.20. The remaining DoFs are kept fixed, i.e., $\bar{F}_E = 22$ N, $\bar{\alpha}_B = 0.95$, $\bar{\theta} = 71.016°$, and $\varepsilon = 10^{-9}$ Nmm. (The results of the level of activation are truncated after three digits).*

iter i	α_T [-]	F_T [-]	F_B [N]	M [Nmm]	$\frac{\Delta M}{\Delta \alpha_T}$ [Nmm]
0	0.190	4.421e+02	4.656e+02	1.561e+03	–
1	0.200	4.483e+02	4.656e+02	1.403e+03	-1.576e+04
2	0.289	5.028e+02	4.656e+02	1.459e+01	-1.559e+04
3	0.290	5.034e+02	4.656e+02	1.600e-01	-1.542e+04
4	0.290	5.034e+02	4.656e+02	2.061e-05	-1.542e+04
5	0.290	5.034e+02	4.656e+02	2.910e-11	-1.542e+04

This particular perturbation (i.e. the perturbation of α_T from 0.29 to 0.20) results in an initial resulting moment of 1403 Nmm. After only two iterations, the level of activation of the triceps brachii deviates by less than 1% from its target solution. After three iteration steps, the resulting moment has decreased to $M = 0.740$ Nmm. The stopping criterion, Equation (8.8), is reached after five iteration steps. The resulting moment is then below 10^{-9} Nmm and the system is in equilibrium. Note, since the elbow position and the level of activation of the biceps have not been changed, the exerted biceps force does remain constant.

Since both, the elbow position and the biceps activation, does not change, the biceps force does not change either. The last column in Table 9.1, the differential quotient, defined in Equation (8.5), which describes the secant of the approximation, is shown. The first value of $\frac{\Delta M}{\Delta \alpha_T}$ is already a quite good approximation of the change as it remains almost constant for the entire iteration process.

Like for the triceps, the level of activation of the biceps brachii has been perturbed from $\bar{\alpha}_B = 0.95$ to $\alpha_B = 0.56$. The remaining DoFs are kept fixed and the iteration process for a position-driven scenario (cf. Section 8.1.1) is employed. The results are shown in Table 9.2.

Within this test case, there exists an initial resulting moment of -4903 Nmm. After three iteration steps, the absolute value of the resulting moment is less than 2 Nmm and the level of activation deviates from its exact solution by approximately 0.2%. After six iteration steps, the convergence requirement of $M^{(6)} < 10^{-9}$ Nmm is met. While this is one more iteration step than for the results of perturbing the level of activation for the triceps, it should be noted that the perturbation of the second example represents a larger relative change, i.e. $\Delta\alpha_B = 0.4$. The triceps force does not change as θ and α_T are

Table 9.2: *Iterative procedure for perturbing α_B from 0.95 to 0.56. The remaining DoFs are kept fixed, i.e. $\bar{F}_E = 22$ N, $\bar{\alpha}_T = 0.29$, $\bar{\theta} = 71.016°$, and $\varepsilon = 10^{-9}$ Nmm. (The results of the level of activation are truncated after three digits).*

iter i	α_B [-]	F_T [-]	F_B [-]	M [Nmm]	$\frac{\Delta M}{\Delta \alpha_B}$ [Nmm]
0	0.550	5.034e+02	3.435e+02	-4.903e+03	–
1	0.560	5.034e+02	3.468e+02	-4.773e+03	1.309e+04
2	0.925	5.034e+02	4.584e+02	-2.911e+02	1.229e+04
3	0.948	5.034e+02	4.652e+02	-1.821e+01	1.152e+04
4	0.950	5.034e+02	4.656e+02	-6.736e-02	1.148e+04
5	0.950	5.034e+02	4.656e+02	-1.544e-05	1.147e+04
6	0.950	5.034e+02	4.656e+02	-1.091e-11	1.147e+04

constant. In the last column, the differential quotient $\frac{\Delta M}{\Delta \alpha_B}$ is shown. As the moment is negative, the slope of the differential quotient is positive.

9.2.2 Activation-Driven Scenario

Similar results are observed, for perturbing the initial angle and keeping fixed the levels of activation, $\bar{\alpha}_T$ and $\bar{\alpha}_B$, and the external force, $\bar{F}_E$. To demonstrate this, the angle θ is perturbed from $\bar{\theta}$ to $\theta = 99°$ while the remaining DoFs remain as in the reference solution. Then, the iterative procedure described in Section 8.1.2 is employed. The results are presented in Table 9.3.

Table 9.3: *Iterative procedure for perturbing θ from $\bar{\theta}$ to $\theta = 99°$. The remaining DoFs are kept fixed, i.e., $\bar{F}_E = 22$ N, $\bar{\alpha}_T = 0.29$, $\bar{\alpha}_B = 0.95$, and $\varepsilon = 10^{-9}$ Nmm.*

iter i	θ [°]	F_T [N]	F_B [N]	M [Nmm]	$\frac{\Delta M}{\Delta \theta}$ [Nmm/°]
0	60.000	4.270e+02	5.199e+02	4.668e+03	–
1	99.000	6.552e+02	3.003e+02	-1.053e+04	-3.896e+02
2	71.981	5.098e+02	4.605e+02	-4.059e+02	-3.745e+02
3	70.897	5.026e+02	4.662e+02	5.002e+01	-4.207e+02
4	71.016	5.034e+02	4.656e+02	-7.541e-02	-4.213e+02
5	71.016	5.034e+02	4.656e+02	-1.322e-05	-4.213e+02
6	71.016	5.034e+02	4.656e+02	7.276e-12	-4.213e+02

After perturbing the elbow angle by $\Delta\theta = +27,984°$, a resulting moment of -$1.053{\cdot}10^4$ Nmm is computed. After the first iteration, the angle deviates already by less than 1°. While the absolute difference of the angle θ between the second iteration and the exact solution is already less than 0.12°, the stopping criterion based on the moment ($|M^{(i)}| < 10^{-9}$ Nmm) is not reached until completing the fifth iteration. As the exerted muscle force of both muscles depends on the elbow angle and the contact between the muscle and bone, the muscle forces for both muscles need to be re-computed at every iteration step.

9.2.3 Force-Driven Scenario

For the force-driven approach, three successive external forces are defined and applied at three distinct "time" instances. For each external load, similar convergence procedures, to the ones presented in Section 8.1.1 and 8.1.2, are following each other. After finding the equilibrium within one time instance, the external force is changed to a different level and the equilibrium seeking procedure is repeated. For the first external load, the system converges as shown in the last two sections. Yet, for the following external loads, the last solution of the last external load is chosen as starting configuration. Hence, one reuses the resulting moment for the differential quotient. In case of the activation-driven example, an increase in external load reflects a lowering, i.e. a reduction in elbow angle, while a decrease in external load leads to flexion, i.e. an increase in elbow angle.

To demonstrate this behaviour and the ability to quickly converge, an initial external load of $F_E|_{t=1} = 21\,\mathrm{N}$ is assumed. In the following time steps, the external load is first increased to $F_E|_{t=2} = 41\,\mathrm{N}$ before it is lowered to $F_E|_{t=3} = 5\,\mathrm{N}$.

The first example is a position driven scenario where the triceps activation is selected to be the DoF. The prescribed values, which are not changing throughout the example, are the elbow angle, $\theta = 66.4$, and the biceps activation, $\alpha_B = 0.95$. The external load, F_E is changing with each time step. The initial triceps activation is chosen to be $\alpha_T = 0.19$

Table 9.4 presents the results for the iterations of each time step. Respectively, 6, 7, and 7 steps are required per time step to satisfy a convergence criterion of $\varepsilon = 10^{-9}$ Nmm. For the first time instance, i.e. with an external load of $F_E|_{t=1} = 21\,\mathrm{N}$, the system converged for $\alpha_T = 0.440$. After detecting the equilibrium for the first condition, the differential quotients raises dramatically to find its adequate value after one or two more iteration steps. For the second and third external load condition, the system converged for an triceps activation of $\alpha_T = 0.099$ and $\alpha_T = 0.744$, respectively. Note that, for every time instance other than the first one, the initial values ($i = 0$) are needed to determine the secant within the iteration procedure. For $t > 1$, the initial condition stem from the equilibrium position of the previous time instance.

Even though the number of iteration steps might be large, it does not need to relate to the computation time. Iteration steps with close to no change in their conditions do not take much computational effort as the first guess for that iteration step is already close to the solution.

The second example is an activation driven scenario where the elbow angle is selected to be the DoF. The prescribed values, which are not changing throughout the example, are the biceps activations and the triceps activation $\alpha_T = 0.29$ and $\alpha_B = 0.95$, respectively. Again, the external load, F_E is changing with each time step. The initial elbow angle is chosen to be $\theta = 0.60$.

Table 9.5 presents the results for each iteration. Again, only 6 iterations are needed to satisfy the convergence criterion with $\varepsilon = 10^{-9}$ Nmm. For the first time instance with an external load of $F_E|_{t=1} = 21\,\mathrm{N}$, the system converged for $\theta = 71.654°$. For the second and third external load conditions, the system converged for an elbow angle of $\theta = 60.041°$ and $\theta = 82.659°$, respectively.

The differential quotient can be seen as the convergence rate. This can also be seen in Figure 9.26, which graphically depicts the results of Table 9.5. The red line marks the convergence limit of $10^{-9}\,\mathrm{Nmm}$. After the sixth iteration step, the convergence limit is passed, the load condition is changed and the resulting moment raises immediately.

Table 9.4: *Converging procedure of the Upper Limb Model where α_T is the DoF. The other DoFs are prescribed to be, $\theta = 66.4$, $\alpha_B = 0.95$, while F successively take three different values, $F_E = 21, 41, 5\,N$. The converging criterion is chosen to be less than 10^{-9} Nmm.*

iter i	α_T [-]	F_T [-]	F_B [-]	M [Nmm]	$\frac{\Delta M}{\Delta \alpha_T}$ [Nmm]
Time step 1 with force $F_E(t=1) = 21\,\mathrm{N}$					
0	0.190	4.118e+02	4.892e+02	3.749e+03	0
1	0.200	4.179e+02	4.892e+02	3.594e+03	-1.551e+04
2	0.432	5.541e+02	4.892e+02	1.145e+02	-1.502e+04
3	0.439	5.584e+02	4.892e+02	4.500e+00	-1.443e+04
4	0.440	5.586e+02	4.892e+02	6.733e-03	-1.441e+04
5	0.440	5.586e+02	4.892e+02	3.976e-07	-1.441e+04
6	0.440	5.586e+02	4.892e+02	-3.638e-12	-1.441e+04
Time step 2 with force $F_E(t=2) = 41\,\mathrm{N}$					
0	0.440	5.586e+02	4.892e+02	-5.177e+03	1.865e+19
1	0.440	5.586e+02	4.892e+02	-5.177e+03	1.000e+06
2	0.445	5.615e+02	4.892e+02	-5.252e+03	-1.439e+04
3	0.080	3.443e+02	4.892e+02	2.951e+02	-1.520e+04
4	0.099	3.563e+02	4.892e+02	-1.008e+01	-1.572e+04
5	0.099	3.559e+02	4.892e+02	-5.394e-03	-1.571e+04
6	0.099	3.559e+02	4.892e+02	1.149e-07	-1.571e+04
7	0.099	3.559e+02	4.892e+02	3.638e-12	-1.571e+04
Time step 3 with force $F_E(t=3) = 5\,\mathrm{N}$					
0	0.099	3.559e+02	4.892e+02	9.319e+03	3.950e+19
1	0.099	3.559e+02	4.892e+02	9.319e+03	-3.084e+04
2	0.401	5.365e+02	4.892e+02	4.705e+03	-1.527e+04
3	0.709	7.029e+02	4.892e+02	4.552e+02	-1.379e+04
4	0.742	7.197e+02	4.892e+02	2.690e+01	-1.298e+04
5	0.744	7.207e+02	4.892e+02	1.320e-01	-1.291e+04
6	0.744	7.207e+02	4.892e+02	3.674e-05	-1.291e+04
7	0.744	7.207e+02	4.892e+02	5.093e-11	-1.291e+04

The steepness of the line segments between to iteration steps visualises the value of the differential quotient. For example, the steep increase at $i = 0|_{t=2}$ is the high value of $\frac{\partial M^{(i)}}{\partial \alpha_T} = -1.258 \cdot 10^{17}\,\mathrm{Nmm}$. The jump back to a large resulting moment is due to changing the external load.

Instead of changing the external force, F_E, it is also possible to successively change the muscle activation. If, for example, the biceps activation is successively increased, the forearm would raise.

9.2.4 Comparing the Resulting Equilibrium Angles

So far, Section 9.2 proved numerical evidence that the Upper Limb Model can find equilibrium positions. The presented convergence procedures of Section 9.2 used the displacement determined lever arms and the muscle reaction forces of the MTC model including tendon tissue.

It is left to investigate whether the method with which the lever arms are determined has an influence on the resulting equilibrium and how strong it is. As the resulting elbow moment is a sum of the products of the muscle reaction force and the muscle lever arm,

Table 9.5: *Iterative procedure for assuming three different external loads and seeking the resulting elbow angles while assuming constant values of $\alpha_T = 0.29$ and $\alpha_B = 0.95$. The external force, F_E, successively takes three different values, $F_E = 21, 53, 5\,N$. The converging criterion is met if the resulting momenent is less than 10^{-9} Nmm.*

iter i	θ [°]	F_T [N]	F_B [N]	M [Nmm]	$\frac{\Delta M}{\Delta \theta}$ [Nmm/°]
Time step 1 with force $F_E(t=1) = 21\,\mathrm{N}$					
0	60.000	4.270e+02	5.199e+02	4.912e+03	0
1	100.00	6.589e+02	2.939e+02	-1.055e+04	-3.865e+02
2	72.710	5.147e+02	4.566e+02	-4.416e+02	-3.703e+02
3	71.518	5.067e+02	4.630e+02	5.712e+01	-4.182e+02
4	71.654	5.077e+02	4.622e+02	-9.921e-02	-4.189e+02
5	71.654	5.077e+02	4.622e+02	-2.099e-05	-4.189e+02
6	71.654	5.077e+02	4.622e+02	1.819e-11	-4.189e+02
Time step 2 with force $F_E(t=2) = 41\,\mathrm{N}$					
0	71.654	5.077e+02	4.622e+02	-5.363e+03	-1.258e+17
1	71.654	5.077e+02	4.622e+02	-5.363e+03	-5.973e+02
2	62.676	4.459e+02	5.074e+02	-1.233e+03	-4.600e+02
3	59.997	4.269e+02	5.199e+02	2.106e+01	-4.679e+02
4	60.042	4.273e+02	5.197e+02	-2.494e-02	-4.684e+02
5	60.041	4.273e+02	5.197e+02	-2.454e-07	-4.684e+02
6	60.041	4.273e+02	5.197e+02	-7.276e-12	-4.684e+02
Time step 3 with force $F_E(t=3) = 5\,\mathrm{N}$					
0	60.041	4.273e+02	5.197e+02	8.811e+03	-6.200e+17
1	60.041	4.273e+02	5.197e+02	8.811e+03	-7.680e+02
2	71.514	5.067e+02	4.630e+02	4.345e+03	-3.893e+02
3	82.677	5.766e+02	4.009e+02	-6.918e+00	-3.899e+02
4	82.660	5.765e+02	4.010e+02	-1.491e-01	-3.815e+02
5	82.659	5.765e+02	4.010e+02	8.047e-06	-3.815e+02
6	82.659	5.765e+02	4.010e+02	3.638e-12	-3.815e+02

there are different combinations possible to yield the elbow moment. So far, three different possibilities to determine the lever arms have been presented:

1. tendon-displacement method (TDM),
2. vector-resulting lever arm method (VRLA), and
3. vector-resulting lever arm method including the replacement of the point of action (VRLA+).

Just considering the MTC muscle model, the muscle reaction forces have been determined either by:

1. considering the effects of contact or by
2. not considering the effects of contact.

In the author's opinion, the rigid-tendon model will not give any further insights. As the rigid-tendon model is just a model simplification without systematic differences, the resulting forces are similar to each other. Hence, no further studies are considered.

In Figure 9.27a, the resulting equilibrium angles are plotted using the TDM, the VRLA method, and the VRLA+ method with considering contact. The prescribed values are

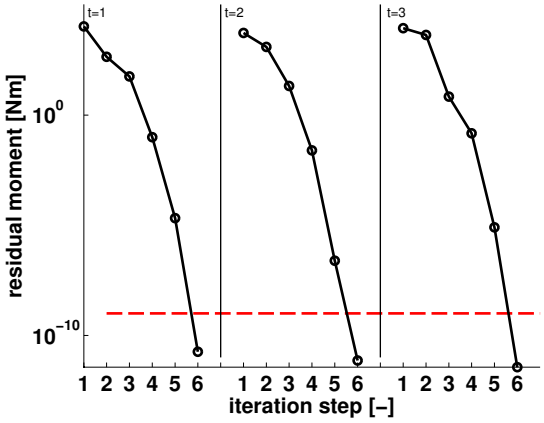

Figure 9.26: *Convergence study of the Upper Limb Model for the same set up as depicted in* Table *9.3. The results are plotted in a semi-log in a semi-log scale. The convergence criterion of* $\varepsilon = 10^{-9}$ *Nmm is indicated by the dashed, red line.*

$\bar{F}_E = 20\,\mathrm{N}$ and a varying set of muscle activations. Within that plot, each vertex is a result of a simulation as presented in Table 9.3. The chosen scenario is just one snap shot. The equilibrium angles can be increased or decreased by varying the external force. As, it will be outlined in the next paragraph, the difference between the equilibrium angle of the different cases is about 40° and hence restricts the choice of other adequate scenarios. The selected scenario is only a small excerpt, yet represents a reasonable sample.

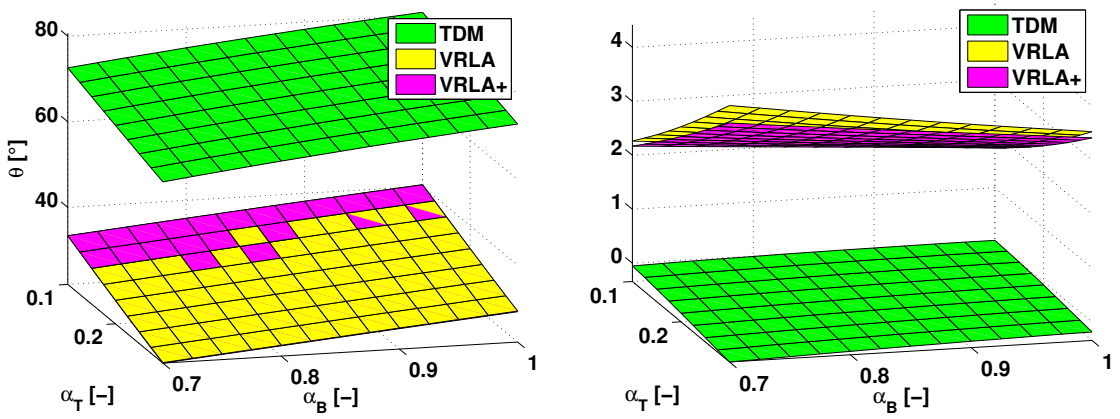

(a) *equilibrium angle, including contact* **(b)** *comparing the influence of contact*

Figure 9.27: *The resulting equilibrium elbow angle determined for a varying set of muscle activations (x- and y-axis) using* $\bar{F}_E = 20\,N$. *The muscle forces are determined using the full MTC model and considering contact (left). The right depicts the difference between including and not including the effects contact for the three different cases.*

It can be seen in Figure 9.27a that the resulting equilibrium angle for the TDM is in the range of $\theta = 60° - 80°$ while the equilibrium for the other two cases ranges between $\theta = 20° - 40°$. The difference between the to equilibrium angle resulting from the TDM and the VRLA/VRLA+ method is around 40°. This is due to the fact that the biceps'

(flexor) lever arm resulting from the TDM is roughly four-times larger than the one resulting from the VRLA method. The other two methods have very similar equilibrium angles. In this elbow range, the triceps' (extensor) lever arm is roughly the same for all methods. For the VRLA method the influence of the updated point of action is included but only plays a minor role. The magenta surface and yellow surface are very similar.

Figure 9.27b depicts the importance of the contact for each case. This is done by subtracting the equilibrium angle obtained from the different methods from each other. As it can be seen, the effects of contact play a minor role for the TDM, especially for the range investigated in this example ($60° < \theta < 80°$). For the VRLA method, contact is more important and changes the equilibrium angle by 2-4°. There are two possible reasons: (i) The scenario is in an elbow range where contact becomes more influential. (ii) The influence of contact on the lever arm is more pronounced for the triceps, see Figure 9.23. As the difference between the second and the third case is small, it is assumed that the effects of contact are influencing both possibilities to the same extend.

Figure 9.28a compares the different methods with each other by depicting the difference of the results using the VRLA method and the TDM. Figure 9.28b compares the results obtained from the vector-resulting lever arm method with and without including the offset of the point of action by subtracting the equilibrium angles from each other. Figure 9.28 shows the difference for considering and not considering contact.

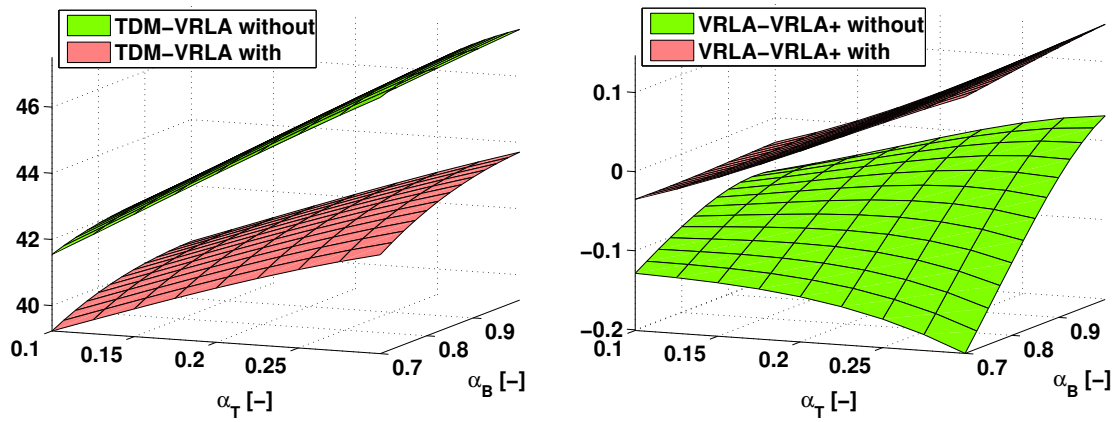

(a) *subtracting the results of the TDM case from the VRLA case*

(b) *subtracting the results of the VRLA+ from VRLA*

Figure 9.28: *Subtracting the results of different cases to see the impact of the different phenomena. Green presents the case when no muscle-bone contact is considered and magenta when contact is taken into account.*

The already mentioned deviation of about 40° between the VRLA method and the TDM can be nicely seen. Furthermore, it can be seen that the effects of contact influence the equilibrium angle by about 2° in Figure 9.28a. The relocation of the point of action has only a minor influence (see Figure 9.28b). The deviation is in the range of 0.1°. The difference between considering contact has also only a minor impact on the resulting equilibrium angle. The results are only deviating by less than 0.3°.

It worth noting again that the change in the point of action cannot be considered with the TDM as it derives the lever arm by just using the muscle length. If the proximal

and distal relocation of the points of actions are considered, the muscle length would only change by negligible amount and the influence on the lever arm would be even smaller.

9.3 EMG-driven Forward-Dynamics Model

To obtain time-dependent activation dynamics from experiments, the experimental data need to be processed. This is done by the forward-inverse model proposed by Buchanan et al. (2004). By processing the raw EMG of the different muscles, the forward-inverse model determines next to the muscle activation also the acting elbow torques and reaction forces of the muscles. These data can be used within the Upper Limb Model and the measured moments and motion can then be subsequently used for validation.

The forward-inverse model, introduced in Section 8.2.5, consists of

- an OpenSim model, providing the model's kinematics,
- the activation dynamics, converting raw EMG into muscle activation,
- the forward-dynamics model,
- the inverse-dynamics model,
- the optimiser, minimising the difference between the results of the forward- and inverse-dynamics method by changing parameters of the activation dynamics and muscle dynamics, and last but not least,
- the experimental data, which serve as model input.

In Section 9.3.1, the results of the forward-inverse model are presented whereas in Section 9.3.2, the muscles' reaction forces of the forward-inverse model are replaced by those of the Upper Limb Model.

9.3.1 Results of the Forward-Inverse Model

During the measurements, both EMG trains and elbow moments are measured using different frequencies, see Section 8.2.1. During the processing phase, the frequencies for the different data are matched. The elbow moment can directly be measured and is used as golden standard for the results of the forward-inverse model. Figure 9.29 shows the data train of the measured torques and the torque resulting from the forward-dynamics model. The experimental data, measured by a Biodex, is the reference solution and is represented by the blue lines. The green lines in Figure 9.29a and 9.29b are the elbow moments resulting from two different calibration procedures. The spiky appearing data are composed by stringing together separate trials. The first trial (spike) is conducted at $\theta = 10°$ with 100% effort, whereas the second trial is conducted at the same elbow angle but with half the effort. Naturally, the 50% effort is hard to estimate for the proband. The sequence is continued with alternating effort at increasing elbow angles of $\Delta\theta = 10°$ steps. The last trial, starting after about 10.000 time frames, is the passive trial. Here, the arm is moved by the Biodex three times over the full range of motion. It is used to investigate the passive properties of the subject's musculoskeletal system.

The difference between the trails in Figure 9.29 cannot be seen very easily. Yet, when details are closely compared, differences become apparent. In general, it can be said that the partial effort is reproduced better by the forward-inverse model. For the full

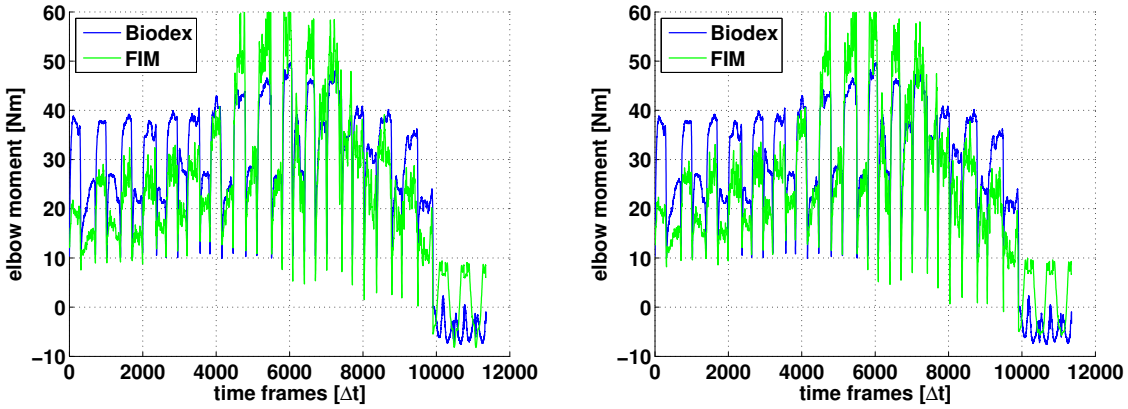

(a) *calibration procedure one* **(b)** *calibration procedure two*

Figure 9.29: *The continuous moment measured by the Biodex (blue) and resulting from the forward-inverse model (green) from different calibration procedures. The first trial (spike) is conducted at $\theta = 10°$ with 100% effort whereas the second trial with 50% effort. The sequence is continued with alternating effort at increasing elbow angles in $\Delta\theta = 10°$ steps.*

effort trials, in particular for $80° \leq \theta \leq 120°$, the measured elbow moments are overestimated whereas for smaller and larger elbow angles the measured elbow moments are underestimated.

When the results of the isokinematic trials are considered, which are not visualised here, it can be seen that the flexing part of the motion is better approximated as the extending part.

The time series for the isometric trials can be averaged to one value per trial. Hence, all but the last trial, which is the passive movement, can be condensed to a single mean value. For the full effort trials, the resulting mean is shown in Figure 9.30. Again, the measured torque is the blue curve and the results of the forward-dynamics model is depicted in green. As different calibrations produce different results, two calibrations are shown, exemplary. The average of the two calibrations is depicted by the black curve. It can be seen that the difference between the two different calibration procedures is very small. Hence, it will not be further differentiated between different calibration procedures. Furthermore, the presented results are always the mean of the two calibration procedures from here on.

In order to extract the muscle activation and the muscle forces from the forward-inverse model, the model solves the *Newton-Euler* equations for each time increment. Hence, a time continuous series of data for the resulting muscle activation and resulting muscle reaction force does exist for each trial. Exemplarily, Figure 9.31a and 9.31b show the time series for the full effort trial at $\theta = 10°$ of the first calibration procedure.

The muscle activation ramps up from the resting state to reach its isometric contraction state. For the data processing, the toe region in the beginning and the end is cut off by selecting a threshold criterion which demands a certain elbow torque requirement. Hence, a relatively nice plateau region is left for the investigations. For the results of Figure 9.31, the flexor activation is in the range between 40 – 60% while the extensor activation is around 20%.

The resulting muscle forces are of course coupled to the muscle activation by the muscle

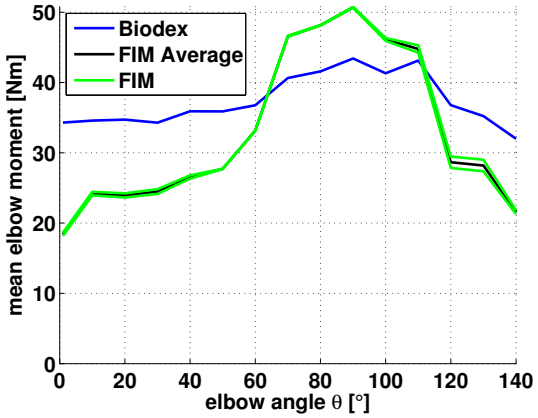

Figure 9.30: *The blue curve shows the mean value of the isometric 100% effort trials for the experimental data. The green curves show the from the forward-inverse model simulation resulting moment determined by two different calibration procedures. The black curve is the mean from the two green curves.*

dynamics. Within Figure 9.31b, the biceps is the strongest muscle with muscle forces of about 1100 N, followed by the brachialis with around 600 N, and the brachioradialis and the triceps with about 180 N.

The information of each isometric trial is condensed to a muscles' mean value as it is done for the torque data. The cut-off criterion is determined by the torque and the average is determined by the remaining time frames. The result of taking the mean of each isometric trial is shown in Figure 9.32. For these two figures, only the full effort trials are used. The muscle activations are not fluctuating strongly throughout the different trials. Exceptions are the biceps activation changing from 54% at $\theta = 110°$ to 26% at $\theta = 120°$ and the brachialis activation changing from 44% at $\theta = 60°$ to 63% at $\theta = 70°$.

Except from the biceps' activation, the activation of the other muscles are not fluctuating strongly throughout the different trials.

Due to the fluctuation of the muscle activation, the resulting muscle force curves are also fluctuating. As the proband was asked to pull, the triceps activation is the lowest, the other muscle are around 0.5 (even though the proband was asked to pull as strong as he can!).

As the resulting active muscle forces are increasing for extending muscles, it can also be concluded, that the muscles of the forward-inverse model are only acting on the ascending part of the force-length relation. Otherwise, the active force ought to reduce or at least stagnate.

9.3.2 Comparing the Results of the Forward-Inverse Model and the Upper Limb Model

One possibility to compare the results of the forward-inverse model to the results of the Upper Limb Model is to reproduce the results of the forward-inverse model using the Upper Limb Model. Therefore, the triceps and biceps muscle force of the forward-inverse model is substituted by the ones generated by the Upper Limb Model. In order to generate comparable results, the FE simulation apply the activation and the elbow angle

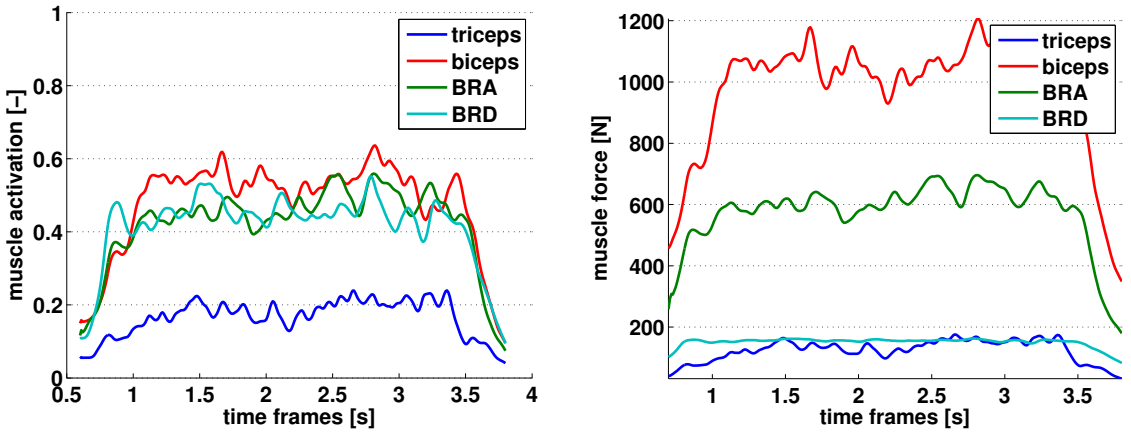

(a) *muscle activation* **(b)** *muscle force*

Figure 9.31: *Example of an isometric contraction with full effort at $\theta = 10°$. The muscle brachialis and brachioradialis are abbreviated with BRA and BRD, repectively.*

determined by the forward-inverse model to the muscles of the Upper Limb Model.

The results are shown in Figure 9.33. Like in Figure 9.30, the blue curve represents the measurements, the green one represents the forward-inverse model result, and the black one represents a combination of the Upper Limb Model muscles with the brachialis and brachioradialis from the forward-inverse model. Within the next figures, the results of the forward-inverse model are abbreviated by "FIM" and the one of the combination of Upper Limb Model and forward-inverse model by "ULM". The lever arm and the muscle forces for triceps brachii and biceps brachii from the forward-inverse model are substituted by the results of the Upper Limb Model while brachialis and brachialis are still used from the forward-inverse model. It is already mentioned that the results of the forward-inverse model are not perfectly reproducing the measurements. The results obtained from combining the muscle forces of Upper Limb Model and the forward-inverse model are even further off. Yet, the error can be characterised by a parallel shift. Whereas the results of the forward-inverse model are deviating in both directions.

So far, none of the two models is able to adequately represent the experimental data. An attempt to improve the resulting moment including the Upper Limb Model's muscle is conducted by increasing the active part of the muscle force. It is increased from $\sigma_{\max} = 300\,\text{kPa}$ to $\sigma_{\max} = 350, 400$, and $500\,\text{kPa}$.

In Figure 9.34a the muscle forces resulting from the forward-inverse model are compared to the one of the Upper Limb Model. As expected, the resulting muscle forces are also increasing with increasing $\sigma_{\max}$. Hence, it is not surprising that the improvement, seen in Figure 9.34 is not large but tends to go in the right direction. The triceps force is with $\sigma_{\max} = 300\,\text{kPa}$ already quite close to the muscle force of the forward-inverse model. For the biceps, increasing $\sigma_{\max}$ is not enough to close the gap between the continuum-mechanical model to the *Hill* muscle.

In Figure 9.34b, the four black lines are the result of the four differently used $\sigma_{\max}$. As for each curve both muscles use the same $\sigma_{\max}$, the curves are improving on one side – where the flexor is strengthened – and worsen on the other side – where the extensor is strengthened.

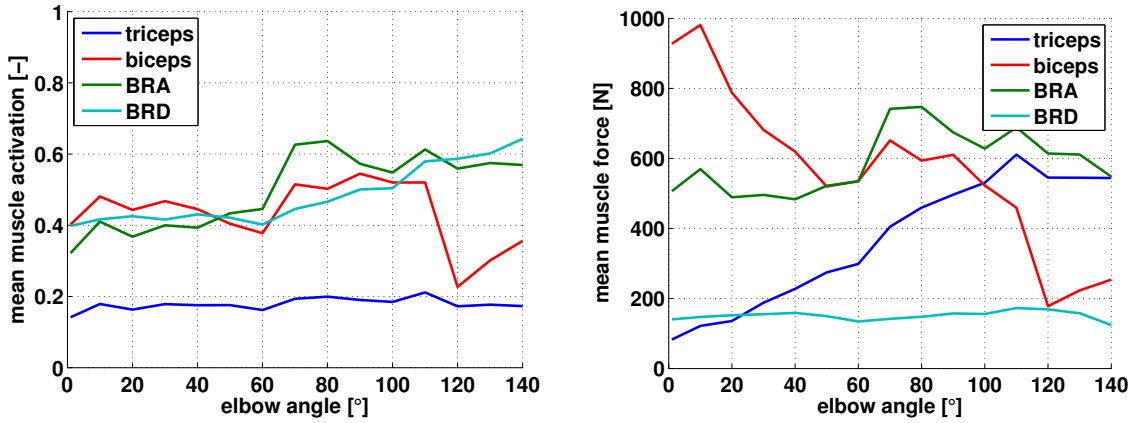

(a) *averaged muscle activation* **(b)** *averaged muscle force*

Figure 9.32: *Averaged muscle activation and force for the 100% effort trials and the participating muscles.The muscle brachialis and brachioradialis are abbreviated with BRA and BRD, repectively.*

In Figure 9.35, the strong flexor and the weak extensor is chosen to improve the elbow moment. The black line is generated by choosing $\sigma_{\max} = 300\,\text{kPa}$ for the triceps and $\sigma_{\max} = 500\,\text{kPa}$ for the biceps. Even though, there is still a gap between the Biodex and the Upper Limb Model, the result is further improving. The trend is at least better than the one produced by the forward-inverse model. Further adjustments could be done by increasing the biceps prestretch or increasing the biceps volume.

Note, a limitation of the procedure is that the geometry of the Upper Limb Model is taken from the virtual human male. The forward-inverse model framework employs the author of this thesis to scale the OpenSim and to conduct the experiments.

One possibility to compare situations at arbitrary locations could be achieved by interpolating the resulting muscle forces and muscle activations of the forward-inverse model. The mean muscle forces resulting from the 100% effort trials are used to fit second-order polynomials. The resulting fits for the muscle forces are depicted in Figure 9.36.

The resulting approximations are a very rough fit, as the muscle forces are fluctuating strongly due to the also fluctuating muscle activations. Yet, the resulting curves seem to be quite reasonable.

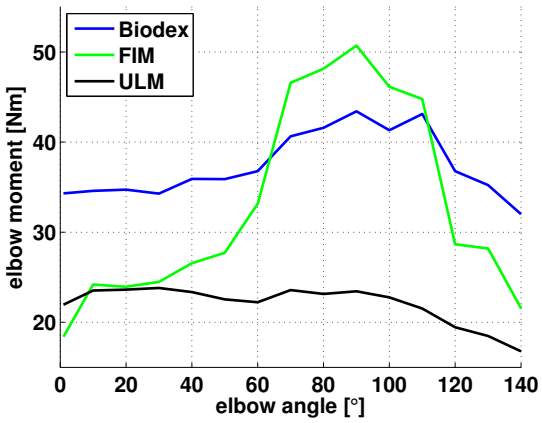

Figure 9.33: *Comparing the model results. The blue curve is the Biodex data. The green curve is the result of the forward-inverse model (FIM). The black curve is the result of using the muscle forces from the Upper Limb Model (ULM) using* $\sigma_{\max} = 300\,kPa$.

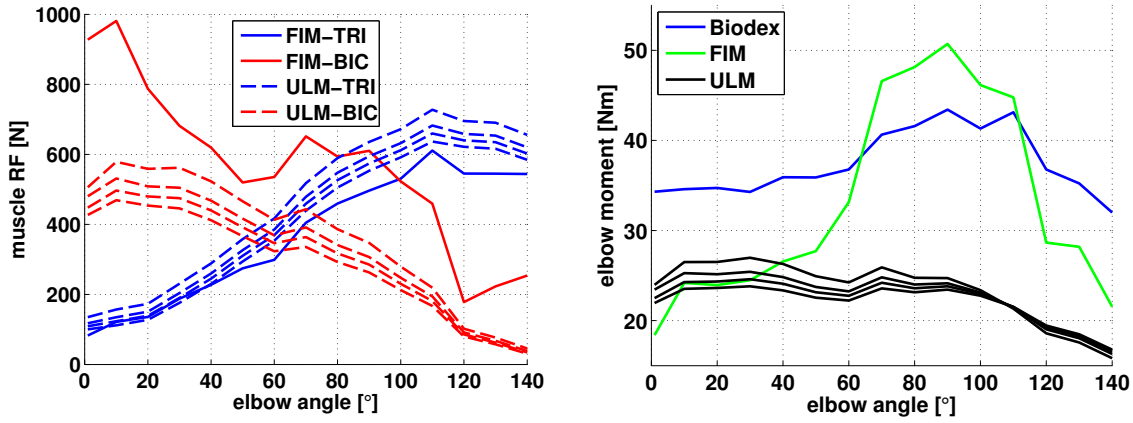

(a) *triceps and biceps muscle reaction force* **(b)** *resulting model elbow moments*

Figure 9.34: *To investigate the influence the Upper Limb Model muscle reaction forces on the resulting elbow moment,* $\sigma_{\max}$ *is changed from 300 kPa to 350, 400, and 500 kPa. As the flexor and extensor are changed to both extend, the model improvement is limited.*

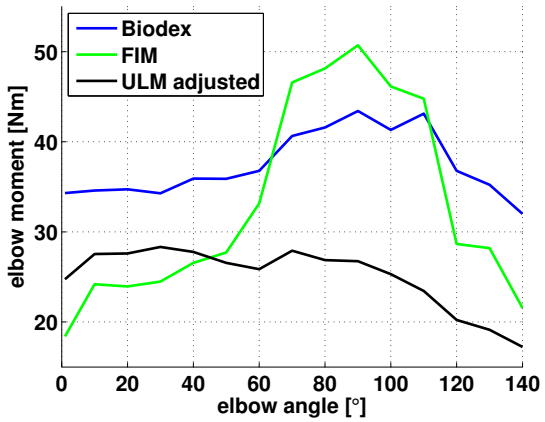

Figure 9.35: *Using the strengthened biceps ($\sigma_{\max} = 500\,kPa$) and the weak triceps $\sigma_{\max} = 300\,kPa$, the Upper Limb Model resulting elbow moment can be improved considerably.*

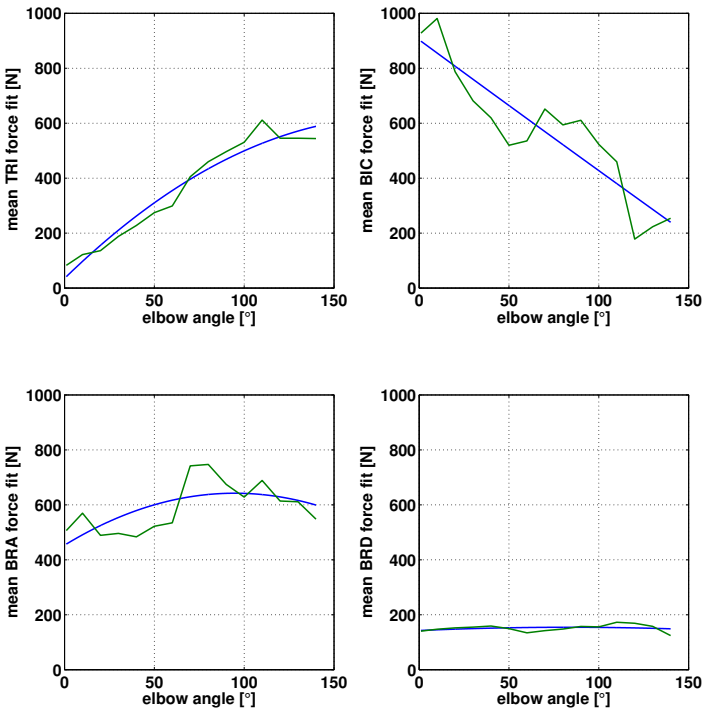

Figure 9.36: *Polynomial fit to the from the forward-inverse model resulting muscle forces. The abbreviations used are TRI for triceps, BIC for biceps, BRA for brachialis, and BRD for brachioradialis.*

10 Discussion

This work presents a first attempt to model a part of the musculoskeletal system using a continuum-mechanical approach. The Upper Limb Model and its equivalent static system is a strongly simplified model. Yet, it enables first investigations of an antagonistic muscle pair acting within a realistic musculoskeletal system. As it is the first investigation of its kind, there are no studies or methods to compare with. The author will outline the assumptions this model is based on and report on the resulting benefits and drawbacks. As the results are already presented and to some degree discussed in Section 9, this chapter will focus on the model assumptions, model limitation and the concatenation of the results. The discussion is methodologically differentiated into different sections.

Mechanical Model

The Theory of Finite Elasticity has proven to provide an adequate framework for the continuum to represent large deformations occurring in soft biological tissues such as skeletal muscles. In combination with the finite element method, which provides a well developed and powerful discretisation method, biological soft tissue such as muscles, inner organs, skin, bone, and close to everything else could be mechanically investigated.

Furthermore, the finite element method enables to modularly include a contact formulation. In this case here, contact is defined to occur between the skeletal muscle tissue and the bones, which are assumed to be rigid.

Muscle-bone contact forces can be several hundreds of *Newton*s, see Figure 9.14. The *Coulomb* friction coefficient between bone and muscle are about 0.3, see (Shacham et al., 2010). As soft tissues between the biceps and the triceps brachii and the humerus are not considered, it is uncertain whether the model correctly represents the contacting surfaces and whether the model predictions are in good agreement with reality. However, experimental measurements of these contact forces are nearly impossible. This is certainly true for the superficial biceps brachii, which is just of other flexor muscles adjacent to the humerus and the biceps's muscle tissue. Due to these deficiencies, the restriction of a frictionless contact formulation is considered to be acceptable. The advantage of the chosen framework is that it provides a way to in silico investigate the impact of friction between muscle and bone may be.

Within the considered model, contact between muscles does not occur, as the humerus separates the considered muscles. This is no longer true,if multiple muscles are considered. Even though, muscle-muscle contact would be challenging, it should be considered when synergistic muscles effects are taken into account in an extended model. Further, considering bone-bone contact within the joint would provide additional realism, but also tremendously increase the complexity of the model. However, to make the joint movement realistic and natural, the surrounding tissue (i.e. ligaments, cartilage, and further muscles) that restrains and pulls needs to be included. Hereby, both the model complexity as well as the model DoFs would increase to a degree, which makes the model nearly unsolvable.

Speed-ups are possible, but they require the optimisation of the existing code, use an analytical tangent, and/or the use of massively parallel simulations on larger computer cluster.

Muscle Model

The muscle tissue's constitutive model is based on approaches without further innovations. The muscles' activation state is a scalar-valued function, which is spatially not varying. The addition of a more complex activation-dynamics model, such as, for example introduced by Heidlauf and Röhrle (2014), would increase the numerical costs and complexities without any methodological effect on the multi-muscle musculoskeletal system.

The muscle model, established in Section 4.3, is adequate to represent the rigid-tendon model consisting of only muscle tissue. Only two more material parameters, namely γ^{M} and γ^{ST} are needed, to extend the rigid-tendon model to represent next to muscle tissue also tendon, and other soft tissue, see of Section 4.4. The stiffness of tendon tissue is about a thousand times higher than the stiffness of muscle tissue. The physiological strain of tendons is smaller than 5%. The muscle's strain raises easily up to 50%. Locally, due to highly different material behaviour, the numerical challenge becomes considerable. Yet, macroscopically, when the muscle belly gradually tapers and changes towards tendon tissue, the connective tissue ratio increases while the cross-section area reduces. Therefore, as the tendon cross-section is much smaller than the muscle belly cross-section, the overall stiffness of the different muscle compartments may not change as dramatically as the relative material stiffness may indicate. Furthermore, a change of the muscle's level of activation changes the ratio between muscle and tendon tissue stiffness changes. It was observed, that while the muscle belly's stiffness is weaker than the tendons' stiffness for low activation, the stiffness ratio may assimilate for muscle activations close to one.

As there is hardly any data available for describing the muscle-connective tissue ratio, a possibility to overcome that absence of information is to relate the change of the muscle cross-section area to the muscle-connective tissue ratio (Sprenger et al., 2013). Thereby, the transition zones can be used to define a gradual change of the material parameter, γ_{M}. Though, due to the large difference in the stiffness between the muscle and the tendon tissue, special care has to be taken by defining a transition zone to achieve realistic deformations, realistic muscle reaction forces, and a robust finite element simulation.

The material parameters for the passive contribution of the material law could be determined by fitting the presented relations to experimental data. Yet, it was necessary to increase c_1 by a factor of 10^2 to prevent numerical stability issues. Not increasing c_1 leads to a too large ratio between the along-fibre stiffness and the transverse-fibre stiffness. As a consequence of increasing the isotropic parameter, the muscles bulk behaviour prediction is too stiff. This is especially true for the compressive region. Here, it is assumed that the muscle tissue behaves much softer. Unfortunately, the basis for such fittings is very bad. For example, no data for the compressive region exist for both the isotropic and the transverse isotropic contributions. Hence, it is not possible to fit the muscle to a more realistic behaviour. The experimental data for the biceps and triceps are very diverse and obviously not matching to the Virtual Human Male data set. Hence, the parameters for the active contribution are adopted manually to provide a realistic active force contribution. Different material parameters are used for both muscles, see Table 7.1 for the rigid-tendon model and 7.2 for the MTC model.

When material parameters are changed within the elements, stress and strain oscillations are observed. The reason for that observation lies in the definition of the incompressible *Mooney-Rivlin* constitutive law (Equation (4.22)), the initial pressure (Equation (4.32)) and the fact that the primary variables (space and hydrostatic pressure) are discretised using differently ordered shape functions (2^{nd} order in space and one order less for the hydrostatic pressure to fulfil the LBB condition). For an incompressible material, the initial pressure was defined by Equation (4.32) to $p(\boldsymbol{\chi}, t = 0) = 2\,c_1 + 4\,c_2$. When the material parameters, within an element, are distributed with a higher-order function than a linear one, then the hydrostatic pressure with its linear interpolation is not able to (pointwise) fulfil the zero initial stress condition throughout each element (at each *Gauss* point). To get rid of the inconsistency, the compressible formulation is employed instead of the incompressible formulation of the *Mooney-Rivlin* material. Note, the compressible formulation of the *Mooney-Rivlin* is used within an incompressible material description. The advantage of the compressible formulation is that it needs to be able to equal the initial stress to zero by itself as within an compressible formulation an hydrostatic pressure does not exist. To intrinsically set the initial stress to zero, one more material parameter is included:

$$\Psi_{\text{iso}}(I_1, I_2, I_3) = c_1\,(I_1 - 3) - c_2\,(I_2 - 3) + c_5\,(J - 1)^2\,. \tag{10.1}$$

The additional material parameter, c_5, is according to Equation (4.32) adequately determined such that the hydrostatic pressure is zero for the initial condition, i.e.

$$c_5 = 2\,c_1 + 4\,c_2\,. \tag{10.2}$$

Thereby, the issue regarding the choice of the different ordered shape functions is resolved. The only drawback is that one more parameter and one more term in the isotropic part of the constitutive law has to be evaluated throughout the simulation. Compared to the overall amount of evaluations, that carries little weight.

Muscle Mesh

As mentioned in Section 7.2, the original mesh, derived from the Virtual Human Male data set was established by the Auckland Bioengineering Institute. Initially, the geometry was described using tri-cubic *Hermite* shape functions. For this work, the cubic-*Hermite* shape functions are substituted by quadratic shape functions. Here, 27-node hexahedron elements are used to represent the mesh. The reason for the conversion are (i) the reduction of DoFs, as tri-cubic *Hermite* elements have more DoFs than quadratic ones (*Hermites* have 192 DoFs per element and 27-node hexahedrons have 81 DoFs per element) and (ii) avoiding C^1-continuity of the tri-cubic *Hermite* shape functions, for the stress continuity across element boundaries. As, if material parameters vary element-wise within the muscle, the solution space should also be able to reflect element-wise jumps of the stress and therefore also sharp corners at the element vertices.

During the development of the muscles' mesh, it turned out that the simulations are more robust if the tendon heads are changed at the junction of the muscle heads from V-shaped to U-shaped geometries. Further, for numerical reasons, the emerging gap between the different heads is filled with isotropic soft tissue to avoid singularities in the corners. Due to the definition of the muscle-tendon-complex constitutive model (Section 4.4), the

soft tissue is defined using the isotropic behaviour of the muscle tissue, which is very soft compared to the overall behaviour and will not have any further impact on the overall mechanical behaviour of the muscle. This can be validated by checking the nodal residuals at the insertion sites. The soft tissues nodal residuals are small compared to the tendon tissue ones.

To fulfil the requirements of a thorough finite element analysis, it would be necessary to investigate the behaviour of the solution when the mesh is refined similar to Röhrle et al. (2008). However, as the generation of a mesh is very time consuming and challenging. The focus of this work however was on enabling a musculoskeletal system simulation appealing to continuum-mechanical muscles and not on mesh quality.

The mesh for the rigid-tendon model consists of 144 elements and 1625 nodes for the triceps, and 64 elements and 765 nodes for the biceps, see Figure 7.3. The muscle-tendon-complex model's mesh (cf. Figure 7.5) has the same number of elements and nodes than the rigid-body model. Yet, the MTC model has to cover a larger volume and hence the mesh is less fine. The stated number of elements and nodes is not a really high number, yet the computation time for the simulation of one raising arm movement took more than one day on an AMD SR5670/SP5100 CPU core of 3,2 GHz with 128 GB of RAM. A speed up can be achieved through providing an analytical material tangent or through a parallelised computation as it is introduced in OpenCMISS, the successive version of CMISS. OpenCMISS is a new open-source software library based on OpenMPI and OpenMP, see Bradley et al. (2011).

Unfortunately, an authentic fibre field orientation for the biceps and triceps brachii is not available. A study by Fernandez et al. (2012) compared the influence of an artificially chosen fibre orientation with a fibre field, determined by diffusion tensor MRI (DT) data, on the resulting muscle shape. Their results showed, that fibre distributions resulting from DT-MRI are able to reproduce much more realistic muscle shapes than the artificial chosen orientation. Further, the fibre orientation does not only have a strong influence on the muscle's shape but also on the numerical robustness. Hence, special care has to be taken by defining the muscle's fibre orientation. The chosen fibre distribution within the Upper Limb Model is based on anatomical features, yet geometrically simplified to capture the key characteristics.

Last but not least, the mesh may also influence the quality of the contact mechanical results. If the elements are too big, the number of contact points, defined within the contact faces, are to small for a good representation of the contact surfaces. By increasing the number of elements, it is easier for the slave's geometry to follow the master's shape. As it could be seen in Figure 9.14a, when the elements vertices suddenly move over the bones surface, force peaks can emerge. These effects are artificial and due to numerical artifacts. These jumps will not occur in reality.

The central aponeurosis is defined for the triceps only in the MTC model. Without the aponeurosis layer, the triceps muscle reaction forces are too low, the deformation of the muscle tissue are too high, and the deformations in the tendon tissue region are too low. The central aponeurotic layer, with its high stiffness, solved all these problems at once.

Muscle Prestretch

In non-linear mechanics, the definition of the initial state is very important as it has a big influence on the mechanical behaviour of the system. For biological systems, the definition

of the initial state is one of the most basic but also one of the most difficult one. In the literature, a recipe of how to determine the initial configuration does not exist and may be very hard to establish as it also varies for different applications. First attempts are made for some soft tissues and artery walls by Holzapfel and Weizsäcker (1998); Zamir and Taber (2004); Cardamone et al. (2009), or Schröder and Brinkhues (2014). For muscles, the continuum-mechanical community has not assessed the amount of prestretch yet. The methodology to include pre-stretched *Hill*-type muscle models is totally different and not useful for continuum-mechanical purposes. This may also explain why experimental set-ups have not provided information for the continuum-mechanics community.

For this work, it is assumed that each muscle does not produce a compressive force within its range of motion. Each muscle is always under tension. To the author's opinion, this is the best choice, as a living organisms should not invest energy to push a muscle. Muscles are antagonistic to enable movements of the articulation in several directions and do not waste energy due to compressive loads of antagonistic muscles.

Besides the chosen solution to establish the desired prestretch (see Section 7.2), there are alternatives which might have advantages. The first alternative is probably the easiest but also mechanically incorrect. CMISS offers a functionality to change the initial fibre stretch. Unfortunately, the definition of the subroutine is not general enough to apply it to this BVP. Hereby, it would have been very simple to change the fibre's prestretch state. The disadvantages of this option are (i) that the deformation is uniquely spread over the geometry, which is unrealistic in a complex geometry and (ii) that the deformation state is not coherently defined throughout the different material law contributions. The reason is that only the anisotropic contributions depend on the fibre stretch whereas the isotropic part does not. Hence, while the fibre contribution can be influenced in its initial condition, the isotropic contribution cannot.

Perhaps, the best alternative to determine the pre-stretched state would have been to run a simulation to change the muscle length to its target length, and redefine the resulting current configuration to a new initial configuration. This procedure would have several advantages compared to other options. First, for pragmatic reasons, it would be quite simple to change the prestretch state. One has to just select a new initial target length, run the simulation, and redefine the initial state. Second, the resulting muscle state includes all mechanical complexities: the orientation of resulting fibres is inhomogeneous, the strain is locally varying, and as the material is hyperelastic, the mechanical states are reversible. Third, by compressing the muscle to its shortest length, it would appear quite bulgy in its prestretch state, as it needs to be compressed compared to the other alternatives. On the other hand, the biceps would not appear too slim and slender, as it does e.g. in Figure 9.11a, when the forearm is fully extended. Maybe the most important reason for that alternative is that by changing the muscle's length, the initial volume of the muscle is preserved and hence also the muscle's producing force capacity would be preserved. Unfortunately, this is not the case for the choice made in this thesis, compare Section 7.2.

Upper Limb Model

One of the main challenges investigating musculoskeletal systems is the fact that it consists of more unknowns than there are equations. In order to solve such a system, more equations need to be defined in order to find the best among all feasible solutions. This is

exactly the aim of solving an optimisation problem. The field of optimisation is a complex field in itself and goes beyond the scope of this thesis. To employ optimisation problems as for MBS, it is of utmost importance to have fast-solving skeletal muscle models. Current volumetric models are still too complex and too slow. Therefore, alternatives are sought to circumvent an optimisation problem.

As outlined in Section 1.2, the choice of an optimisation method is tricky. One possibility is the definition of further objective functions which can be more or less physically motivated. The problem is that the definition of an objective function directly influences the best choice out of the pool of feasible solutions.

A second possibility would be to use control theory. Neither option is a promising alternative as it further increases a computationally consuming continuum-mechanical approach. In the author's opinion, in near future continuum-mechanical simulations are numerically too expensive to being able to solve the optimisation problem or muscle redundancy problem.

To avoid the muscle redundancy problem, the Upper Limb Model is introduced in Section 7.3. Thereby, all synergistic muscle effects are avoided. By employing the equivalent static system to investigate equilibrium positions of the Upper Limb Model, one equation including four DoFs is employed. As the equivalent static system formulates the momentum balance for a one DoF joint, it can only solve for one of the four DoF without running in an optimisation problem.

A *Newton-Raphson* method is chosen to solve the resulting nonlinear problem (7.4) for one DoF. It could be shown, that the momentum balance resulting from the static equilibrium system is able to find an equilibrium position reasonable fast: in less than 7 iteration steps. Within the solution process, oscillating effects were expected due to the length-dependent muscle behaviour and since the equilibrating forces act in the opposite direction. This is especially true, if θ is the DoF. Then, both muscle forces oppositely change sing at the same time.

Single Muscle Results

The single muscle results are outlined in detail. The reason is that the intrinsic behaviour of the single muscle obviously influences the overall behaviour of the model. Each component within the model is highly nonlinear. Therefore, it is very difficult, if not impossible, to distinguish between different effects when the overall Upper Limb Model is investigated. Hence, attempts were being made to identify as many effects as possible separately.

The presented results are the first ones that integrate continuum-mechanical muscles into a joint system. At first sight, this may not have too many amplifications, but it strongly influences all boundary constraints, e.g. the muscle length or the geometrical restrictions imposed due to contacting neighbours.

The muscle reaction forces of Figure 9.12 reveal the importance of contact. If contact is included into the simulations, the triceps reaction force declines around $\theta = 110°$ much faster compared to simulations that ignore contact. Including Figure 9.13 in this consideration, one can see that the active part of the reaction force is close to independent on the contact formulation, i.e. the additional reaction force is just developing due to the contact induced muscle elongation. The increasing fibre stretch does not have a significant impact on the active force-length relation but on the overall muscle force. Hence, one can conclude that the increasing passive stretch is responsible for the increasing force.

It is often discussed whether the muscles are acting on the ascending or descending branch of the force-length relation. Even though the discussion is always difficult, it is slightly easier for Hill-type muscle models than for continuum-mechanical models. Hill-type models use a lumped-muscle length which holds for the bulk of the muscle. When this value is smaller than the optimal muscle length, the muscle is on the ascending part of the relation. When it is larger than the optimal muscle length, it is on the descending part of the force-length relation. Hence, it is much easier to tell whether the force contribution is increasing or decreasing due to a changing muscle length or whether the muscle acts on the ascending or descending part of the force-length curve.

For continuum-mechanical models, the behaviour becomes more complex as the length dependency exists at each integration point. Therefore, it is possible that in some parts of the muscle, the muscle acts on the ascending part of the force-length relation while in other locations of the muscle, the fibre stretch is much larger and the muscle acts on the descending part of the force-length relation, compare Figure 9.15. Hence, the macroscopic response of the muscle is probably not as clearly distinguishable as several microscopic phenomena take place at the same time.

The triceps' active force including the tendon reduces by about 100 N after reaching the maximum while the biceps' active force only reduces by about 50 N. As the number of triceps muscle fibres which exceed the optimal length is very small (see Figure 9.15), the decline in the active force is due to a reducing muscle and fibre stretch length. For the biceps, the overall length always increases. As the number of fibres trespassing λ_f^{opt} is quite numerous (see Figure 9.15), it is very likely that the resulting decline is caused by the descending part of the force-length curve.

Another phenomenon can be seen in Figure 9.3 and 9.13. As the activation is proportional to the active stress contribution in Equation (4.23), the resulting reaction forces are close of being equally-distributed between the passive and the fully activated curves. Yet on the other hand, as the active stress contribution is proportional to α, the minimal and maximal fibre stretch where the active force contribution starts and ends, should always be the same. The results of Figure 9.3 and 9.13 reveal a different behaviour especially for the biceps. Here, the elbow angle where the active force contribution begins, strongly changes with the biceps' level of activation. This result is similar to experimental observations by e.g. Guimaraes et al. (1994). Even if it is not exactly the same, it is shown that, by linearly scaling the muscle force-length relation with the muscle activation, the macroscopic result varies strongly with the input. Due to the complex model, the parameters responsible to convert the simple input to the macroscopic output is unknown. But when the model results are like this, they may also change to something else that is more similar to the measurements of Guimaraes et al. (1994).

To the author's knowledge, there is no clear definition of the state when a muscle acts maximally on a joint. Sometimes, the muscle is said to produce its maximal force when the muscle is at its resting length or when the joint is in its neutral position. Experiments on the elbow show that the joint angle, where the elbow torques at its maximum is between 60° (Amis et al., 1980) and 100° (Buchanan et al., 1998). Mechanically, the muscle's optimum can be defined when either the muscle reaction force is maximal, where the active contribution of the muscle reaction force is maximal, where the moment of one muscle acting an a joint is maximal, or where the moment of all muscles acting on a joint is maximal.

Traditionally in skeletal muscle modelling, the optimal length of a muscle is the length at which it produces its highest force. This value can be evaluated in experiments by dissecting one muscle from its system. However, how good can the realistic operating range in the in vitro experiments be reproduced? And how is that possible considering the results of Section 9.1.1 and 9.1.2?

For the triceps and the biceps brachii, the ranges of operation are very similar to the results presented by Murray et al. (2000). The optimal elbow joint angle is always towards the end of either flexion or extension. Is it possible for an isolated muscle to have its maximal force somewhere in the middle of its range of motion while the passive contribution increases with further stretching the muscle? When the results of Figure 9.34a are consulted, one has to conclude that the force is increasing when the muscle length is increasing. Hence, when a muscle's optimal angle is in its mid range of motion, the muscle length is no longer monotonically increasing, as it is the case for the triceps' length (cf. Figure 7.6a). Murray et al. (2000) presents a range of motion that is much larger for the biceps than for the triceps. The biceps is mostly acting on the ascending part of the force-length curve or at least has a monotonically increasing reaction force. In contrary, the triceps's force decreases with increasing flexion angle. The triceps' range of motion is, referring to Murray et al. (2000), on the last part of the ascending and the beginning of the descending part of the force-length relation. However, maybe the choice of the optimal length is not the only possible explanation and also the reduction of the triceps length and the fibre length contributes to that characteristic?

It can be measured that the elbow torque a human being can generate is maximal between $\theta = 90$ and $100°$. Yet, is it most likely not possible to reach a maximal elbow torque at $\theta = 90 - 100°$ for a single muscle. Can it be only a product from the interplay of several acting muscles? To push the optimal elbow angle for a single muscle more towards $\theta = 90°$ or $\theta = 100°$, a first, naive idea would be to either increase the prestretch of the muscle or by choosing a smaller optimal fibre stretch to adapt the muscle force accordingly. Unfortunately, both options do not lead to the desired result as on the one hand, the active part of the muscle moves towards the middle of its range of action, yet, on the other hand, the passive behaviour of the muscle starts to dominate earlier. Hereby, the muscle reaction forces are only dominated by the passive force, which is definitely not physiologically motivated. Of course, also the muscle lever arms have a strong impact on the resulting muscle moment. Yet, the resulting biceps moment of Figure 9.25b demonstrates that the moment is linearly increasing with increasing muscle stretch or forearm flexion. Therefore, one can only conclude that an optimal elbow angle of $90°$ to $100°$ can only be achieved from the interplay of several muscles acting at the same time. Last but not least, the impact of the lever arm is also contributing strongly.

Comparing Rigid-Tendon Model Results to Muscle-Tendon-Complex Model Results

For single muscle simulations, tendons might not be that important. Hence in the continuum-mechanics muscle community, tendons are very often assumed to be rigid and neglected Van Loocke et al. (2006). It is claimed that due to the tendon stiffness, the resulting small deformations do not have a strong influence on the overall skeletal muscle. However, by comparing the results of the raising arm movement of the rigid-tendon model with the results of the MTC model, tendons have a strong influence on skeletal muscle mechanics even though the strain in the tendon material is quite small, see also Scheepers

et al. (1997).

Considering Section 2.4 and modelling aspects, the main elements when muscle-tendon complexes act on a joint are the following:

(i) Due to their slender structure, they strongly influence the lever arm and the muscle's line of action.

(ii) Much more realistic muscle attachment site can be defined when tendons are included. Smaller attachment faces provide less restrictions to the muscle geometry and the area of fixed nodes is smaller.

(iii) A consequence from the last two items is that tendons increase the deformation modes of the muscle belly, i.e. the slender tendon shape provides more modes of deformation by rotational and translational movements of the belly.

(iv) Within the different muscle tissues, i.e. tendon tissue, muscle tissue, or the transition zone, structural properties such as the connective tissue ratio, material parameters, and the fibre orientation vary strongly.

When the deviation of the reaction force's orientation of the MTC and rigid-tendon model is compared, several observations can be made to underpin the importance of (i). First the rigid-tendon model exhibits deviations that are nearly independent to contact. For the biceps, the results of Figure 9.10 are dominated by the badly defined prestretch as the surface rise where the reaction forces are close to zero. Before the orientation of the reaction force becomes indifferent, the deviation of the orientation is in the range of a few degrees. For the triceps, the deviation increases up to 15°, independent of contact. In case of the MTC model, the deviation strongly depends on the effects of contact. Without considering contact, the deviation is only a few degrees. The deviation increases up to 40° for the triceps and up to 20° for the biceps when contact is included. The difference can also be nicely seen in the bottom row of Figure 9.1 and Figure 9.11.

The relocation of the point of action is for both muscles and both models independent of the effects of contact. Yet, even though the cross-section of the insertion sites of the MTC complex are much smaller, the relocation of the point of action are very similar in both models. For the triceps, the relocation within the MTC model is larger than within the rigid-tendon model. So, item (ii) not only enables a more natural attachment site, but also does not seem to mechanically penalise the slenderness.

When the simulations of the raising arm movement of Figure 9.1 is compared to Figure 9.11, it can be seen that the biceps moves differently at different attachment sites. This also influences the way the muscle and the bone interact with each other. Contact looks much more natural. One probable reason for this is that due to the long and slender tendons, translational movements of the belly are much more likely, see item (iii).

Item (iv) can probably be best explained by comparing the results of Figure 9.5 with those in Figure 9.15. The rigid-tendon model can only reflect the fibre stretch distribution of the muscle belly. As the MTC model does not only include the muscle belly but also the tendon region and the transition zones, the resulting patterns of Figure 9.15 are more complex. Yet, the patterns of the belly are still distinguishable.

Lever Arm

Besides the muscle reaction force, the second parameter directly influencing the joint moment is the muscle lever arm. Before the tendon-displacement method derived lever arm is employed, two alternatives were considered.

In the first attempt, the lever arm was determined by utilising experimental results from Amis et al. (1979) and Murray et al. (2002). The second attempt was an analytical relation on the basis of the static equilibrium system using trigonometry. Unfortunately, both methods provided a lever arm with which the equivalent static system failed to find an equilibrium position. The reason for this failure was never identified or understood. The tendon-displacement was the third attempt and an equilibrium position was found. A possible reason for the tendon-displacement method and the vector-resulting lever arm to work, and the measured data and the analytical relation not is that it seems to be important, that the used data set is coherent.

The lever arm derived from the tendon-displacement method only depends on the linear muscle length between muscle origin and insertion. Therefore, only the geometry and size of the humerus, ulna, radius, and the muscle attachment sites influence the muscle lever arms. Within the Upper Limb Model, the line from muscle origin to insertion is neither deflected by surrounding muscles nor other soft tissues or bones. Hence, this linear assumption is the most accurate choice to approximate the muscle length. Nevertheless, the tendon-displacement method has proven over several decades to give reasonably good results, and the lever arm resulting from this approach are in agreement with the lever arm mentioned in Section 1.2.2.

An improvement of the tendon-displacement method could be achieved by using the continuum-mechanical muscle model and the idea of the line of action which is introduced in Section 7.5. Assuming that the evolving muscles' line-of-action is not always straight but curved, the muscle length deviates from the line approach. By determining the point of action incrementally along the longitudinal muscle axis, (similar to the one depicted in Figure 10.1b), the adapted muscle length could also be determined piecewise linear. As the adapted length will vary for different fibre orientations, muscle shapes, and the level of activation, the lever arm resulting from the tendon-displacement method differs from the "linear" version.

The problem with this method is that it worked for nicely shaped cubes. But during strong deformations, as it can be seen in Figure 10.1b, the cross-section on which the integration is evaluated is not plain any more. This problem becomes severe when the geometry becomes arbitrary as is no longer straight forward to define intersecting planes to evaluate the stress. In theory, the finite element method allows to evaluate the stress tensor at every point, yet in reality, this becomes difficult.

The vector-resulting lever arms differ quite strongly from the lever arms resulting from the tendon-displacement method. For the biceps, despite the strong deviation of the orientation of the reaction force when considering contact, the lever arm remains close to constant over the whole input space ($10° \leq \theta \leq 150°$ and $0 \leq \alpha \leq 1$). In the literature, the biceps lever arm is strongly dependent on the elbow flexion angle (Murray et al., 1995; Amis et al., 1979). As it is already mentioned, the lever arms resulting from the tendon-displacement method are in agreement with the literature, cf. Murray et al. (1995) or Amis et al. (1979). However, mathematically speaking, the lever arm obtained by means of taking the actual position and the actual orientation of the force is exact.

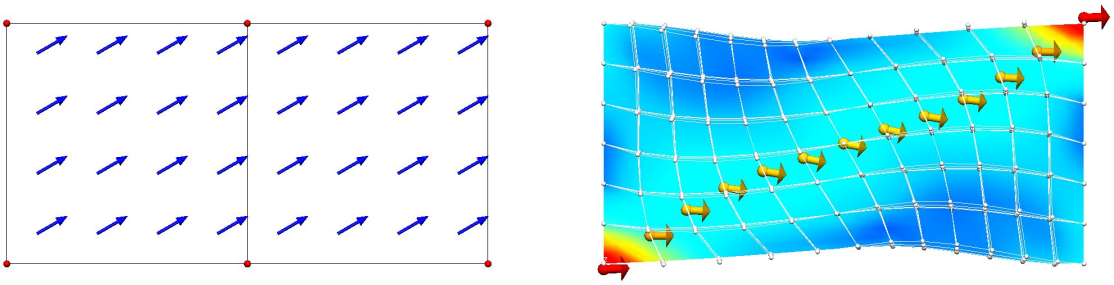

(a) *Unipennate uniform muscle cube. A pennation angle of 30° is assumed and visualised by the blue arrows.*

(b) *The resulting cube's line of action. The contour plot depicts the* von Mises *stress, the yellow arrows the resulting traction vectors for each cross-section while the point of action is evaluated using the procedure introduced in* Section *7.5*

Figure 10.1: *Investigating a cube's the line-of-action.*

The muscle force orientation is a result of the FE simulation and depends on e.g. the fibre architecture, contact, or the muscle geometry. Possible faults can be attributed to the employed geometry, the location of the attachment sites as well as in the choice of the fulcrum. In the author's opinion, the newly developed vector-resulting lever arm has to be applied to more muscles in order to argue more courageous against the existing results and to find reasons for the large deviations. Yet, it should be kept in mind that such large discrepancies exist between the different model results.

Multi-Muscle Forward-Dynamics Simulation

It was mentioned many times, that in the author's opinion, the continuum-mechanical approach is numerically too costly to solve the muscle redundancy problem. Within this thesis, three possible approaches are presented to tackle the problem anyhow.

The first attempt unpretentiously assumes or prescribes the DoFs. The intention of this scenario is to show that the Upper Limb Model and its equivalent static system can find an equilibrium state. The results of Section 9.2 proved the applicability as a stand-alone framework.

In a second step, the forward-inverse model has been utilised to determine realistic muscle activation. Within the community, it is a respected modelling framework, which is employed for two purposes: (i) It provides muscle activation to drive the Upper Limb Model. (ii) It is used to provide data to compare and validate the Upper Limb Model.

The influence of the lever arm on the equilibrium position can be seen in Figure 9.28a. The deviation due to the different lever arms is more than 40°. Figure 9.28a also demonstrated the impact of the relocation of the point of action. The deviation from the tendon-displacement method to the vector-resulting lever arm method is about 40°, while it is only around 2° more for including the relocation of the point of action.

Contact does not have a major impact in these scenarios. The difference between contact and no contact is less than $\Delta\theta = 1°$, or less than $\Delta\alpha = 0.2\%$ for the tendon-

displacement method and about $\Delta\theta = 2°$ for the vector-resulting lever arm.

When the measured elbow moment is compared to the reproduced elbow moment of both models, it can be said that the quality of the forward-inverse model is not optimal yet. The resulting elbow moment is too small for elbow angles smaller than 60° and larger than 120° and too large for $80° < \theta < 120°$, see Figure 9.34a. The results may be improved by increasing the range of the parameters determined in the calibration phase. The deviation of the results of the Upper Limb Model may be larger, yet the shape of the resulting elbow moment better resembles the experimental data.

As already discussed, the muscle forces of the different models are already similar. The discrepancy between the different resulting elbow moments may be due to different muscle lever arms. Hence, the lever arms of the OpenSim model are compared to the lever arms determined from the tendon-displacement method in Figure 10.2.

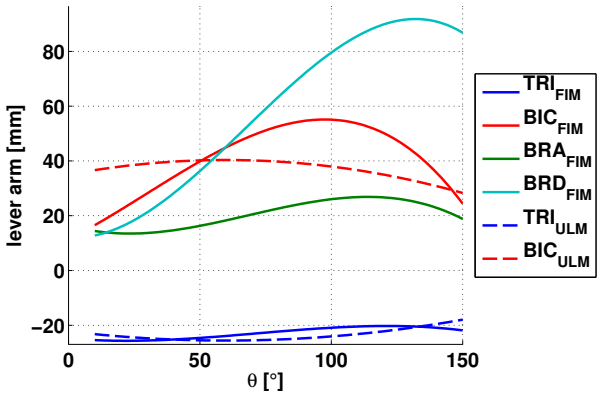

Figure 10.2: *Comparing the lever arms of the forward-inverse model and the Upper Limb Model.*

It can be seen that the triceps' lever arms are similar. The biceps' lever arm, on the other hand, deviates up to 50% (or 20 mm). This obviously has a big impact on the resulting elbow moment as the biceps is the strongest elbow flexor. For example, when the biceps lever arm of the Upper Limb Model is replaced by the one of the forward-inverse model, the Upper Limb Model's resulting moment is improving considerably as the flexor becomes about 50% more powerful.

When the biceps reaction forces resulting from the forward-inverse model and the Upper Limb Model of Figure 9.34a are compared, a methodological difference becomes apparent. Not only is the biceps force from the forward-inverse model stronger than the force from the Upper Limb Model but more importantly for the fully flexed elbow, the biceps reaction force from the forward-inverse model is greater than 200 N while the Upper Limb Model's biceps reaction force is only around 50 N. A possible explanation for the overall smaller muscle force is that the biceps' force of the different subjects within the forward-inverse model and the Upper Limb Model are not coinciding. By increasing within the continuum-mechanical skeletal muscle model of the biceps the parameter $\sigma_{\max}$, the biceps reaction force increases and reduces the gap between the two model solutions. On the other hand, the Upper Limb Model's reaction force still tends towards zero for flexing the forearm. The cause for the difference is that the active force-length relation of the forward-inverse model is wider. This implies that the biceps of the forward-inverse model is able to generate a force in a fully flexed forearm position and the biceps of the Upper Limb Model not.

11 Summary and Outlook

11.1 Summary

In this thesis, a suitable theoretical modelling procedure was presented, providing numerical simulations of the material behaviour of muscle-tendon complexes that are included into an articulation. In order to do that, it was first necessary to introduce the anatomical and physiological fundamentals of the musculoskeletal system and in particular the upper limb. Caused by the complex microscopic property of the participating muscles, appropriate constitutive equations for the muscle, tendon, and other soft tissues were presented and embedded into the Theory of Finite Elasticity which provides a suitable framework in describing the finite deformation regime.

The resulting set of coupled partial differential equations was spatially discretised using the finite element method, which has proven to provide a powerful numerical technique for finding approximate solutions to such BVP. A contact formulation was modularly included to the finite element method to consider contact between the elastic muscle-tendon complexes and rigid bones. The solution of the subject specific BVP was achieved within CMISS. The resulting system of equations was solved in a monolithic manner. While the material mechanical contribution was linearised numerically, the contact mechanical contribution was linearised analytically.

The geometry of the Upper Limb Model was established from the virtual human data set. By introducing the Upper Limb Model with its static equivalent system, a continuum-mechanically based framework could be established. This enabled stand-alone investigations as well as a coupling to other frameworks. Three different concepts to facilitate the muscle activation were presented in order to use the Upper Limb Model and the equivalent static system. In a first step, muscle activation was prescribed to demonstrate the feasibility of the system and investigated its convergence behaviour as a stand-alone framework. In a second step, the Upper Limb Model was linked to the forward-inverse model established by Prof. David Lloyd's Musculoskeletal Research Group. Therefore, experimental data is acquired and processed. The results of the forward-inverse model are compared to those of the Upper Limb Model. The third step was conceptually introduced but not implemented. Yet, this concept of coupling FE simulations to MBS is very promising.

Besides the well known tendon-displacement method, a second method to determine the lever arm was established by employing properties of the muscle force such as its point of action and orientation.

The in silico experiments produced muscle reaction forces, muscle fibre stretch distributions, lever arms, and equilibrium positions. In addition, the impact of contact on a musculoskeletal system was investigated. These results were elaborately visualised and discussed to provide a better mechanical understanding of the examined musculoskeletal system.

11.2 Own Contributions

The purpose of this section is to emphasise the newly introduced achievements within this thesis. The main focus of this dissertation is to introduce a first approach towards modelling a musculoskeletal system appealing to continuum-mechanical muscles.

The continuum-mechanical description of the muscle-tendon complex itself is specified by a constitutive relation embedded in the Theory of Finite Elasticity. The constitutive relation for the muscle tissue is a state-of-the-art continuum-mechanical approach. Yet, I extended this approach to represent a full muscle-tendon complex, including muscle tissue, tendon tissue, and transition zones, by only introducing two more material parameters.

State-of-the-art musculoskeletal system models are based on rigid-body simulations. To enable investigations of a continuum-mechanically based framework as a stand-alone framework and to enable the coupling of this framework to other frameworks, the first step is to choose a relatively simple part of the musculoskeletal system that is representative of the musculoskeletal system. Probably, the most simple joint is a 1-DoF hinge joint driven by an antagonistic muscle pair. For this thesis, I choose the upper limb as the musculoskeletal system of interest.

The Upper Limb Model involves three rigid bones (humerus, radius, and ulna) articulating in the elbow joint. To keep the system simple, the elbow is assumed to be a one-DoF joint that is driven by the antagonistic muscle pair (biceps brachii and triceps brachii). To enable investigations of the Upper Limb Model as a stand-alone continuum-mechanically based framework and to enable the coupling to other frameworks, the equivalent static system is introduced in Section 7.3.

Three different concepts to facilitate the muscle activation are presented in order to use the Upper Limb Model and the equivalent static system. In a first step, the muscle activation is prescribed to test the feasibility of the Upper Limb Model and test its convergence behaviour. In a second step, the Upper Limb Model is linked to the forward-inverse model established by Prof. David Lloyd's Musculoskeletal Research Group. Therefore, experimental data is acquired and processed. The results of the forward-inverse model are compared to those of the Upper Limb Model.

When static conditions of musculoskeletal systems are investigated, the joint moment need to be balanced for the participating members. Besides the muscle reaction force, the second term contributing to the muscle moment acting on a joint is the muscle lever arm. Rigid-body simulations are restricted to the tendon-displacement method to determine the lever arms. Due to the geometric concept that was used within this work, a second method to determine the muscle lever arms could be established by employing intrinsic properties of the muscle force, namely the muscle reaction force's point of action and its orientation.

So far, volumetric muscle are only investigated within isolation. The single muscle results of Section 9.1 demonstrate how outreaching the consequences of a single muscle are that is included into a musculoskeletal system. The musculoskeletal system defines by specifying the kinematics of the bones the muscle's range of motion and the impact of the contact formulation on the muscles.

Furthermore, the author provides an idea to unite rigid-body simulations and finite element simulations to one modelling framework. The idea is based on nested iteration procedures. A rigid-body simulation solves the musculoskeletal system and delivers an

initial guess to a FE muscle simulation. The FE model solves the system based on detailed geometrical measures, which can again serve as inputs to improve the physiological reliability of MBS.

11.3 Outlook

Up to now, the Upper Limb Model and its static equivalent system showed that simulations of the musculoskeletal system based on continuum-mechanical muscle models are possible. The model can be utilised as a stand-alone framework and could also be associated to other frameworks. As the Upper Limb Model is a rudimentary model, there is still plenty of potential for improvement.

One of the most fundamental improvement may be achieved with new in vivo muscle experiments. Most of the state-of-the-art experiments on muscles are adapted to the needs of *Hill*-type muscle models. As continuum-mechanical based muscle models have different needs, it would be a major leap forward to find (i) a reliable initial state or pre-stretched state, (ii) data where the geometry corresponds to a full set of mechanical tests (including in-fibre, transfers-fibre tension and compression tests as well as the standard isometric, quick-release, eccentric, and concentric activation experiments), and (iii) corresponding fibre field orientation of the tested muscle. Hereby, the muscle models could reproduce a much more realistic and natural muscle behaviour.

The strong impact of the fibre field orientation on the resulting muscle behaviour is well known. Hence, a large improvement would be possible if a fibre field orientation was established by employing diffusion MRI data. These optical data could also be used to spatially distinguish between different muscle, connective, and other soft tissue contributions.

A conceptual improvement would be the extension of the current quasi-static limitation to a fully dynamic formulation. This would not only enable to investigate fast movements but also inertial forces. As wobbling masses are considered to be an important damping feature within the musculoskeletal system, it would be interesting to investigate such phenomena within a continuum-mechanical based framework. Additionally, a fully dynamic model would simplify the comparison with a dynamic rigid-body model.

As the single muscle results of Section 9.1 put in evidence, the contact forces can be up to 350 N. Thus, their impact cannot be considered negligible. Shacham et al. (2010) showed that the muscle-bone *Coulomb* friction coefficient is about 0.3. Therefore, it could be worth investigating how muscles change their shape and mechanical behaviour due muscle-bone friction. As CMISS already consists of a frictional formulation, the effort to conduct this investigation are unlikely to be very complex and time consuming.

In the author's opinion, it may not be possible to substitute the static equivalent system with a full continuum-mechanical framework, as it is very challenging to achieve a realistic and natural articular movement by constraining the bones to all required or naturally occurring forces. To achieve the joint movement, it may be necessary to include the whole articular capsule within such a model, i.e. all ligaments and surrounding muscles. Yet, it should be possible to add some of these components to the Upper Limb Model or to a similar model in the near future. Synergistic muscles would be possibly the most interesting components to add. Synergistic muscles increase the number of muscle forces acting on a joint and the contact formulation would become even more important for the

resulting system, as there is not only muscle-bone contact but also muscle-muscle contact. Yet, as more muscles are acting within one system, it becomes even more important to couple the continuum-mechanical based model to other frameworks as muscle redundancy plays a crucial role again. As the different muscles are strongly interacting, a promising approach could be to assume several synergistic muscles as one FE grid. Thereby, muscle-muscle contact is intrinsically included in the FE model. The differentiation between different muscles could be established by locally defining the fibre orientation and material parameters, as it was done for the MTC model. Yet, special care should be taken when the mesh is defined. It is advisable to define the mesh vertices along the different muscles.

The framework of how to couple simulations of the musculoskeletal system appealing to continuum-mechanical muscle and *Hill*-type muscle was already introduced in Section 8.3. For realisation, a software engineer student already set up an appropriate web-service during his master-thesis project. This web-service includes a wrapper and an orchestration application which are needed to exchange the necessary data between the frameworks while keeping track of the simulation status. Furthermore, this web-service is programmed such that it enables the necessary flexibility. Special care has to be taken for the different model results. It is very important to investigate every modelling framework independent from each other in a first step. In a second step, the results of the different modelling frameworks should be compared to ensure similar solutions. If the modelling results are not similar, both modelling frameworks may not match their solutions.

It has been argued that musculoskeletal systems appealing to continuum-mechanical muscle models are computationally too expensive to solve the muscle redundancy problem or other optimisation problems. One option to circumvent the coupling of a continuum-mechanical based framework to other frameworks is a dramatic computational speed up using model reduction techniques (Wirtz, 2013). Hereby, the muscle mechanics could be intensively investigated in an offline phase. The trained reduced model is able to reproduce the muscle simulations much faster in an online phase. This may enable investigations on a multi-muscle musculoskeletal system as a stand-alone framework.

Bibliography

Alexander, R. M. and Vernon, A. (1975). The dimensions of knee and ankle muscles and the forces they exert. *Journal of Human Movement Studies*, 1(1):115–123.

Amis, A. A., Dowson, D., and Wright, V. (1979). Muscle strengths and musculoskeletal geometry of the upper limb. *Engineering in Medicine*, 8(1):41–48.

Amis, A. A., Dowson, D., and Wright, V. (1980). Analysis of elbow forces due to high-speed forearm movements. *Journal of Biomechanics*, 13(10):825–831.

An, K. N., Kaufman, K. R., and Chao, E. Y. S. (1989). Physiological considerations of muscle force through the elbow joint. *Journal of Biomechanics*, 22(11):1249–1256.

An, K. N., Takahashi, K., Harrigan, T. P., and Chao, E. Y. (1984). Determination of muscle orientations and moment arms. *Journal of biomechanical engineering*, 106(3):280–282.

Anderson, A. E., Ellis, B. J., and Weiss, J. A. (2007). Verification, validation and sensitivity studies in computational biomechanics. *Computer Methods in Biomechanics and Biomedical Engineering*, 10:171–184.

Anderson, F. C. (1999). *A dynamic optimization solution for a complete cycle of normal gait*. PhD thesis, University of Texas at Austin.

Anderson, F. C. and Pandy, M. G. (2001). Static and dynamic optimization solutions for gait are practically equivalent. *Journal of biomechanics*, 34(2):153–161.

Ball, R. S. (1900). *A Treatise on the Theory of Screws*. Cambridge University Press.

Barbenel, J. C. (1974). The mechanics of the temporomandibular jointa theoretical and electromyographical study. *Journal of Oral Rehabilitation*, 1(1):19–27.

Biodex Medical Systems, I. (2006). *BIODEX MULTI-JOINT SYSTEM - PRO, SETUP and OPERATION MANUAL*. www.biodex.com.

Blausen gallery 2014 (2014). Blausen.com staff. *Wikiversity Journal of Medicine*.

Blemker, S. S. and Delp, S. L. (2005). Three-dimensional representation of complex muscle architectures and geometries. *Annals of biomedical engineering*, 33(5):661–673.

Blemker, S. S., Pinskya, P. M., and Delp, S. L. (2005). A 3d model of muscle reveals the causes of nonuniform strains in the biceps brachii. *Journal of Biomechanics*, 38:657–665.

Böl, M. and Reese, S. (2008). Micromechanical modelling of skeletal muscles based on the finite element method. *Computer methods in biomechanics and biomedical engineering*, 11(5):489–504.

Böl, M., Sturmat, M., Weichert, C., and Kober, C. (2011). A new approach for the validation of skeletal muscle modelling using mri data. *Computational Mechanics*, 47(5):591–601.

Bonet, J. (1997). *Nonlinear continuum mechanics for finite element analysis*. Cambridge university press.

Bradley, C., Bowery, A., Britten, R., Budelmann, V., Camara, O., Christie, R., Cookson, A., Frangi, A. F., Gamage, T. B., Heidlauf, T., et al. (2011). Opencmiss: a multi-physics & multi-scale computational infrastructure for the vph/physiome project. *Progress in biophysics and molecular biology*, 107(1):32–47.

Bradley, Chris, P., Pullan, Andrew, J., and Hunter, P. J. (1997). Geometric modeling of the human torso using cubic hermite elements. *Annals of Biomedical Engineering*, 25:96–111.

Buchanan, T. S., Almdale, D. P. J., Lewis, J. L., and Rymer, W. Z. (1986). Characteristics of synergic relations during isometric contractions of human elbow muscles. *Journal of Neurophysiology*, 56(5):1225–41.

Buchanan, T. S., Delp, S. L., and Solbeck, J. A. (1998). Muscular resistance to varus and valgus loads at the elbow. *Journal of biomechanical engineering*, 120(5):634–639.

Buchanan, T. S., Lloyd, D. G., Manal, K., and Besier, T. F. (2004). Neuromusculoskeletal modeling: estimation of muscle forces and joint moments and movements from measurements of neural command. *Journal of applied biomechanics*, 20(4):367.

Burkholder, T. J., Fingado, B., Baron, S., and Lieber, R. L. (1994). Relationship between muscle fiber types and sizes and muscle architectural properties in the mouse hindlimb. *Journal of Morphology*, 221(2):177–190.

Cardamone, L., Valentin, A., Eberth, J., and Humphrey, J. (2009). Origin of axial prestretch and residual stress in arteries. *Biomechanics and modeling in mechanobiology*, 8(6):431–446.

Challis, J. H. and Kerwin, D. G. (1993). An analytical examination of muscle force estimations using optimization techniques. *Proceedings of the Institution of Mechanical Engineers, Part H: Journal of Engineering in Medicine*, 207(3):139–148.

Chung, J.-H. (2008). *Modelling Mammographic Mechanics*. PhD thesis, Auckland Bioengineering Institute - The University of Auckland - New Zealand.

Chung, J.-H., Rajagopal, V., Nielsen, P. M. F., and Nash, M. P. (2008). A biomechanical model of mammographic compressions. *Biomechanics and modeling in mechanobiology*, 7(1):43–52.

CMISS (1979-now). *An interactive computer program for Continuum Mechanics, Image analysis, Signal processing and System Identification*. In CMISS (now).

Corcos, D. M., Gottlieb, G. L., Latash, M. L., Almeida, G. L., and Agarwal, G. C. (1992). Electromechanical delay: An experimental artifact. *Journal of Electromyography and Kinesiology*, 2(2):59–68.

Crowninshield, R. D. and Brand, R. A. (1981). A physiologically based criterion of muscle force prediction in locomotion. *Journal of biomechanics*, 14(11):793–801.

Ehlers, W. (2010). Vector and tensor calculus: An introduction. Technical report, Institut für Mechanik.

Erdemir, A., McLean, S., Herzog, W., and van den Bogert, A. J. (2007). Model-based estimation of muscle forces exerted during movements. *Clinical Biomechanics*, 22(2):131 – 154.

Feldman, A. G. (1986). Once more on the equilibrium-point hypothesis (λ model) for motor control. *Journal of motor behavior*, 18(1):17–54.

Fernandez, J., Shim, V., Hunter, P., and Mithraratne, K. (2012). Diffusion tensor imaging of lower limb muscle architecture to inform muscle mechanics. *Journal of Biomechanics*, 45:S453.

Fernandez, J. W. and Hunter, P. J. (2005). An anatomically based patient-specific finite element model of patella articulation: towards a diagnostic tool. *Biomechanics and modeling in mechanobiology*, 4(1):20–38.

Fitts, R. H., McDonald, K. S., and Schluter, J. M. (1991). The determinants of skeletal muscle force and power: Their adaptability with changes in activity pattern. *Journal of Biomechanics*, 24, Supplement 1(0):111 – 122. Proceedings of the {NASA} Symposium on the Influence of Gravity and Activity on Muscle and Bone.

Forster, E., Simon, U., Augat, P., and Claes, L. (2004). Extension of a state-of-the-art optimization criterion to predict co-contraction. *Journal of Biomechanics*, 37(4):577 – 581.

Freivalds, A. (2011). *Biomechanics of the upper limbs: mechanics, modeling and musculoskeletal injuries*. CRC press.

Fung, Y. C. (1981). *Biomechanics - Mechanical Properties of Living Tissues*. Springer-Verlag.

Fung, Y. C. and Tong, P. (2001). *Classical and Computational Solid Mechanics*. World Scientific.

Garner, B. A. and Pandy, M. G. (2000). The obstacle-set method for representing muscle paths in musculoskeletal models. *Computer methods in biomechanics and biomedical engineering*, 3(1):1–30.

Gordon, A. M., Huxley, A. F., and Julian, F. J. (1966). The variation in isometric tension with sarcomere length in vertebrate muscle fibres. *The Journal of physiology*, 184(1):170–192.

Guimaraes, A. C., Herzog, W., Hulliger, M., Zhang, Y. T., and Day, S. (1994). Effects of muscle length on the emg-force relationship of the cat soleus muscle studied using non-periodic stimulation of ventral root filaments. *The Journal of experimental biology*, 193(1):49–64.

Günther, M. and Ruder, H. (2003). Synthesis of two-dimensional human walking: a test of the λ-model. *Biological Cybernetics*, 8:89–106.

Günther, M., Schmitt, S., and Wank, V. (2007). High-frequency oscillations as a consequence of neglected serial damping in hill-type muscle models. *Biological Cybernetics*, 97(1):63–79.

Hardt, D. E. (1978). Determining muscle forces in the leg during normal human walkingan application and evaluation of optimization methods. *Journal of Biomechanical Engineering*, 100(2):72–78.

Hatze, H. (1978). A general myocybernetic control model of skeletal muscle. *Biological cybernetics*, 28(3):143–157.

Hawkins, D. and Bey, M. (1994). A comprehensive approach for studying muscle-tendon mechanics. *Journal of biomechanical engineering*, 116(1):51–55.

Heckathorne, C. W. and Childress, D. S. (1981). Relationships of the surface electromyogram to the force, length, velocity, and contraction rate of the cineplastic human biceps1. *American Journal of Physical Medicine & Rehabilitation*, 60(1):1–19.

Heidlauf, T. and Röhrle, O. (2014). A multiscale chemo-electro-mechanical skeletal muscle model to analyze muscle contraction and force generation for different muscle fiber arrangements. *Frontiers in Physiology*, 5(498):1–14.

Heine, R., Manal, K., and Buchanan, T. S. (2003). Using hill-type muscle models and emg data in a forward dynamic analysis of joint moment: Evaluation of critical parameters. *Journal of Mechanics in Medicine and Biology*, 3(02):169–186.

Hill, A. V. (1938). The heat of shortening and the dynamic constants of muscle. *Proc. R. Soc. Lond. Ser. B Biol. Sci.*, 126(843):136–195.

Hof, A. L. and Van Den Berg, J. W. (1977). Linearity between the weighted sum of the emgs of the human triceps surae and the total torque. *Journal of biomechanics*, 10(9):529–539.

Holzapfel, G. A. (2000). *Nonlinear Solid Mechanics: A Continuum Approach for Engineering*. John Wiley & Sons.

Holzapfel, G. A., Gasser, T. C., and Ogden, R. W. (2000). A new constitutive framework for arterial wall mechanics and a comparative study of material models. *Journal of elasticity and the physical science of solids*, 61(1-3):1–48.

Holzapfel, G. A., Schulze-Bauer, C. A. J., Feigl, G., and Regitnig, P. (2005). Monolamellar mechanics of the human lumbar annulus fribosus. *Biomechanics and Modeling in Mechanobiology*, 3:125–140.

Holzapfel, G. A. and Weizsäcker, H. W. (1998). Biomechanical behavior of the arterial wall and its numerical characterization. *Computers in biology and medicine*, 28(4):377–392.

Holzbaur, K. R. S., Murray, W. M., and Delp, S. L. (2005). A model of the upper extremity for simulating musculoskeletal surgery and analyzing neuromuscular control. *Annals of Biomedical Engineering*, 33(6):829–840.

Hughes, T. J. R. (2012). *The finite element method: linear static and dynamic finite element analysis*. Courier Dover Publications.

Johansson, T., Meier, P., and Blickhan, R. (2000). A finite-element model for the mechanical analysis of skeletal muscles. *Journal of theoretical Biology*, 106:131–149.

Kannus, P. (2000). Structure of the tendon connective tissue. *Scandinavian journal of medicine & science in sports*, 10(6):312–320.

Kendall, F. P., McCreary, E. K., Provance, P. G., and Rodgers, M. (1993). *Muscles, testing and function: with posture and pain*. Williams & Wilkins Baltimore, MD.

Kim, S. D., Lee, C.-O., Manteuffel, T. A., McCormick, S. F., and Röhrle, O. (2006). First-order system least squares for the oseen equations. *Numerical Linear Algebra with Applications*, 13(7):523–542.

Laursen, T. A. (2002). *Computational contact and impact mechanics: fundamentals of modeling interfacial phenomena in nonlinear finite element analysis*. Springer Science & Business Media.

Lee, S.-H., Sifakis, E., and Terzopoulos, D. (2009). Comprehensive biomechanical modeling and simulation of the upper body. *ACM Transactions on Graphics (TOG)*, 28(4):99.

Lemos, R., Epstein, M., Herzog, W., and Wyvill, B. (2001). Realistic skeletal muscle deformation using finite element analysis. In *Computer Graphics and Image Processing, 2001 Proceedings of XIV Brazilian Symposium on*, pages 192–199. IEEE.

Lemos, R. R., Rokne, J., Baranoski, G. V. G., Kawakami, Y., and Kurihara, T. (2005). Modeling and simulating the deformation of human skeletal muscle based on anatomy and physiology. *Comptater Animation and Virtual Worlds*, 16:319–330.

Lewandowski, A. (1982). *Issues in model validation*. International Institute for Applied Systems Analysis.

Lloyd, D. G. and Besier, T. F. (2003a). An emg-driven musculoskeletal model for estimation of the human knee joint moments across varied tasks. *Journal of Biomechanics*, 36:765–776.

Lloyd, D. G. and Besier, T. F. (2003b). An emg-driven musculoskeletal model to estimate muscle forces and knee joint moments in vivo. *Journal of biomechanics*, 36(6):765–776.

Lorussi, F., Galatolo, S., Caudai, C., Tognetti, A., and De Rossi, D. (2006). Compliance control and feldman's muscle model. In *Biomedical Robotics and Biomechatronics, 2006. BioRob 2006. The First IEEE/RAS-EMBS International Conference on*, pages 1194–1199. IEEE.

Maas, R. (2014). *Biomechanics and optimal control simulations of the human upper extremity*. PhD thesis, Friedrich-Alexander-Universität Erlangen-Nürnberg.

MacIntosh, B. R., Gardiner, P. F., and McComas, A. J. (2006). *Skeletal Muscle - Form and Function*. Human Kinetics.

Manal, K. and Buchanan, T. S. (2003). A one-parameter neural activation to muscle activation model: estimating isometric joint moments from electromyograms. *Journal of Biomechanics*, 36(8):1197 – 1202.

Manal, K., Gonzalez, R. V., Lloyd, D. G., and Buchanan, T. S. (2002). A real-time emg-driven virtual arm. *Computers in Biology and Medicine*, 32(1):25 – 36.

Markert, B., Ehlers, W., and Karajan, N. (2005). A general polyconvex strain-energy function for fiber-reinforced materials. *PAMM*, 5(1):245–246.

Martini, F. H. and Nath, J. L. (April 2008). *Fundamentals of Anatomy and Physiology*. Pearson Education.

MATLAB (2014). *version 8.3.0 (R2014a)*. The MathWorks Inc., Natick, Massachusetts.

Maurel, W., Thalmann, D., Hoffmeyer, P., Beylot, P., Gingins, P., Kalra, P., and Magnenat Thalmann, N. (1996). A biomechanical musculoskeletal model of human upper limb for dynamic simulation. In Boulic, R. and Hgron, G., editors, *Computer Animation and Simulation 96*, Eurographics, pages 121–136. Springer Vienna.

Messier, R. H., Duffy, J., Litchman, H. M., Paslay, P. R., Soechting, J. F., and Stewart, P. A. (1971). The electromyogram as a measure of tension in the human biceps and triceps muscles. *International Journal of Mechanical Sciences*, 13(7):585–598.

Mooney, M. (1940). A theory of large elastic deformation. *Journal of applied physics*, 11(9):582–592.

Morrison, J. B. (1970). The mechanics of the knee joint in relation to normal walking. *Journal of biomechanics*, 3(1):51–61.

Murray, W. M., Buchanan, T. S., and Delp, S. L. (2000). The isometric functional capacity of muscles that cross the elbow. *Journal of Biomechanics*, 33(8):943 – 952.

Murray, W. M., Buchanan, T. S., and Delp, S. L. (2002). Scaling of peak moment arms of elbow muscles with upper extremity bone dimensions. *Journal of Biomechanics*, 35(1):19–26.

Murray, W. M., Delp, S. L., and Buchanan, T. S. (1995). Variation of muscle moment arms with elbow and forearm position. *Journal of biomechanics*, 28(5):513–525.

Nash, M. P. and Hunter, P. J. (2000). Computational mechanics of the heart. *Journal of elasticity and the physical science of solids*, 61(1-3):113–141.

Oomens, C. W. J., Maenhout, M., van Oijen, C. H., Drost, M. R., and Baaijens, F. P. (2003). Finite element modelling of contracting skeletal muscle. *Philosophical Transaction of the Royal Society B*, 358:1453–1460.

OpenStax College (2013). *Skeletal Muscle*. OpenStax College, http://cnx.org/content/-m46476/1.3/. OpenStax-CNX.

Otten, E. (2003). Inverse and forward dynamics: models of multi–body systems. *Philosophical Transactions of the Royal Society of London. Series B: Biological Sciences*, 358(1437):1493–1500.

Pandy, M. G., Zajac, F. E., Sim, E., and Levine, W. S. (1990). An optimal control model for maximum-height human jumping. *Journal of biomechanics*, 23(12):1185–1198.

Patriarco, A. G., Mann, R. W., Simon, S. R., and Mansour, J. M. (1981). An evaluation of the approaches of optimization models in the prediction of muscle forces during human gait. *Journal of Biomechanics*, 14(8):513–525.

Rajagopal, V., Lee, A., Chung, J.-H., Warren, R., Highnam, R. P., Nash, M. P., and Nielsen, P. M. (2008). Creating individual-specific biomechanical models of the breast for medical image analysis. *Academic Radiology*, 15(11):1425–1436.

Rivlin, R. S. (1948). Large elastic deformations of isotropic materials. iv. further developments of the general theory. *Philosophical Transactions of the Royal Society of London. Series A, Mathematical and Physical Sciences*, 241(835):379–397.

Röhrle, O. (2010). Simulating the electro-mechanical behavior of skeletal muscles. *IEEE Computing in Science and Engineering*, 12(6):48–58.

Röhrle, O., Davidson, J. B., and Pullan, A. J. (2008). Bridging scales: A three-dimensional electromechanical finite element model of skeletal muscle. *Journal on Scientific Computing*, 30:2883–2904.

Röhrle, O. and Pullan, A. J. (2007). Three-dimensional finite element modelling of muscle forces during mastication. *Journal of biomechanics*, 40(15):3363–3372.

Saini, H. S. (2012). Analysis of contact between molars during clenching with 3d fea. Master's thesis, University of Stuttgart.

Scheepers, F., Parent, R. E., Carlson, W. E., and May, S. F. (1997). Anatomy-based modeling of the human musculature. In *Proceedings of the 24th annual conference on Computer graphics and interactive techniques*, pages 163–172. ACM Press/Addison-Wesley Publishing Co.

Schipplein, O. and Andriacchi, T. P. (1991). Interaction between active and passive knee stabilizers during level walking. *Journal of Orthopaedic Research*, 9(1):113–119.

Schmitt, S. (2006). *Über die Anwendung und Modifikation des Hill'schen Muskelmodells in der Biomechanik*. PhD thesis, Institut für Astronomie und Astrophysik, Eberhard-Karls-Universität Tübingen.

Schröder, J. and Brinkhues, S. (2014). A novel scheme for the approximation of residual stresses in arterial walls. *Archive of Applied Mechanics*, 84(6):881–898.

Seireg, A. and Arvikar, R. (1975). The prediction of muscular load sharing and joint forces in the lower extremities during walking. *Journal of Biomechanics*, 8(2):89 – 102.

Seireg, A. and Arvikar, R. J. (1973). A mathematical model for evaluation of forces in lower extremeties of the musculo-skeletal system. *Journal of biomechanics*, 6(3):313–326.

Shacham, S., Castel, D., and Gefen, A. (2010). Measurements of the static friction coefficient between bone and muscle tissues. *Journal of biomechanical engineering*, 132(8):084502.

Sharafi, B., Ames, E. G., Holmes, J. W., and Blemker, S. S. (2011). Strains at the myotendinous junction predicted by a micromechanical model. *Journal of biomechanics*, 44(16):2795–2801.

Sharafi, B. and Blemker, S. S. (2010). A micromechanical model of skeletal muscle to explore the effects of fiber and fascicle geometry. *Journal of Biomechanics*, 43(16):3207–3213.

Spencer, A. J. M. (1971). Theory of invariants. *Continuum physics*, 1(Part III):239–352.

Spitzer, V., Ackerman, M. J., Scherzinger, A. L., and Whitlock, D. (1996). The visible human male: A technical report. *Journal of the American Medical Informatics Association*, 3:118–130.

Sprenger, M., Karajan, N., Schmitt, S., and Röhrle, O. (2011). On the coupling of 3d-1d muscle models for lumbar spine mechanics. *PAMM*, 11(1):125–126.

Sprenger, M., Schmitt, S., and Röhrle, O. (2013). Towards modelling the dynamics of a 3d continuum-mechanical two-muscle musculoskeletal system. *PAMM*, 13(1):65–66.

Tözeren, A. (2000). *Human body dynamics: classical mechanics and human movement*. Springer.

Truesdell, C. and Noll, W. (2004). *The non-linear field theories of mechanics*. Springer.

Van der Helm, F. C. T., Veeger, H. E. J., Pronk, G. M., Van der Woude, L. H. V., and Rozendal, R. H. (1992). Geometry parameters for musculoskeletal modelling of the shoulder system. *Journal of Biomechanics*, 25(2):129 – 144.

Van Donkelaar, C. C., Drost, M. R., Van Mameren, H., Tuinenburg, C. F., Janssen, J. D., and Huson, A. (1995). Three-dimensional reconstruction of the rat triceps surae muscle and finite element mesh generation of the gastrocnemius medialis muscle. *European journal of morphology*, 34(1):31–37.

Van Leeuwen, J. L. and Spoor, C. W. (1992). Modelling mechanically stable muscle architectures. *Philosophical Transactions of the Royal Society of London. Series B: Biological Sciences*, 336(1277):275–292.

Van Loocke, M., Lyons, C. G., and Simms, C. K. (2006). A validated model of passive muscle in compression. *Journal of biomechanics*, 39(16):2999–3009.

van Zuylen, E. J., van Velzen, A., and Denier van der Gon, J. J. (1988). A biomechanical model for flexion torques of human arm muscles as a function of elbow angle. *Journal of Biomechanics*, 21(3):183 – 190.

Vankan, W. J., Huyghe, J. M., Janssen, J. D., and Huson, A. (1995). A 3-d finite element model of blood perfused rat gastrocnemius medialis muscle. *European journal of morphology*, 34(1):19–24.

Wang, Y. K., Nash, M. P., Pullan, A. J., Kieser, J. A., and Röhrle, O. (2013). Model-based identification of motion sensor placement for tracking retraction and elongation of the tongue. *Biomechanics and modeling in mechanobiology*, 12(2):383–399.

Weiss, J. A. and Gardiner, J. C. (2001). Computational modeling of ligament mechanics. *Critical Reviews in Biomedical Engineering*, 29(3):303–371.

Wirtz, D. (2013). *Model Reduction for Nonlinear Systems: Kernel Methods and Error Estimation*. PhD Thesis, University of Stuttgart.

Woittiez, R. D., Huijing, P. A., Boom, H. B. K., and Rozendal, R. H. (1984). A three-dimensional muscle model: A quantified relation between form and function of skeletal muscles. *Journal of Morphology*, 182(1):95–113.

Woods, J. J. and Bigland-Ritchie, B. (1983). Linear and non-linear surface emg/force relationships in human muscles: An anatomical/functional argument for the existence of both. *American Journal of Physical Medicine & Rehabilitation*, 62(6):287–299.

Wriggers, P. (2002). *Computational Contact Mechanic*. Wiley, New York.

Wu, T., Hung, A. P.-L., Hunter, P., and Mithraratne, K. (2013). Modelling facial expressions: A framework for simulating nonlinear soft tissue deformations using embedded 3d muscles. *Finite Elements in Analysis and Design*, 76:63–70.

Wünsche, B. (1999). The visualization of 3d stress and strain tensor fields. In *Proceedings of the 3rd New Zealand Computer Science Research Student Conference, University of Waikato, Hamilton, New Zealand, Apirl*, pages 109–116.

Yucesoy, C. A., Koopman, B. H. F. J. M., Huijing, P. A., and Grootenboer, H. J. (2002). Three-dimensional finite element modeling of skeletal muscle using a two-domain approach: linked fiber-matrix mesh model. *Journal of biomechanics*, 35(9):1253–1262.

Zajac, F. E. (1989). Muscle and tendon: properties, models, scaling, and application to biomechanics and motor control. *Critical reviews in biomedical engineering*, 17(4):359–411.

Zamir, E. A. and Taber, L. A. (2004). On the effects of residual stress in microindentation tests of soft tissue structures. *Journal of biomechanical engineering*, 126(2):276–283.

Zhe, Z., Ling-li, Q., Wen-bin, H., and Hong-wei, W. (2004). Effective stress and strain in finite deformation. *Applied Mathematics and Mechanics*, 25(5):595–604.

Zheng, Y. and Mak, A. F. T. (1999). Objective assessment of limb tissue elasticity: development of a manual indentation procedure. *Journal of Rehabilitation Research & Development*, 36(2).

Zhu, J., Taylor, Z. R. L., and Zienkiewicz, O. C. (2005). *The finite element method: its basis and fundamentals*. Butterworth-Heinemann.

Zuniga, E. N. and Simons, E. G. (1969). Nonlinear relationship between averaged electromyogram potential and muscle tension in normal subjects. *Archives of physical medicine and rehabilitation*, 50(11):613–620.

Curriculum Vitae

Personal Data:

Name:	Michael Sprenger
Parents:	Dieter Sprenger and Barbara Forstmann
Siblings:	Carola Schade
Date of birth:	July 11, 1981
Place of birth:	Aalen, Germany
Nationality:	German
Marital status:	unmarried

Education:

09/1988 – 07/1992	Grundschule Gültlingen
09/1992 – 06/2002	Andreae Gymnasium Herrenberg
06/2002	degree: "Allgemeine Hochschulreife"
10/2003 – 07/2009	studies in "Umweltschutztechnik" at the University of Stuttgart
07/2006 – 06/2007	ERASMUS at NTNU Trondheim, Norway
07/2009	degree: "Diplom-Ingenieur (Dipl.-Ing.) Umweltschutztechnik"

Internships:

05/2008 – 07/2008	StatoilHydro, Bergen, Norway
07/2007	student assistant at the Department of Civil and Transport Engineering, NTNU Trondheim, Norway
03/2007	research project at the Department of Arctic Technology at UNIS, Svalbard, Norway
10/2004 – 06/2006	student assistant at the Institute of Applied Mechanics (CE), Chair II, University of Stuttgart, Germany
05/2003 – 06/2003	A-D-W, Wildberg, Germany

Civilian Service:

07/2002 – 04/2003	DRK-Pflegeheim Franziska-von-Hohenheim-Stift, Jettingen, Germany

Professional Occupation:

08/2009 – 10/2015	teaching and research assistant at the Continuum Biomechanics and Mechanobiology Research Group at the Institute of Applied Mechanics (CE) at the University of Stuttgart, Germany and at the Stuttgarter Research Centre for Simulation Technology (SimTech - Cluster of Excellence), University of Stuttgart

Released Report Series

CBM-01 Thomas Heidlauf: *Chemo-Electro-Mechanical Modelling of the Neuromuscular System*, September 2015

CBM-02 Michael Sprenger: *A 3D Continuum-Mechanical Model for Forward-Dynamics Simulations of the Upper Limb*, October 2015